

Inferring Geodesic Cerebrovascular Graphs: Image Processing, Topological Alignment and Biomarkers Extraction

Stefano Moriconi

A dissertation submitted in partial fulfillment
of the requirements for the degree of
Doctor of Philosophy
of
University College London.

Medical Physics and Biomedical Engineering
University College London

February 20, 2020

I, Stefano Moriconi, confirm that the work presented in this thesis is my own. Where information has been derived from other sources, I confirm that this has been indicated in the work.

Abstract

A vectorial representation of the vascular network that embodies quantitative features - location, direction, scale, and bifurcations - has many potential neurovascular applications. Patient-specific models support computer-assisted surgical procedures in neurovascular interventions, while analyses on multiple subjects are essential for group-level studies on which clinical prediction and therapeutic inference ultimately depend. This first motivated the development of a variety of methods to segment the cerebrovascular system. Nonetheless, a number of limitations, ranging from data-driven inhomogeneities, the anatomical intra- and inter-subject variability, the lack of exhaustive ground-truth, the need for operator-dependent processing pipelines, and the highly non-linear vascular domain, still make the automatic inference of the cerebrovascular topology an open problem. In this thesis, brain vessels' topology is inferred by focusing on their connectedness. With a novel framework, the brain vasculature is recovered from 3D angiographies by solving a connectivity-optimised anisotropic level-set over a voxel-wise tensor field representing the orientation of the underlying vasculature. Assuming vessels joining by minimal paths, a connectivity paradigm is formulated to automatically determine the vascular topology as an over-connected geodesic graph. Ultimately, deep-brain vascular structures are extracted with geodesic minimum spanning trees. The inferred topologies are then aligned with similar ones for labelling and propagating information over a non-linear vectorial domain, where the branching pattern of a set of vessels transcends a subject-specific quantized grid. Using a multi-source embedding of a vascular graph, the pairwise registration of topologies is performed with the state-of-the-art graph matching techniques employed in computer vision.

Functional biomarkers are determined over the neurovascular graphs with two complementary approaches. Efficient approximations of blood flow and pressure drop account for autoregulation and compensation mechanisms in the whole network in presence of perturbations, using lumped-parameters analog-equivalents from clinical angiographies. Also, a localised NURBS-based parametrisation of bifurcations is introduced to model fluid-solid interactions by means of hemodynamic simulations using an isogeometric analysis framework, where both geometry and solution profile at the interface share the same homogeneous domain. Experimental results on synthetic and clinical angiographies validated the proposed formulations. Perspectives and future works are discussed for the group-wise alignment of cerebrovascular topologies over a population, towards defining cerebrovascular atlases, and for further topological optimisation strategies and risk prediction models for therapeutic inference. Most of the algorithms presented in this work are available as part of the open-source package VTrails.

Impact Statement

The thesis describes a completely novel way to look at angiographic data, allowing, for the first time, the extraction of a fully vectorial representation of the cerebrovascular system within a consistent mathematical framework. The associated published manuscripts have been presented at the biennial conference on Information Processing in Medical Imaging in 2017, one of the most prestigious international conferences in the field (acceptance $<30\%$); also a substantial portion of this work has been presented at MICCAI 2018 (oral presentation – Top 4% of papers), towards the alignment of over-connected vascular topologies.

From an academic perspective, the formulated methodology is consistently applied to multi-modal images of the brain vasculature, where the novel technical contribution is likely to be of interest for multi-compartmental vascular image analyses, high-order image synthesis, geodesic information propagation and vascular network embedding, allowing a wide range of further scientific investigations and technical developments.

The introduction of a vascular vectorial representation stands indeed as a key-enabling technology for currently unavailable vascular group-wise and population-based analyses.

From a translational perspective, a number of clinical cardio- and neurovascular applications can be derived: from extracting patient-specific vascular models supporting interventional neuroradiology and vascular surgery, to group-wise studies of comparative neurology and cerebrovascular diseases, by aligning the vectorial vascular topologies and by embedding clinically relevant biomarkers.

Prospectively, the advances described in this thesis represent an essential con-

tribution for population studies on which both clinical prediction and therapeutic inference ultimately depend. Some of the introduced concepts constitute part of the processing bedrock for the High-Dimensional Translational Neurology Programme (Wellcome £4.5m), with the aim of automating high-dimensional outcome prediction in stroke, transforming thus the national neurological care, also in terms of early cerebrovascular diagnosis, clinical risk assessment, and long-term therapy.

On a more general scale, the work presented in this thesis would pave the way towards the development of a comprehensive, quantitative and data-driven vascular atlas of the human brain, which will help better understand neurovascular morphology and functional normality, its variability and associated pathological phenotypes.

For reproducibility and broad accessibility, all the algorithms presented in this thesis have been released on GitHub as a publicly available open-source platform VTrails, further increasing the impact of the work.

Acknowledgements

I would like to thank my primary supervisor, Dr. M. Jorge Cardoso, for his advices and guidance over the last few years. I am also very grateful for his support, flexibility and friendship.

My gratitude goes as well to all my secondary supervisors, Dr. Maria A. Zu-luaga, Prof. Rolf Jager and Dr. Parashkev Nachev who always provided me with valuable support over the course of my doctoral programme.

I would like to thank all my London-based PhD colleagues and friends, especially François, Liane, Efthymios, Sotiris, Kostas, Jonas, João, Kerstin, Marta, Rafael, Luis, Michael and Loïc, who made our office a multi-cultural, welcoming and heart-warming working place, and a crazy circus at the same time.

I am very thankful to everyone I collaborated with over these last years within the Translational Imaging Group, the Centre for Medical Image Computing, the Dementia Research Centre and King's College London. Also, I would like to thank all my work-related friends and acquaintances I had the opportunity to meet at international conferences, who confirmed me we all belong to the same big family.

Lastly, very special thanks go to my native Family, and to my brothers in arms Dome and Righe who always backed me and never made me forget about my roots, and to my sisters Bea and Capa for planning holidays when I never had the time to.

*a Riccardo, con stima e affetto,
per esserci ritrovati dopo diversi anni.*

Contents

1	Introduction	32
1.1	Cerebrovascular Imaging	32
1.2	Clinical Angiography Assessment	35
1.3	Challenges in Cerebrovascular Image Analysis	36
1.4	Thesis Outline & Contributions	39
2	State-of-the-Art	43
2.1	Models in Vascular Image Analysis	43
2.1.1	Vascular Appearance and Geometrical Models	44
2.1.2	Vessel Features and Image Measures	46
2.1.3	Segmentation Extraction Schemes	49
2.1.4	Emerging Segmentation Approaches: Deep-Learning	53
3	Vessel Enhancement	55
3.1	SLoGS Curvilinear Filterbank	56
3.1.1	Numerical Dictionary of Filtering Kernels	60
3.2	Tubular Saliency Map and Orientation Sampling	61
3.3	Connected Vesselness Map and the Tensor Field	63
3.4	Multi-Scale Maximal Integration	66
3.5	Experiments on Synthetic and Clinical Data	68
3.5.1	Connectedness of the Scalar Vesselness Map	70
3.5.2	Synthesised Tensor Field	75
3.5.3	Robustness of SLoGS Parameters	76

3.5.4	Computational Cost and Implementation	77
3.6	Observations and Remarks	78
4	Vascular Connectivity	80
4.1	Joining Vessels by Minimal Paths	81
4.2	Acyclic Connectivity Paradigm	82
4.2.1	Isotropic vs. Anisotropic Front Propagation	84
4.2.2	Experiments on Synthetic and Clinical Data	86
4.2.3	Accuracy, Precision and Recall	87
4.3	Exhaustive Connectivity Paradigm	88
4.3.1	Vascular Minimum Spanning Tree	94
4.3.2	Experiments on Synthetic and Clinical Data	94
4.3.3	Results of Geometrical and Topological Accuracy	99
4.4	Observations and Remarks	104
4.4.1	The Over-Connected Geodesic Vascular Graph	109
5	Vascular Alignment	111
5.1	Pairwise Non-rigid Registration of Vascular Graphs	113
5.2	Graph Matching Optimisation Problem	114
5.2.1	Vascular Graphs Similarity Metrics	115
5.3	Elastic Registration Pipeline	118
5.3.1	Rigid Pre-alignment	118
5.3.2	Fine Node Association with Graph Matching Algorithms . .	118
5.4	Experiments on Synthetic and Clinical Data	119
5.4.1	Results of Matching Accuracy	120
5.4.2	Cyclic and Non-isomorphic Anastomoses: Circle of Willis .	122
5.5	Observations and Remarks	124
5.6	Perspectives on Group-wise Vascular Alignment	130
5.6.1	Fusing Topologies towards Cerebrovascular Atlases	136
6	Vascular Biomarkers	143
6.1	Biomarkers from Hemodynamic Simulations	144

6.2	Lumen Segmentation with Geodesic Snakes	149
6.2.1	Accuracy of Geodesic Snakes	151
6.3	Vascular Graph-based Analog-Equivalents	153
6.3.1	Hybrid Vascular Lumped-Parameters Model	154
6.3.2	Graph-based Analog-Equivalent	155
6.3.3	Modelling Perturbations on Vascular Topologies	155
6.3.4	Preliminary Experiments: Vascular Trees	156
6.3.5	Neurovascular Resilience	160
6.4	NURBS Parametrisation for Hemodynamics with Isogeometric Analysis	168
6.4.1	Parametrisation Pipeline.	169
6.4.2	G^2 Periodic Closed Contours	173
6.4.3	Junction Control Octagons and Scaffolding	173
6.4.4	Surface Coons Patches and G^2 Control Net	177
6.4.5	Multi-compartmental Solid Patches	181
6.4.6	Parametrisation Validation	182
6.5	Observations and Remarks	187
7	Discussion	191
7.1	Future Research Directions	195
7.1.1	Topological Optimisation of Vascular Networks	196
7.1.2	Patient-Specific Models for Life-Long Risk Prediction	199
7.2	Closing Remarks	201
A	Open Source Effort	202
A.1	VTrails	202
	Bibliography	213

List of Figures

1.1	Examples of typical cerebrovascular abnormalities: a. Occlusion of the middle cerebral artery, causing ischaemic stroke; b. and c. Stenoses with different level of severity; d. Pronounced cerebrovascular tortuosity; e. and f. Small and large aneurysms respectively.	33
1.2	Common imaging modalities employed in cerebrovascular applications: from top to bottom, left to right, Digital Subtraction Angiography (DSA); axial, sagittal and coronal view of a Computed Tomography Angiography (CTA); Ultrasound (US) scan of the Common Carotid Artery (CCA) bifurcating into the External and Internal Carotid Artery, respectively ECA and ICA; three canonical orthogonal views of a cerebral MRI Time-of-Flight (TOF).	34
1.3	Thesis Outline: Macro-Section Flowchart. <i>Cerebrovascular Imaging</i> in Chapter 1 and <i>State-of-the-Art</i> in Chapter 2. <i>Vessel Enhancement</i> in Chapter 3. <i>Vascular Connectivity</i> in Chapter 4. <i>Vascular Alignment</i> in Chapter 5. <i>Vascular Biomarkers</i> in Chapter 6. <i>Discussion and Future Work</i> in Chapter 7.	42
3.1	SLoGS filterbank: Top. Filter impulse-response Γ and associated integral orientation basis Φ_Γ ; Derivative SLoGS filter kernel $K_{(\Gamma)}$, and associated ellipsoidal tensor form $T_{(\Gamma)}$. Bottom. Definition of a dictionary of filtering kernels (DFK), including the linear $\Gamma_{\text{tube}} = \Gamma(\mathbf{x}, \sigma_1 > \sigma_2 = \sigma_3, \mathbf{c} = \mathbf{0})$	56

- 3.2 Synthesis of the vesselness maps: multi-scale processing image pyramid; early tubular saliency map V_{tube} with a subset of voxel binary seeds \tilde{S} and associated principal orientations; connected vesselness map (\mathcal{V}_s) and tensor field (\mathcal{M}_s) at scale s 61
- 3.3 Orientation ω_{ico} sampling using a representative icosphere of subdivision level equal to 1. (Left) Subset of orientations accounting for rotations around a fixed principal axis (red arrow). The complete set ω_{ico}^{all} encodes all rotations around the principal axes. For purely symmetric kernels, such as Γ_{tube} , ω_{ico}^{all} boils down to a reduced set. (Right) Representative subset of orientations from a randomised sampling of the complete set of orthonormal bases ω_{ico}^{all} . . . 62
- 3.4 Seeds \tilde{S} detection as in eq. 3.7. Representative slice where voxels in red, blue, green colours satisfy the respective conditions. The resulting intersection is highlighted with white seeds \tilde{S} 64
- 3.5 Representative synthesis of a tensor field in 2D. (Left-top) Steering a tensor patch along the orientation θ with a rigid mapping in the Log-Euclidean space. (Left-bottom) Re-sampling the steered tensor patch with adequate padding in the Log-Euclidean space, to preserve the tensor patch size. (Right-top) Three independent components of the 2D tensor patch in the Log-Euclidean space. Six independent components are determined for a 3D tensor patch. (Right-bottom) Sliding tensor patch-sweep for each independent component on the tensor field domain. The resulting tensor field $\mathcal{M}_s, (LE)$ is recovered by independently processing each Log-Euclidean component. 65

- 3.6 Representative synthesis of a tensor field in 2D. (Left) Patch-sweep element-wise weighted-sum in the pixel (or voxel) neighbourhood as in eq. 3.12. Each contribution is element-wise multiplied and summed over the one-to-one corresponding pixel (or voxel) in the tensor field domain. (Right) Representative contributions of the cumulative normalising weight map W , as in eq. 3.13, for a scalar SLoGS filter response $V_S^{(v,K,\theta)}$, for a scalar Gaussian impulse response $\Gamma_{(K)}^{(\theta)}$ of the steered kernel, and for the 2D blending Hann window Ξ 67
- 3.7 Connectedness of the vesselness response maps for Frangi (FFR) [70], Optimally Oriented Flux (OOF) [106], and proposed scalar connected vesselness map on a digital phantom (HCP) example and on data of a phase contrast (PC) cerebral venogram. 70
- 3.8 Representative filter-response for the synthetic degraded vascular trees [82] with different vascular ridge detectors: Top: Original image, FFR, OOF and \mathcal{V} from VTrails. Bottom: Noisy and corrupted image NL_b^{II} , RORPO, HDCS, and \mathcal{M} from VTrails. 72
- 3.9 Representative filter-response for clinical cerebrovascular angiographies (RAA, PC, MRA, and CTA) with VTrails using SLoGS: Original scan with manual annotation gold standard (GS); scalar connected vesselness map \mathcal{V} and associated tensor field \mathcal{M} 73
- 3.10 Foreground (fG) and background (bG) intensity distribution for degraded synthetic vascular trees [82] using FFR, OOF, RORPO, HDCS and VT (\mathcal{V}): Histogram overlap for at different noise corruption levels. 74
- 3.11 Synthesised tensor fields for: Left. 3D hand-crafted phantom (HCP). Right. 2D toy-examples of a synthetic vascular tree [82], together with a subregion of a retinal angiography. 76

3.12	Parameters robustness and performance analysis on 3 DFKs and using a convoluted phantom of size $1.0\times$, $1.5\times$ and $2.0\times$ $[50\times 50\times 100]$ voxels.	77
4.1	Greedy and sequential acyclic connectivity paradigm on a 2D synthetic phantom. From Initialisation to Convergence, the intermediate steps are shown at Collision, Path Extraction and Fast Updating Scheme. Geodesic values are represented with a shaded colormap, whereas colliding, merging and updating regions are shown in solid colours.	82
4.2	Comparison of iso-curves for the isotropic and anisotropic level-set propagation on the given Riemannian potential \mathcal{P} . Anisotropic iso-contours show a more elongated pattern and profile, accordingly with the local anisotropy of the potential.	85
4.3	Geodesic extraction and fully connected tree using the acyclic connectivity paradigm with both isotropic and anisotropic front propagations. Left: synthetic phantom of convoluted structure, where short-cuts occur for the isotropic level-set. Similarly, short-cuts are found in the retinal subregion, even for large vessels (red circle). . .	86
4.4	Comparison of the vascular connected trees against the respective ground-truth for a representative set of synthetic data, and for a carotid CTA and for a middle cerebral artery TOF MRI. Note that main branches are correctly identified and connected.	87
4.5	Exhaustive geodesic connectivity paradigm: Anisotropic level-set from the Riemannian potential \mathcal{P} and subsequent extraction of a minimal path from a pair of initial seeds \mathbf{p}_A and \mathbf{p}_B . – The paradigm follows in Fig. 4.7	90

- 4.6 Representative example of geodesic energy profiles for a 1D generic case with two source points \mathbf{p}_A and \mathbf{p}_B . (Top) Geodesic energy profiles $\mathcal{U}_{\mathbf{p}_A}$ and $\mathcal{U}_{\mathbf{p}_B}$ are given in blue and red solid lines respectively for the pair of source points. (Centre) Intermediate energy contributions: $(\mathcal{U}_{\mathbf{p}_A} + \mathcal{U}_{\mathbf{p}_B})$ in green; $|\mathcal{U}_{\mathbf{p}_A} - \mathcal{U}_{\mathbf{p}_B}|$ in magenta solid lines. Respective local minima (circles) and global minima (bullets). (Bottom) Resulting energy functional \mathcal{F}_{AB} , with a unique global minimum in the correspondence of \mathbf{m}_{AB} 91
- 4.7 Exhaustive geodesic connectivity paradigm: topological inference of the over-connected graph Π and of its geodesic minimum spanning tree ζ . *Vector* topology of the over-connected graph Π (first iteration), of its minimum spanning tree ζ (first iteration), and resulting tree topology at convergence. – The paradigm starts in Fig. 4.5 93
- 4.8 Representative example of noisy synthetic vascular tree NL_b^H : resulting minimum spanning tree inferred with VT_{auto} 100
- 4.9 Inference of the geodesic vascular network for representative cerebrovascular angiographies with VT_{auto} : Original scan with annotation (GS); Geodesic Vascular Graph Π at convergence and Minimum Spanning Trees ζ for deep-brain vascular structures. – The Riemannian vesselness potential is in Fig. 3.9. 105
- 4.10 RAA topological inference with VT_{auto} . Left: Geodesic Vascular Graph Π . Right: Minimum Spanning Tree ζ of the underlying anatomical vascular tree. Missing branch in ζ , due to a geodesic short-cut from *kissing-vessels*. Bottom: Vectorial representation in the form of a connected hierarchical graph. 108

- 4.11 Close-up of RAA topological inference with VT_{auto} from Fig. 4.10 (red arrow). Left: Portion of the Geodesic Vascular Graph preserving the vascular segmentation with redundant and uncertain connecting geodesics. Right: Portion of the associated Minimum Spanning Tree, where a missing branch occurs due to cyclic aberration by the kissing-vessel artifact. 109
- 5.1 Geodesic Vascular Graph and GM problem of non-linearly deformed topologies. Left: Extraction of a fully-connected topology from an initial set of nodes, as in Section 4.3. Right: Associated graph representations and minimum spanning trees for two topologically different instances (\mathcal{G}^A and \mathcal{G}^B) of the same underlying vascular anatomy. 113
- 5.2 Graph Matching Optimisation Problem: Resulting elastic graph alignment and nodes matching for the generalised GM problem. Instances \mathcal{G}^A and \mathcal{G}^B in this case, the over-connected geodesic vascular graphs Π as in Fig. 5.1 114
- 5.3 Vascular graphs' similarity metrics – Representative nodes and edges factorisation matrices, $\mathbf{K}_{\mathbf{n}^{AB}}$ and $\mathbf{K}_{\mathbf{e}^{AB}}$, together with the resulting affinity matrix \mathbf{K} for: a pair of Geodesic Vascular Graphs Π (top); the associated pair of minimum spanning trees ζ (bottom). Note the deprived information in the affinity matrix \mathbf{K}^{ζ} compared to \mathbf{K}^{Π} , due to the deterministic connectivity of the minimum spanning trees. 116
- 5.4 Topological vascular alignment: Experimental datasets. Left: Synthetic geodesic vascular graph Π_{synth} – Original instance and representative composition of simulated deformations. Right: Basilar Artery geodesic vascular graph (Π_{angio}) and label set [91]. 119

- 5.5 Alignment of synthetic geodesic vascular graphs Π_{synth} : Left. Rigid alignment of the geometrical embedding with Go-ICP [208]. Right: Fine Node association mapping with Graph Matching techniques (FGM). Correct matching is highlighted in green, whereas mismatched correspondences are shown in red. 121
- 5.6 Alignment of Basilar Artery geodesic vascular graphs Π_{angio} : Left. Rigid alignment of the geometrical embedding with Go-ICP [208]. Right: Fine Node association mapping with Graph Matching techniques (FGM). Accuracy is evaluated on the correct correspondences, given the labelled association ground-truth. Correct matching is shown in green, whereas mismatched associations are shown in red. 122
- 5.7 Synthetic Graph Matching Accuracy of different GM algorithms: Π_{synth} vs. ζ_{synth} for different levels of non-linear deformation. . . . 123
- 5.8 Cerebrovascular Cyclic Anastomosis: Circle of Willis (CoW) – Geodesic vascular graph (Π^{CoW}) and manually annotated landmarks [91], Front and Top view. 124
- 5.9 Vascular Topological Alignment: Elastic registration of cyclic anastomoses - Circle of Willis (CoW) using the over-connected geodesic vascular graphs Π for a representative set of subjects ($sbjA$, $sbjB$ and $sbjC$). Top: Complete-to-Complete anastomoses registration. Bottom: Complete-to-Incomplete anastomoses registration. 125
- 5.10 Representative Performance of Graph Matching Algorithms: Accuracy for Synthetic Geodesic Vascular Graphs Π_{synth} 128
- 5.11 Representative Performance of Graph Matching Algorithms: Accuracy for Basilar Artery Geodesic Vascular Graphs Π_{angio} 129

5.12	Group-wise Global-to-Local Topological Alignment and Matching Propagation: Top: possible adaptation of the implicit manifold to native networks, as first proposed in the Geodesic Information Flows by Cardoso et al. [33]. Bottom-Left: Geodesic Vascular Graphs $\Pi _{\{a,b,c,d\}}$ embedded on each node, given the pair-wise and jointly optimised correspondence matrices \mathbf{X} . Bottom-right: Par- tition and decomposition for a representative topology into sub- graphs, sub-nets and cliques.	137
6.1	Lumen Segmentation with Cross-Sectional Geodesic Snakes. Rep- resentative phantom combined with the previously inferred vascular tree. Vessel lumen delineation are consistent along the tubular-like elongated structures, with local overlap at the respective junctions. Closed-contours are enforced using the geodesic snakes (active con- tour) formulation.	149
6.2	Vessel Segmentation with Geodesic Snakes: representative an- giographies in [6] and [28] repositories (top); a MR time-of-flight angiography of the Circle of Willis (bottom).	152
6.3	Hybrid Vascular Lumped-Parameters Model of a Phantom: lu- men segmentation with geodesic snakes as in Section 6.2 (left); Impedance (red), Flow (gray) and Pressure drop (blue) asymptotic values (right).	153
6.4	Hemodynamic analog equivalent and steady-state blood flow sim- ulation with the described lumped-parameters model for a cerebral vascular tree from [6].	157
6.5	Full-brain set of deep-cerebral vascular trees from [28].	158
6.6	Hemodynamic analog equivalent and steady-state blood flow sim- ulation for a the deep-brain atrerial trees ζ_a and ζ_b as in Fig. 6.5. Analog resistance equivalent R , simulated blood flow rate Q and blood pressure drops ΔP	159

- 6.7 Hemodynamic analog equivalent and steady-state blood flow simulation for a the deep-brain arterial trees ζ_c and ζ_d as in Fig. 6.5. Analog resistance equivalent R , simulated blood flow rate Q and blood pressure drops ΔP . Note the functionally implausible hemodynamic values for the entire sub-tree of ζ_d 160
- 6.8 Circle of Willis: manually annotated landmarks and graph equivalent for an exact network, i.e. given the anatomical prior \mathcal{A} . Sources SRC (\diamond) and potential grounds GND (\blacktriangledown) are shown for the anatomical blood inlets and outlets. 161
- 6.9 Autoregulation mechanisms: blood flow, pressure and network resilience ρ for unperturbed graphs, and for the simulated stenotic ICA and occluded PCOM - Full Cycle – Both PCOMs – Phenotype . . . 162
- 6.10 Autoregulation mechanisms: blood flow, pressure and network resilience ρ for unperturbed graphs, and for the simulated stenotic ICA and occluded PCOM - One Posterior Communicating Artery Phenotype 163
- 6.11 Autoregulation mechanisms: blood flow, pressure and network resilience ρ for unperturbed graphs, and for the simulated stenotic ICA and occluded PCOM - Absent Posterior Communicating Arteries Phenotype. 163
- 6.12 Flow and pressure distributions (boxplots) for unperturbed anatomically exact topologies and for 3 perturbation classes of increasing stenoses and tortuosity. Increasing perturbations from dark (unperturbed) to light colours. 164
- 6.13 Hypertension histogram interpolated with a gamma function for unperturbed anatomically exact topologies and for 3 perturbation classes of increasing stenoses and tortuosity. Decreasing resilience indices ρ for increasing perturbations, from dark (unperturbed) to light blue (m_3). 165

- 6.14 Vascular graph sampling with hemodynamically-compatible simulations: spatial and matricial embeddings of \mathcal{G} and $\tilde{\mathcal{G}}$, before and after pruning, respectively. 166
- 6.15 End-to-end parametrisation on vascular junctions: from geodesic snakes on clinical angiographies to hemodynamic simulations using IGA. 169
- 6.16 NURBS primitives adopted in the parametrisation. (Left) A curvilinear segment with form $\mathbf{C}(u)$. (Centre) A non-planar quadrilateral surface patch of the form $\mathbf{S}(u, v)$. (Right) A Hexahedral solid patch of the form $\mathbf{V}(u, v, w)$. In the NURBS homogeneous space, u -, v -, and w -directions map the circumferential, the longitudinal and the radial tube directions, respectively. 170
- 6.17 Cross-sectional segmentation of a vascular phantom. (Left-centre) Planar geodesic snake extraction as in section 6.2. (Right) Conversion of the snake into a closed parametric curve with a shape preserving fit. Eight unique control points $\hat{\mathbf{p}}_{i=0,1,\dots,7}$ define the closed parametric contour $\hat{\mathbf{C}}(\hat{u})$. A geometrical G^2 condition enforces $\hat{\mathbf{p}}_0 = \hat{\mathbf{p}}_8$, $\hat{\mathbf{p}}_1 = \hat{\mathbf{p}}_9$, and $\hat{\mathbf{p}}_2 = \hat{\mathbf{p}}_{10}$. Eight open curvilinear segments $\mathbf{C}(u)$ are re-parametrised as separate patches, each preserving the geometrical G^2 condition. The boundary control points \mathbf{p}_0 and \mathbf{p}_7 of $\mathbf{C}(u)$ coincide in pairs with the internal $\hat{\mathbf{p}}_i$ of $\hat{\mathbf{C}}(\hat{u})$ (green dashed lines). 172

- 6.18 Junction parametrisation: (top) proximal octagons $\Sigma^{(b)}$ (dashed blue lines, square vertices) and mutually-intersecting contours; set of directional vectors (6.7) for CV, CX and CVX quadrants; (middle) construction of control octagons: non-planar projective $\Pi^{(b)}$ (solid blue lines, circle vertices), and planar capping $\Theta^{(b)}$ (dotted blue lines, triangular vertices); piece-wise G^2 NURBS curves of the control octagons along u ; (bottom) orderly lofting the curvilinear pieces along v on the CV quadrant for the guiding surfaces \mathbf{S}^{loft} ; G^2 construction scaffolding, resulting in closed sets of quadrilateral acrs. 174
- 6.19 Patch-based junction surface: (top) G^0 -continuous set of Coons patches from the scaffolding; Hexagonal pattern of the CV quadrant and associated control net. Creases are observed at the boundaries/interfaces among the neighbouring patches; (bottom) optimised G^2 -continuous set of Coons patches with algorithm 2; resulting control net in the CV quadrant and coplanar neighbourhood of the control point corner in blue. 178
- 6.20 Multi-compartmental partition of the junction: patch-based inner blood-fluid (\mathbf{V}_{bf}) and outer vessel wall (\mathbf{V}_{vw}), given a constant wall thickness θ . Individual patches are delineated in red; sectioning view by resecting the CV quadrant. 182
- 6.21 Representative set of synthetic junctions for the evaluation of the patch-based parametrisation and surface continuity. \mathbf{J}_{Σ} and \mathbf{J}_{Π} model strong variations induced by pathology with irregular cross-sections and swollen junctions for stenoses and aneurysms, respectively. 183
- 6.22 Clinical angiographic modelling & fluid dynamic simulations using an IGA framework: (top) tubular phantom construction outline and associated fluid pressure and velocity streamlines computed within the \mathbf{V}_{bf} domain. 185

6.23	Clinical angiographic modelling & fluid dynamic simulations using an IGA framework: cerebral artery with aneurysm – fusion of multi-step construction paradigm and fluid dynamic simulations using <i>geoPDEs</i> [55], solving a canonical Stokes’ problem.	186
7.1	Redundant and Over-Connected Geodesic Vascular Graph Π . Comparison of the geometrical and purely topological embedding of the network. Local uninformative connecting overhead, here in the elongated linear segments (graph’s <i>flares</i>) can be conservatively simplified, streamlining the topology towards a more compact and sparse representation.	196
7.2	Topological Optimisation Strategies. From the original over-connected geodesic vascular graph Π of the Basilar Artery phantom, a bootstrapped version ($\hat{\Pi}$) and a further phylogenetically simplified one ($\hat{\hat{\Pi}}$) are retrieved, conservatively reducing both nodes’ and edges’ cardinalities and increasing the overall graph compactness. Note that graph’s flares are eventually simplified, whereas the connecting uncertainty at the vascular junction is preserved, as well as possible topological cycles.	197
7.3	Graph Hierarchical Partition and Decomposition. Representative toy example of a condensed network, where non-disjoint sub-nets and topological partitions can be derived and further re-combined, allowing flexibility for multi-scale graph-cuts. Green and pink edges are non-disjoint shared sub-graph cliques and inherited ones, respectively, throughout the topological decomposition.	199
A.1	The logo of the VTrails toolkit, available at https://vtrails.github.io/VTrailsToolkit/	202
A.2	Graphic User Interface for the Definition of an Arbitrary Dictionary of Filtering SLoGS Kernels. Tutorial: https://youtu.be/f3LahhqzHFc	205

- A.3 VTrails Demo: Fully-automatic processing pipeline for the extraction of vascular trees from angiographic images. `VTrailsDEMO_01.m` – Connected Vesselness Map, Tensor Field, Over-Connected Geodesic Vascular Graph and resulting Minimum Spanning Tree. . . 212

List of Tables

3.1	SLoGS parameters of the adopted DFK.	60
3.2	Synthetic datasets of vascular trees generated with [82]	68
3.3	Histogram overlap ($fG \cap bG$), foreground vs. background separation range ($fG \leftrightarrow bG$), foreground interquartile range (fG_{IQR}), and foreground Spearman correlation (fG_ρ) with the uncorrupted image, for FFR, OOF, RORPO, HDCS and VT scalar vesselness (mean \pm sd). \dagger : significantly worse ($p < 0.05$) and $*$: significantly better ($p < 0.05$) than VT in paired Wilcoxon signed-rank test. . . .	75
4.1	Connectivity tree error distances, precision and recall (mean \pm SD). Left: synthetic vascular tree at degradation levels N_1 and N_2 . Note the invariance of all metrics regardless the degradation level. Right: TOF and CTA.	88
4.2	Synthetic trees at different noise levels (NL) – Symmetric error ε_S [mm] (<i>a.</i>) and Hausdorff _{95%} distance ε_H [mm] (<i>b.</i>) for the minimum spanning trees (ζ). Values are reported mean \pm SD. Best accuracy for the semi-supervised connectivity in <i>italic</i> font; best accuracy VT _{auto} vs. VT _{semi} in bold font.	100
4.3	Synthetic trees at different noise levels (NL) – Symmetric error ε_S [mm] (<i>a.</i>) and Hausdorff _{95%} distance ε_H [mm] (<i>b.</i>) for the branch-points (bp) location. Values are reported mean \pm SD. Best accuracy for the semi-supervised connectivity in <i>italic</i> font; best accuracy VT _{auto} vs. VT _{semi} in bold font.	101

4.4	Synthetic trees at different noise levels (NL) – Topological accuracy [%]: TED _{ov} ($a.$) and DIADEM ($b.$) metrics. Values are reported mean \pm SD. Best accuracy for the semi-supervised connectivity in <i>italic</i> font; best accuracy VT _{auto} vs. VT _{semi} in bold font.	102
4.5	Clinical Angiographies – Symmetric error ϵ_S [mm] and Hausdorff distance ϵ_H [mm] of trees (ζ) and branchpoints (bp) (mean \pm SD) – Topological tree accuracy DIADEM [%] metric.	104
5.1	Clinical Graph Matching Accuracy: Inter-subject registration of Π_{angio} vs. ζ_{angio} . Values are mean \pm SD, (median), $* = p < 0.05$	123
5.2	Comparison of the Computational Complexity for the Current State-of-the-Art Multi-Graph Matching Algorithms. Table taken from Yan et al. [205].	135
6.1	Accuracy of geodesic snakes vs. GS: average symmetric error $\bar{\epsilon}$, median ϵ_{Q_2} and Hausdorff-95 $\epsilon_{H_{95}}$ [mm] (mean \pm SD), averaging on the complete datasets in [6, 28].	153
6.2	NURBS parametrisation for a curvilinear primitive $C(u)$ along the circumferential direction u . Note that for curvilinear primitives along different directions, the longitudinal v or the radial w are considered, instead of u	172
6.3	Root mean square errors ϵ of both Jacobian and Hessian components evaluated at the boudaries of the surface patches for the synthetic junctions \mathbf{J}_{iso} , $\mathbf{J}_{\tilde{\Sigma}}$ and $\mathbf{J}_{\tilde{\Pi}}$. Median values are reported together with the first- and third-quartile respectively.	184

Acronyms and Abbreviations

ACA Anterior Communicating Artery.

aFM Anisotropic Fast Marching Algorithm.

BA Basilar Artery.

bG Image Background.

CAD Computed Aided Design.

CFD Computational Fluid Dynamic.

CNN Convolutional Neural Network.

CoW Circle of Willis.

CT Computed Tomography.

CTA Angiographic Computed Tomography - CT Angiography.

DFK Dictionary of Filtering Kernels.

FEM Finite Element Method.

FFR Frangi Filter.

fG Image Foreground.

$fG \cap bG$ Foreground and Background Histogram Overlap.

$fG \leftrightarrow bG$ Foreground and Background Histogram Separation Range.

fG_{IQR} Foreground Values Interquartile Range.

FGM Factorised Graph Matching Algorithm.

GA Graduated Assignment Algorithm.

GM Graph-Matching.

GND Potential Ground.

Go-ICP Globally-optimal Iterative Closest Point Algorithm.

GS Gold Standard.

GT Ground-Truth.

HCP Hand-Crafted Phantom.

HDCS Hybrid Diffusion with Continuous Switch Filter.

ICA Internal Carotid Artery.

IGA Isogeometric Analysis.

IPFP-U/SM Integer Projected Fixed Point Algorithm.

MRA Cerebral TOF MR Angiography.

MRI Magnetic Resonance Imaging.

MST Minimum Spanning Tree.

NL Noise Level.

NURBS Non-Uniform Rational B-Splines.

OOF Optimally Oriented Flux Filter.

PC Phase Contrast.

PCOM Posterior Communicating Artery.

PM Probabilistic Matching Algorithm.

QAP Quadratic Assignment Problem.

RAA Rotational Angiography of Cerebral Aneurysms.

ROI Region of Interest.

RORPO Ranking the Orientation Responses of Path Operators Filter.

RRWM Re-weighted Random Walk Matching Algorithm.

SLoGS Steerable Laplacian of Gaussian Swirls.

SM Spectral Matching Algorithm.

SMAC Spectral Matching with Affine Constraints Algorithm.

SRC Source of Potential.

TED Tree Edit Distance.

TOF Time-of-Flight.

VMTK Vascular Modelling Toolkit.

VT VTrails.

Related Publications

Peer-reviewed Journal Papers

- **Stefano Moriconi**, Maria A. Zuluaga, H. Rolf Jäger, Parashkev Nachev, Sébastien Ourselin and M. Jorge Cardoso – *Inference of Cerebrovascular Topology with Geodesic Minimum Spanning Trees*, IEEE Transactions on Medical Imaging, 2018.

Peer-reviewed Conference Papers

- **Stefano Moriconi**, Maria A. Zuluaga, H. Rolf Jäger, Parashkev Nachev, Sébastien Ourselin and M. Jorge Cardoso – *VTrails: Inferring Vessels with Geodesic Connectivity Trees*, Information Processing in Medical Imaging – IPMI, 2017.
- **Stefano Moriconi**, Maria A. Zuluaga, H. Rolf Jäger, Parashkev Nachev, Sébastien Ourselin and M. Jorge Cardoso – *Elastic Registration of Geodesic Vascular Graphs*, Medical Image Computing and Computer Assisted Intervention – MICCAI, 2018.
- **Stefano Moriconi**, Rafael Rehwald, Maria A. Zuluaga, H. Rolf Jäger, Parashkev Nachev, Sébastien Ourselin and M. Jorge Cardoso – *Towards Quantifying Neurovascular Resilience*, MICCAI, CVII-STENT Workshop, 2019.

Peer-reviewed Conference Abstracts

- Rafael Rehwald, **Stefano Moriconi**, Carole H. Sudre, M. Jorge Cardoso, H. Rolf Jäger – *The Intracranial Vasculature in a Tri-ethnic Population-based Study (SABRE): an MRA Study of Incidental Findings, Anatomical Variations, and Vessel Tortuosity*, European Congress of Radiology – ECR, 2018.
- Rafael Rehwald, **Stefano Moriconi**, Lorna Smith, Carole H. Sudre, M. Jorge Cardoso, Jonathan H. Gillard, H. Rolf Jäger – *Prevalence of Incidental Intracranial Vascular Findings in a Tri-ethnic Population-based Study* – ECR, 2019.

Editorial Effort

- *Intravascular Imaging and Computer Assisted Stenting and Large-Scale Annotation of Biomedical Data and Expert Label Synthesis – CVII-STENT and LABELS Workshop at MICCAI, 2018* – Editors: Danail Stoyanov, Zeike Taylor, Simone Balocco, Raphael Sznitman, Anne Martel, Lena Maier-Hein, Luc Duong, Guillaume Zahnd, Stefanie Demirci, Shadi Albarqouni, Su-Lin Lee, **Stefano Moriconi**, Veronika Cheplygina, Diana Mateus, Emanuele Trucco, Eric Granger and Pierre Jannin.
- *Machine Learning and Medical Engineering for Cardiovascular Health and Intravascular Imaging and Computer Assisted Stenting – MLMECH and CVII-STENT Workshops at MICCAI, 2019* – Editors: Hongen Liao, Simone Balocco, Guijin Wang, Feng Zhang, Yongpan Liu, Zijian Ding, Luc Duong, Renzo Phellan, Guillaume Zahnd, Katharina Breininger, Shadi Albarqouni, **Stefano Moriconi**, Su-Lin Lee and Stefanie Demirci.

Chapter 1

Introduction

1.1 Cerebrovascular Imaging

Modern clinical practice makes extensive use of imaging techniques to assess and evaluate the structural and functional pathophysiology in several cases. The World Health Organization [128] addresses diseases of the cerebral vasculature as the most relevant cause of morbidity and mortality in the world together with cardiovascular events happening in the heart. Amongst those, the prevalent classes of cerebrovascular diseases include atherosclerosis, stroke, cerebral aneurysm and arterio-venous malformations, small vessel disease, and altered circulation in neoplastic vascularisation [124] (Fig. 1.1). These not only cause primary damages to the brain due to altered blood flow as in thrombo-embolic ischaemia and major intra-cerebral haemorrhage, they also relate to progressive, often age-related, more complex and subtle cognitive decline and vascular dementia caused by subcortical infarcts and cerebral microbleeds at finer scale [196]. Implications of abnormalities in the cerebrovascular system are also observed in advancing Alzheimer's disease [64]. In neurology and in neuro-vascular interventional units, head-neck angiographies are obtained from routine medical imaging of the cerebrovascular system with different methods to understand and visualise the brain blood flow and supply [124]. Cerebrovascular angiographies from X-ray digital subtraction, computed tomography (CT), ultrasound, and magnetic resonance imaging (MRI) constitute the main modalities in neuro-vascular applications (Fig. 1.2). These play a predominant role in

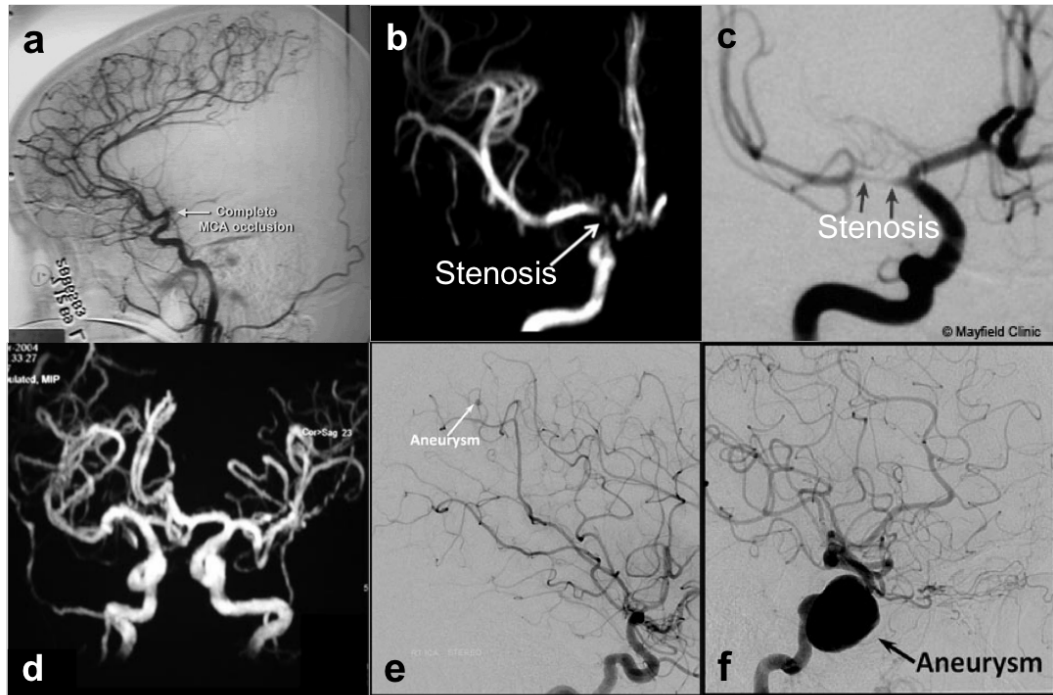


Figure 1.1: Examples of typical cerebrovascular abnormalities: a. Occlusion of the middle cerebral artery, causing ischaemic stroke; b. and c. Stenoses with different level of severity; d. Pronounced cerebrovascular tortuosity; e. and f. Small and large aneurysms respectively.

early diagnosis of neuro-vascular events, as well as in guiding patient management for acute or long-term therapies. CT angiography (CTA) is the standard imaging modality. Typical CTA scans provide volumetric images of the underlying vascular structure with high spatial resolution (down to isotropic 0.4 mm) [137]. These, on the one hand, reliably detect calcified atherosclerotic plaques causing the narrowing (stenosis) of the vessels' lumen; on the other hand, they detect (or exclude) intracranial hemorrhage from ischaemic stroke and identify eligible patients to be treated with thrombolysis therapy [96]. In the latter case, digital subtraction projections provide neurovascular surgeons with high temporal (4-15 Hz) and spatial resolution (isotropic 0.1 mm) guidance, by independently contrasting the flow in different vessels through the injection of a iodine-based contrast agent with a hemodynamically minimally invasive catheter. Ultrasound imaging is an effective approach to study the extracranial vessels, in particular, to determine the presence and severity of atherosclerotic plaques in carotid arteries [144]. Although MRI is not

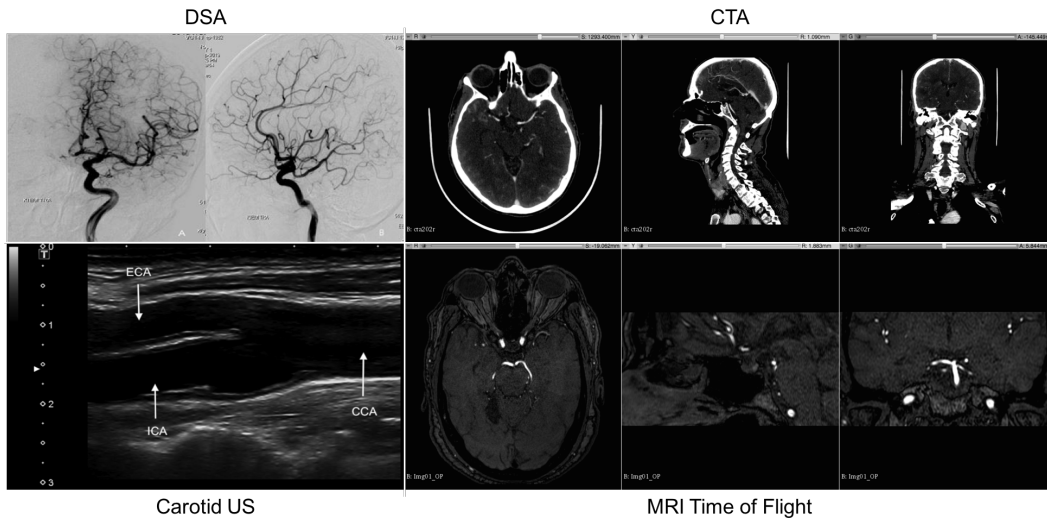


Figure 1.2: Common imaging modalities employed in cerebrovascular applications: from top to bottom, left to right, Digital Subtraction Angiography (DSA); axial, sagittal and coronal view of a Computed Tomography Angiography (CTA); Ultrasound (US) scan of the Common Carotid Artery (CCA) bifurcating into the External and Internal Carotid Artery, respectively ECA and ICA; three canonical orthogonal views of a cerebral MRI Time-of-Flight (TOF).

always the primary cerebrovascular imaging method suitable for all patients, structural and functional MRI techniques have shown a relevant impact in the field of cerebrovascular disease in the past few years by characterizing the cerebrovascular system with varying informative content and features of different nature [124, 141]. Amongst these, a combination of time-of-flight (TOF), phase contrast (PC), dynamic contrast-enhanced and arterial spin labelling imaging protocols, together with spectroscopic imaging, diffusion tensor and diffusion weighted imaging, and blood oxygenation level-dependent functional MRI, allow clinicians to outline the assessment of tissue condition, perfusion and diffusion, also to classify and differentiate (sub)types of arterial events. In other cases, the assessment of isolated cortical vein thrombosis [52], neuroinflammatory diseases [2, 19], and intracranial hypertension, susceptibility weighted imaging [81] and quantitative susceptibility mapping [80] allow for the depiction of the anatomy of deep cerebral veins and their abnormalities. From an interventional perspective, these modalities are extremely valuable for planning a variety of image-guided neurosurgical procedures such as identifying vessel-free paths for insertion of a biopsy needle or the implantation of deep-brain

stimulation probes or stereotaxic electro encephalography electrodes [23].

1.2 Clinical Angiography Assessment

Upon the vast extent of neuro-vascular imaging modalities and considering novel emerging MRI techniques, the clinical analysis and the accurate assessment of the cerebral vasculature is however performed manually by inspecting intensity projections, or image slices one at a time, or using multiple views of 3D rendering and visualization techniques [118]. This often results in high inter-observer variability, as the assessment relies on clinical experience to minimise foreshortening and vessel overlap [116]. In particularly complex cases, the agreement can be relatively poor even among experienced clinicians [78]. The cerebrovascular system is indeed highly complex. Appreciable differences and high variability of the vascular structure in the brain can be observed in the first instance among healthy subjects, where phylogenetic relations or undisclosed factors determine different vascular morphologies and topologies even for major vessels. Main arterial examples are: the complete Circle of Willis (CoW) occurring in approximately one third of the worldwide population and its incomplete variants [22]; the fenestration of the basilar artery (BA), constituting the splitting of the trunk of the vessel which rejoins afterwards; the variable course of the anterior inferior cerebellar artery, anastomosing with both the posterior inferior cerebellar artery and the superior cerebellar artery, which results in a variable amount of blood supply to the cerebellum, depending upon the posterior arterial dominance, to name a few.

Also, age-related modifications of the vascular structures are observed in healthy subjects such as the increase of vascular tortuosity, change in size and curvature. This shows therefore a high degree of morphological variability of the cerebrovascular system in healthy subjects. Furthermore, some of the mentioned pathologies, such as atherosclerotic plaques and subsequent vessel stenoses, cerebral aneurysms and vascular malformations produce structural cerebrovascular abnormalities which affect and may substantially alter the vascular network pattern in the brain at different branch-points and scale levels. In order to provide quantitative

and repeatable measures to support early diagnosis, therapeutic inference and interventional guidance, a number of image-based vascular processing and segmentation techniques have been designed and proposed, these coping with different degrees of complexity and detail for the cerebrovascular system.

1.3 Challenges in Cerebrovascular Image Analysis

In the past years, the medical interest in vascular segmentation and the associated challenges have motivated an extensive amount of research. Most of the biomedical engineering research effort was focused on extracting clinically useful subject-specific models by means of automatic and semi-automatic segmentation techniques. However, population-based and group-wise analyses were limited to qualitative cerebrovascular differences and incidental vascular findings in clinical trials in radiology. The image-based and quantitative evaluations of a cohort of subjects require indeed a range of complex and multi-disciplinary tasks. Among those, the segmentation of the structures, the alignment and labelling of the vascular instances, and lastly the extraction and integration of clinically relevant biomarkers should be designed in a homogeneous domain.

In Chapter 2, a comprehensive summary of image-based vascular segmentation techniques and models is given, where an overview of the state-of-the-art and of traditional approaches in vascular image analysis frame the challenges of detecting and delineating vascular structures. In details, the problem of robustly enhancing the desired regions of interest over a background, or challenges in reducing image-related non-idealities arising from poor contrast due to image resolution, fragmented structures and topological non-linearities (bifurcations) were addressed by established and emerging methodologies for image-based vessels segmentation. These focused first on exploiting different vessel characteristics and image-based features to ultimately extract patient-specific cerebrovascular models and clinically relevant indices and parameters. In early neurovascular applications [14, 169, 192], the final goal was to locate brain vessels in relation to their neighbouring structures, for example, to avoid them during neurosurgery or to measure their dimensions at some

specific point (e.g. diameter of carotid, level of stenosis or grading of a cerebral aneurysm). In these cases, a raster representation of the underlying vascular structures is perfectly adequate, and the problem reduces to detecting the anatomical structures and voxel-wise segmenting the volume of an object of characteristically local linear morphology. The challenge of reconstructing a connected network of vascular branches was addressed by Bullit et al. and Kwitt et al. [29, 104] from a set of initial manually-sampled seeds, disconnected branches, or fragmented centerlines. However, traditional approaches for vascular enhancement and structural reconstruction seemed to address the problem of vascular connectivity in a rather independent and disjoint manner. Recently Shahzad et al. [176] proposed a more complete and connectivity-oriented approach for the extraction and labelling of the vascular tree from 3D whole-body angiography. However the extraction was limited to major arterial ramifications from the aortic arch up to the carotids and down to major periferic limbs.

Whilst many methods exist for quantifying cerebrovascular parenchymal changes (i.e. local vessel morphology, presence of atherosclerotic plaques, surrounding brain lesions), employing raster representations of tissue classes, no methods exist for quantifying vascular change where the representations are necessarily *vectorial*: the connected geometry of the underlying vascular network. Such vectorial representations could compactly encode relative, spatial and connectivity-related vascular features, by transcending a predefined and quantized spatial grid, typical of a subject-specific raster angiography [85]. A vectorial representation is not only useful in guiding interventions in individual patients, e.g. guiding intracranial electrode placement [217], catheter motion planning, (un)safe occlusion points identification [29, 112], or endovascular aneurysms repair and stent placement for recanalization [114, 159], but essential for the group-level studies on which both clinical prediction and therapeutic inference ultimately depend. For without a satisfactory means of registering vascular trees across a cohort of patients it is impossible to draw general conclusions about any specific vascular feature. A vectorial representation of the vascular network would therefore allow different forms of group

level analysis: *i.* intersubject comparison of geometrical features of the vascular tree (e.g. junction points, branching numbers, tortuosity, and overall haemodynamic properties), and *ii.* intersubject comparisons of various non-vascular parenchymal features, where the brain image-volume is rather registered by its vascular topology. By referring to *vectorial* cerebrovascular topology, the descriptive connectivity and branching pattern of a given set of vascular structures in the brain is obtained by adopting a spatially- and connectedness-aware embedding of a graph, which simultaneously encodes vessel centerlines as geodesics (minimal paths), disregarding any predefined anatomical compartment and subject-specific raster grid [85]. In general, the quantitative vectorial description and characterisation of a network become more complex and challenging as the network increases in size and allows for variable connectivity patterns. Here, the cerebrovascular anatomical intra- and inter-subject variability [91] does not allow for a unified and globally standardised vessel network extraction yet. Malformations and pathologies can also dramatically increase the complexity of the vasculature topology, where a compact representation is sometimes impractical. Complex topologies are required for the characterisation of the whole cerebrovascular system: anastomoses such as the Circle of Willis and those of the capillary bed in the cortex [22, 85] show cyclic connecting patterns at varying scales and depth. In these cases, hierarchical tree-like structures cannot adequately model the underlying anatomy, and a more general and unconstrained graph formulation is required. However, the topological inference of major deep-brain arterial (or venous) vascular trees can be locally projected to multiple-tree extraction strategies. Few topological references and data-driven gold standards of vascular connectivity are available. These, often fragmented or limited to a region of interest, require the thorough annotation of experts at different levels of vascular branching, where minor mis-classifications may significantly affect the topology of the resulting vascular graph [140]. The thorough segmentation of a whole-brain vascular image dataset is considered intractable [23], and it can take up to 8 weeks of manual labor per subject [142]. This constitutes a considerable limitation for any method's validation. Given the substantial complexity of the segmentation task and

of vectorial translation of the associated brain vascular network, considering also the lack of an extensive ground-truth for complete vascular topologies, the accurate and exhaustive extraction of the vessel connectivity still remains an open problem.

1.4 Thesis Outline & Contributions

With regards to this thesis and considering the aforementioned challenges in cerebrovascular image analysis, the problem of processing and analysing brain vessels from multi-modal angiographies is formulated under a different vascular key-feature. The idea is to exploit the intrinsic *connectedness* of the cerebral vessels together with its peculiar topology to determine a fully-connected graph. Such a vectorial representation would potentially describe not only spatial anatomical and functional features of either the arterial or venous compartments in the brain up to a pre-determined level of detail, it can also further allow the registration and alignment of cerebrovascular topologies for automatic labelling, information propagation and statistical analyses, towards the definition of an over-complete neurovascular atlas representative of a cohort of subjects, or of a whole population. On a more general scale, it could potentially further embed relevant clinical parameters such as hemodynamic parameters, physio-pathological biomarkers and risk-factors in a graphical, compact and intuitive representation. This would result in a multi-purpose cerebrovascular tool, which may impact the clinical practice with high-level cues and descriptive information on different scales: from patient-specific models employed in supported diagnosis, decision making, interventional treatment planning and surgical guidance, to longitudinal or cross-sectional long-term population studies.

Following the “common thread” of the vascular connectedness, a novel framework for cerebrovascular image analysis is presented in the following chapters. This novel mathematical framework, called *VTrails*, is step-by-step described, where a model accounting for local vessel shape priors, together with anisotropic directional features as descriptors of the vascular structural anisotropy, aims at extracting implicitly either the arterial or the venous connected network in the form of a graph

from 3D clinical angiographies. Then a pairwise non-rigid alignment approach is introduced for over-connected vascular topologies, leveraging the redundancy and connecting uncertainty of the network, within a standardised and established graph-matching framework used in computer vision applications. Lastly, a set of biomarkers and surrogate measurements from hemodynamic simulations are devised and integrated on the vascular topology, leveraging both the global connected network of the vascular structure and the local geometries at the bifurcations. These account for different degrees of perturbations, simulating both healthy and diseased scenarios.

Along with the structure of this thesis, the introduced unified connectivity-oriented framework VTrails enhances the connectedness of bifurcating, fragmented and tortuous vessels from angiographic scans through non-linear, scalar and tensorial vascular models. The orientation-aware vascular maps are fed into a connectivity-optimised paradigm, which infers the unknown connected vascular network minimising the cost of the associated geodesic graph under the assumption that vessels join by minimal paths. The pairwise elastic registration of vascular graphs is formulated as a coarse-to-fine optimisation problem, which retrieves the vascular branch-points correspondence for pairs of non-strictly isomorphic topologies in a fully automatic fashion. Lastly two vectorial hemodynamic simulation approaches are described over the inferred topologies to determine biomarkers and vascular descriptors leveraging both global and local views of the cerebrovascular network. In conclusion, perspectives and future works are discussed towards group-wise alignment, topological atlas integration and long-term risk prediction models.

Following an introductory overview about the state-of-the-art models employed in vascular image analysis in Chapter 2, the structured outline of this thesis' contributions is given in Fig. 1.3, where the VTrails framework is introduced for:

- *Vessel Enhancement* in Chapter 3: a compact Steerable Laplacian of Gaussian Swirls (SLoGS) enhancing filter-bank is defined and employed in a multi-resolution, curvilinear- and rotation-invariant filtering framework to simultaneously and consistently synthesise scalar- and tensorial-saliency maps, whose combination yields a smoothly connected Riemannian vesselness po-

tential.

- *Vascular Connectivity* in Chapter 4: both greedy and exhaustive connectivity paradigms are designed from an anisotropic level-set over the synthesised Riemannian vesselness potential, determining the underlying vascular tree(s) and the fully-connected geodesic vascular graph, respectively.
- *Vascular Alignment* in Chapter 5: a pairwise non-rigid alignment of non-isomorphic geodesic vascular graphs is described with a coarse-to-fine registration strategy comprising geometrical, geodesic and connectivity features within a Graph-Matching (GM) optimisation framework.
- *Vascular Biomarkers* in Chapter 6: biomarkers and surrogate measures from hemodynamic simulations are estimated for representative cerebrovascular graphs by globally solving analog-equivalent circuits in presence of perturbations, and by solving a Stokes' problem on vascular bifurcating geometries using a parametrisation based on Non-Uniform Rational B-Splines (NURBS) and an isogeometric analysis (IGA) framework.

VTrails framework's validation is also presented along with the methodological insights for a set of hand-crafted phantoms, synthetic angiographies and real clinical multi-modal scans throughout the body of this thesis. Current and active research directions following this thesis are also addressed in Chapter 7 towards the optimisation of the inferred vascular network, and the potential of long-term risk prediction models for the cerebrovascular system is lastly envisioned. Some of these latter formulations are supported with simple toy-examples and preliminary results, however these require further extensive evaluations in future research. To finalise, an initial overview of the available VTrails' open source implementation is given in the Appendices A. Further references and insights are specifically introduced throughout the body of this thesis, to better frame the multi-disciplinary contributions of the proposed framework.

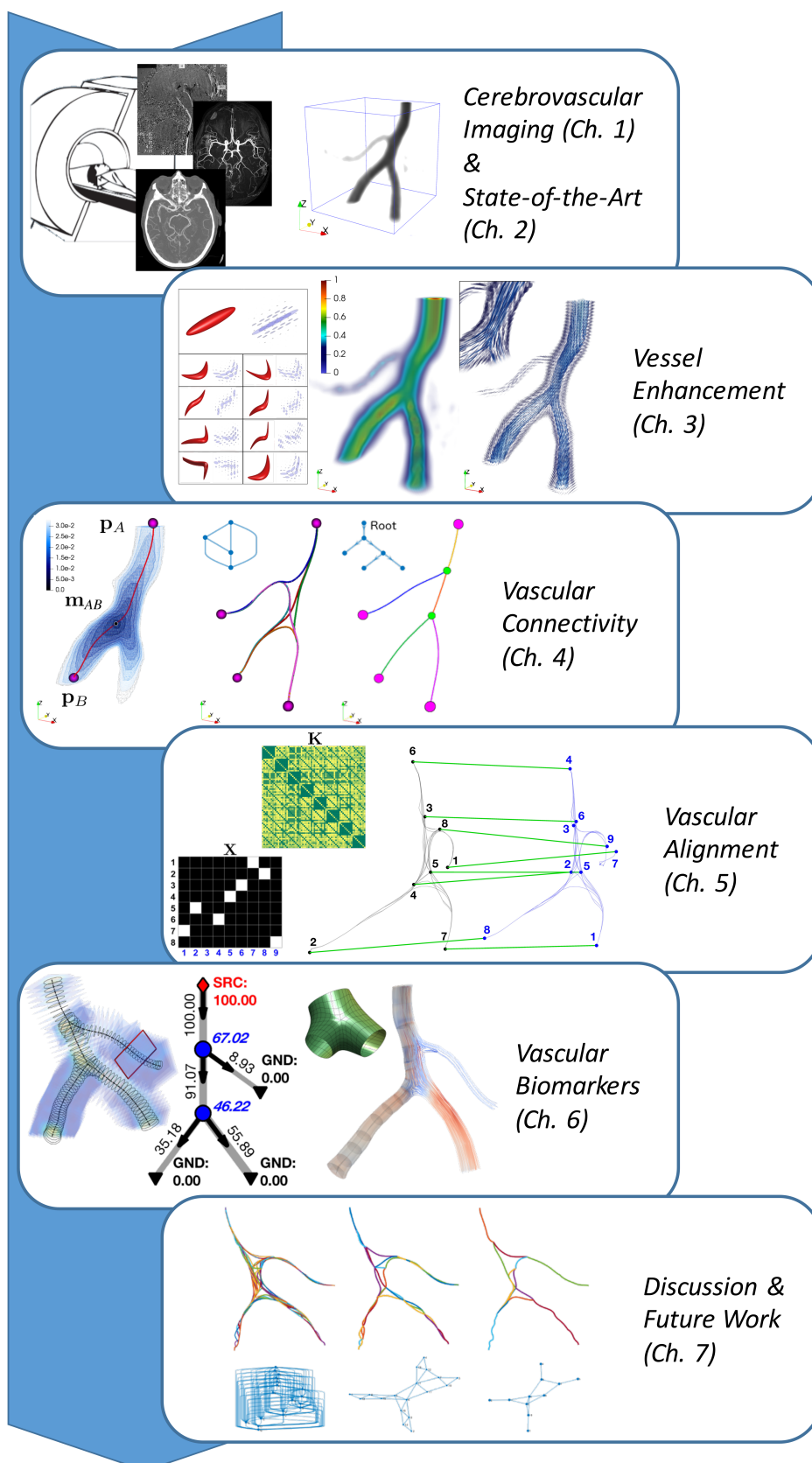


Figure 1.3: Thesis Outline: Macro-Section Flowchart. *Cerebrovascular Imaging* in Chapter 1 and *State-of-the-Art* in Chapter 2. *Vessel Enhancement* in Chapter 3. *Vascular Connectivity* in Chapter 4. *Vascular Alignment* in Chapter 5. *Vascular Biomarkers* in Chapter 6. *Discussion and Future Work* in Chapter 7.

Chapter 2

State-of-the-Art

2.1 Models in Vascular Image Analysis

The impact of vascular diseases has motivated a considerable amount of research dedicated to vascular image analysis. In the first instance, diagnosis assistance, treatment and surgery planning require the segmentation (i.e. the identification and delineation of regions of interest within the image) of vascular structures for the accurate visualisation of vessels in complex datasets and for the quantification of abnormalities and pathologies. Since most angiographic clinical routines still rely on manual operations, and given the considerable amount of data generated by modern 3D scanners, vessel segmentation and assessment may sometimes suffer from long time processing and inter-operator variability. To overcome these limitations, and considering the complexity of the vascular system and of the surrounding context, automatic and semi-automatic tools have been an object of research and development for the specific and challenging problem of vessel segmentation. Following the outline proposed in [112] and [99], methods for vessel lumen segmentation can rely on a complex combination of strategies, here grouped according to three main high-level categories: *i.* appearance and geometric vascular models; *ii.* vessel-related image measures and features; *iii.* algorithmic designs and extraction schemes for vessel segmentation. Other techniques also focused on different vascular image analysis tasks, such as vessel outer wall segmentation and thrombus segmentation [143, 191]. These often embed specific prior and leverage particular

combinations of processing pipelines, which sometimes result in less generalisable ad-hoc applications.

2.1.1 Vascular Appearance and Geometrical Models

Models are meant to embed prior knowledge or information regarding the target structures. Appearance models express the luminance properties of either vascular or a combination of vascular and surrounding structures by exploiting intrinsic informations arising from the imaging modality. *Vessel-only* models focus on the intensity distribution associated to the vasculature according to a theoretical or pre-defined estimation of the intensity range (e.g. Contrast-Enhanced CT angiographies). Following this assumption, several statistical distributions, such as Gaussian [67], Cauchy [4], or double sigmoid models [158], can be defined to account for the intensity variability produced by inhomogeneity of the contrast agent. Also, by considering the information from surrounding structures and tissues, it is possible to model the respective intensity distributions from a simple brighter (or darker) relationship between the vascular structures against the background, rather than a more advanced mixture of statistical models [48], accounting for inhomogeneities of the considered tissues [170]. Other acquisition-dependent nonidealities, such as noise and spatial blurring, can be estimated and incorporated as part of an appearance model. Generally, these nonidealities are implicitly integrated in hybrid models, which also account for spatial and geometric features of the structures of interest.

Purely geometrical models exploit the characteristic shape of blood vessels to encode their spatial and topological features, i.e. the elongation, the radius range or scale and furcations. Surface models rely on the assumption of local tubularity of the vessel surface to regularise with active shape models the lumen segmentation extracted by active contour techniques [54, 69]. Conversely, centerline models consider vessels as primarily mono-dimensional structures. The centerline, i.e. the geometrical locus of points centred inside the vessel lumen, reduces the complexity of the blood vessel to a 1D curve, which is particularly valuable for visual inspection tasks as well as for stenosis and aneurysms description and quantification. Also, to

model the centerline as a smooth curve, several parametric models [27, 105] were used to enforce smoothness and regularity in vessel extraction processes such as path prediction techniques [93] and particle filters [12]. The association of a surface with respect to a centerline further produced the generalised cylinder models, where the vessel walls are defined as 2D cross-sectional contours sweeping along the centerline. Examples of cross-sectional profiles are classical circles or ellipses, rather than more complex parametric curves such as closed 3D B-splines [69, 115]. More recent methods optimise and fit the geometrical surface on the data, under the assumption that the centerline estimation is reliable.

Hybrid models combine vascular luminance and appearance features together with vessel geometry. By observing the radial intensity profile within vessels, a simple *bar-like* model was initially proposed, which corresponds to a local cylinder with homogeneous intensity [26]. This was further refined as a *bar-like convolved profile* model, where the cross-sectional intensity plateau is filtered with a Gaussian kernel to account for spatial blur and partial volume effect [103, 201]. Conversely, intensity ridge models assume vessels as boundaries of the image hyper-surface, and they correlate multi-scale and intensity-related ridge responses to vessel spatial locations [14, 16, 72]. Also, template-based shape priors constitute a widely employed set of models, whose prototypes are based on second-order intensity variations (Hessian matrix analysis). In particular, different combinations of the Hessian eigenvalues are used to locally match bright (or dark) vessels to elongated blobs, ellipsoids and superellipsoids respectively [70, 118, 189]. On the same note, more recent techniques try to compensate also for noise and neighbouring structures, by analysing the voxel-wise vicinity in the tensor-space, namely *tensor voting* [216, 217].

Further geometrical model extensions included (bi)furcations and pathological anomalies and treatments such as calcifications and atherosclerotic plaques, aneurysms, stenoses and stent implants. Although precise modeling of the anomalies can substantially improve the vessel segmentation robustness, it is rather difficult to embed specific priors as the complexity of the model can dramatically in-

crease. Simple geometric models were proposed indeed, where Y- or X-shaped furcations are considered [3,4], or single-branch bifurcations are defined *a contrario* as deviations from cylindrical segments in terms of inertial moments [84,87]. Differently from calcifications and stents that result in hyper-intense structures, stenoses and aneurysms are generally implicitly modelled as sudden radius decrease and increase, respectively. Stenosis can be explicitly modelled by the double-cone detector, based on the Hessian analysis [118], whereas aneurysms can be learned from a database or can be detected *a posteriori* by evaluating volumetric and morphological criteria on the segmented vasculature. Lastly, other problem-specific models have been employed in literature by making use of probabilistic geometrical models and atlases to guide the vascular segmentation, as in [149] for the cerebrovascular system.

In practice, the choice of the model is however influenced by the prior knowledge of the acquisition modality for the vessel luminance and appearance, and by the specific application for the respective geometrical assumptions. Any given vessel segmentation algorithm can rely on several complementary models providing thus a more robust, multi-layer and coarse-to-fine description of the vascular structure.

2.1.2 Vessel Features and Image Measures

Vessel-specific features quantitatively express a prior knowledge, typically derived from an underlying model. A vascular feature is defined by measuring or estimating a vessel characteristic on image data upon the individual elongation, direction, scale and cross-sectional shape assumptions, or by considering a combination of those. Isotropic features such as location and/or scale do not exploit assumptions on the directionality of the vessels. Relying on the brightness of the structures, a set of candidate points mostly lying inside the vessels can be obtained by a locally scale-persistent robust intensity maxima extraction [181]. Alternatively, a medialness operator can be defined using a 3D multi-scale ridge detector (Laplacian of Gaussian), assuming that vascular intensities are locally maximum [14]. This latter approach was further extended using explicitly the vessel directionality in [16,72]. Another

isotropic feature was introduced by the spherical flux measure [192], which computes the gradient flux through the boundaries of multi-scale spheres with maximal responses at the center of the vessel, at the corresponding scale.

By exploiting instead vessels' specific local geometry in conjunction with their intensity, a set of features can be defined to characterize the tubular-like pattern and directionality of the vascular structures. Popular derivative features make use of the principal curvatures of the image intensities to describe the local geometry. The principal vessel direction and the orthogonal cross-sectional plane can be estimated through the eigendecomposition of the second-order spatial image derivative (Hessian matrix) [100]. Following this principle, several flavours of Hessian-based multiscale filters were presented for vessel enhancement [70, 118, 169]. These rely on Hessian eigenvalues to discriminate between blob-, plane-, and tubular-like structures. The well established Frangi *vesselness* filter [70] has been widely used in a number of vascular applications for its intuitive formulation, however its sensitivity is affected when the vascular structure deviates from the tubular assumption (e.g. stenosis, aneurysm and bifurcation). Also, the specificity of the vesselness response can be reduced by additional image noise and nearby non-vascular structures. As Hessian-based features rely on multi-scale filtering frameworks to account for vessels of different size, scale selection is often a critical aspect. On the one hand the Gaussian linear scale-space should consider vessel scales so that their vesselness response is maximal; on the other hand the vesselness response of these filters can be perturbed by other hyper-intense surrounding structures. With this view and to reduce such perturbations, Bauer and Bischof [17] proposed a similar vesselness formulation by considering the Jacobian of a gradient vector flow field. Alternatively, other methods exploited the spatial covariance of image gradient vectors through the analysis of the structure tensor matrix [3, 4], which better discriminate simple vascular segments from vascular nodules and bifurcations. The optimally oriented flux [106] exploits the distribution of gradient vectors to estimate a more accurate, stable and robust vesselness measure, less sensitive to surrounding structures. Similarly to the spherical flux, vessels are enhanced by measuring the gradient flux

through the boundary of local spheres, however, by explicitly making use of the vessel directionality, the flux is maximised through the estimation of an optimal gradient projection axis at different scales. As an alternative to derivative methods, second-order inertia moments of image intensities are used as integrative features for vascular structures. By considering the eigendecomposition of the inertia matrix and the respective ratio of eigenvalues, vascular integral filters can be determined, which provide similar curvature and geometric informations and are theoretically less sensitive to image noise and degradation [84, 87]. Conversely to derivative approaches, integrative filters do not benefit however from a well-defined scale-space framework.

Different strategies focus conversely on 2D cross-sectional features. Under the hypothesis of a vessel with closed-shape, compact and regular cross-sectional contour, the problem of the lumen segmentation is downscaled to two dimensions, however a single estimation of principal vessel orientation can be subject to noise and local perturbations. Following these concepts, Aylward and Bullit [16] proposed cross-sectional circular ridge detectors tracking for the definition of a medialness measure, by tracking the vessel along its directionality estimated using the Hessian's eigenvectors. Further refinements developed the formulation of the *core* framework for vascular structures, where a medial atom response is obtained by filtering the image with directional Gaussian derivative kernels located at the end of equi-angular radial spokes [71], so that the core medialness feature fits the image edges with a circular cross-sectional model for a given location, orientation and radius.

In this case, bifurcations are identified by a specific-pattern ridge detector coupled with the core response. The core framework has been employed in cerebrovascular image analysis with interesting and promising results, introducing the possibility of automatically extracting vascular tree-like structures. Limitations of the method were however reported in case of bifurcating and scale-varying branches, where the observed sensitivity is reduced. Currently the core framework has been further extended and developed in the *TubeTK* open-source project, Kitware [15].

Following the idea of a 2D cross-sectional compact vessel contour, ray-casting features were investigated to either detect accurate vessel walls or to better evaluate the centerness of a point in the vessel. Ray-casting features do not rely on a parametric shape prior for the cross-sectional contour, and they generally yield robust and high-performance results by casting and averaging numerous 1D rays [79].

Lastly, vascular features for bifurcations and anomalies were analysed to increase the vascular segmentation robustness. Among these, bifurcations were associated to the emergence of different vascular principal directions [3], or branch-point candidates were selected upon an inertia moment heuristic [84,87]. However, most other anomalies and bifurcating features are based on a posteriori topological analysis of the extracted vascular segmentation.

2.1.3 Segmentation Extraction Schemes

Several algorithmic designs have been proposed to extract the vascular segmentation on the basis of the afore mentioned models and features. Usually, vessel segmentation extraction schemes comprise a pipeline of image processing steps: vascular pre-processing aims at better contrasting the vascular structure against the background, enhancing therefore particular vascular features; this is then generally followed by a vessel-dedicated extraction scheme based on three main methodological subcategories, i.e. region-growing, active-contours and centerline-based approaches. Eventually, post-processing techniques refine the segmentation results.

Popular pre-processing techniques employ Hessian-based derivative filters [70, 169] or flux-based filters [106, 107] to enhance the vessels by providing a *vesselness* response map, which potentially reduces the image noise level, while preserving thin and weakly contrasted vessels. With the same aim, vessel-dedicated anisotropic diffusion schemes were also proposed [125, 126] for angiography enhancement, where further anisotropic directional information is extracted from the analysis of the Hessian matrix or from the structure tensor [198]. Together with vascular enhancement pre-processing schemes, algorithms for the extraction of rough vessel priors or pre-segmentation, e.g. spatial localisation seeds and/or regions of interest (ROI), were introduced to initialise the following vascular extraction

schemes. Most of pre-segmentation techniques are based on pixel- or voxel-wise processes, such as vesselness hard-thresholding and local maxima selection of intensity peaks, however these are particularly prone to fragmented outputs per se.

Starting from seed points, region-growing techniques incrementally segment the vascular structure by recruiting neighbouring points which satisfy some inclusion criteria. The simplicity and computational efficiency of region-growing schemes is related to the greedy and low-level inclusion rules, resulting in a sparse exploration of the data, particularly suitable for large 3D datasets. As a downside, inputs and seed points are generally provided manually, and classical region-growing schemes tend to be prone to false-negatives (holes) and false-positives (leaks), requiring therefore subsequent topological corrections [132]. Wave or front propagation techniques can be seen as ordered region-growing approaches with the advantage of enforcing the evolution of a well-formed and spatially coherent interface within the vessel. An accurate front propagation scheme is the *fast-marching* algorithm [1, 175]. It is derived as a general level-set numeric solver and visits pixels (or voxels) according to an estimation of their geodesic distance from seed points. Also, the fast-marching algorithm can be used for the optimisation of minimal paths allowing for different speed potentials and functions. As major benefit, the spatially coherent propagation of the front yields an implicit handling of branching and bifurcations, as well as allowing the connectivity of the propagating interface to be exploited for topological analysis.

Active-contours represent another class of segmentation techniques that evolve an interface through the coupling of internal (image-derived) and external (model-based) forces to constrain the geometry and the regularity of the vascular structure. Examples are 2D *snakes* that deform a tubular model following the direction of target vessels by evaluating the principal component analysis of the gradient vectors' distribution, avoiding self-intersection artifacts [187, 188, 210]. Also a parametric deformable snake model evolving a centerline curve with varying radius was proposed for 2D and further extended for 3D applications respectively in [133, 134]. Alternative implicit active-contours techniques rely instead on the vessel contour

evolution through partial derivative equations and level-set formulations. As the level-set framework does not suffer from explicit model parametrisation problems, complex topologies of the vascular structure are embedded as zero-level of a converged higher-dimension function. From 1D curves (called ε -level-set [122]) to higher order active-contours [163, 164], vessel segmentation has showed interesting and promising results, although 3D extensions have raised a considerably more complex algorithmic paradigm and higher computational cost. Among these, a 3D framework for vascular geometrical modelling was proposed in [7] for computing patient-specific computational hemodynamics, which resulted in the *Vascular Modelling Toolkit* (VMTK) open-source effort [9]. The vascular lumen surface is implicitly determined as intersecting iso-contours. These are obtained from an isotropic propagation of front-waves travelling from two manually parsed seeds over an image-based intensity potential. Also in this case, the fast-marching algorithm was employed to solve the implicit surface discrete evolution in combination with subsequent surface regularisation (shape-preserving smoothing) strategies to reduce artifacts arising from noise and image degradation. Consequently, the centerline is extracted a posteriori as the medial axis of the structure by solving a minimization problem on a functional determined by the internal Voronoi diagram and the maximal inscribed sphere radius feature. Centerline extraction is therefore recast into a minimal cost path problem, whose solution is given again by the fast marching method for the Eikonal equation extended to non-manifold surfaces. Interestingly, this approach was observed to implicitly produce connected centerlines at bifurcations and in correspondence of anomalies with further applications to cerebral vasculature and aneurysms [155]. Although the resulting segmentation model shows a smooth and appealing vascular reconstruction, the segmentation accuracy and the resulting vascular topology rely on the quality of the data and on the user-dependent supervision in selecting the seed-points and in refining spurious geometries.

Conversely from previous approaches, centerline-based methods focus on extracting directly the vessel mid-line, followed by centerline-to-contours refining

segmentation approaches. Centerline-based segmentation techniques rely indeed on high-level vascular information, such as localisation, direction and scale. Direct centerline extraction techniques require input seed points, usually the root of the vascular tree, and the tracking process is performed by alternating prediction and correction steps. Following vessel directionality features, Kalman filtering was proposed as an optimal prediction and correction scheme, under the assumption of Gaussianity and linearity of the data [202]. Also, to ensure robust tracking, direct centerline extraction techniques make use of medialness measures and cross-sectional features to recentre and correct the centerline location [109]. Overall, direct centerline tracking may however remain prone to premature stopping in the presence of anomalies, and requires a fair amount of user interactivity to handle branching via manual reseeded and to extract a complete tree. Alternative approaches follow the idea of extracting centerlines as vascular minimal paths. With this view, a cumulative monotonic cost metric, integrated along the centerline path, is minimised using dynamic programming schemes, resulting in good robustness even in case of corrupted data or anomalies, such as severe stenosis. Algorithmic designs include L_1 path optimization using Dijkstra-like graph-based schemes [58], and the fast-marching algorithm, which approximates in the first instance the isotropic Euclidean (L_2) cumulative cost. Refinement of such algorithms is the *freezing* scheme [56], which prevents paths from being propagated further when the cumulative cost is too high. An anisotropic version of the fast marching with freezing scheme has been shown to greatly reduce the amount of exploration space [118]. Together with a spatial centerline extraction, [21] proposed to incorporate an additional dimension, i.e. the associated vessel radius, to the problem formulation. Considering a native 3D domain, this yields a *4D minimal path* extraction technique where two speed potentials were defined concurrently based on multi-scale spheres and image-intensity features. Particular interest, however, was focused on exploiting directional information in a minimal path framework, specifically the anisotropic fast-marching formulation favours the propagation towards certain orientations. The multi-scale optimally oriented flux [106] was exploited

to design an adequate anisotropic metric for the vessel directionality in 3D [21], whereas a 4D propagation accounting for space, scale and orientation was proposed for 2D centerline tracking in [151]. However the high computational cost represents the major limitation for 3D applications. These minimal path techniques generally are semi-automatic, as they require an interactive framework for defining start- and end-points for each target vessel and a user-defined stopping criterion. Eventually, geodesic-voting techniques [165] and a posteriori pruning approaches can be employed to refine and correct complex vascular graphs obtained by a number of minimal paths.

A further effort to improve robustness in vessels centerline tracking was the formulation of a *multi-hypothesis* framework, such as stochastic particle filters. These benefit from well-established Bayesian theoretical frameworks and allow for high-level implicit designs. Particle filters handle non-linear processes through probabilistic and non-parametric Monte-Carlo methods, relying thus on a discrete population of samples (particles). The particle population is evolved by following and updating iteratively the probability distribution of several features on the state-space, such as vessel location, scale, orientation and appearance parameters. The increase of robustness, especially in noisy contexts, introduces high computational costs proportional to the number of particles [68, 113, 170, 171].

Lastly, most of the mentioned methods usually require a post-processing step, which mainly aims either at restoring and regularising fragmented portions of the vascular segmentation or at correcting the topology of the vascular tree due to missing or misconnected branches. In this step, spatial coherence can be enforced with morphological operators, as well as with more complex graph-based approaches such as pruning and region completion or splitting, by following *fuzzy connectedness* criteria and fuzzy models at different scales, from heuristic fuzzy-spheres to probabilistic graphical atlases [3, 181].

2.1.4 Emerging Segmentation Approaches: Deep-Learning

Deep-Learning based approaches are gaining popularity for vascular segmentation tasks [136]. As opposed to other supervised and unsupervised machine-learning

algorithms, where both feature extraction and selection require an underlying understanding of the most suitable features for the specific segmentation task, deep-learning approaches directly extract an internal representation of the image and associated cues, upon the increasing availability of computational power and datasets. Convolutional Neural Networks (CNNs) are a type of feed-forward neural network. Given a set of training pairs, i.e. image and labelled segmentation, these architectures produce a raster binary output, stating whether the pixel (or voxel) belongs to a vessel or background according to the given gold standard. Although these techniques have been recently applied to 2D angiographies of the retinal fundus [53, 119, 135], emerging advances in the segmentation of cerebrovascular structures were proposed by Phellan et al., Chin et al., and Chen et al., [41, 44, 154]. In detail, bi-dimensional manually annotated image patches are first used to train a CNN for automatically segmenting the vessels in TOF MRI angiographies; also, an automated early ischaemic stroke detection system is presented using CNN on CT scans of the brain; lastly, and automatic detection of microbleeds in cerebral susceptibility-weighted images is proposed by taking advantage of the deep-learning based 3D feature representation. Overall, the performance of deep-learning approaches in vascular imaging show promising results in terms of retrieval, accuracy and processing throughput, however the lack of an extensive labelled ground-truth or detailed gold standard seem to currently limit the generalisation power of the inferred rules to a restricted set of specific applications. Also, as observed in the previous section, these methods may eventually require further post-processing to better address the restoration and regularisation of disconnected or mis-labelled vascular portions. Nonetheless, vessel segmentation may rapidly evolve with advanced deep-learning approaches as the availability of labelled datasets scales up to cover most of the aforementioned vascular variability and non-linearity, together with unsupervised or weakly-supervised deep-learning strategies (e.g. reinforcement [172], generative networks [160], recurrent networks [61]), yet unavailable for vascular segmentation tasks.

Chapter 3

Vessel Enhancement

Existing methods in literature are known to provide poor enhancement in the correspondence of vascular junctions, non-linearities, and tortuous and highly curvilinear segments. Also, localised absence of signal arising from poor quality imaging disconnects vascular structures in multiple small fragmented portions with variable contrast. In this case, denoising strategies or traditional vessel enhancement filters are not able to recover a smoothly connected vascular saliency map, nor any directional feature of the underlying fragmented anatomy. The aim here is to recover a smoothly connected vesselness map particularly suitable for fragmented and disconnected vascular structures from low-quality imaging, and for a generic angiographic modality in 3D. Such a vesselness map should also enhance non-linear bifurcating patterns as well as tortuous and elongated vessels with high-dimensional directional cues as to best model convoluted vessels observed in brain angiographies.

Inspired by Sato et al. [169], Frangi et al. [70], and Law and Chung [106], who proposed tubular enhancing methods in 3D with the aim of better contrasting vessels over a background, an initial scale-dependent filtering process is formulated here to recover an ultimate Riemannian *vesselness* measure, representing the smoothly connected vascular saliency map. As in traditional applications in signal processing [157], such a vessel-enhancement filtering process stands as a multi-resolution and high-dimensional analysis/synthesis filterbank as initial filtering step in the proposed *VTrails* framework. In particular, a 3D filterbank of Steerable Laplacian of Gaussian Swirls (*SLoGS*) is first introduced, which filters the angiographic

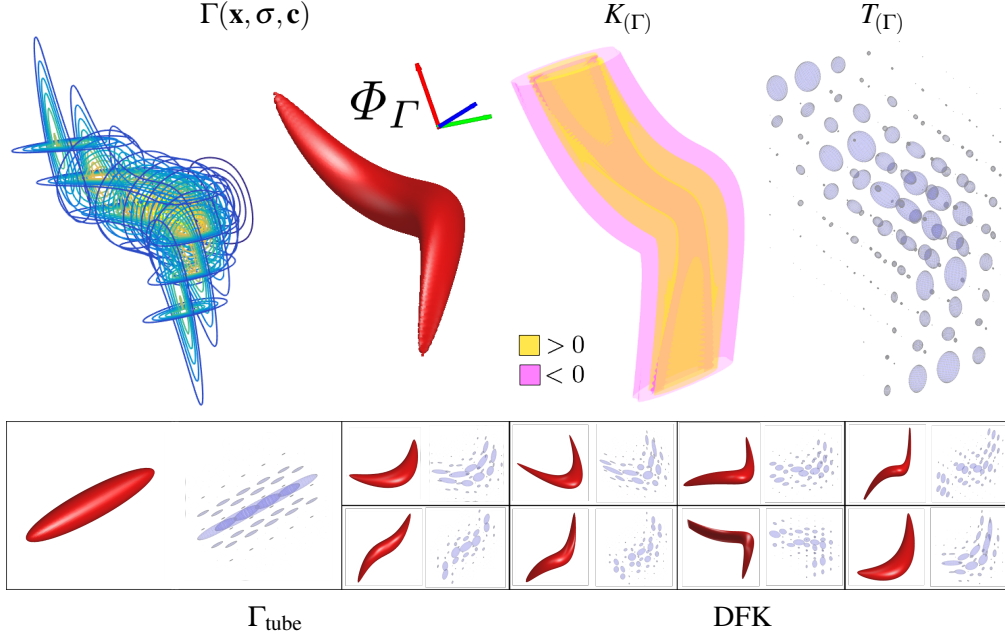


Figure 3.1: SLoGS filterbank: Top. Filter impulse-response Γ and associated integral orientation basis Φ_Γ ; Derivative SLoGS filter kernel $K_{(\Gamma)}$, and associated ellipsoidal tensor form $T_{(\Gamma)}$. Bottom. Definition of a dictionary of filtering kernels (DFK), including the linear $\Gamma_{\text{tube}} = \Gamma(\mathbf{x}, \sigma_1 > \sigma_2 = \sigma_3, \mathbf{c} = \mathbf{0})$.

image in a multi-scale, rotation- and curvature-invariant fashion. The elongated and curvilinear SLoGS kernels show both scalar and tensorial components, which recover a smooth and orientation-aware vesselness map with local maxima at vessels' mid-line. Together with a scalar vascular saliency map, the associated tensor field is simultaneously and coherently synthesised to better detect junction points and trace vascular branches, by automatically embedding higher-order metrics (i.e. anisotropic tensors), as in a tractography-like framework, further exploiting vessel anisotropy, directionality and local asymmetry.

3.1 SLoGS Curvilinear Filterbank

Considering an image $V : \mathbb{R}^3 \rightarrow \mathbb{R}$, the respective filter response is obtained as $V^{\text{filt}} \triangleq V * K$, for any predefined filtering kernel $K : \mathbb{R}^3 \rightarrow \mathbb{R}$. Following the concepts first introduced by [5, 117], the SLoGS filtering kernel K is derived here by computing the second-order directional derivative in the gradient direction of a curvilinear Gaussian trivariate function $\Gamma : \mathbb{R}^3 \times \mathbb{R}_+^3 \times \mathbb{R}^3 \rightarrow \mathbb{R}$. The gradient direction and

its perpendicular constitute the first-order gauge coordinates system (ω, ν) , where $\omega = \frac{\nabla \Gamma}{\|\nabla \Gamma\|}$, and $\nu = \omega_\perp$, with the spatial gradient ∇ . The function Γ has the form

$$\Gamma(\mathbf{x}, \boldsymbol{\sigma}, \mathbf{c}) \propto \prod_{d=1}^3 \frac{1}{\sqrt{2\pi\sigma_d^2}} e^{-\frac{\mathcal{X}_d^2}{2\sigma_d^2}}, \quad \text{with} \quad \begin{cases} \mathcal{X}_1 = x_1, \\ \mathcal{X}_2 = x_2 + c_1 x_1 + c_2 x_1^2, \\ \mathcal{X}_3 = x_3 + c_3 x_1^3, \end{cases} \quad (3.1)$$

where $\mathbf{x} = x_1 \mathbf{i} + x_2 \mathbf{j} + x_3 \mathbf{k}$, with $\{\mathbf{i}, \mathbf{j}, \mathbf{k}\}$ the unit-vectors associated to the Cartesian image reference system. The standard deviations $\boldsymbol{\sigma} \in \mathbb{R}_+^3$ modulate the cross-sectional profiles and the elongation of the Gaussian spatial distribution, and the factor \mathbf{c} accounts for both planar asymmetry and two levels of curvilinear properties (e.g. bending and tilting), by quadratic- and cubic-wise deforming the support. Given $\boldsymbol{\sigma}$ and \mathbf{c} , $\Gamma(\mathbf{x}, \boldsymbol{\sigma}, \mathbf{c})$ represents the smooth impulse response of the 3D Gaussian kernel. By operating a directional derivative on Γ along ω , i.e. ∇_ω , the SLoGS kernel K is defined as $K = \nabla_\omega [\nabla_\omega \Gamma] = \nabla_\omega [\omega^T \nabla \Gamma]$, thus being

$$K \triangleq \omega^T H(\Gamma) \omega, \quad \text{where} \quad H(\Gamma) = \begin{bmatrix} \Gamma_{ii} & \Gamma_{ij} & \Gamma_{ik} \\ \Gamma_{ji} & \Gamma_{jj} & \Gamma_{jk} \\ \Gamma_{ki} & \Gamma_{kj} & \Gamma_{kk} \end{bmatrix} \quad (3.2)$$

is the Hessian matrix of the Gaussian function Γ . With the compact notation Γ_i , Γ_j and Γ_k the first partial derivatives are indicated for $\frac{\partial}{\partial \mathbf{i}} \Gamma$, $\frac{\partial}{\partial \mathbf{j}} \Gamma$ and $\frac{\partial}{\partial \mathbf{k}} \Gamma$ respectively. Similarly, the notation Γ_{ii} , Γ_{ij} , Γ_{ik} , \dots , indicate in short-form the second partial derivatives $\frac{\partial^2}{\partial i^2} \Gamma$, $\frac{\partial^2}{\partial i \partial j} \Gamma$ and $\frac{\partial^2}{\partial i \partial k} \Gamma$, \dots , respectively. Since Γ is twice continuously differentiable, then $H(\Gamma)$ is well defined. Also, since $H(\Gamma)$ is symmetric, an orthogonal matrix \mathbf{Q} exists, so that $H(\Gamma)$ can be decomposed and diagonalised as $H(\Gamma) = \mathbf{Q} \Lambda \mathbf{Q}^T$. The eigenvectors \mathbf{q}_l form the columns of \mathbf{Q} , whereas the eigenvalues λ_l , with $l = 1, 2, 3$, constitute the diagonal elements of Λ , so that $\Lambda_{ll} = \lambda_l$ and $|\lambda_1| \leq |\lambda_2| \leq |\lambda_3|$. For any point \mathbf{x} , the SLoGS derivative kernel $K(\mathbf{x})$ can be rewritten as $K(\mathbf{x}) = \omega^T (\mathbf{Q} \Lambda \mathbf{Q}^T) \omega$. Geometrically, the columns of \mathbf{Q} represent a rotated orthonormal basis in \mathbb{R}^3 relative to the image reference system so that every \mathbf{q}_l is aligned with the principal directions of Γ at any point \mathbf{x} . The diagonal matrix Λ characterizes the topology of the hypersurface in the neighbourhood of \mathbf{x} (e.g. flat area, ridge, valley or saddle point in 2D) and modulates the variation of slopes, since the eigenvalues λ_l are the second-order derivatives along the principal direc-

tions of Γ . Factorizing $K(\mathbf{x})$, the form $K(\mathbf{x}) = (\omega^T \mathbf{Q}) \Lambda (\mathbf{Q}^T \omega) = (\mathbf{Q}^T \omega)^T \Lambda (\mathbf{Q}^T \omega)$ is obtained, and the gradient direction ω is mapped onto the principal directions of Γ . Solving eq. 3.2, it is possible to demonstrate that K has the form of a spatially warped 3D Laplacian of Gaussian, as

$$\begin{aligned}
 K(\mathbf{x}) &= G \underbrace{\begin{bmatrix} \Gamma_i \\ \Gamma_j \\ \Gamma_k \end{bmatrix}}^T \underbrace{\begin{bmatrix} q_{11} & q_{21} & q_{31} \\ q_{12} & q_{22} & q_{32} \\ q_{13} & q_{23} & q_{33} \end{bmatrix}}_{\mathbf{Q}} \underbrace{\begin{bmatrix} \lambda_1 & 0 & 0 \\ 0 & \lambda_2 & 0 \\ 0 & 0 & \lambda_3 \end{bmatrix}}_{\Lambda} \underbrace{\begin{bmatrix} q_{11} & q_{12} & q_{13} \\ q_{21} & q_{22} & q_{23} \\ q_{31} & q_{32} & q_{33} \end{bmatrix}}_{\mathbf{Q}^T} \underbrace{\begin{bmatrix} \Gamma_i \\ \Gamma_j \\ \Gamma_k \end{bmatrix}}_{H(\Gamma)} \\
 &= \sum_{l=1}^3 \gamma_l \lambda_l = \gamma_1 \frac{\partial^2}{\partial \mathbf{q}_1^2} \Gamma + \gamma_2 \frac{\partial^2}{\partial \mathbf{q}_2^2} \Gamma + \gamma_3 \frac{\partial^2}{\partial \mathbf{q}_3^2} \Gamma,
 \end{aligned} \tag{3.3}$$

where $\gamma_l = G \cdot (\Gamma_i \mathbf{q}_{l1} + \Gamma_j \mathbf{q}_{l2} + \Gamma_k \mathbf{q}_{l3})^2$ modulates the respective components of the Laplacian of Gaussian filter [101] oriented along the principal directions of Γ , and $G = \frac{1}{\Gamma_i^2 + \Gamma_j^2 + \Gamma_k^2}$. Note that for vanishing spatial gradients, e.g. at $\mathbf{x} = \mathbf{0}$, the modulation is equivalent to $\gamma_l = \frac{1}{3}$. Given any arbitrary orientation as an orthonormal basis similar to \mathbf{Q} , the arbitrarily defined dictionary of filtering kernels can steer by computing a rotation transform. Such a rigid rotation transform maps the principal direction basis of each Gaussian kernel (depicted as Φ_Γ in Fig. 3.1) on any arbitrary orientation in 3D. This ultimately allows to steer and align each filtering kernels along any orthogonal basis with a numerical re-sampling procedure.

Together with the SLoGS kernel K , the second-moment matrix T associated to the smooth impulse response Γ is introduced by adopting the ellipsoid model in the continuous neighbourhood of \mathbf{x} . Thanks to the intrinsic log-concavity of Γ , a symmetric tensor $T(\mathbf{x})$ is derived from the eigendecomposition of $H(\tilde{\Gamma})$, with $\tilde{\Gamma} = -\log(\Gamma)$, as $T(\mathbf{x}) = \mathbf{Q} \Psi \mathbf{Q}^T$, where Ψ is the diagonal matrix of the canonical unit volume ellipsoid

$$\Psi = \left(\prod_{l=1}^3 \psi_l \right)^{-\frac{1}{3}} \cdot \begin{bmatrix} \psi_1 & 0 & 0 \\ 0 & \psi_2 & 0 \\ 0 & 0 & \psi_3 \end{bmatrix}, \quad \text{being} \quad \begin{cases} \psi_1 = \frac{\tilde{\lambda}_1}{\sqrt{\tilde{\lambda}_2 \tilde{\lambda}_3}}, \\ \psi_2 = \frac{\tilde{\lambda}_2}{\tilde{\lambda}_3}, \\ \psi_3 = 1 \end{cases} \tag{3.4}$$

the respective semiaxes' lengths. Note that the eigenvalues $\tilde{\lambda}_l$ are derived from

the decomposition and diagonalisation of $H(\tilde{\Gamma})$. The tensor field T is a symmetric positive definite matrix, since $\tilde{\Gamma}$ has a convex quadratic form. The manifold of the obtained tensors can be mapped into six independent components in the Log-Euclidean space, which greatly simplifies the computation of Riemannian metrics and statistics [11]. The continuous and spatially smooth tensor field T inherits the steerable property of the scalar counterpart K . Resembling diffusion tensor MRI, the SLoGS kernel shows a preferred diffusivity pattern for a given energy potential (see Γ in Fig. 3.1). This allows to eventually determine an arbitrary SLoGS dictionary of filtering kernels (DFK) which embeds anisotropy and high-order directional features to scalar curvilinear templates, enhancing and locally resembling typical, smooth vessels.













Given an angiography and a pre-defined SLoGS dictionary of filtering kernels, the following filtering approach devises a series of convolutions to synthesise a scalar filter response, and a series of element-wise patch-sweeping sums to synthesise the tensorial counterpart. The intrinsic smooth profiles of the Gaussian SLoGS kernels, combined with an extensive and iterative filtering approach, is prone to recover a blurry filter response, where boundaries of the vascular lumen are smoothly blended with the parenchymal background. For this reason, an extra pair of degenerate kernels is here introduced, aiming at balancing the contrast of vascular boundaries and the background components of the angiographic image. In particular, the pseudo-impulsive K_δ is an isotropic derivative filter given by the Laplacian of Gaussian of $\Gamma_\delta(\mathbf{x}, \sigma, \mathbf{c} = \mathbf{0})$, representing a Dirac delta function for $\sigma \rightarrow \mathbf{0}$. The pseudo-impulsive K_δ is intrinsically sensitive to sharp intensity transitions, capturing therefore edges of tubular-like structures in 3D. The uniformly flat derivative filter K_v is the second degenerate Laplacian of Gaussian kernel, which derives from $\Gamma_v(\mathbf{x}, \sigma, \mathbf{c} = \mathbf{0})$, assuming a uniform, constant-value for $\sigma \rightarrow \infty$. Analogously, K_v is sensitive to regions of homogeneous intensities, capturing thus surrounding non-tubular parenchymal structures. Since both degenerate kernels K_δ and K_v have singularities and represent isotropic degenerate kernels, only their scalar component is defined.

All the scalar and tensorial SLoGS filters have been numerically determined. The considered numeric kernels satisfy the analytical conditions as described above and minor deviations are bound to a numeric machine error. In the following section a technical compendium is provided comprising the numerical parameters for the dictionary of filtering kernels adopted throughout the body of this thesis.

3.1.1 Numerical Dictionary of Filtering Kernels

Finite SLoGS kernels are derived by opportunely sampling the 3D continuous impulse-response Γ and the associated second-order derivative filtering kernel K . Analogously, the discrete ellipsoidal tensorial matrix T is sampled in the Log-Euclidean space. In the present thesis, templates of $5 \times 5 \times 5$ voxels were adopted for all the aforementioned instances. The adopted dictionary of filtering kernels (DFK) was generated as a one-time configuration step prior to all filtering, and accounted for a total number of 12 different SLoGS (i.e. $\text{DFK} = \text{DFK}_{12}$) of varying shape and curvilinear bending/tilting of the support. The cardinality of the dictionary, as well as the standard deviations σ and the curvilinear parameters \mathbf{c} , have been chosen to best represent in a compact set the vascular elongated and curvilinear patterns on a local scale as observed on real datasets. A list of parameters is detailed in table 3.1 for each SLoGS in the DFK, along with the discrete degenerate scalar kernels Γ_δ, K_δ and Γ_v, K_v . Note that the first SLoGS in table 3.1 corresponds to the purely linear kernel Γ_{tube} , as in Fig. 3.1.

Table 3.1: SLoGS parameters of the adopted DFK.

												
σ_1	5.0	5.5	6.0	5.0	5.0	5.5	6.0	6.0	6.0	6.0	5.5	5.5
σ_2	1.0	1.4	1.8	1.0	1.0	1.4	1.8	1.8	1.8	1.8	1.4	1.4
σ_3	1.0	1.0	1.0	1.0	1.5	1.3	1.1	1.3	1.2	1.2	1.0	1.0
c_1	0.00	0.00	0.00	0.00	0.00	0.00	0.00	0.00	-0.60	0.60	0.40	-0.40
c_2	0.00	0.10	0.20	0.00	0.00	0.10	0.20	0.20	0.20	0.20	0.10	0.10
c_3	0.00	0.00	0.00	0.03	0.05	0.03	0.01	0.03	0.02	0.02	0.00	0.00

The discrete impulse-response Γ_δ, Γ_v and derivative filtering kernel K_δ, K_v are

defined as degenerate kernels for a finite $3 \times 3 \times 3$ cubic template as

$$\Gamma_{\delta} = \begin{cases} 1 & \text{for } \mathbf{v} = [2, 2, 2], \\ 0 & \text{otherwise,} \end{cases} \quad K_{\delta} = \begin{cases} -\frac{26}{27} & \text{for } \mathbf{v} = [2, 2, 2], \\ \frac{1}{27} & \text{otherwise,} \end{cases}$$

$$\Gamma_{\mathbf{v}} = \frac{1}{27} \quad \forall \mathbf{v}, \quad K_{\mathbf{v}} = \frac{1}{27} \quad \forall \mathbf{v},$$

with \mathbf{v} the indexed voxel position within the cubic template.

3.2 Tubular Saliency Map and Orientation Sampling

As recalled in Section 3.1 and similarly to [73, 97], the idea is to convolve finite SLoGS kernels with a discrete vascular image in a multi-resolution, curvilinear- and rotation-invariant framework, to obtain simultaneously the scalar connected vesselness map and the associated tensor field. For simplicity and compactness, the multi-resolution filtering will be detailed for a generic scale s . Scale-invariance is achieved by keeping the size of the compact-support SLoGS fixed, while the size of the image V varies accordingly with the multi-scale pyramid (Fig. 3.2). Also, different spatial band-pass frequencies can be modulated with different σ of the SLoGS kernels. V is down-sampled first at the scale s as in [32] to obtain V_{down} . An

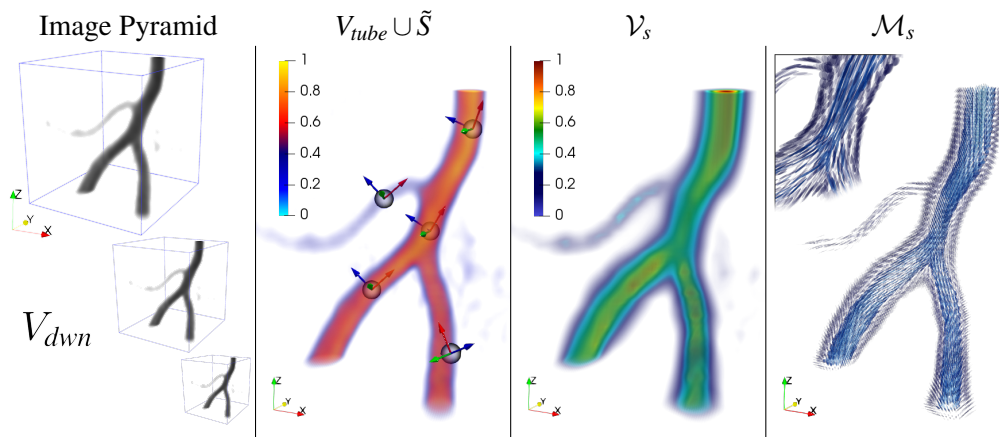


Figure 3.2: Synthesis of the vesselness maps: multi-scale processing image pyramid; early tubular saliency map V_{tube} with a subset of voxel binary seeds \tilde{S} and associated principal orientations; connected vesselness map (V_s) and tensor field (\mathcal{M}_s) at scale s .

early tubular saliency map V_{tube} is then determined as

$$V_{tube} = \sum \omega_{ico} V_{tube}^{(\omega_{ico})}, \quad (3.5)$$

$$\text{with } V_{tube}^{(\omega_{ico})} = \max \left(0, V_{down} * K_{tube}^{(\omega_{ico})} \right). \quad (3.6)$$

The derivative filtering kernel K_{tube} is obtained from the discretized tubular kernel $\Gamma_{tube}(\mathbf{x}, \sigma_1 > \sigma_2 = \sigma_3, \mathbf{c} = \mathbf{0})$ (Fig. 3.1), whereas ω_{ico} are the orthonormal bases determined using an icosphere of subdivision level equal to 2. By using an icosphere, a rather complete set of 3D orientations can be obtained by combining all the orthogonal directions recovered as vectors joining any vertex to the centre of the icosphere (Fig. 3.3). Specifically, by combining triplets of orthogonal directions, multiple different orientations are sampled accounting also for rotations around the principal axes. In particular, an icosphere of subdivision level equal to 2 produces an initial number of 1080 different orthonormal bases, i.e. ω_{ico}^{all} , which further reduces to 81 different orthonormal bases ($\omega_{ico} < \omega_{ico}^{all}$) when *only* the Γ_{tube} and K_{tube} kernels are employed, due to their spatial symmetry.

The synthesis of an image-based scalar and tensorial filter response using SLoGS would conversely account for all curvilinear kernels in the dictionary. Ideally, each kernel should be steered along every possible orientation in 3D, then it

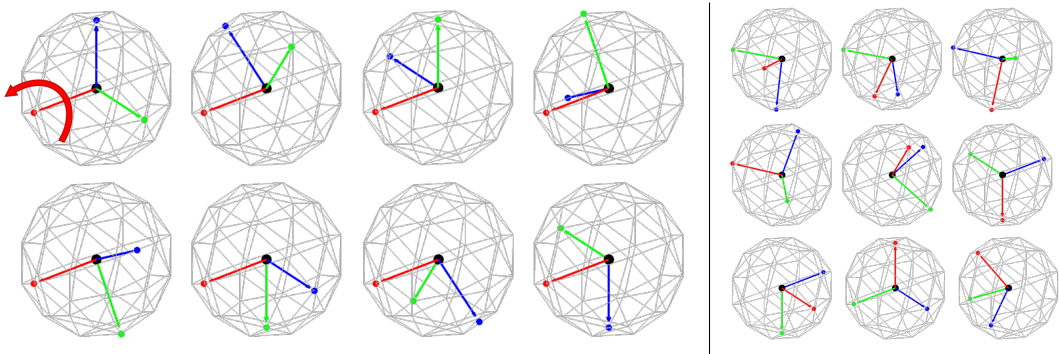


Figure 3.3: Orientation ω_{ico} sampling using a representative icosphere of subdivision level equal to 1. (Left) Subset of orientations accounting for rotations around a fixed principal axis (red arrow). The complete set ω_{ico}^{all} encodes all rotations around the principal axes. For purely symmetric kernels, such as Γ_{tube} , ω_{ico}^{all} boils down to a reduced set. (Right) Representative subset of orientations from a randomised sampling of the complete set of orthonormal bases ω_{ico}^{all} .

should be convolved with the down-sampled image V_{down} at each scale s . Such a filtering process would exhibit an intractable complexity even for a rather compact dictionary of filtering kernels. To overcome this computational bottleneck, the convolution space is slimmed down for a data-driven set of orientations determined on the tubular saliency map V_{tube} .

The purely tubular filter response V_{tube} is indeed meant to provide an initial, coarse, although highly-sensitive set of saliency features in V_{down} : the vessel *spatial locations* and *principal orientations* (Fig. 3.2). Identifying such features has two advantages; first it restricts the problem of the rotation-invariant filtering to an optimal complexity in 3D, avoiding unnecessary convolutions; also, a localised subset of vessel samples can be obtained. The vessel spatial locations are mapped as voxel binary seeds \tilde{S} , and the associated set of principal orientations Θ forms a group of orthonormal basis in \mathbb{R}^3 . The seeds \tilde{S} are defined as logical intersection in the form of a binary map as

$$\tilde{S} = \text{div}(\nabla V_{tube}) < 0 \wedge \lambda_{1,2,3}^{V_{tube}} < 0 \wedge V_{tube} \geq q_p(V_{tube}^+) , \quad (3.7)$$

where $\text{div}(\nabla V_{tube})$ is the divergence of V_{tube} 's spatial gradient field, $\lambda_{1,2,3}^{V_{tube}}$ are the eigenvalue maps derived from the voxel-wise eigendecomposition of $H(V_{tube})$, and $q_p(V_{tube}^+)$ is the p -quantile of the positive V_{tube} samples' pool (Fig. 3.4).

With the seeds \tilde{S} , the orientations Θ are automatically determined as the set of eigenvectors associated to $\lambda_{1,2,3}^{V_{tube}}$ (Fig. 3.2). The greater the intensity threshold $q_p(V_{tube}^+)$, the greater the image noise-floor rejection, the lower the retrieved seeds and the fewer the details detected by V_{tube} . Also, the cardinality of the seeds \tilde{S} and of the associated orientations Θ is a trade-off with the convolutional complexity at each scale.

3.3 Connected Vesselness Map and the Tensor Field

The filtering step consists in a convolutional analysis/synthesis signal processing pipeline in 3D for the scalar filter response and in a voxel-wise weighted-sum using a high-dimensional patch-sweep approach for the tensor field. The filtering

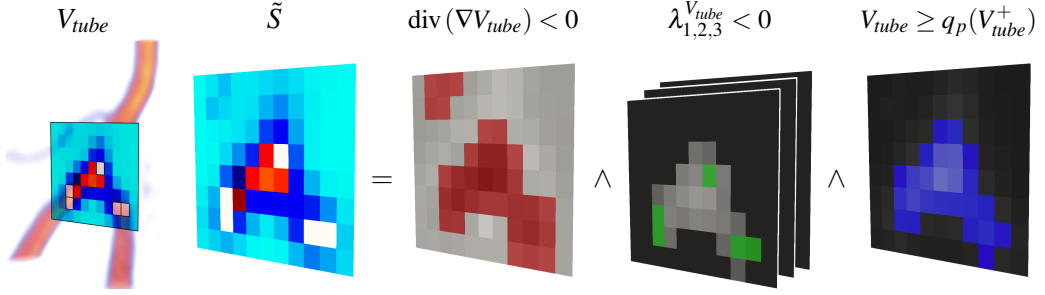


Figure 3.4: Seeds \tilde{S} detection as in eq. 3.7. Representative slice where voxels in red, blue, green colours satisfy the respective conditions. The resulting intersection is highlighted with white seeds \tilde{S} .

step can be embedded in a fully parallel filtering framework, by considering the down-sampled image V_{down} and the filtering kernels in DFK, each steered along every principal orientation Θ . The integral connected vesselness map \mathcal{V}_s , at any scale s , has the form

$$\mathcal{V}_s = \sum_{K \in DFK} \sum_{\theta \in \Theta} V_S^{(K, \theta)}, \quad (3.8)$$

$$\text{where } V_S^{(K, \theta)} = \max\left(0, V_{down} * K^{(\theta)}\right) \quad (3.9)$$

is the filter response given the considered SLoGS kernel (Fig. 3.2). Similarly, the boundaries and background scalar maps, i.e. \mathcal{D}_s and \mathcal{B}_s respectively, are determined at each scale s

$$\mathcal{D}_s = \bar{V}_{down} * K_\delta, \quad (3.10)$$

$$\mathcal{B}_s = \max(0, \bar{V}_{down} * K_v), \quad (3.11)$$

where, in this case, \bar{V}_{down} is the image negative of V_{down} , i.e. assuming values in V_{down} range within $[0, 1]$, the image negative is defined as $\bar{V}_{down} = 1 - V_{down}$.

Similarly to defining a single tensorial SLoGS kernel patch T , the synthesis of the image-based tensor field \mathcal{M}_s produces a high-dimensional vascular map representative of both vascular directionality and anisotropy in the form of voxel-based ellipsoids. Conversely from the single SLoGS kernel patch T , the image-based tensor field \mathcal{M}_s is formulated with a voxel-wise sum of multiple tensor patches. These account for all different curvilinear patterns in the dictionary of filtering kernels and for all detected orientations Θ in 3D. In details, the tensorial synthesis is de-

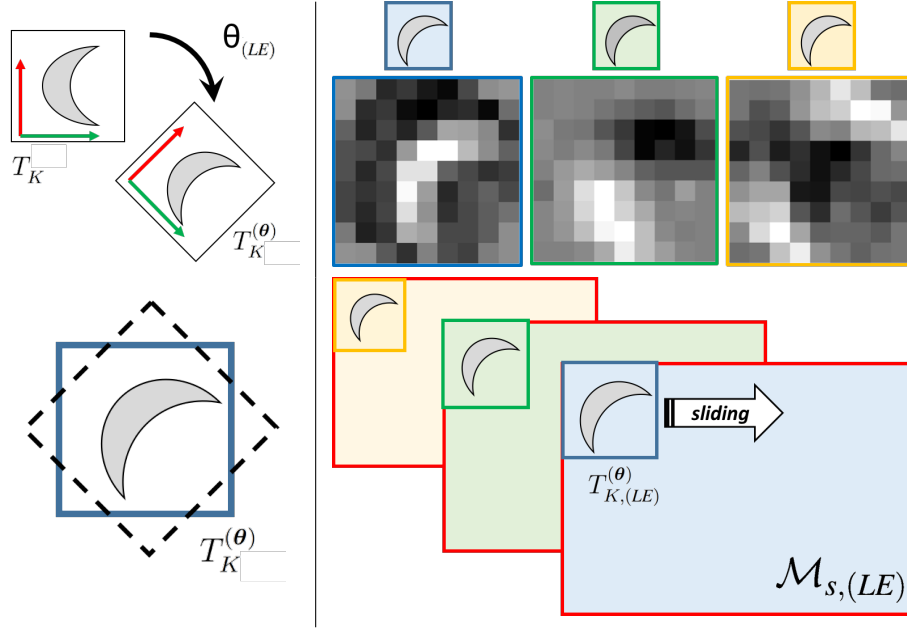


Figure 3.5: Representative synthesis of a tensor field in 2D. (Left-top) Steering a tensor patch along the orientation θ with a rigid mapping in the Log-Euclidean space. (Left-bottom) Re-sampling the steered tensor patch with adequate padding in the Log-Euclidean space, to preserve the tensor patch size. (Right-top) Three independent components of the 2D tensor patch in the Log-Euclidean space. Six independent components are determined for a 3D tensor patch. (Right-bottom) Sliding tensor patch-sweep for each independent component on the tensor field domain. The resulting tensor field $\mathcal{M}_{s,(LE)}$ is recovered by independently processing each Log-Euclidean component.

finied here as a voxel-wise discrete weighted-sum of a tensor patch sliding the image domain. Operations on tensors, such as steering, re-sampling, rotating the patch and summing values, require the processing being performed in the Log-Euclidean (subscript LE) space. Matrix logarithm and matrix exponential operators are employed to map tensors from the Euclidean space to the Log-Euclidean one and vice-versa as in [11]. In particular, each of the 6 independent tensorial components is separately synthesised in 3D, as a scalar volume of same size of V_{down} , with a sliding patch-sweep. Each independent tensorial component is determined for each voxel with a *weighted-sum* accounting for each curvilinear kernel in the dictionary, and for each steerable orientation. In eq. 3.12, the single-component of the synthesised tensor field \mathcal{M}_s is given as

$$\mathcal{M}_{s,(LE)} = \frac{1}{W} \sum_{K \in DFK} \sum_{\theta \in \Theta} \underbrace{\left(\sum_{\substack{\text{weights} \\ \text{patch}}} V_S^{(\mathbf{v}, K, \theta)} \cdot \Gamma_{(K)}^{(\theta)} \cdot \Xi \cdot T_{K,(LE)}^{(\theta)} \right)}_{\text{patch-sweep}} \Big|_{[\mathbf{v}]}, \quad (3.12)$$

$$\text{with } W = \sum_{K \in DFK} \sum_{\theta \in \Theta} \left(\sum V_S^{(\mathbf{v}, K, \theta)} \cdot \Gamma_{(K)}^{(\theta)} \cdot \Xi \right) \Big|_{[\mathbf{v}]}, \quad (3.13)$$

where W is the cumulative normalizing weight-map accounting for the steered curvilinear kernels. The patch-sweep operation is highlighted within round brackets in both eq. 3.12 and eq. 3.13, where $V_S^{(\mathbf{v}, K, \theta)}$ is the modulating SLoGS filter response centred at the specific voxel \mathbf{v} , as in eq. 3.8. The Gaussian impulse response $\Gamma_{(K)}^{(\theta)}$ associated to the kernel K is steered along the orientation θ . The Hann smoothing window Ξ is centred at the voxel \mathbf{v} and blends the multiple overlapping tensor patches in the neighbourhood $[\mathbf{v}]$ of the considered voxel. In eq. 3.12, $T_{K,(LE)}^{(\theta)}$ is one of the six independent components of the discrete tensors patch T that has been steered along the orientation θ , rotated and re-sampled in the Log-Euclidean domain. Note that the neighbourhood $[\mathbf{v}]$ is chosen to have the same size of the single-component tensors patch $T_{K,(LE)}^{(\theta)}$. Also, note that the synthesis of the tensor field \mathcal{M}_s is not a convolution. Lastly, the synthesised tensor field \mathcal{M}_s is normalised so that at each voxel it would represent an ellipsoid of unitary volume.

3.4 Multi-Scale Maximal Integration

The values of each scale-dependent contribution map are normalised within the range $[0, 1]$. Then each scale-dependent map is iteratively *up*-sampled (i.e. $\tilde{\mathcal{V}}_s^{up}$) and cumulatively integrated with a weighted sum as

$$\mathcal{V} = \sum_s \tilde{\mathcal{V}}_s, \quad (3.14)$$

$$\text{with } \tilde{\mathcal{V}}_s = \tilde{\mathcal{V}}_{s-1}^{up} + \max \left(\alpha_s (\mathcal{V}_s \cdot \epsilon_s), \tilde{\mathcal{V}}_{s-1}^{up} \right), \quad (3.15)$$

$$\text{and } \epsilon_s = \max(0, \mathcal{D}_s \cdot (1 - \mathcal{B}_s)). \quad (3.16)$$

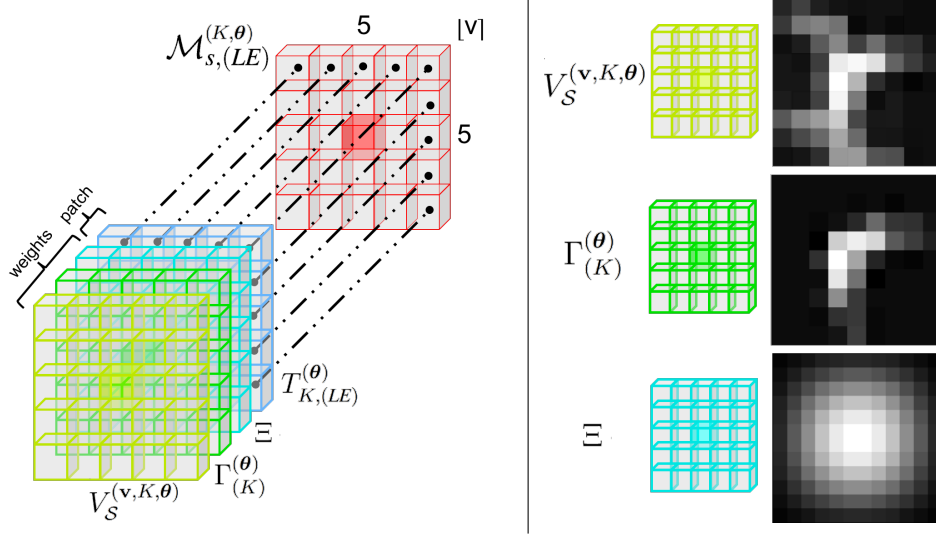


Figure 3.6: Representative synthesis of a tensor field in 2D. (Left) Patch-sweep element-wise weighted-sum in the pixel (or voxel) neighbourhood as in eq. 3.12. Each contribution is element-wise multiplied and summed over the one-to-one corresponding pixel (or voxel) in the tensor field domain. (Right) Representative contributions of the cumulative normalising weight map W , as in eq. 3.13, for a scalar SLoGS filter response $V_S^{(v,K,\theta)}$, for a scalar Gaussian impulse response $\Gamma_{(K)}^{(\theta)}$ of the steered kernel, and for the 2D blending Hann window Ξ .

Analogously, each independent component of the tensor field \mathcal{M} is integrated in the Log-Euclidean domain as

$$\mathcal{M}_{(LE)} = \frac{1}{\mathcal{V}} \sum_s \tilde{\mathcal{V}}_s \cdot \mathcal{M}_{s,(LE)}. \quad (3.17)$$

The vesselness contributions are weighted here so that the resulting multi-resolution maximal filter response is balanced and equalised across scales. The boundary and background maps' contributions in ε_s boost the spatial resolution of nearby tubular structures. The intensities of \mathcal{V} can be further skewed towards high, rather than low, spatial frequency bands by modulating the gain α_s . Here $\alpha_s = 1$ is adopted. The Euclidean form of the resulting tensor field \mathcal{M} is also enforced to have unitary determinant at each voxel. In this way the tensors' magnitude, expressed by the connected vesselness map \mathcal{V} , is decoupled from the anisotropic and directional features throughout the whole multi-scale process. The synthesised and integrated \mathcal{V} and \mathcal{M} maps constitute a consistent Riemannian vesselness potential.

Table 3.2: Synthetic datasets of vascular trees generated with [82]

Label	▼	Gaussian	Salt&Pepper	Shadows	△	Leaves
NL_{∇}^{\triangle}	a	$\mathcal{N}(0, 15)$	0‰	0	I	20
	b	$\mathcal{N}(0, 50)$	2‰	0	II	30
	c	$\mathcal{N}(0, 50)$	10‰	1	III	40

3.5 Experiments on Synthetic and Clinical Data

Since the SLoGS filterbank is part of the whole VTrails framework, the following experimental results in figures and tables are indicated, for compactness, under the ‘VTrails’ (VT) label, where \mathcal{V} and \mathcal{M} are the scalar and tensorial components of the Riemannian vesselness map, respectively.

In the following, as proof of concept, initial experiments employing the proposed approach have been performed on synthetic phantoms and on some representative clinical angiographies. A 3D hand-crafted tortuous and convoluted phantom (HCP) is designed to account for complex vessel patterns, i.e. branching, kissing vessels, scale and shape variations induced by pathologies. Also a cerebrovascular Phase-Contrast MRI (PC) ($0.86 \times 0.86 \times 1.0$ mm) is considered for qualitative assessment. The scalar vesselness responses of both HCP and PC images are determined using the popular Frangi filter (FFR) [70], and Optimally Oriented Flux (OOF) [106]. The connected vesselness map and the associated tensor field are simultaneously synthesised for the same testing dataset as previously described. In first instance, the connectedness of the considered scalar maps is visually evaluated in Section 3.5.1.1.

A more extensive and quantitative validation of the proposed method is presented on synthetic angiographies of vascular trees ($128 \times 128 \times 128$ voxels, isotropic 1 mm) generated using VascuSynth [82] considering also three levels of increasing noise and increasing terminal branches (Table 3.2). Here, the scalar vesselness responses of the considered synthetic images are determined using the SLoGS filterbank as described in the previous sections. Also, the classical Frangi filter (FFR)¹ [70], the Optimally Oriented Flux (OOF)² [106], the current state-of-the-art

¹<http://www.tubetk.org>

²<https://www.mathworks.com/matlabcentral/fileexchange/41612->

method by Ranking the Orientation Responses of Path Operators (RORPO)³ [131], and the noise-reduction anisotropic Hybrid Diffusion with Continuous Switch filter (HDCS)¹ [129] are considered for the evaluation of the scalar vesselness responses.

In Section 3.5.1.2, the quantitative evaluation was performed on the histogram of the scalar vesselness maps at different noise levels (NL). In detail, foreground (fG) – i.e. the tubular structures – and background (bG) components are initially determined from the uncorrupted images. The associated histogram overlap ($fG \cap bG$) is quantified for the obtained scalar filter responses from each method. Similarly, the foreground-background separation range ($fG \leftrightarrow bG$) is determined as the absolute difference between the 90-percentile of the background intensities and the 10-percentile of the foreground ones. The foreground interquartile range (fG_{IQR}) is determined as well as the index of the intensity spread for the enhanced tubular structures. Lastly, the correlation of the foreground components with the uncorrupted images is evaluated with the Spearman correlation coefficients fG_ρ . Significant differences of the considered methods against the proposed one are evaluated with a pairwise Wilcoxon signed rank test.

Lastly, both scalar and tensorial maps are shown for a representative set of multi-modal clinical angiographies: a Rotational Angiography of cerebral Aneurysms (RAA) from the Aneurisk⁴ dataset [6]; a cerebral time of flight MR Angiography (MRA) from the Kitware⁵ dataset [28]; and a cerebral Computed Tomography Angiography (CTA) (isotropic 0.4 mm). For these angiographies qualitative observations are drawn for the synthesised tensor field \mathcal{M} in Section 3.5.2. Analogously, the tensorial response from the initial hand-crafted phantom, for the noisy Phase-Contrast MRI and for a representative case of the synthetic vascular trees are visually evaluated, together with two intuitive toy-examples as a 2D vascular tree and a clinical retinography, for completeness. In conclusion, a technical compendium of the SLoGS filter-bank is provided, comprising the evaluation of the

optimally-oriented-flux--oof--for-3d-curvilinear-structure-detection

³<http://path-openings.github.io/RORPO>

⁴<http://ecm2.mathcs.emory.edu/aneuriskweb/index>

⁵<https://data.kitware.com/#collections>

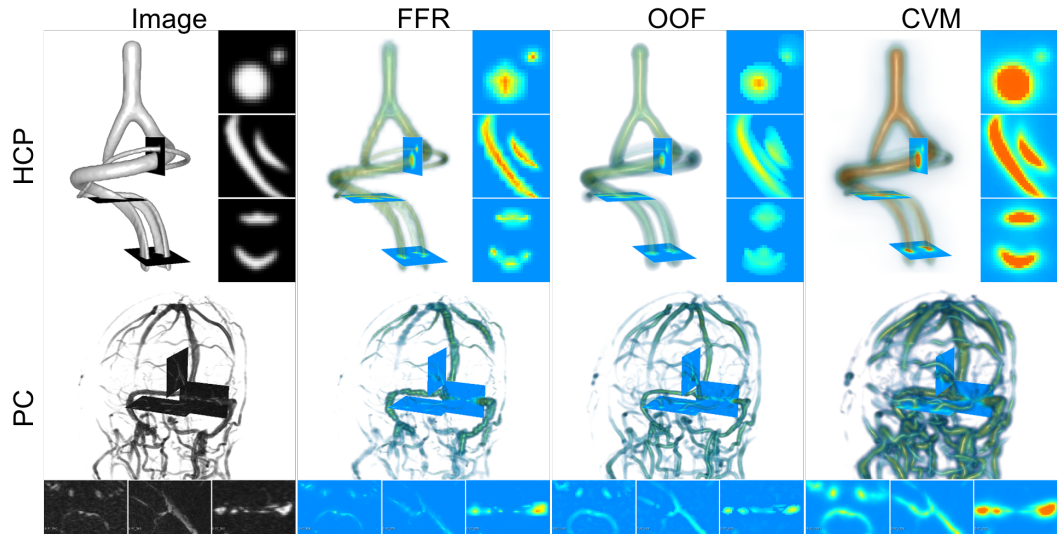


Figure 3.7: Connectedness of the vesselness response maps for Frangi (FFR) [70], Optimally Oriented Flux (OOF) [106], and proposed scalar connected vesselness map on a digital phantom (HCP) example and on data of a phase contrast (PC) cerebral venogram.

robustness of SLoGS parameters accounting for different dictionaries of filtering kernels. Also the computational cost and performance benchmarking are given for the proposed implementation.

3.5.1 Connectedness of the Scalar Vesselness Map

3.5.1.1 Qualitative Evaluation

Fig. 3.7 shows the connectedness of vessels recovered from popular vascular enhancers and curvilinear ridge detectors FFR and OOF together with the proposed connected vesselness map for the synthetic hand-crafted phantom and the real PC images.

On the synthetic phantom, FFR shows a fragmented and rough vesselness response in correspondence of irregularly shaped sections of the structure. Also, the response at the bifurcation is not smoothly connected with the branches (triangular loop). Conversely, OOF recovers the phantom connectedness at the branch-point, and the vesselness response is consistent along the tortuous curvilinear section, however ghosting artifacts are observed as the shape of the phantom becomes irreg-

ular (C-like) or differs from a cylindrical tube. Also, close convoluted structures, which change scale rapidly in the HCP, produce inconsistent responses of OOF (Fig. 3.7). The connected vesselness map shows here a strongly connected vesselness response in correspondence of both regular and irregular tubular sections, with local maxima at the structures' mid-line. The connectedness of the structures is emphasized regardless of the complexity of the shape, and it resolves spatially the tortuous curvilinear 'kissing vessels' without additional ghosting artifacts, despite the smooth profile.

Similar results are observed on the PC dataset: FFR has a poor connected response in the noisy and low-resolution image. Vessels are overall enhanced, however thin and fragmented structures remain disconnected. Overall, the vesselness response is not uniform within the noisy structures, where maximal values are often off-centred. A more consistent response is obtained from OOF, where the connectedness of vessels is improved. A maximal response is observed at the mid-line of vessels, however, noise rejection is poor. The connected vesselness map strongly enhances here the vessel connectivity. The fragmented vessels of PC have a continuous and smooth response in the proposed saliency map with higher values and a more defined profile. Large vessels show solid connected regions with local maxima at the mid-line as in OOF. Conversely from OOF, the connected vesselness map shows improved noise rejection in the background.

Fig. 3.8 show the scalar and tensorial vesselness maps synthesised using the SLoGS filterbank with VTrails (VT), and the scalar response obtained with FFR, OOF, RORPO and HDCS for a representative 3D synthetic vascular tree. VT scalar component strongly enhances the vessel connectivity, where low-resolution, noisy and fragmented vessels are recovered with a continuous and spatially smooth filter response (\mathcal{V}). High values and more defined local maxima are observed at the structures' mid-line, in correspondence with more regular and irregular tubular cross-sections, even with degraded SNR, with improved noise rejection in the background. In Fig. 3.9 the scalar and tensorial component of the synthesised Riemannian vesselness map is shown only for the SLoGS filter responses with VTrails

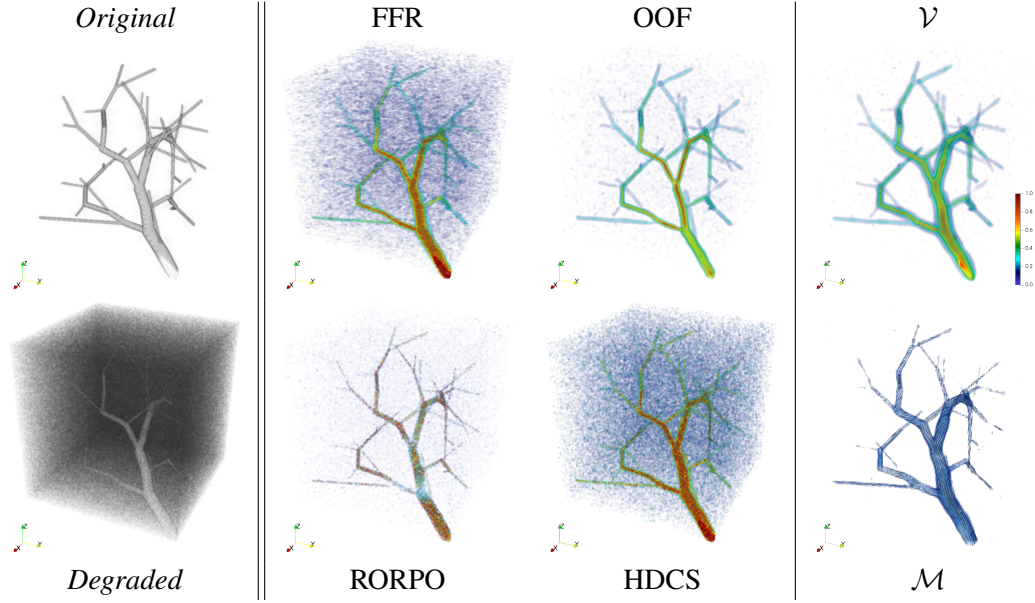


Figure 3.8: Representative filter-response for the synthetic degraded vascular trees [82] with different vascular ridge detectors: Top: Original image, FFR, OOF and \mathcal{V} from VTrails. Bottom: Noisy and corrupted image NL_b^{II} , RORPO, HDCS, and \mathcal{M} from VTrails.

in a representative set of clinical cerebrovascular angiographies. Also in this case, the connectedness of the vasculature is emphasised regardless of the complexity of its shape, by spatially resolving nearby, tortuous and highly curvilinear vessels.

3.5.1.2 Quantitative Evaluation

For the collection of synthetic vascular trees (Table 3.2), the respective histograms are reported in Fig. 3.10, for the considered levels of increasing noise and for the considered enhancing methods, i.e. the Frangi Filter, the Optimally Oriented Flux, the state-of-the-art by Ranking the Orientation Responses of Path Operators, and the noise-reduction anisotropic Hybrid Diffusion with Continuous Switch filter.

After filtering, the discrimination of both foreground, i.e. vessels, and background shows different trends for the considered enhancing methods (Table 3.3). Foreground and background intensity distribution (Fig. 3.10) are obtained from the comprehensive analysis of 30 synthetic images per noise-level.

By comparing the considered enhancing methods, the area of histogram overlap ($fG \cap bG$), i.e. the confusion between foreground and background components, is lower in VT and FFR, compared to all other methods in all cases. For increas-

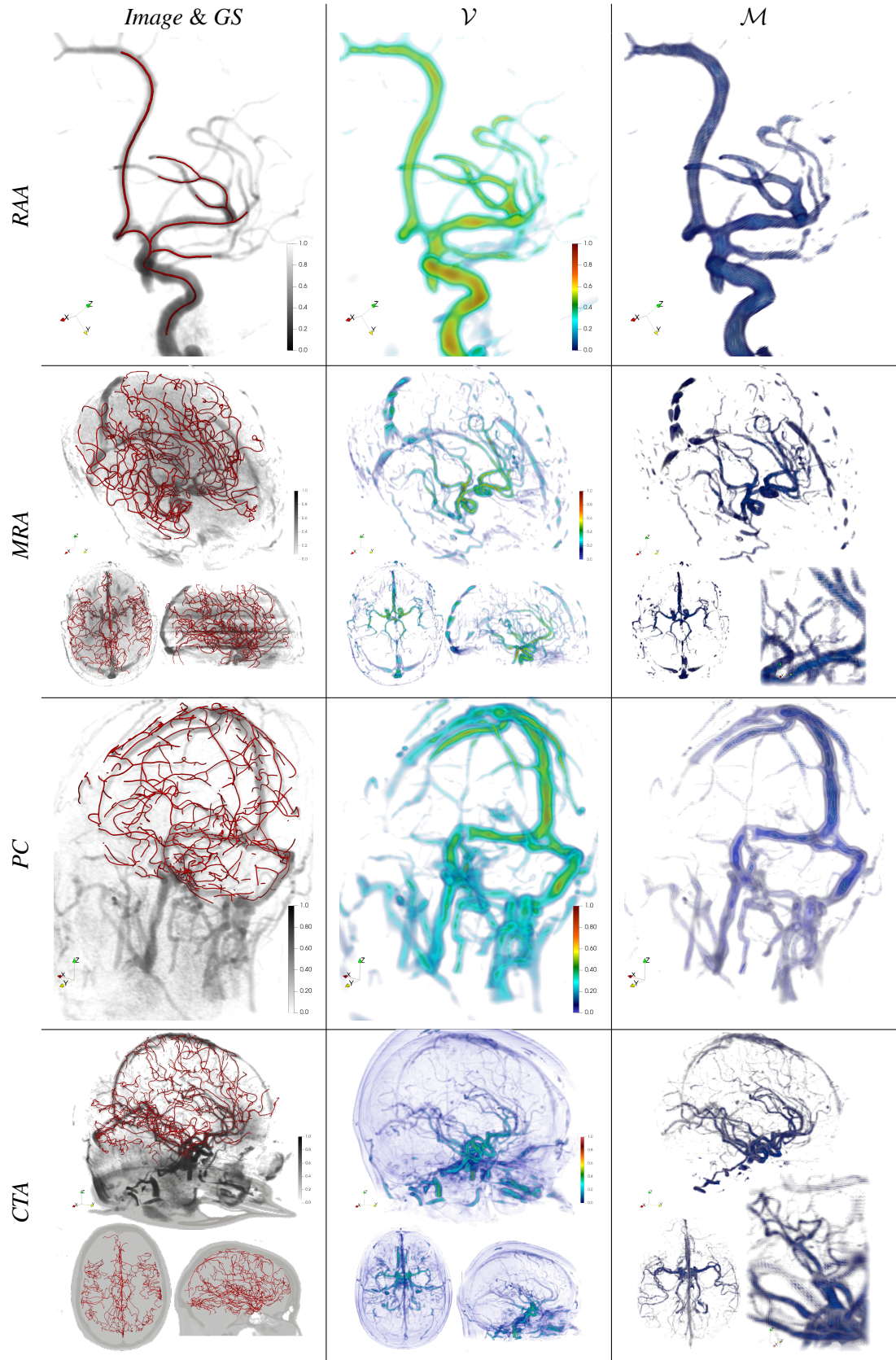


Figure 3.9: Representative filter-response for clinical cerebrovascular angiographies (RAA, PC, MRA, and CTA) with VTrails using SLoGS: Original scan with manual annotation gold standard (GS); scalar connected vesselness map \mathcal{V} and associated tensor field \mathcal{M} .

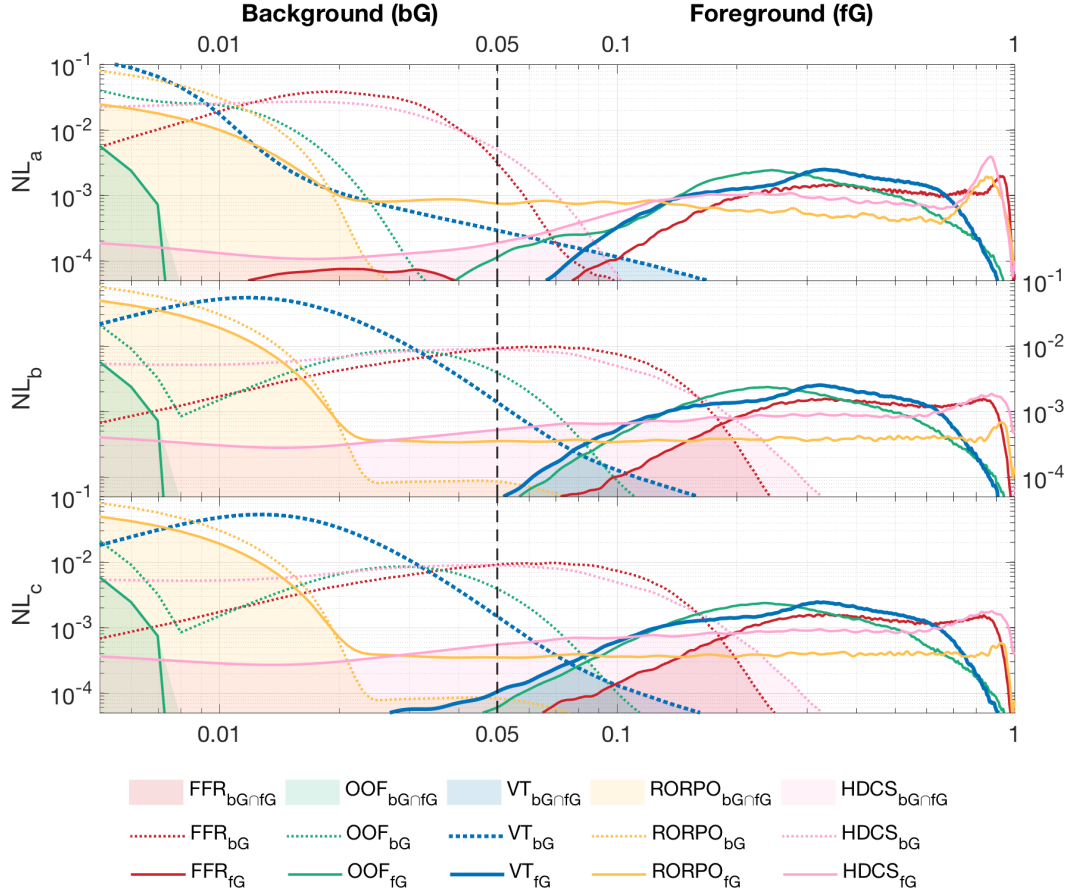


Figure 3.10: Foreground (fG) and background (bG) intensity distribution for degraded synthetic vascular trees [82] using FFR, OOF, RORPO, HDCS and VT (\mathcal{V}): Histogram overlap for at different noise corruption levels.

ing noise, higher confusion between foreground and background is observed, with significantly higher ($p < 0.05$) histogram overlap values. Similarly, the separation of both foreground- and background-distribution tails ($fG \leftrightarrow bG$) shows comparable values for FFR and VT with mild corrupting noise, whereas a reduced range of separation between foreground and background is observed for all FFR, OOF, RORPO and HDCS, with significantly worse separation ($p < 0.05$) at moderate-to-severe degradation levels. The intersection value of both foreground and background distributions is consistent in VT at different levels of corrupting noise, and lays in the vicinity of the ideal threshold (Fig. 3.8, black dashed-line). The foreground interquartile range (fG_{IQR}) quantifies the smooth connectedness of the scalar filter response for the tubular structures, where a more compact and limited range suggests homogeneity and regularity of the scalar intensities in the neighbourhood of

Table 3.3: Histogram overlap ($fG \cap bG$), foreground vs. background separation range ($fG \leftrightarrow bG$), foreground interquartile range (fG_{IQR}), and foreground Spearman correlation (fG_ρ) with the uncorrupted image, for FFR, OOF, RORPO, HDCS and VT scalar vesselness (mean \pm sd). \dagger : significantly worse ($p < 0.05$) and $*$: significantly better ($p < 0.05$) than VT in paired Wilcoxon signed-rank test.

		FFR	OOF	RORPO	HDCS	VT
NL_a	$fG \cap bG$	0.01 \pm 0.02	0.19 \pm 0.02 †	0.23 \pm 0.07 †	0.02 \pm 0.03	0.01 \pm 0.01
	$fG \leftrightarrow bG$	0.21 \pm 0.04	0.01 \pm 0.01 †	0.01 \pm 0.01 †	0.14 \pm 0.03 †	0.20 \pm 0.03
	fG_{IQR}	0.44 \pm 0.03 †	0.27 \pm 0.04	0.70 \pm 0.07 †	0.51 \pm 0.04 †	0.25 \pm 0.02
	fG_ρ	0.78 \pm 0.05	0.70 \pm 0.04	0.70 \pm 0.14	0.87 \pm 0.07*	0.76 \pm 0.05
NL_b	$fG \cap bG$	0.04 \pm 0.03	0.20 \pm 0.02 †	0.51 \pm 0.05 †	0.15 \pm 0.03 †	0.01 \pm 0.01
	$fG \leftrightarrow bG$	0.12 \pm 0.02 †	0.05 \pm 0.01 †	0.00 \pm 0.00 †	0.03 \pm 0.01 †	0.16 \pm 0.02
	fG_{IQR}	0.39 \pm 0.02 †	0.27 \pm 0.02	0.51 \pm 0.09 †	0.48 \pm 0.03 †	0.24 \pm 0.01
	fG_ρ	0.76 \pm 0.05	0.70 \pm 0.04	0.66 \pm 0.09	0.80 \pm 0.06*	0.74 \pm 0.04
NL_c	$fG \cap bG$	0.05 \pm 0.02 †	0.21 \pm 0.02 †	0.52 \pm 0.03 †	0.16 \pm 0.02 †	0.02 \pm 0.01
	$fG \leftrightarrow bG$	0.11 \pm 0.03 †	0.05 \pm 0.01 †	0.00 \pm 0.00 †	0.02 \pm 0.01 †	0.15 \pm 0.02
	fG_{IQR}	0.39 \pm 0.02 †	0.27 \pm 0.03	0.49 \pm 0.07 †	0.48 \pm 0.03 †	0.25 \pm 0.02
	fG_ρ	0.75 \pm 0.05	0.69 \pm 0.05	0.66 \pm 0.06	0.79 \pm 0.06*	0.73 \pm 0.05

enhanced structures. VT and OOF show comparable fG_{IQR} in terms of smooth filter-response connectedness, whereas significantly higher ($p < 0.05$) intensity ranges are found for FFR, RORPO and HDCS, suggesting increased variability or more distributed intensities for the filtered structures. High correlation coefficients (fG_ρ) are found for HDCS, FFR and VT, where the intensities of the enhanced tubular-like structures monotonically correlate with the respective uncorrupted ones. In this case, HDCS has better performances ($p < 0.05$) for all noise levels, being the associated foreground distribution rather skewed towards saturated hyper-intensities, in line with the intrinsic noise-reduction filter design.

3.5.2 Synthesised Tensor Field

In Fig. 3.8, Fig. 3.9 and Fig. 3.11, the synthesised tensor fields show consistent features. Their characteristics are in line with the connectedness of the scalar filter response \mathcal{V} : enhanced and connected vessels are associated with tensors of high anisotropy, whereas background areas show a predominant isotropic component. Also, tensors orientation smoothly captures vessel directionality. This is moreover clear from Fig. 3.9, where it is possible to appreciate how the tensorial component

determined with VTrails captures and effectively represents the directionality of the underlying vascular structure also in an intuitive 2D dataset. Note that in Fig. 3.9 the magnitude of the ellipsoids representing the tensors is proportional to the scalar connected vesselness response.

Considering the irreducible deterioration of rendering 3D structures in 2D, it is possible to visually assess the synthesised tensor fields with 3D rotating video-clips available at <https://www.youtube.com/channel/UCC24bCFUO9uhUBLNQk1zjJw/videos>.

3.5.3 Robustness of SLoGS Parameters

The analysis of the robustness of SLoGS parameters is performed here by considering the original DFK (here also identified as DFK_{12}), and other 2 similar dictionaries of different cardinality, i.e. DFK_6 and DFK_{18} consisting of 6 and 18 kernels respectively. The evaluation of the filter response of the considered dictionaries accounts for the voxel-wise Pearson correlation $\rho(V, \mathcal{V})$ between the original image and the resulting connected vesselness map, and the voxel-wise Pearson correlation $\rho(\mathcal{M}^{fit}, \mathcal{M})$ of the tensor field directionality and anisotropy with the tensor gold standard in the Log-Euclidean space. Performance benchmarking was also done in terms of DFKs physical memory load and empirical computational time. For the evaluation, a convoluted hand-crafted phantom presented in [139] was employed at different sizes and resolutions (Fig. 3.12).

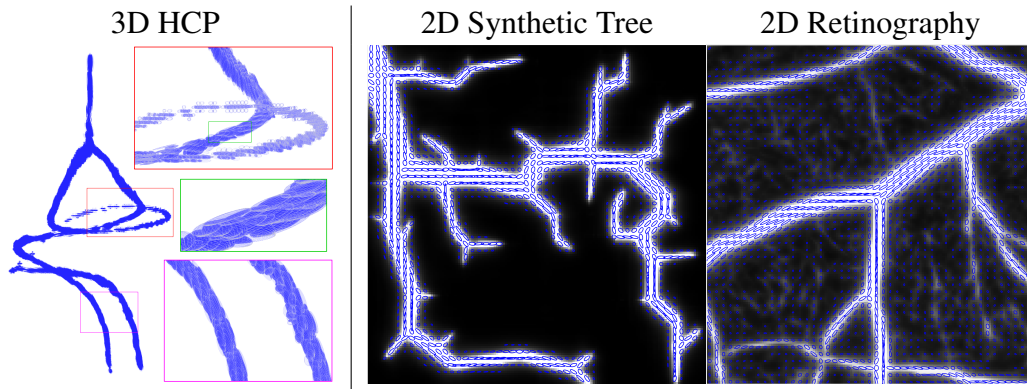


Figure 3.11: Synthesised tensor fields for: Left. 3D hand-crafted phantom (HCP). Right. 2D toy-examples of a synthetic vascular tree [82], together with a subregion of a retinal angiography.

The correlation values of the synthesised maps with the respective ground-truths are shown in Fig. 3.12. Since no publicly available ground-truth for direction and anisotropy exists, a gold standard \mathcal{M}^{fit} was derived by fitting the tensor field over the original phantom V . Similarly to eq. 3.4, positive-definiteness of the ellipsoidal matrix is enforced in this case, by considering the absolute value of the image-based Hessian eigenvalues. Overall, similar and comparable correlations were observed for the considered DFKs, by processing the phantom at different image size. This suggested reproducible results and overall good robustness of the DFKs by adopting similar varying parameters. Clusters of values ranged between $0.82 \sim 0.90$ and $0.62 \sim 0.69$ for $\rho(V, \mathcal{V})$ and $\rho(\mathcal{M}^{fit}, \mathcal{M})$, respectively. A slight decrease of the linear correlations was found for DFK₆. Following this trend, a further reduction of the dictionary cardinality may result in poor tensorial vesselness maps.

3.5.4 Computational Cost and Implementation

As observed in Section 3.3 and in Section 3.6, the complexity of the framework hinges on the density (or sparsity) of different tubular structures in the image and on the desired level of vascular detail. A performance analysis is shown in Fig. 3.12 for the aforementioned set of DFKs combined with a phantom at multiple image size. Both filtering time and physical memory load of the DFKs reported an underlying power-law trend (dashed lines in Fig. 3.12) in the adopted implementation. The estimated range of memory load was $30 \sim 200$ MB, and a maximum filtering time

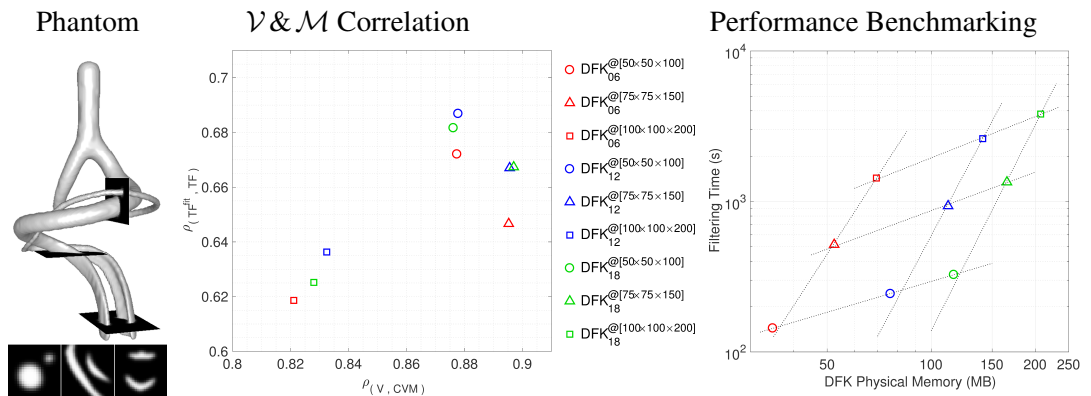


Figure 3.12: Parameters robustness and performance analysis on 3 DFKs and using a convoluted phantom of size $1.0 \times$, $1.5 \times$ and $2.0 \times [50 \times 50 \times 100]$ voxels.

of approximately 1 hour was observed for the complete DFK_{18} combined with the most dense and detailed phantom. Heuristically, for a representative experiment on clinical angiography – whole-brain isotropic 1 mm (approximately $200 \times 200 \times 150$ voxels), an average processing time of $2 \sim 5$ hours was observed with the adopted $\text{DFK} = \text{DFK}_{12}$. This includes the full-scale-range analysis/synthesis of both scalar and tensorial maps, together with the exhaustive connectivity paradigm, accounting for an exploration neighbourhood of $10 \sim 25$ mm diameter.

The choice of DFK is justified as a trade-off between the correlation indices previously observed, and the overall computational performance. The filter-bank was numerically determined and tested in Matlab.

3.6 Observations and Remarks

In this chapter a vessel connectivity enhancement approach is introduced for the proposed VTrails framework. By means of a novel dictionary of filtering kernels (i.e. SLoGS), fragmented, bifurcating and tortuous vessels are recovered from 3D angiographic images in a multi-scale, rotation- and curvature-invariant fashion. The introduced filtering process yields a smoothly connected Riemannian vesselness map, whose scalar and tensorial components capture the underlying directionality of the vascular structures. Whilst other ridge detectors and vessel enhancement methods may be particularly designed for noise-reduction purposes and some others can provide a raster vascular segmentation, as observed in Chapter 2, the proposed method does not aim at segmenting vessels by thresholding the resulting vesselness maps. By using the SLoGS filterbank within a coherent mathematical framework, the simultaneous synthesis of both scalar and tensorial vesselness maps consistently embeds smoothly connected tubular responses together with the underlying vascular anisotropy and directionality. Contrary to Cetin et al. [37, 38], where tensors are derived from fitting the image data, the proposed method has the advantage of generating high-order vascular maps with few curvilinear templates. The vesselness maps recovered with SLoGS was less sensitive to noise and artifacts, and did not require any further regularisation or positive-definiteness constraint, since

anisotropic tensors are well defined for the described smooth and compact Gaussian kernels. Results in Sections 3.5.1.1 and 3.5.1.2 demonstrate the robustness of the proposed method to different levels of corrupting noise. This mainly stands as a sanity test with regards to traditional and popular tubular ridge detectors and enhancement techniques [70, 106, 129, 131] in cases of images with severely impaired SNR. Regarding the enhancement and reconstruction of tortuous and convoluted tubular structures, as observed by Aylward and Bullit [16], the multi-resolution scale factor and the seed points cardinality introduced in 3.3 play also here a critical role. On the one hand, they allow for a fully automatic processing pipeline; on the other hand, they modulate the computational complexity of the filtering step. A full-scale-range analysis/synthesis of the multi-resolution image pyramid should account for vascular structures of different size. Also, a reasonable choice for the seed points cardinality, here expressed with a fixed seeds p-quantile threshold $q_p = 0.75$ as in eq. 3.7, should trade-off between the computational complexity and the informative content of the filter-response. From the presented experiments, a low quantile (i.e. high seeds cardinality) can severely increase the complexity of the filtering step, without introducing information to the resulting scalar and tensorial (\mathcal{V} and \mathcal{M}) maps; whereas, a high-value quantile can reduce dramatically the complexity, and therefore the computational time, to the detriment of vascular details.

In the following chapter, both the scalar and high-order vascular components are combined as a smooth Riemannian metric for automatically inferring the unknown connected vascular network from a subset of initialization nodes.

Chapter 4

Vascular Connectivity

As observed in Section 1.3, a vectorial vascular representation should compactly encode the connected geometry of the underlying vascular network. On the basis of traditional topological reconstructions as proposed by Dokládal et al. [60], and Saha et al. [167, 168], the extraction of connected neighbouring structures is addressed with the centerlines derived from a given raster segmentation by means of a skeletonisation process. In some cases, simplicial or cubical complex frameworks may be required when topological busy junctions are found in 2D or 3D finite raster grids, as suggested by Cardoso et al. [31], Cointepas et al. [49], Couprie [50], and Dłotko and Specogna [59]. Alternatively, the topological skeleton can be obtained with shape-preserving morphological operators, e.g. erosion and opening. The formulation presented so far, however, does not aim at segmenting vessels by adopting an optimal raster thresholding. As reported in Section 2.1.3, other formulations proposed by Kimmel and Sethian [98, 175] can extract l_0 level-sets, consisting in minimal paths (i.e. geodesics), to implicitly define connecting branches. Following these approaches, and upon the estimation of a prior high-order vascular representation, which coherently embeds connected non-linear tubular responses and their associated anisotropic tensor field (in Chapter 3), the extraction of the connected network of vessels is addressed here with an anisotropic level-set combined with a connectivity paradigm. Under the assumption that vessels join by minimal paths, the proposed framework VTrails infers the unknown fully-connected vascular graph from a subset of nodes automatically estimated and enforces the resulting topology

to be a connected network.

4.1 Joining Vessels by Minimal Paths

Following the formulation introduced by Benmansour and Cohen [20] for the carotid bifurcation segmentation, as in [83], an anisotropic front propagation algorithm is defined so that in combination with a connectivity paradigm it joins multiple sources S propagating concurrently on a Riemannian speed potential \mathcal{P} . A geodesic path π is determined by minimising an integral positive energy \mathcal{U} associated to the set of all possible paths joining two points on the domain of the speed potential as

$$\mathcal{U}(\mathbf{x}) = \min_{\text{all } \pi} \int_{\pi} \mathcal{P}(\pi(s), \pi'(s)) ds \quad (4.1)$$

where s is, in this case, the arc-length parameter. For each point \mathbf{x} in the domain, the Eikonal partial differential equation is satisfied

$$\|\nabla \mathcal{U}(\mathbf{x})\| = 1; \quad (4.2)$$

$$\mathcal{U}(\mathbf{p}) = 0. \quad (4.3)$$

Given the spatial location \mathbf{p} of a source S and a target point \mathbf{x} in the domain, the energy \mathcal{U} can be ultimately regarded as a time-of-arrival map for a front propagating from \mathbf{p} with oriented velocity as in the speed potential. Null energy is initialised for each point \mathbf{p} for the set of source(s) S of the front propagation. A numeric solution to the is computed by the anisotropic Fast Marching (*aFM*) algorithm [20]. The adopted speed potential \mathcal{P} describes the infinitesimal distance along the path π , relative to the anisotropic tensor \mathcal{M} . In this case, \mathcal{M} is the same tensor field synthesised in Section 3.3, which anisotropically modulates the direction of the front propagation in the domain. The adopted magnitude of the speed potential is proportional to the inverse of the scalar vesselness map \mathcal{V} as synthesised in Section 3.3. Note that the anisotropic propagation is a generalised version of an isotropic propagation medium, where the tensor is identically defined as $\mathcal{M} \equiv I_3$ (Identity). The locations corresponding to the initially detected seeds \tilde{S} , as in Section 3.3,

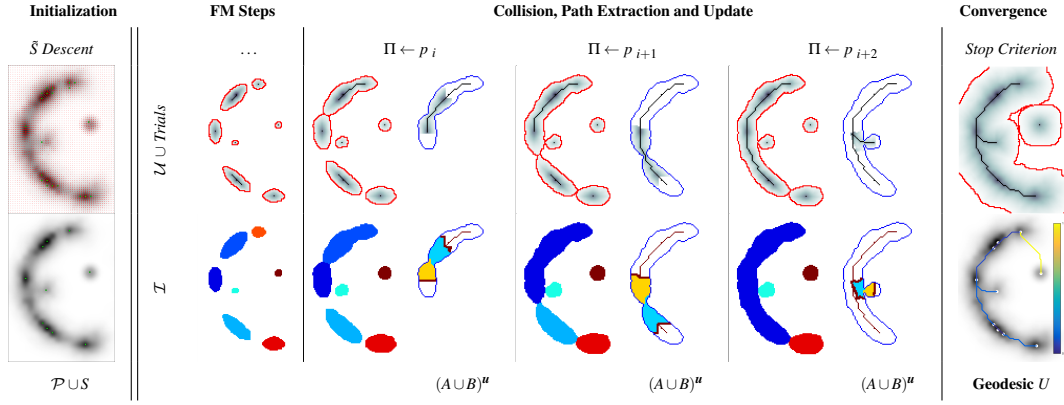


Figure 4.1: Greedy and sequential acyclic connectivity paradigm on a 2D synthetic phantom. From Initialisation to Convergence, the intermediate steps are shown at Collision, Path Extraction and Fast Updating Scheme. Geodesic values are represented with a shaded colormap, whereas colliding, merging and updating regions are shown in solid colours.

are first aligned to the local maxima of the scalar component of the speed potential, determining a centred set of source seeds S . On a 3D finite grid, the anisotropic Fast Marching front propagation is discretised and solved for neighbouring simplicial elements of a voxel, as described in [21].

In the following section an acyclic and *greedy* connectivity paradigm is described, where the anisotropic Fast Marching (*aFM*) is run in conjunction with the concurrent extraction of a set of multiple connected geodesics Π , until convergence. This automatically determines a completely connected vascular network in the form of an acyclic graph, i.e. a vascular tree.

4.2 Acyclic Connectivity Paradigm

With the aim of extracting a vascular tree in one-shot, a multi-sources front propagation is introduced. The fronts independently propagate from each source, and concurrently grow on the domain with associated energy \mathcal{U} . For each source, neighbouring explored voxels form connected regions labelled in a Voronoi Index map \mathcal{T} . Each propagating region is internally subdivided into *Front*, *Visited*, and *Far* voxels according to a Tag map \mathcal{T} , representing the state of each grid-point following the anisotropic Fast Marching scheme as in [20]. The basic idea to recover the connectivity is that a geodesic path is determined when two different regions first collide

due to the growing fronts. Following a greedy first-come-first-served regions collision detection, a sequence of connecting minimal paths are iteratively obtained by exploring the speed potential domain in one-shot. In particular, minimal paths are determined by back-tracing the energies \mathcal{U} in the respective collided regions. Then, the collided regions are merged, and further path extraction is inhibited within the merged regions. The connecting geodesic π is extracted minimising \mathcal{U} at the collision grid-points. The energy \mathcal{U} , the Voronoi index map \mathcal{V} , and the Tag \mathcal{T} , are then updated within the collided regions, so that these fuse as one and the front is consistent with the unified resulting region. This paradigm is continued until all regions with different labels collide and merge in a single connected component. A schematic summary of the sequential algorithm is shown in Fig. 4.1, and further details are given for each algorithmic step. An intuitive visualisation of the acyclic connectivity paradigm is available at <https://youtu.be/DBGqYcxZD30>

4.2.0.1 Initialisation

As mentioned in Section 4.1, the seeds \tilde{S} are first aligned towards the vessels' mid-line with a constrained gradient descent on the scalar vesselness saliency map, resulting in an initial set S of centred sources of cardinality p . All 26-connected components from the set of seeds S , being those either segments or isolated points, are treated as paths $\pi_p^{(S)}$. These initialise the *aFM* maps, so that the energy is null $\mathcal{U}(\pi_p^{(S)}) = 0$; the Voronoi index map is associated to the p -th label $\mathcal{I}(\pi_p^{(S)}) = p$; and the state of the grid voxels is set to 'front' $\mathcal{T}(\pi_p^{(S)}) = \text{Front}$. Note that the considered initial connected components also constitute the initial set of geodesics $\pi_p^{(S)} \rightarrow \Pi$.

4.2.0.2 Fast Marching Step

The *aFM* maps are updated by following an informative propagation scheme. In the *aFM* step the geodesic functional \mathcal{U} is minimised by considering the wave-front propagation through the 3D discrete 48 simplexes connected components within the 26-neighbourhood of the *Front* grid-point with minimal \mathcal{U} . Implementation details can be found in [20].

4.2.0.3 Connecting Path Extraction

Collision is detected when *Visited* grid-points of different regions are adjacent. A connecting π is determined by linking the back-traced minimal paths from the collision grid-points to their respective sources $\pi_A, \pi_B \in \Pi$ with a gradient descent on \mathcal{U} (Fig. 4.1). The associated integral geodesic length $U_\pi = \int_{\pi_A}^{\pi_B} \mathcal{U} d\pi$ is computed and the connectivity in the set of geodesics Π is updated in the form of an adjacency list. Lastly, the grid-points of the extracted π are further considered as path seeds in the updating scheme, since bifurcations can occur at any level of the connecting minimal paths.

4.2.0.4 Fast Updating Scheme

A nested *aFM* is run only in the union of the collided regions $(A \cup B)$ using a temporary independent layer of *aFM* maps, where $\tilde{\mathcal{U}}(\pi) = 0$, $\tilde{\mathcal{T}}(\pi) = \text{Front}$, and $\tilde{\mathcal{T}}_{(\overline{A \cup B})} = \text{Visited}$. Ideally, the nested *aFM* is run until complete domain exploration. However, to speed up the process, the propagation domain is divided into the solved and *unsolved* sub-regions, and the update is focused on the latter $(A \cup B)^u$ (Fig. 4.1). The boundary geodesic values of $(A \cup B)^u$ equal the geodesic distances \mathcal{U} at the collision grid-points. Lastly, the *aFM* maps are updated as

$$\mathcal{U}_{(A \cup B)^u} = \min \{ \mathcal{U}_{(A \cup B)^u}, \tilde{\mathcal{U}}_{(A \cup B)^u} \} \quad (4.4)$$

$$\mathcal{I}_{(A \cup B)} = \min \{ \mathcal{I}_A, \mathcal{I}_B \}, \quad (4.5)$$

$$\mathcal{T}_{(A \cup B)^u} = \tilde{\mathcal{T}}_{(A \cup B)^u}. \quad (4.6)$$

4.2.1 Isotropic vs. Anisotropic Front Propagation

As observed in [20], the choice of the front-propagating potential \mathcal{P} can be crucial for the geodesic path extraction. In Fig. 4.2 the comparison of the level-set iso-curves is shown for an isotropic front-propagation against an anisotropic one on the same phantom used in Fig. 4.1. Here, as sanity test of the implemented method, full exploration of the image domain is performed. However, no connectivity paradigm is enforced. Observing the pattern of the iso-contours, the connecting segments,

i.e. geodesics, for tubular structures obtained with the anisotropic level-set would likely lie on actual vascular portions, limiting therefore possible short-cuts within a greedy approach. The elongation of the level-set profiles accordingly follows the anisotropic directionality of the enhanced structure. In Fig. 4.3, two examples are presented in 2D; a synthetic phantom of a convoluted structure and a portion of a retinal angiography. By coupling the front propagating level-set with an acyclic connectivity paradigm, the extracted fully connected tree is shown for both isotropic and anisotropic propagation. In both cases, the greedy connectivity paradigm, coupled with the isotropic front-propagation resulted in erroneous short-cut(s) of the locally convoluted structures. By considering the same initialization, the resulting topology of the network shows several connecting differences. In particular, in the retinal image, where the vascular structure shows a more complex pattern, the graph topology and connectivity changes consistently. From the intuitive example in Fig. 4.3, the isotropic version of the greedy connectivity paradigm produced mis-connected branches even in larger vessels, compared to the anisotropic version, due to the spatial neighbouring of the tubular structures themselves. In the following section, as well as in the remainder of this thesis, any front-propagating level-set will account for the anisotropic formulation. In Section 4.2.2, the proposed acyclic

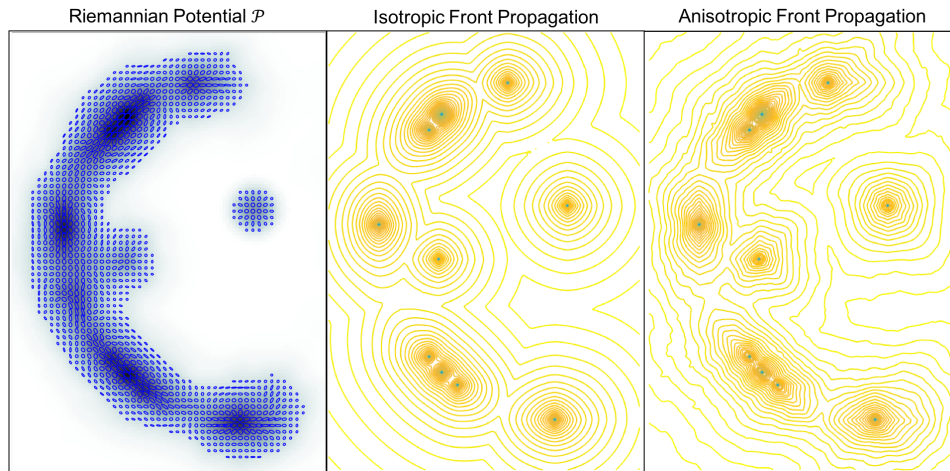


Figure 4.2: Comparison of iso-curves for the isotropic and anisotropic level-set propagation on the given Riemannian potential \mathcal{P} . Anisotropic iso-contours show a more elongated pattern and profile, accordingly with the local anisotropy of the potential.

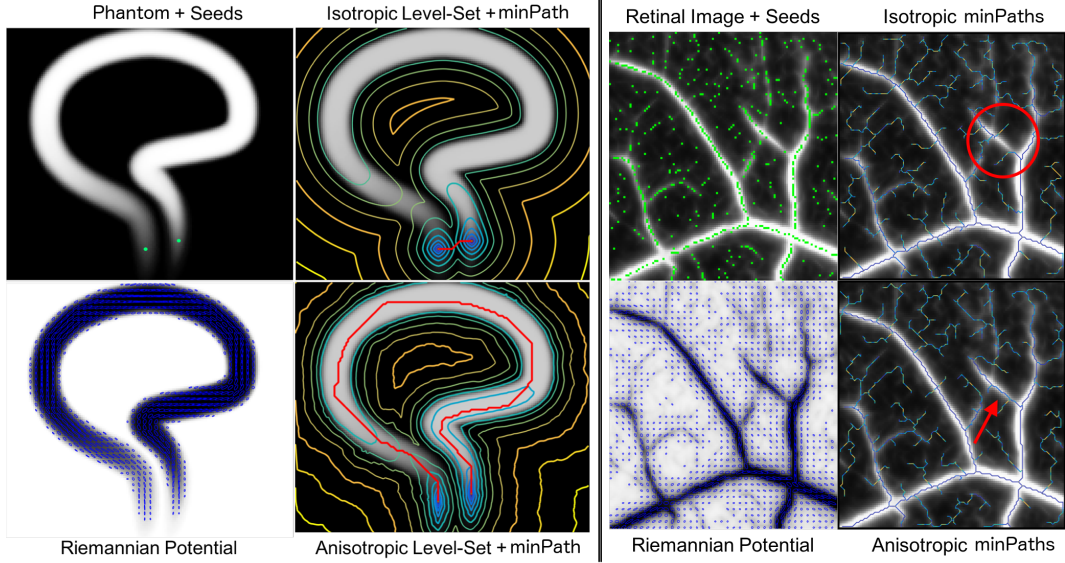


Figure 4.3: Geodesic extraction and fully connected tree using the acyclic connectivity paradigm with both isotropic and anisotropic front propagations. Left: synthetic phantom of convoluted structure, where short-cuts occur for the isotropic level-set. Similarly, short-cuts are found in the retinal subregion, even for large vessels (red circle).

connectivity paradigm is further evaluated for synthetic vascular trees and for a representative set of clinical angiographies.

4.2.2 Experiments on Synthetic and Clinical Data

Synthetic data together with few representative clinical angiographies were first processed as described in Chapter 3 to extract the connected vesselness map and the associated tensor field. Differences in the reconstructed topology of the resulting vascular trees are quantitatively reported in the following section in terms of accuracy, precision and recall for the detected connected branches. In particular, the robustness of the topological reconstruction is evaluated with respect to image degradation for a set of 20 synthetic vascular trees obtained from Vascusynth [82] and on a cerebral Time of Flight MRI (TOF) ($0.36 \times 0.36 \times 0.5$ mm) and a carotid CTA ($0.46 \times 0.46 \times 0.45$ mm). The synthetic dataset of vascular trees (64x64x64 voxels) was generated considering two levels of additional noise: N_1 : $\mathcal{N}(0, 5)$ + Shadows: 1 + Salt&Pepper: 1%; N_2 : $\mathcal{N}(0, 10)$ + Shadows: 1 + Salt&Pepper: 2%. Vascular network ground-truths

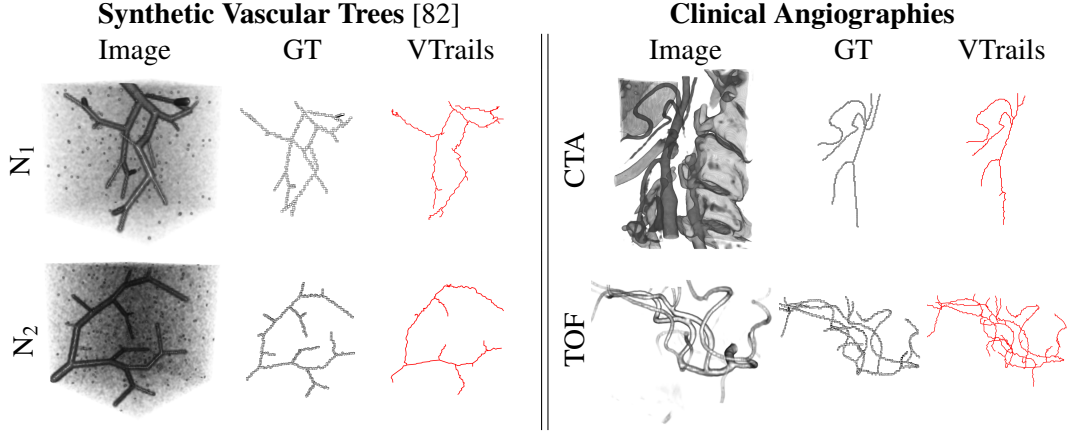


Figure 4.4: Comparison of the vascular connected trees against the respective ground-truth for a representative set of synthetic data, and for a carotid CTA and for a middle cerebral artery TOF MRI. Note that main branches are correctly identified and connected.

(GT) are given in the form of connected centerlines in the voxel-wise image for all the synthetic images and for both TOF and CTA, respectively. Before the quantitative evaluation, the resulting reconstructed topology of connecting geodesic paths Π is verified to be an acyclic graph with a depth-first search, then the topology is compared against the respective GT.

4.2.3 Accuracy, Precision and Recall

Representative examples of degraded images from the synthetic vascular trees and the respective GT are shown in Fig. 4.4 together with the connected graphs extracted by the proposed acyclic connectivity paradigm. In the same fashion, results are shown for the real angiographies TOF and CTA in Fig. 4.4. Qualitatively, the extracted set of connected geodesic paths shows remarkable matching with the provided GT in all cases. First, the acyclic nature of the graph is verified: neither cycles, nor spurious degenerated graphs, i.e. individual unconnected nodes, were found, meaning that the extracted set of connected geodesic paths Π represents a fully-connected geodesic tree. Precision and recall are then evaluated for the identified branches. The accuracy, precision and recall were determined voxel-wise for each branch by setting an arbitrarily small tolerance factor ρ . Also, error distances are determined with the binary distance map of the connected tree is evaluated at

GT. Average errors ($\bar{\epsilon}$) precision and recall are reported (mean \pm SD) in Table 4.1. Note that no pruning of any spurious branches is performed in the analysis. Overall, good results were observed from the initial validation, considering the proposed fully-automatic network extraction paradigm. Missing branches occurred in correspondence of small vessels, where the effect of degradation is predominant: tiny terminal vessels completely occluded by the corrupting shadows (from VascuSynth) will not automatically produce propagating seeds, therefore they cannot be recovered under an automatic configuration. Globally, ϵ values are comparable to the evaluation tolerance ρ , suggesting that the extracted connected geodesic paths lie in the close neighbourhood of the vessels' centerlines. Moreover, the reported values are comparable regardless the level of degradation. As a global observation, the anisotropic formulation of the proposed acyclic connectivity paradigm reduces mis-connections and possible short-cuts on major structures of the vascular tree. As a further remark, the local collision and fast update scheme presented in Section 4.2 represents an optimal solution for the extraction of simplified networks, where the exploration of the image domain becomes computationally intensive and few structures are present, even in case of low signal-to-noise ratio. Also, in this case and for the proposed vascular application, no anatomical priors of the network are enforced, other than its acyclic nature.

4.3 Exhaustive Connectivity Paradigm

The assumption of a vascular tree, in general, provides a natural and anatomically valid constraint for 3D cerebrovascular images, with few – sometimes rare – ex-

Table 4.1: Connectivity tree error distances, precision and recall (mean \pm SD). Left: synthetic vascular tree at degradation levels N_1 and N_2 . Note the invariance of all metrics regardless the degradation level. Right: TOF and CTA.

		Synthetic Vascular Trees [82]			Clinical Angiographies	
		N_1	N_2		TOF	CTA
$\bar{\epsilon}$	[voxels]	2.15 ± 0.65	2.09 ± 0.37	[mm]	1.07 ± 2.65	1.1 ± 1.63
ρ		2			1.42	1.57
Precision		$88.21 \pm 2.58\%$	$87.93 \pm 2.56\%$		77.12%	89.67%
Recall		$68.31 \pm 7.44\%$	$69.18 \pm 3.69\%$		89.49%	83.97%

ceptions, such as the complete circle of Willis and the fenestration of the Basilar Artery and further rare macroscopic anastomoses observed in the posterior cerebral circulation [22, 91, 197, 209]. Although the acyclic connecting paradigm proposed in the previous section provides an initial and fairly accurate estimation of the underlying vascular tree, the explicit greediness of the extraction scheme is incompatible with cyclic vascular topologies. Also, uncertain, ambiguous and poorly spatially-resolved structures, such as foreshortening, neighbouring and convoluted vessels more often observed in clinical angiographies, usually produce cyclic vascular aberrations which result in geodesic short-cuts and branch mis-connections due to *kissing-vessel* artifacts. These non-idealities potentially disrupt automatic extraction of the vascular network and stand as the main limitation of the proposed acyclic connectivity paradigm, even when coupled with an optimal anisotropic front propagation.

As a further contribution of this thesis and in order to introduce a more flexible and generalisable connectivity paradigm to VTrails framework, the acyclic constraint is *relaxed* in the following section. This is achieved by simultaneously and iteratively extracting multiple and independent connecting minimal paths until convergence. This allows having a novel redundant topological representation of the vascular structure in the form of an over-connected geodesic graph Π . The following exhaustive geodesic search of connecting minimal paths explores the whole image domain and accounts for a complete connectivity pattern by considering all possible seeds pairs. Also, an adaptive and self-organising connecting strategy is introduced here to automatically refine the network topology regardless the seeds' initialisation. Lastly the inference of the underlying anatomical vascular trees is performed by extracting the minimum spanning trees of the fully-connected network. Note that multiple trees can be inferred from the same over-connected geodesic graph.

4.3.0.1 Initialization

As in Section 4.2, the set of binary seeds \tilde{S} is first aligned towards the vessels' mid-line with a constrained gradient descent on the connected vesselness map \mathcal{V} , so

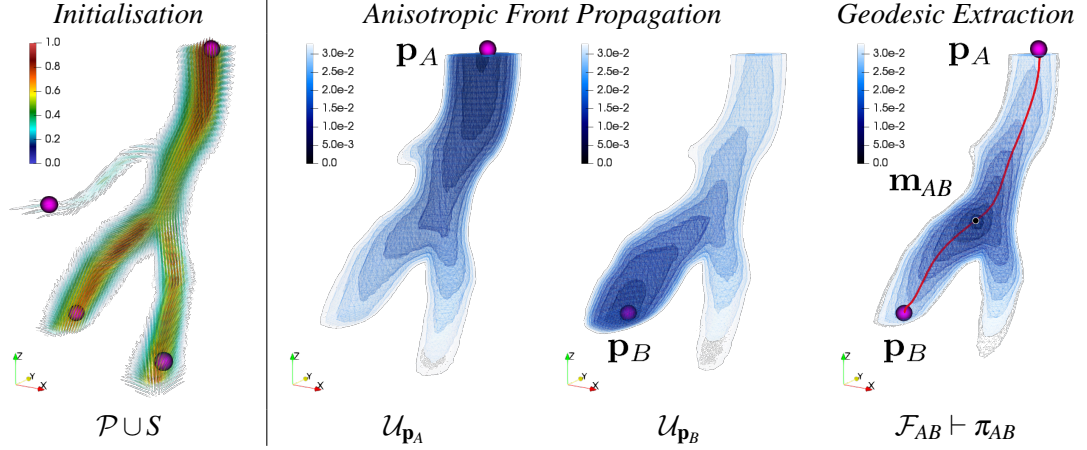


Figure 4.5: Exhaustive geodesic connectivity paradigm: Anisotropic level-set from the Riemannian potential \mathcal{P} and subsequent extraction of a minimal path from a pair of initial seeds \mathbf{p}_A and \mathbf{p}_B . – The paradigm follows in Fig. 4.7

that the aligned individual seeds, together with the endpoints and branch-points of possible connected components, constitute the initial set of source points $\mathbf{p} \in S$, and initialise the anisotropic front propagation (Fig. 4.5).

4.3.0.2 Connectivity Paradigm

For any source point \mathbf{p} , propagating on \mathcal{P} , the geodesic energy map $\mathcal{U}_{\mathbf{p}}$ is iteratively computed and updated until complete exploration of the potential's domain (or up to a pre-determined spatial neighborhood of \mathbf{p} for computational efficiency), similarly to a front wave arrival-time map. In this case, the implementation of the whole anisotropic front propagation algorithm follows the formulation proposed by Konukoglu et al. [102]. Given a pair of source points, an energy functional \mathcal{F}_{AB} is determined as

$$\mathcal{F}_{AB} = (\mathcal{U}_{\mathbf{p}_A} + \mathcal{U}_{\mathbf{p}_B}) + |\mathcal{U}_{\mathbf{p}_A} - \mathcal{U}_{\mathbf{p}_B}|. \quad (4.7)$$

The monotonic profiles of both geodesic energy maps $\mathcal{U}_{\mathbf{p}_A}$ and $\mathcal{U}_{\mathbf{p}_B}$ are so combined to obtain a locus of minimal energy in the correspondence of the connecting path between \mathbf{p}_A and \mathbf{p}_B . Fig. 4.6 shows a representative example of geodesic energy profiles in 1D, for a generic case of two source points spatially located on the x-axis. For the energy functional \mathcal{F}_{AB} , both the intermediate contributions $(\mathcal{U}_{\mathbf{p}_A} + \mathcal{U}_{\mathbf{p}_B})$ and $|\mathcal{U}_{\mathbf{p}_A} - \mathcal{U}_{\mathbf{p}_B}|$ are depicted in green and magenta solid lines, respectively. The first

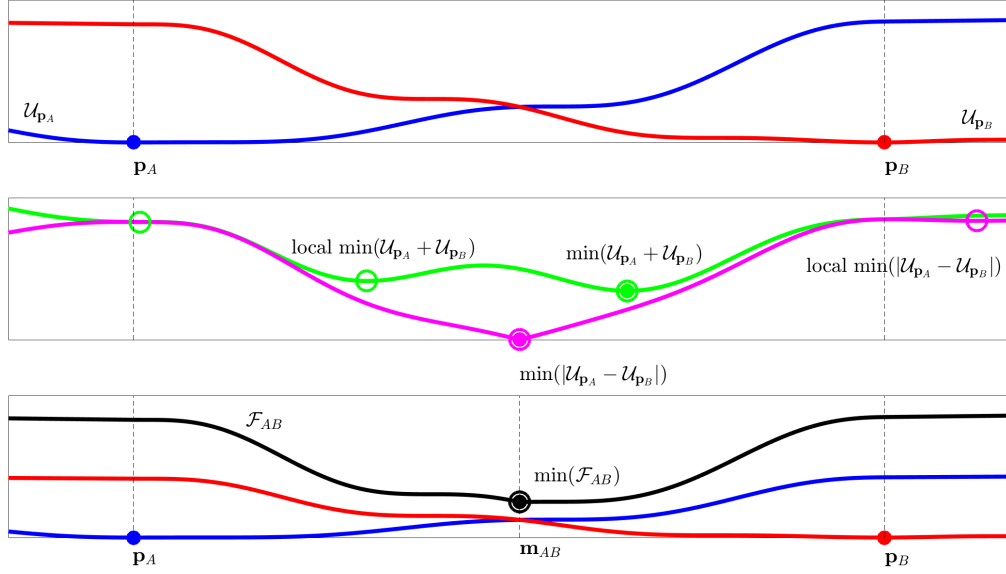


Figure 4.6: Representative example of geodesic energy profiles for a 1D generic case with two source points \mathbf{p}_A and \mathbf{p}_B . (Top) Geodesic energy profiles $\mathcal{U}_{\mathbf{p}_A}$ and $\mathcal{U}_{\mathbf{p}_B}$ are given in blue and red solid lines respectively for the pair of source points. (Centre) Intermediate energy contributions: $(\mathcal{U}_{\mathbf{p}_A} + \mathcal{U}_{\mathbf{p}_B})$ in green; $|\mathcal{U}_{\mathbf{p}_A} - \mathcal{U}_{\mathbf{p}_B}|$ in magenta solid lines. Respective local minima (circles) and global minima (bullets). (Bottom) Resulting energy functional \mathcal{F}_{AB} , with a unique global minimum in the correspondence of \mathbf{m}_{AB} .

contribution $(\mathcal{U}_{\mathbf{p}_A} + \mathcal{U}_{\mathbf{p}_B})$ shows an increasing monotonic profile outside the spatial range enclosed by \mathbf{p}_A and \mathbf{p}_B , however several local minima (green circles in Fig. 4.6 with the global minimum as a green bullet) are observed within the same spatial range. Conversely, the second contribution $|\mathcal{U}_{\mathbf{p}_A} - \mathcal{U}_{\mathbf{p}_B}|$ shows a unique global minimum (magenta bullet in Fig. 4.6) within the spatial range enclosed by \mathbf{p}_A and \mathbf{p}_B , whereas local minima (magenta circles in Fig. 4.6) can be found outside the same spatial range. By independently considering either one of these two contributions, the geodesic path extraction between \mathbf{p}_A and \mathbf{p}_B is not guaranteed to converge to the desired solution. Each possible pair of source points, \mathbf{p}_A , \mathbf{p}_B , is connected with a geodesic minimal path π_{AB} , by back-tracing \mathcal{F}_{AB} from the source points \mathbf{p}_A and \mathbf{p}_B to the respective connecting geodesic point of minimal energy \mathbf{m}_{AB} , identified as

$$\mathcal{F}_{AB}(\mathbf{m}_{AB}) = \min(\mathcal{F}_{AB}) \quad (4.8)$$

as shown in Fig. 4.5. The connecting geodesic path π_{AB} is therefore obtained by

the union of two geodesics, each of which is traced with a gradient descent on \mathcal{F}_{AB} . From Fig. 4.6 it is possible to observe how the resulting energy functional \mathcal{F}_{AB} exhibits an increasing monotonic profile outside the spatial range enclosed by the source points \mathbf{p}_A and \mathbf{p}_B , and, at the same time, it presents a unique global minimum (black bullet in Fig. 4.6 coinciding with the only local minima as a circle) in the correspondence of the point \mathbf{m}_{AB} . This allows to solve the geodesic back-tracing of \mathcal{F}_{AB} , providing therefore a unique minimal path π_{AB} connecting the pair of source points.

The associated integral geodesic length $F_{(\pi_{AB})} = \int_{\mathbf{p}_A}^{\mathbf{p}_B} \mathcal{F}_{AB} d\pi$ is determined along the extracted path π_{AB} and the connectivity of the graph Π is accordingly updated. Here, Π can be directly expressed adopting a canonical undirected weighted graph notation as $\Pi = \mathcal{G}(N, E)$ comprising a set of *nodes* N , i.e. the set of points \mathbf{p} , and a set of *edges* E , i.e. the set of connecting paths π , respectively. By using a symmetric adjacency matrix, the integral geodesic length $F_{(\pi_{AB})}$ is then attributed to the edge's weight, which connects the pair of nodes $(\mathbf{p}_A, \mathbf{p}_B)$. It is clear that, by terminating the minimal paths extraction only with the initial set of source points S , the topology of the resulting geodesic connecting graph Π would hinge on the initialisation, thus on the initial guess of the nodes, and would also constrain the connecting paths (i.e. the vascular branches) to connect (or bifurcate) only in correspondence to the initial set of source points in S .

4.3.0.3 Adaptive Geodesic Graph

With this view, an adaptive and self-organising connectivity strategy for the geodesic graph Π is introduced in the framework, so that the topology of the graph itself will be refined and updated in a completely automatic fashion. This is obtained by 1) extracting the minimum spanning tree (MST) of Π , i.e. $\zeta = MST(\Pi)$; 2) increasing the density of source points (nodes) at each connecting path (edge) of ζ , and 3) running the connectivity paradigm as in Section 4.3.0.2 among the new set of nodes and the existing ones. Note that the adaptive connectivity strategy employs an iterative process that will converge to a pre-defined spatial node density. In detail, the minimum spanning tree ζ is defined as the subset of the connected edges that

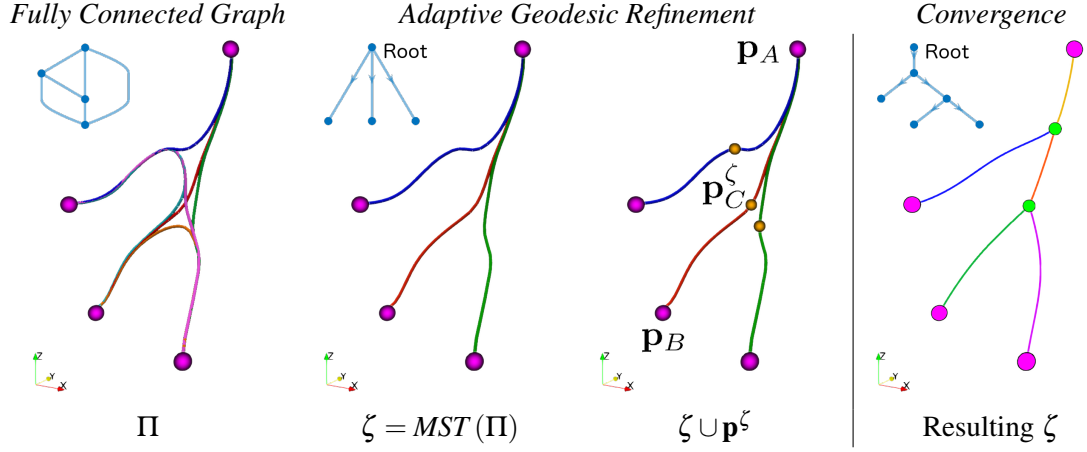


Figure 4.7: Exhaustive geodesic connectivity paradigm: topological inference of the over-connected graph Π and of its geodesic minimum spanning tree ζ . Vector topology of the over-connected graph Π (first iteration), of its minimum spanning tree ζ (first iteration), and resulting tree topology at convergence. – The paradigm starts in Fig. 4.5

acyclically link all the nodes together by minimising the sum of total edge weights. Here, the edge weights are the integral geodesic lengths F . Therefore the resulting ζ is the connected subset of geodesic minimal paths. Given its generic connecting path π_{AB}^ζ , a new source point \mathbf{p}_C^ζ is generated between \mathbf{p}_A^ζ and \mathbf{p}_B^ζ so that \mathbf{p}_C^ζ is the respective midpoint of the geodesic path π_{AB}^ζ , and

$$\|\mathbf{p}_A^\zeta - \mathbf{p}_C^\zeta\| \geq \mu, \text{ and } \|\mathbf{p}_B^\zeta - \mathbf{p}_C^\zeta\| \geq \mu. \quad (4.9)$$

μ is here the Euclidean spatial threshold for contiguous nodes and constitutes the pre-defined maximal spatial node density. The new set of source points \mathbf{p}^ζ will be connected with the existing ones following the connectivity paradigm described in Section 4.3.0.2, updating therefore the adjacency matrix that increases in size at each iteration. The process terminates when the pre-defined spatial node density is reached. Note that Π is iteratively refined and the topology, as well as the associated MST, may subsequently change from its initial guess (as in Fig. 4.7, first iteration vs. convergence). Also, the smaller μ , the more dense the set of \mathbf{p}^ζ , the finer the localisation of branch-points and the greater the complexity of the over-connected graph Π . The inference of a geodesic vascular network, as formulated, determines

a topological refining scheme similar to an evolutionary process. In other words, at each automatic refinement step, all the newly generated seeds of the set \mathbf{p}^ζ are associated with a pair of *ancestor* nodes (and obviously an *ancestor* edge). It can be observed how the iterative inference of the underlying network shows a hierarchical and generative scheme, i.e. it follows a phylogenetic *generation*, at each iteration before convergence is reached. An intuitive visualisation of the exhaustive connectivity paradigm is available at <https://youtu.be/gABd0leyFGs>

4.3.1 Vascular Minimum Spanning Tree

The resulting vascular trees ζ are finally determined as the minimum spanning trees of the connected components in Π , as in Section 4.3.0.3, at convergence. Note that for more complex vascular topologies, a set of minimum spanning trees (i.e. a forest of geodesic MSTs) can be extracted for the underlying anatomical tree-like structures under a specific region of interest (ROI), by means of a co-registered binary or multi-class fuzzy mask. Here, the integral Euclidean length $L_{(\pi^\zeta)}$ and the aforementioned integral geodesic length $F_{(\pi^\zeta)}$ of each connecting path π^ζ can be employed to modulate the extension of the resulting vascular trees ζ . Undesired leaves and possible spurious branches detected by the exhaustive connectivity paradigm can be pruned using $L_{(\pi^\zeta)}$ and $F_{(\pi^\zeta)}$, respectively. Lastly, by identifying a root, the hierarchical topology of the undirected vascular trees is automatically determined, and each node is assigned with an univocal *parent-child* relation.

4.3.2 Experiments on Synthetic and Clinical Data

To validate the exhaustive connectivity paradigm towards the extraction and inference of the underlying vasculature, a comprehensive set of synthetic vascular trees, as well as an extensive set of multi-modal cerebrovascular angiographies were considered. In details, a collection of 10-images datasets of synthetic vascular trees ($128 \times 128 \times 128$ voxels, isotropic 1 mm) was generated using VasuSynth [82] as described in Section 3.5 considering three levels of increasing noise and increasing terminal branches (Table 3.2). Among the real clinical angiographies, a total

of 24 Rotational Angiographies of cerebral Aneurysms (RAA) from the Aneurisk¹ dataset [6], 18 cerebral time of flight MR Angiographies (MRA) from the Kitware² dataset [28], 10 head-neck Phase Contrast (PC) MR venograms ($0.86 \times 0.86 \times 1.00$ mm); and 10 cerebral Computed Tomography Angiographies (CTA) (isotropic 0.4 mm³) were considered. Representative examples of the cerebrovascular angiographies have been shown in Section 3.5.1.1, Fig. 3.9 for the visual assessment of the connected vesselness maps. For each synthetic and real angiography, the vascular network ground-truths (GT) or manual annotations Gold Standard (GS) are given as spatial centerlines.

4.3.2.1 Accuracy Scores and Measures

In the following experiments, the inferred connected topologies are quantitatively assessed in the form of trees, under a geometrical and topologically-aware evaluation framework.

Geometrical Accuracy. A symmetric error measure ε_S and the average Hausdorff_{95%} distance ε_H are considered to evaluate the spatial and geometrical accuracy of the recovered vascular trees. In particular, the spatial coordinates of all the extracted connected branches (i.e. all the minimal paths of the tree) and the spatial coordinates of the specific branch-points are evaluated with respect to the available ground-truth or gold standard in a tolerance neighbourhood of 5 mm. The symmetric error measure ε_S is determined by averaging the Euclidean distances between the closest points of considered spatial instances. The average Hausdorff_{95%} distance ε_H is determined in a robust way as the mean of the maximal Euclidean distances between the closest points of the considered spatial instances. Note that with the notation ε_S^ζ and $\varepsilon_S^{\text{bp}}$ the symmetric error is given for all the extracted connected branches in the trees (ζ) and for the specific branch-points (bp), respectively. Similarly, with the notation ε_H^ζ and $\varepsilon_H^{\text{bp}}$ the average Hausdorff_{95%} distance is given for all the branches of the trees and for the specific branch-points.

¹<http://ecm2.mathcs.emory.edu/aneuriskweb/index>

²<https://data.kitware.com/#collections>

Topological Accuracy. The topology of the trees is compared against the GT (or GS) using the tree edit distance (TED)³ [150] *only* for the synthetic vascular trees, whereas the spatially-aware DIADEM⁴ score [75] is computed for all the considered datasets.

The tree edit distance is defined for a pair of trees as the minimum-cost sequence of node-edit operations that transform one tree into another. The considered node-edit operations account for deletion, insertion and renaming the node. Each node-edit operation is given a cost; here node insertion and deletion are equivalently associated to a unitary cost, whereas renaming the node is given a null cost, as the considered trees do not have labels. Since there are multiple sequences of node-edit operations able to topologically transform one tree into another, the tree edit distance provides the sequence with the minimal cost.

The DIADEM score, originally designed to compare the morphological reconstruction of two different neurons, comprises a multi-step alignment process between a target tree and a test tree, by spatially registering both branch-points (nodes) and branches (edges) given an Euclidean distance threshold. The subsequent tree topological matches are then weighted by the evaluated spatial distances and integrated over the size of the sub-tree to which a connection leads.

By using these topological scores, differences are evaluated in terms of branches and branch-points spatial correspondence with DIADEM, and in terms of graph adjustments, i.e. node insertion and deletion with TED respectively. While the DIADEM metric is bounded by [0,1], 1 being the perfect match, the TED score has no upper bound. Low TED scores represent higher topological matching, however, a comparable index of trees overlap is obtained as

$$\text{TED}_{\text{ov}} = \left(1 - \frac{\text{TED}(\zeta_1, \zeta_2)}{\text{TED}(\zeta_1, \{\}) + \text{TED}(\zeta_2, \{\})} \right) \cdot 100\%, \quad (4.10)$$

where ζ_1 and ζ_2 are the trees to be compared, and $\{\}$ represents a void graph. TED_{ov} has the same bound [0,1], 1 being the perfect match for isomorphic trees.

³<http://tree-edit-distance.dbresearch.uni-salzburg.at>

⁴<http://diademchallenge.org/metric.html>

4.3.2.2 Semi-Automatic Connectivity - Synthetic Trees

In the following experiment the accuracy of vascular network inferred with VTrails' exhaustive connectivity paradigm (Section 4.3) is evaluated for different vesselness potentials, given the *same* seeds initialisation, i.e. the end-points of the terminal branches of the synthetic vascular trees. In detail, by adopting a manual, therefore *semi-automatic*, seeds initialisation, the accuracy of the formulated exhaustive connectivity paradigm is tested with respect to different saliency maps, other than the Riemannian potential recovered within VTrails framework. As in Section 3.5.1, the other vesselness potentials were respectively obtained with Frangi filter (FFR) [70], Optimally Oriented Flux (OOF) [106], Ranking the Orientation Responses of Path Operators (RORPO) [131], and the Hybrid Diffusion with Continuous Switch filter (HDCS) [129], as previously shown in Fig. 3.8. Each of these vesselness maps were associated with an isotropic tensor field, whereas the Riemannian vesselness potential \mathcal{P} determined with VTrails was employed as is. Given the semi-automatic seeds initialisation, the accuracy of VTrails' exhaustive connectivity paradigm is here indicated with VT_{semi} . The reconstructed acyclic topology, i.e. the minimum spanning tree at convergence, is therefore compared to the ground-truth (GT). The robustness of the topological inference with respect to image degradation (see Table 3.2) is reported in Section 4.3.3.1, Tables 4.2, 4.3 and 4.4.

4.3.2.3 Fully Automatic Connectivity - Synthetic Trees

Similarly to the previous Section 4.3.2.2, the connected topology of the synthetic trees is here inferred *only* with VTrails framework using, in this case, a fully automatic pipeline (VT_{auto}). Specifically, the Riemannian vesselness is considered as connecting potential and the initial seeds for the exhaustive geodesic connectivity paradigm are *automatically* determined as in Section 3.3. Here, the exploration of the Riemannian potential is limited to a pre-defined spatial neighbourhood of the initial seeds, for computational efficiency. The seeds are automatically determined as in eq. 3.7, considering a p -quantile of 0.75. Given the GT, the evaluation of the geometrical and topological accuracy follows the previous scheme, and results are reported in Section 4.3.3.2, Tables 4.2, 4.3 and 4.4 (column: VT_{auto}), and in Fig.

4.8 for a representative example.

4.3.2.4 Fully Automatic Connectivity - Clinical Data

Each clinical angiography is processed using VTrails' fully automatic connectivity paradigm (VT_{auto}) as in Section 4.3.2.3. As for the synthetic trees, the exploration of the Riemannian potential for the clinical data is also limited to an anatomically-compatible spatial neighbourhood of the initial seeds, for computational efficiency. Also, the seeds are automatically determined as in eq. 3.7, considering a p -quantile of 0.75. The accuracy of the inferred connected vascular topology is evaluated by comparing the resulting minimum spanning trees with the available GT or GS annotations. *RAA* centerlines are obtained with the Vascular Modelling Toolkit (VMTK) [8]; *MRA* ground-truth trees are determined with TubeTK [15]; the gold standard for *PC* and *CTA* datasets is given by the centerlines of the manual lumen segmentation, obtained with a skeletonisation strategy [86]. Note that, for whole-brain vascular datasets, only the intra-cranial volume was considered for the topological inference, by means of a co-registered brain mask, from the brainstem up to the cortex. Also, possible cycles in the GS have been opportunely cut or removed by adopting a ROI-based, conservative and intensity-maximising, minimum spanning tree extraction of the complete GS connected graph. Accordingly with the underlying anatomical tree-like vasculature, the quantitative analysis has been performed for the deep brain arterial trees [91] branching from the Circle of Willis in both *MRA* and *CTA* datasets, whereas the connectivity patterns of the posterior venous sinus in the *PC* datasets was quantitatively evaluated. Note also that additional effort was required to harmonise the provided centerlines in the form of a canonical acyclic graph (tree, or forest of trees), where branch-points corresponds to nodes and vascular branches to edges respectively, since the tree topology cannot be consistently evaluated otherwise. Given the available GT and GS in the form of binary maps or as a set of spatial centerlines, the topological harmonisation was performed with an in-house split-merge-connect strategy similar to [95]. This allowed to convert binary and voxel-wise skeletons to ordered and connected spatial segments, i.e. the vascular branches, in the form of a canonical acyclic graph. Similarly, sub-voxel

spatial centerlines were converted to a connected acyclic topology, by evaluating possible overlapped portions and local branch-points with a tolerance factor equal to the native image voxel size. Quantitative results are reported in Section 4.3.3.3, Table 4.5, and a qualitative evaluation is given in Fig. 4.9.

4.3.3 Results of Geometrical and Topological Accuracy

4.3.3.1 Semi-Automatic Connectivity - Synthetic Trees

The accuracy of the reconstructed synthetic trees using different vesselness potentials is given in Tables 4.2 and 4.3 for the whole trees geometry, for the detected branchpoints location and for the entire topologies. The symmetric error measures (ϵ_S^ζ) showed overall comparable values among the considered vesselness maps (FFR, OOF, RORPO, HDCS and VT_{semi}), where a better performance (*italic text*) has been observed for VT_{semi} (Table 4.2.a). Slightly lower error distances are found on both ϵ_S^ζ and the Hausdorff_{95%} distances (ϵ_H^ζ – Table 4.2.b) in all cases, being the former ones limited always within the voxel size. Above 80% of branchpoints were successfully detected in all cases, even with high level of corrupting noise. The considered enhancing methods yielded comparable values for the accuracy of the branchpoints' location (Table 4.3.a), however VT_{semi} showed overall lower symmetric errors (ϵ_S^{bp}) as well as lower Hausdorff_{95%} distances (ϵ_H^{bp}), especially at high level of degrading noise (Table 4.3.b). This first suggests that the smooth Riemannian vesselness improves the accuracy of branchpoint spatial location, secondly, that the topological inference via the presented connectivity paradigm is considerably more stable even with different vesselness potentials. This is supported by the TED_{ov} indices (Table 4.4.a), where considerable topological overlap is found for all the reconstructed trees. Better performances are observed for VT_{semi} in the great majority of cases, especially for highly noisy images. DIADEM values show however that VT_{semi} outperforms all the other methods with the spatially-aware topological reconstruction of the synthetic trees (Table 4.4.b), where the accuracy of the branch-point spatial location and of the branches geometry is considered jointly with the hierarchical parent-child relation.

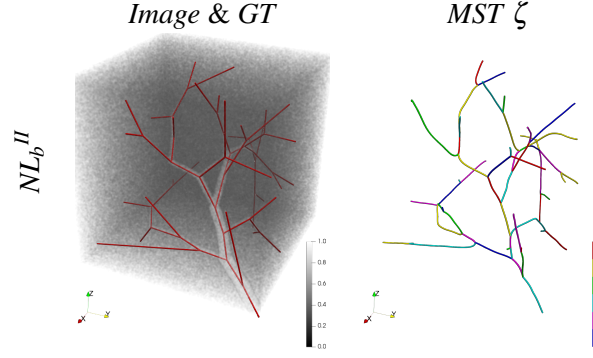


Figure 4.8: Representative example of noisy synthetic vascular tree NL_b^{II} : resulting minimum spanning tree inferred with VT_{auto} .

Table 4.2: Synthetic trees at different noise levels (NL) – Symmetric error ϵ_S [mm] (*a.*) and Hausdorff_{95%} distance ϵ_H [mm] (*b.*) for the minimum spanning trees (ζ). Values are reported mean \pm SD. Best accuracy for the semi-supervised connectivity in *italic font*; best accuracy VT_{auto} vs. VT_{semi} in **bold font**.

<i>a.</i>	ϵ_S^ζ					
	FFR	OOF	RORPO	HDCS	VT_{semi}	VT_{auto}
NL_a^I	0.89 \pm 0.34	0.87 \pm 0.32	0.91 \pm 0.37	0.93 \pm 0.38	<i>0.85\pm0.31</i>	0.99 \pm 0.34
NL_a^{II}	0.93 \pm 0.32	0.93 \pm 0.32	0.95 \pm 0.33	0.99 \pm 0.40	<i>0.90\pm0.31</i>	1.03 \pm 0.34
NL_a^{III}	0.95 \pm 0.35	0.94 \pm 0.37	0.96 \pm 0.37	1.02 \pm 0.46	<i>0.90\pm0.32</i>	1.04 \pm 0.36
NL_b^I	0.91 \pm 0.34	0.88 \pm 0.30	0.98 \pm 0.44	0.96 \pm 0.43	<i>0.84\pm0.30</i>	1.03 \pm 0.47
NL_b^{II}	0.95 \pm 0.36	0.92 \pm 0.35	1.01 \pm 0.46	1.11 \pm 0.71	<i>0.89\pm0.32</i>	1.02 \pm 0.35
NL_b^{III}	0.96 \pm 0.38	0.93 \pm 0.37	1.04 \pm 0.57	1.12 \pm 0.70	<i>0.90\pm0.33</i>	1.51 \pm 1.21
NL_c^I	0.88 \pm 0.35	0.85 \pm 0.33	0.95 \pm 0.44	0.95 \pm 0.47	<i>0.82\pm0.31</i>	1.12 \pm 0.71
NL_c^{II}	0.96 \pm 0.36	0.92 \pm 0.34	1.02 \pm 0.48	1.17 \pm 0.77	<i>0.87\pm0.32</i>	1.04 \pm 0.38
NL_c^{III}	0.96 \pm 0.36	0.95 \pm 0.36	1.07 \pm 0.57	1.25 \pm 0.91	<i>0.90\pm0.33</i>	1.05 \pm 0.39

<i>b.</i>	ϵ_H^ζ					
	FFR	OOF	RORPO	HDCS	VT_{semi}	VT_{auto}
NL_a^I	1.53 \pm 0.21	1.40 \pm 0.17	1.64 \pm 0.23	1.67 \pm 0.21	<i>1.39\pm0.12</i>	1.54 \pm 0.25
NL_a^{II}	1.48 \pm 0.05	1.46 \pm 0.07	1.57 \pm 0.12	1.79 \pm 0.26	<i>1.39\pm0.07</i>	1.57 \pm 0.07
NL_a^{III}	1.59 \pm 0.08	1.61 \pm 0.07	1.66 \pm 0.13	1.96 \pm 0.32	<i>1.43\pm0.07</i>	1.60 \pm 0.07
NL_b^I	1.53 \pm 0.12	1.37 \pm 0.15	1.83 \pm 0.28	1.82 \pm 0.31	<i>1.34\pm0.19</i>	1.93 \pm 1.30
NL_b^{II}	1.58 \pm 0.07	1.52 \pm 0.05	1.96 \pm 0.35	2.65 \pm 1.70	<i>1.42\pm0.04</i>	1.55 \pm 0.06
NL_b^{III}	1.66 \pm 0.07	1.58 \pm 0.05	2.35 \pm 0.51	2.62 \pm 0.63	<i>1.46\pm0.08</i>	3.94 \pm 6.61
NL_c^I	1.50 \pm 0.17	1.45 \pm 0.15	1.85 \pm 0.26	1.75 \pm 0.54	<i>1.35\pm0.19</i>	2.43 \pm 1.78
NL_c^{II}	1.64 \pm 0.11	1.50 \pm 0.07	2.04 \pm 0.25	2.68 \pm 1.12	<i>1.40\pm0.08</i>	1.65 \pm 0.13
NL_c^{III}	1.61 \pm 0.06	1.59 \pm 0.06	2.34 \pm 0.31	3.35 \pm 2.01	<i>1.44\pm0.06</i>	1.67 \pm 0.11

4.3.3.2 Fully Automatic Connectivity - Synthetic Trees

The reconstruction of the synthetic trees is performed in a completely automatic fashion, using therefore VTrails framework (VT_{auto}) for the vesselness potential, for the seeds detection and for the exhaustive connectivity paradigm. With this configuration no further branch pruning is performed. The same aforementioned accuracy indices are reported in Tables 4.2, 4.3 and 4.4 (column: VT_{auto}). As few terminal branches were missing at higher levels of degrading noise (Fig. 4.8), the global ϵ_S^ζ slightly increases compared to the semi-automatic VT_{semi} pipeline. However errors are overall comparable to the voxel size in all cases. Smaller average symmetric

Table 4.3: Synthetic trees at different noise levels (*NL*) – Symmetric error ϵ_S [mm] (*a.*) and Hausdorff_{95%} distance ϵ_H [mm] (*b.*) for the branchpoints (bp) location. Values are reported mean \pm SD. Best accuracy for the semi-supervised connectivity in *italic* font; best accuracy VT_{auto} vs. VT_{semi} in **bold** font.

<i>a.</i>	ϵ_S^{bp}					
	FFR	OOF	RORPO	HDCS	VT _{semi}	VT _{auto}
<i>NL_a^I</i>	2.25 \pm 1.09	2.18 \pm 0.95	2.19 \pm 1.02	2.19 \pm 0.97	<i>1.96\pm0.96</i>	1.91\pm0.78
<i>NL_a^{II}</i>	2.19 \pm 1.00	2.05 \pm 1.03	2.18 \pm 0.99	2.30 \pm 1.11	<i>2.03\pm0.97</i>	1.92\pm0.90
<i>NL_a^{III}</i>	2.38 \pm 1.02	2.42 \pm 1.06	2.39 \pm 1.09	2.41 \pm 1.12	<i>2.06\pm1.07</i>	2.06\pm0.92
<i>NL_b^I</i>	2.38 \pm 0.97	2.23 \pm 1.13	2.50 \pm 1.14	2.66 \pm 1.09	<i>1.89\pm0.92</i>	2.07 \pm 1.05
<i>NL_b^{II}</i>	2.25 \pm 0.97	2.35 \pm 1.05	2.19 \pm 1.08	2.47 \pm 1.04	<i>2.01\pm0.97</i>	2.02 \pm 0.90
<i>NL_b^{III}</i>	2.38 \pm 1.07	2.25 \pm 1.12	<i>2.09\pm1.08</i>	2.46 \pm 1.14	2.15 \pm 1.04	2.16 \pm 1.04
<i>NL_c^I</i>	2.35 \pm 1.04	2.31 \pm 1.12	2.28 \pm 1.09	2.36 \pm 1.00	<i>2.12\pm1.16</i>	2.08\pm0.91
<i>NL_c^{II}</i>	2.33 \pm 1.04	2.23 \pm 1.01	2.23 \pm 1.04	2.41 \pm 1.11	<i>1.95\pm0.98</i>	2.01 \pm 0.88
<i>NL_c^{III}</i>	2.35 \pm 1.04	2.35 \pm 1.08	2.11 \pm 1.09	2.47 \pm 1.02	<i>2.08\pm1.06</i>	2.08\pm0.98

<i>b.</i>	ϵ_H^{bp}					
	FFR	OOF	RORPO	HDCS	VT _{semi}	VT _{auto}
<i>NL_a^I</i>	4.36 \pm 0.41	4.13 \pm 0.60	4.08 \pm 0.77	4.04 \pm 0.77	<i>3.74\pm0.46</i>	3.61\pm0.63
<i>NL_a^{II}</i>	4.08 \pm 0.32	4.12 \pm 0.60	4.03 \pm 0.46	4.29 \pm 0.35	<i>3.82\pm0.68</i>	3.69\pm0.55
<i>NL_a^{III}</i>	4.24 \pm 0.36	4.38 \pm 0.27	4.32 \pm 0.45	4.54 \pm 0.31	<i>4.18\pm0.46</i>	3.84\pm0.35
<i>NL_b^I</i>	4.15 \pm 0.33	4.36 \pm 0.33	4.32 \pm 0.38	4.39 \pm 0.51	<i>3.68\pm0.63</i>	4.21 \pm 0.46
<i>NL_b^{II}</i>	4.09 \pm 0.42	4.29 \pm 0.35	4.38 \pm 0.41	4.13 \pm 0.77	<i>3.93\pm0.52</i>	3.70\pm0.55
<i>NL_b^{III}</i>	4.35 \pm 0.31	4.39 \pm 0.48	4.28 \pm 0.50	4.51 \pm 0.21	<i>4.03\pm0.41</i>	3.75\pm1.41
<i>NL_c^I</i>	4.05 \pm 0.56	4.38 \pm 0.68	4.31 \pm 0.31	<i>3.79\pm0.69</i>	4.43 \pm 0.49	3.69\pm0.59
<i>NL_c^{II}</i>	4.14 \pm 0.40	4.06 \pm 0.71	4.31 \pm 0.37	4.23 \pm 0.78	<i>3.91\pm0.46</i>	3.72\pm0.53
<i>NL_c^{III}</i>	4.15 \pm 0.36	4.28 \pm 0.54	4.19 \pm 0.40	4.13 \pm 0.51	<i>3.92\pm0.47</i>	3.91\pm0.58

errors and $\varepsilon_H^{\text{bp}}$ values are found for the detected branchpoints location, suggesting that the Riemannian vesselness potential, combined with the fully automatic seeds initialisation, accurately recovers the junction points of the network. Such configuration outperforms the semi-automatic approach even with severely degraded images. Similarly to the semi-automatic approaches, the isomorphic topological overlap (TED_{ov}) shows comparable values. No significant differences were found in the pairwise comparison, whereas the spatially-aware DIADEM metric reported higher matching in the majority of cases with sporadic significantly better values ($p < 0.05$) for VT_{auto} vs. the semi-automatic approach VT_{semi} (i.e. NL_a^{II} , NL_a^{III}

Table 4.4: Synthetic trees at different noise levels (NL) – Topological accuracy [%]: TED_{ov} (a.) and DIADEM (b.) metrics. Values are reported mean \pm SD. Best accuracy for the semi-supervised connectivity in *italic* font; best accuracy VT_{auto} vs. VT_{semi} in **bold** font.

a.	TED_{ov}					
	FFR	OOF	RORPO	HDCS	VT_{semi}	VT_{auto}
NL_a^{I}	74.6 \pm 8.2	70.3 \pm 5.3	79.1 \pm 6.7	70.1 \pm 3.3	73.5 \pm 8.5	75.4\pm6.3
NL_a^{II}	78.5 \pm 4.5	74.7 \pm 5.0	72.8 \pm 6.2	60.9 \pm 6.7	78.0 \pm 5.4	75.9 \pm 5.1
NL_a^{III}	73.2 \pm 4.9	69.7 \pm 3.1	71.3 \pm 5.0	58.8 \pm 8.5	74.6 \pm 6.4	74.6\pm4.6
NL_b^{I}	77.6 \pm 5.3	71.8 \pm 4.5	72.2 \pm 4.4	62.4 \pm 5.9	78.4 \pm 6.5	68.4 \pm 10.0
NL_b^{II}	77.8 \pm 5.7	73.5 \pm 7.5	71.6 \pm 3.9	58.6 \pm 8.1	76.8 \pm 4.6	74.6 \pm 6.6
NL_b^{III}	72.9 \pm 5.6	68.8 \pm 4.7	68.9 \pm 3.9	67.1 \pm 5.9	73.4 \pm 4.6	58.8 \pm 9.2
NL_c^{I}	77.2 \pm 6.9	70.7 \pm 6.4	72.1 \pm 3.4	55.4 \pm 12.5	78.7 \pm 7.6	64.7 \pm 4.9
NL_c^{II}	74.7 \pm 7.6	72.0 \pm 7.5	73.8 \pm 3.2	60.2 \pm 9.3	74.3 \pm 3.5	71.6 \pm 7.6
NL_c^{III}	75.6 \pm 3.3	69.5 \pm 4.6	69.5 \pm 3.0	65.1 \pm 3.7	74.8 \pm 4.0	68.4 \pm 4.4

b.	DIADEM					
	FFR	OOF	RORPO	HDCS	VT_{semi}	VT_{auto}
NL_a^{I}	43.3 \pm 28.6	39.0 \pm 28.8	43.6 \pm 29.4	39.3 \pm 30.9	52.4 \pm 18.8	65.1\pm12.3
NL_a^{II}	26.8 \pm 27.5	39.4 \pm 20.0	27.8 \pm 24.5	25.3 \pm 32.2	42.6 \pm 26.9	67.8\pm6.6
NL_a^{III}	44.4 \pm 27.3	25.4 \pm 28.6	51.3 \pm 26.9	22.8 \pm 25.9	57.6 \pm 9.2	71.5\pm6.6
NL_b^{I}	36.6 \pm 30.0	37.2 \pm 32.5	30.2 \pm 28.4	26.8 \pm 30.1	49.7 \pm 25.9	58.5\pm13.7
NL_b^{II}	41.5 \pm 25.1	40.2 \pm 28.4	31.5 \pm 19.8	22.7 \pm 28.8	53.9 \pm 18.1	57.4\pm15.9
NL_b^{III}	39.7 \pm 29.5	31.2 \pm 27.6	39.1 \pm 26.3	32.2 \pm 25.9	60.8 \pm 12.3	44.1 \pm 20.1
NL_c^{I}	42.7 \pm 26.5	36.6 \pm 34.8	30.8 \pm 28.4	12.9 \pm 22.6	54.3 \pm 22.3	44.2 \pm 9.8
NL_c^{II}	45.2 \pm 26.2	32.6 \pm 26.3	50.4 \pm 19.0	26.9 \pm 23.3	51.9 \pm 25.2	57.8\pm5.8
NL_c^{III}	36.1 \pm 24.3	18.9 \pm 27.2	24.0 \pm 27.3	23.4 \pm 26.9	47.7 \pm 21.1	43.8 \pm 20.9

and NL_c^{II}).

4.3.3.3 Fully Automatic Connectivity - Clinical Data

The fully automatic VTrails framework is employed to recover the vascular trees from real angiographies. As in the previous Section 4.3.3.2, the Riemannian vesselness potential, the seeds detection and the exhaustive connectivity paradigm followed a fully automatic configuration in a set of multi-modal brain angiographies. The quantitative assessment of the clinical datasets focused on vascular branches originally defined and provided in the available GT and gold standard. Co-registered ROI-based masks were used to separate intra/extra-cranial vessels and anterior/posterior or left/right-lobe vascular territories, coherently with assumption of deep-brain vascular trees as described in Section 4.3.2.4. Short and terminal vascular branches are pruned from the inferred trees. Accordingly with anatomical considerations and compatibly with the angiographic detail and image quality, terminal leaves shorter than 5 mm in length were removed from the extracted vascular trees. Both geometrical and topological accuracies are reported for each clinical dataset in Table 4.5, where only the DIADEM metric is considered for the evaluation of the tree topology. In this case, TED_{ov} is not used, since the evaluation of the isomorphic tree overlap is uninformative and possibly misleading in an experimental set-up other than simulated and synthetic images. The average symmetric errors ε_S^ζ were comparable to the voxel size, with the average Hausdorff_{95%} distances (ε_H^ζ) that did not exceed 5 mm. Analogously the detected branchpoints reported a mean error ε_S^{bp} of approximately 2 mm, with maximal distances of up to 4-5 mm in all clinical datasets. DIADEM metrics showed a considerably higher correspondence between the available annotation gold standard and the automatically reconstructed tree topology, with overall consistent and comparable values among different imaging modalities. The spatial and topological correspondence can be also qualitatively assessed in Fig. 4.9, where representative examples are shown with associated annotations (GS), geodesic graphs (II) and resulting geodesic minimum spanning trees (ζ). A forest of geodesic MSTs has been extracted for whole brain images, where nodes spatially correspond to vessel junctions and connecting

edges to vascular branches, respectively. This suggests that VTrails framework can automatically and accurately infer the cerebrovascular topology at different scales with a vectorial representation.

4.4 Observations and Remarks

In this chapter a connectivity-optimised level-set was formulated for the VTrails framework, where the combination of a Riemannian vesselness potential and of two different connectivity paradigms are able to automatically infer the topology of the underlying vascular structure, under the assumption that vessels join by minimal paths, i.e. geodesics. Insights of isotropic vs. anisotropic level-sets are given with respect to greedy and exhaustive connectivity paradigms. Overall, the advantage of an anisotropic level-set combined with the exhaustive connectivity paradigm in Section 4.3 consists in optimally exploring and locally refining the geodesic domain of connecting paths, which yields topologically self-organising vascular graphs and the associated minimum spanning trees. In [20], a similar level-set formulation focused on the extraction of shortest paths joining individual (or multiple) pairs of endpoints, without, however, determining the connected topology among the same set of points. In Section 4.3.3.1, the reconstruction of the synthetic trees showed overall good and comparable results even by adopting different vesselness maps. It is likely that an anisotropic level-set as proposed in [20] would have similar accuracies to the proposed framework, by employing the same self-organising connectivity paradigm. In this chapter, the accuracy of an automatically reconstructed set of vascular trees from clinical multi-modal brain angiographies is evaluated within

Table 4.5: Clinical Angiographies – Symmetric error ε_S [mm] and Hausdorff distance ε_H [mm] of trees (ζ) and branchpoints (bp) (mean \pm SD) – Topological tree accuracy DIADEM [%] metric.

	ε_S^ζ	ε_H^ζ	$\varepsilon_S^{\text{bp}}$	$\varepsilon_H^{\text{bp}}$	DIADEM
<i>RAA</i>	0.407 \pm 0.307	1.101 \pm 0.436	1.309 \pm 0.665	2.452 \pm 1.315	78.87 \pm 14.81
<i>MRA</i>	0.535 \pm 0.489	1.167 \pm 1.081	2.084 \pm 1.157	4.167 \pm 0.559	77.68 \pm 8.22
<i>PC</i>	1.761 \pm 1.427	4.983 \pm 2.94	2.505 \pm 0.949	3.749 \pm 1.023	77.47 \pm 10.88
<i>CTA</i>	0.88 \pm 0.648	2.266 \pm 1.143	2.087 \pm 1.021	3.966 \pm 0.883	85.59 \pm 9.56

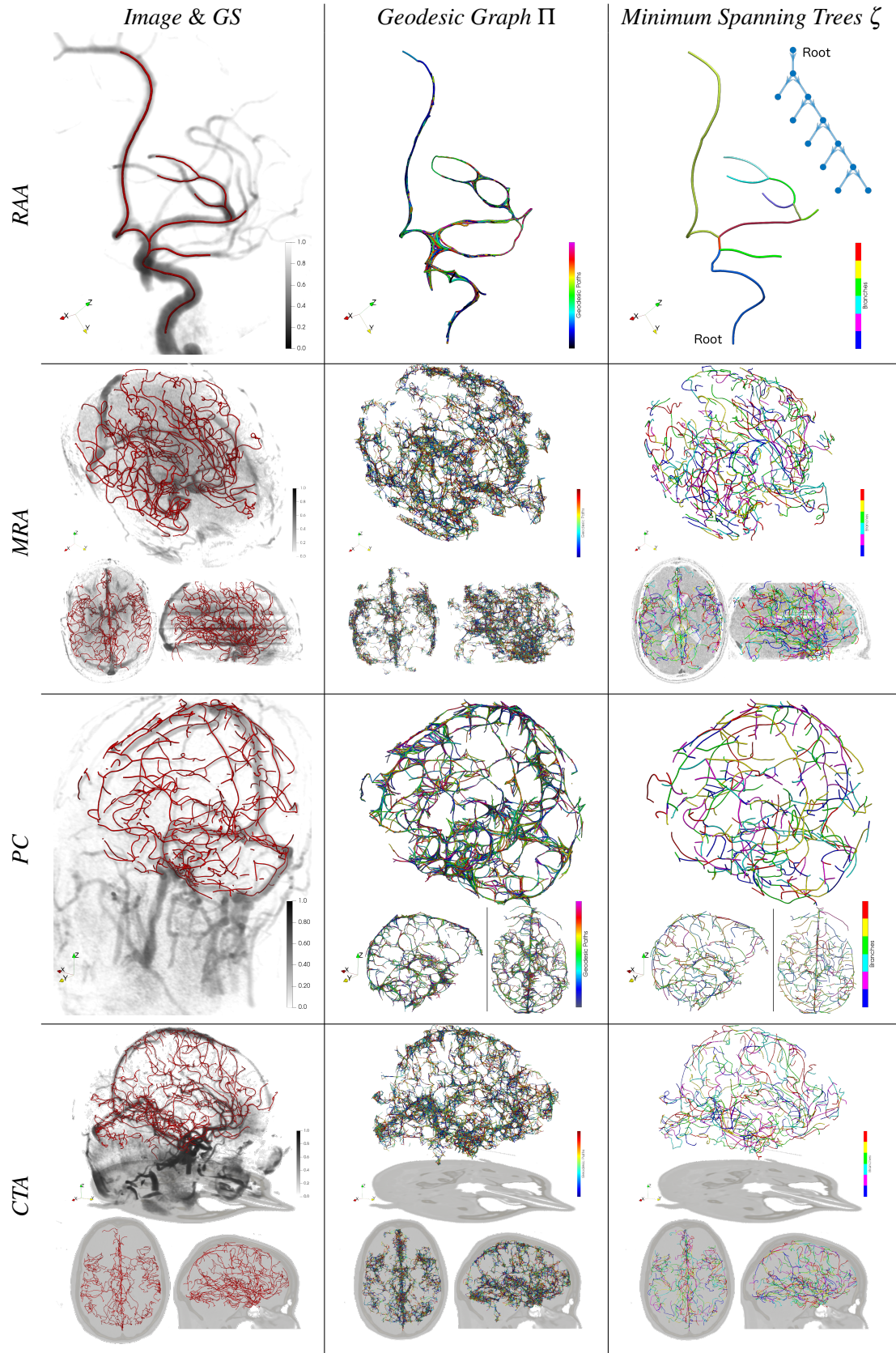


Figure 4.9: Inference of the geodesic vascular network for representative cerebrovascular angiographies with VT_{auto} : Original scan with annotation (GS); Geodesic Vascular Graph Π at convergence and Minimum Spanning Trees ζ for deep-brain vascular structures. – The Riemannian vesselness potential is in Fig. 3.9.

a spatially- and topologically-aware validation framework. In all the considered clinical datasets, both geometrical errors of the geodesic paths and the associated topological similarity evaluated on the centerlines gold standard demonstrate that VTrails is able to accurately recover the cerebrovascular network at different scales with a vectorial representation. The sub-voxel average accuracy reached in the presented experiments suggests that the proposed approach can provide intra-operative guidance with a patient-specific model up to a pre-defined level of detail, where surgical minimally invasive vascular repair is feasible. Given a standardised and topologically-aware evaluation framework for acyclic vascular networks, the quantitative analysis first focused here on major deep-brain arterial (or venous) vascular trees, e.g. the anterior/posterior and left/right arterial branches from the Circle of Willis in *MRA* and *CTA*, as reported in Section 4.3.3.3. In Fig. 4.9 a qualitative inspection of the remaining smaller portions and terminal branches is available. The image resolution of the clinical angiographies does not allow for the inference of capillaries in the cortex (where the anatomy is more prone to show cyclic structures [85]). Also, the evaluation of anastomoses currently suffers from the lack of established quantitative metrics and scores for assessing and comparing cyclic topologies. With the development of standardised metrics for comparing fully-connected networks, along the lines of [35, 123, 162], future works could account for a more specific validation focusing on cyclic structures at different scales. Note that the minimum spanning tree extraction formulation does not enforce any cerebrovascular anatomical prior per se. However, extra vascular-related constraints and associated anatomical connected topologies can be included with a user-defined initialisation to correct for specific locations where the vascular network is not acyclic. For the extraction of major deep-brain vascular structures in the considered full-brain angiographies, co-registered ROI-based territorial masks were used to coherently recover a forest of geodesic MSTs, as described in Section 4.3.2.4, where the intra-cranial volume was considered from the brainstem up to the cortex. For full-brain angiographies, the topological separation between arterial and venous side could be potentially performed by adopting a combination of

multi-modal imaging, and injecting in the connectivity framework such information prior. Possible venous territorial maps can be indeed determined as in [23, 138, 195] using susceptibility-weighted imaging venography and quantitative susceptibility maps. In the considered clinical datasets, major deviations from the centerlines gold standards were observed for small and terminal vessels, where the effect of the limited spatial resolution and image quality degradation is predominant. This suggests that the detection of capillaries and those tiny vessels not well spatially resolved in the image may require a more supervised processing pipeline. In case of undetected capillaries, a prior assessment of the seeds quantile threshold should be devised, e.g. adaptively on the histogram of the scalar vesselness map. Also, different connectivity patterns are found with the proposed method for smaller vessels at high depths of the arterial (or venous) vascular trees. As side note, the considered gold standard centerlines do not constitute an exhaustive and flawless topological reference, since mis-connections, missing branches and manual discontinuous annotations may be present in the datasets. As shown in Fig. 4.9, manual annotations can be noisy, sometimes fragmented and rather prone to misclassification among a pool of experts, especially in case of low contrast-to-noise and low image resolution, as in the *PC* dataset. Moreover, bad gold standard annotations may penalise the accuracy metrics presented in Section 4.3.3.3. For this reason, particular effort was put in selecting and evaluating the manually annotated GS for both *CTA* and *PC* datasets. The skeletonisation of the manual lumen segmentation, as well as the extraction of the territorial GS minimum spanning trees was performed with a conservative and intensity-maximising tree-extraction strategy of the complete GS connected graph, minimising at the same time, the irremediable number of cycles cuts at smaller scales. It can be observed that possible minor mis-classifications in the available gold standards, as well as those from VTrails, may considerably affect the topological similarity metric of vascular trees of different size. Despite the optimal formulation of the Riemannian vesselness potential in conjunction with the proposed exhaustive connectivity paradigm, narrow and spatially close vessels may eventually produce a geodesic short-cut when the ultimate minimum spanning

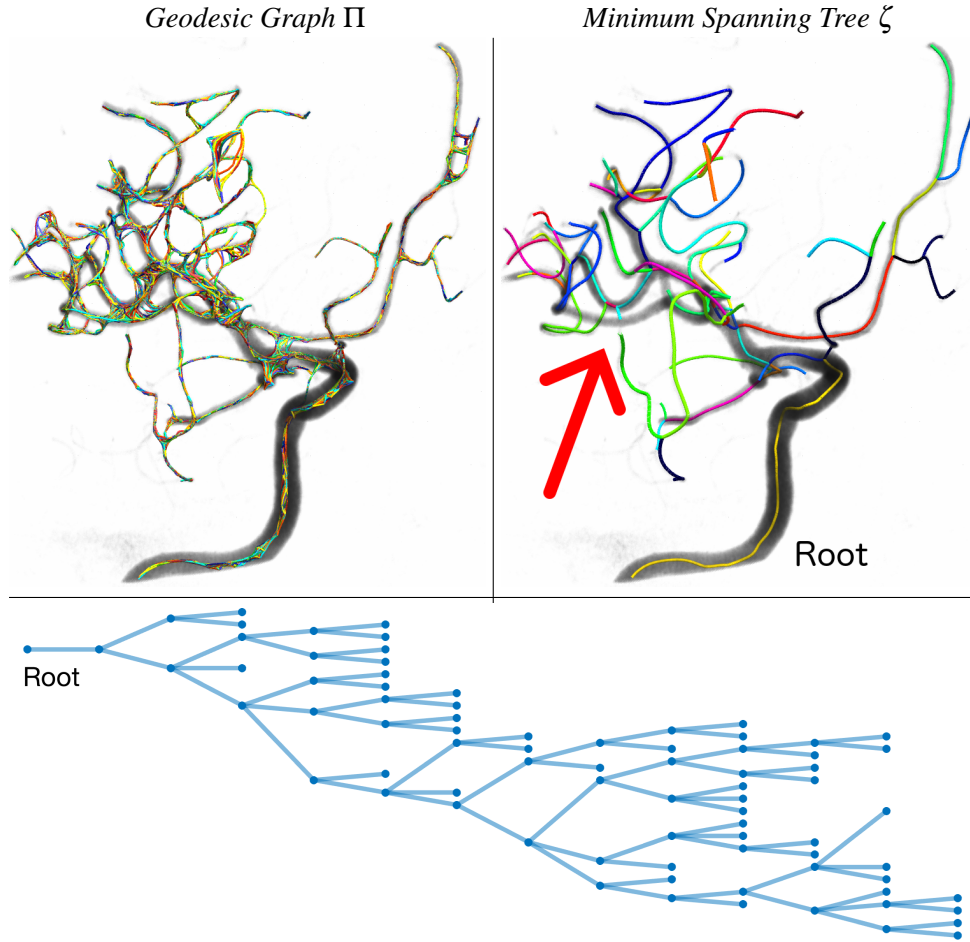


Figure 4.10: RAA topological inference with VT_{auto} . Left: Geodesic Vascular Graph Π . Right: Minimum Spanning Tree ζ of the underlying anatomical vascular tree. Missing branch in ζ , due to a geodesic short-cut from *kissing-vessels*. Bottom: Vectorial representation in the form of a connected hierarchical graph.

tree is determined with VTrails. As shown in Fig. 4.10 for a randomly selected RAA image that was processed without restricting the topological inference, the extraction of the minimum spanning tree underlying the anatomical vascular tree can still result in a missing branch (red arrow) due to a geodesic short-cut from *kissing-vessels*. Conversely, the over-connected geodesic graph encodes and preserves all the redundant connectivity. With this view, the minimum spanning trees should optimally and robustly be extracted *after* the injection of anatomical priors, and propagated through geodesic vascular graph alignment. In this way, such anatomical prior would compensate for biologically incompatible mis-connections and anatomically implausible geodesic short-cuts.

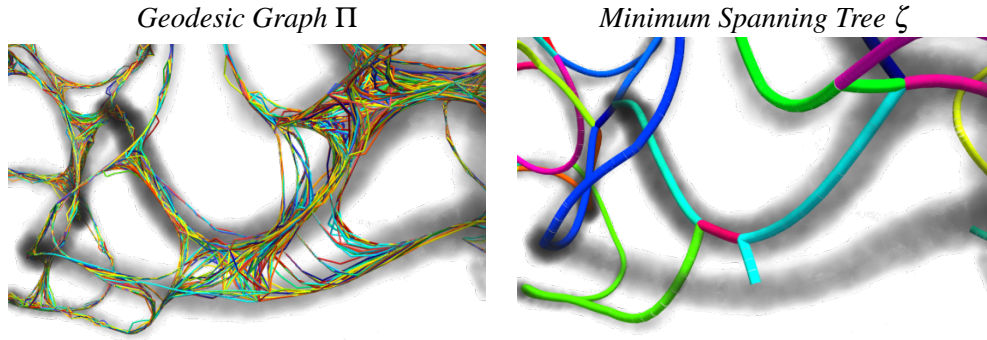


Figure 4.11: Close-up of RAA topological inference with VT_{auto} from Fig. 4.10 (red arrow). Left: Portion of the Geodesic Vascular Graph preserving the vascular segmentation with redundant and uncertain connecting geodesics. Right: Portion of the associated Minimum Spanning Tree, where a missing branch occurs due to cyclic aberration by the kissing-vessel artifact.

4.4.1 The Over-Connected Geodesic Vascular Graph

With the proposed formulation of an exhaustive connectivity paradigm for vascular networks in Section 4.3 the hierarchical and acyclic constraint of a vascular topology is *relaxed*, allowing therefore a more redundant and over-connected representation. The introduced vascular topology as a fully-connected graph should ideally underlie the actual vascular tree with the associated minimum spanning tree. However, in presence of neighbouring and poorly-resolved vascular structures, the direct minimal spanning tree extraction may inevitably produce disrupting and non-anatomically plausible short-cuts. This is intrinsically due to the nature of acyclic topologies: they are deterministic, information deprived, and prone to hierarchical-extraction errors. The formulation of an over-connected vascular graph may produce a counter-intuitive vascular representation, for which a visual assessment may provide confounding or poorly informative cues, due to the comprehensive and redundant geodesic paths. However, such representation would conservatively preserve several degrees of connecting uncertainty in the form of a densely connected graph. This is indeed feasible by considering all possible and geodesically relevant vascular connections. Note that VTrails can fully capture and embed in the over-connected vascular graph all the possible anatomical and geodesic connecting redundancy in the form of multiple local cycles (Fig. 4.9 and Fig. 4.10). Not only anastomoses could be preserved, but also possible inexact branch-points' lo-

cation may also be overcome, as well as the avoidance of privative and detrimental short-cuts in case of pronounced kissing-vessels artifacts (Fig. 4.11), by adopting a redundant and uncertain connectivity pattern. The correct extraction of the underlying anatomical vascular tree should however require a more unconstrained topological extraction strategy following the injection of a population-based prior, propagated through a graph alignment process. Although the introduction of this over-connected topology may result in a complex and counter-intuitive vascular representation, in the following chapter, an elastic topological alignment framework is presented for vascular structures, where the redundant and uncertain connectivity pattern stands as a key-feature to enrich the registration search-space.

Chapter 5

Vascular Alignment

In Section 1.3, a *vectorial* representation of the cerebrovascular network is postulated so that it could allow different forms of group-level analysis, e.g. the inter-subject comparison of geometrical features of the vascular structure (e.g. junction points, branching numbers, tortuosity, and overall haemodynamic properties), and the inter-subject comparisons of various non-vascular parenchymal features, where the brain image-volume is registered by its vascular topology. Also, as previously mentioned in Section 4.4.1, a population-based vectorial prior propagated through a graph alignment process may guide the topological inference of the underlying vascular structure towards its most anatomically plausible realisation. In general, the definition of a group-wise vectorial prior should first embed the likelihood of connectivity patterns from a population, and subsequently inject a probabilistic prior towards the inference of the most meaningful subject-specific topology. Basically, the robust registration of topologies stands as key enabling technology for group-wise analyses, from coherent statistics, to labelling and information propagation. With this view, the alignment of networks and vectorial graphs raised increasing interest and gained popularity in the last decade. The registration of connected structures from clinical scans motivated increasing research effort in vascular image analysis, respiratory and thoracic imaging, and computer aided intervention [39,40,65,153,174,194,204]. For example, Charnoz et al. [39,40] proposed an optimisation approach for a set of matching hypotheses. These are generated from acyclic topologies and the associated costs are minimised for a pair of rooted trees

in the liver. Feragen et al. [65] formulated a hierarchical labelling approach of the airways based on the minimisation of geodesic distances in a geometric tree-space. Other methods introduced different registration techniques, which mostly relied on pairwise matching distances between junction nodes and connecting edges, from the segmented acyclic topologies. Following an initial pre-alignment, these methods usually minimise a similarity cost function or maximise a probabilistic likelihood between pairs of nodes/edges or sub-trees and graph kernels, and hierarchically evaluate the correspondences at different levels of tree-depth. However, whilst only few formulations would register generic spatial graphs as proposed by Serradell et al. [174], in all cases the considered topologies were either hierarchically pre-defined as trees, or determined beforehand on a specific anatomical compartment. Also, since these methods exploit node locations, branches geometry, arborescence depth, or the parent-child relation of a rooted tree, they require the explicit tree topology to accurately capture the underlying vasculature, where each bifurcation is correctly annotated as its connectivity pattern. The registration of noisy topologies, i.e. mis-connections, missing branches and short-cuts; and the alignment of non-linearly deformed geometries remain a challenging and open problem.

In the following sections, aiming at the pairwise alignment of vascular topologies within a deformable and anatomical prior-free framework, the over-connected and redundant geodesic vascular graph introduced in Section 4.3 is employed in conjunction with a graph matching (GM) framework. By relaxing the assumptions on the acyclic (un)directed graph structure of any vascular compartment, VTrails framework leverages the redundant topology encoding the likelihood of connections between neighbouring nodes with minimal paths to enrich the space-search of possible pair-wise correspondences for non-strictly isomorphic topological instances. Ideally, the approach should be flexible and robust enough to account for non-identical graphs. The enhanced connectivity pattern would compensate for topological inaccuracies, for non-linear deformations of branches, and would produce a number of distinctive features, as opposed to deterministic and information-deprived hierarchical structures, i.e. the respective acyclic minimum spanning trees.

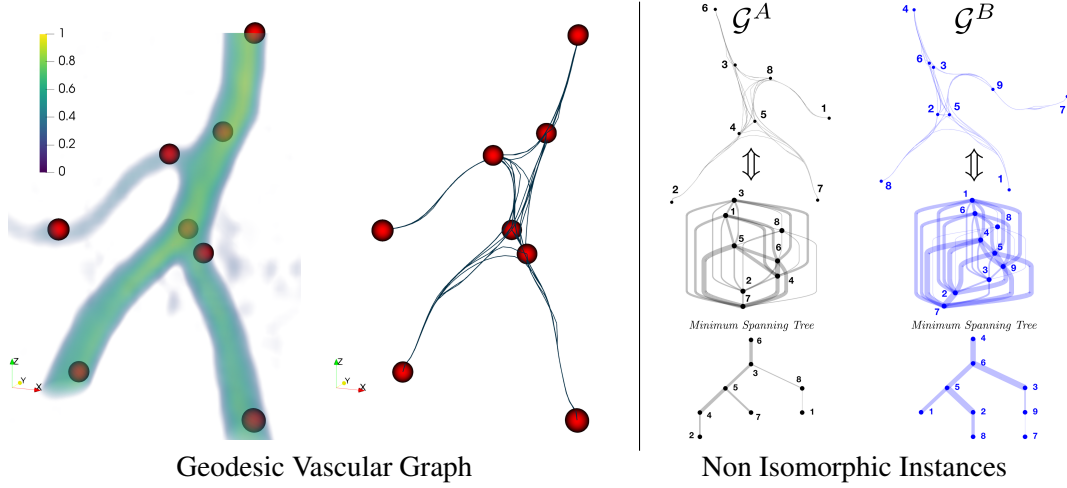


Figure 5.1: Geodesic Vascular Graph and GM problem of non-linearly deformed topologies. Left: Extraction of a fully-connected topology from an initial set of nodes, as in Section 4.3. Right: Associated graph representations and minimum spanning trees for two topologically different instances (\mathcal{G}^A and \mathcal{G}^B) of the same underlying vascular anatomy.

As a further contribution, a viable vascular graph registration strategy is presented in the following sections, where the pairwise topological alignment problem can be solved using generic and popular graph matching algorithms largely employed in computer vision applications. After re-defining the over-connected geodesic vascular graph under a canonical graph-based formulation, comprising nodes' and edges' attributes, the generic GM problem is presented together with the proposed affinity metrics based on vessels geometry and their redundant geodesic connectivity. The two-steps registration pipeline, from an initial coarse rigid pre-alignment to a finer elastic nodes-association mapping. The latter is further investigated by making use of different GM algorithms employed in computer vision applications.

5.1 Pairwise Non-rigid Registration of Vascular Graphs

In general, with the notation $\mathcal{G} = (N, E)$ an undirected spatial graph is defined in 3D as the set of nodes of cardinality i and the associated set of connecting edges of cardinality v encoding the graph adjacency list. The same notation can be used in the following to encode a geodesic vascular graph, as inferred in Sections 4.3 and

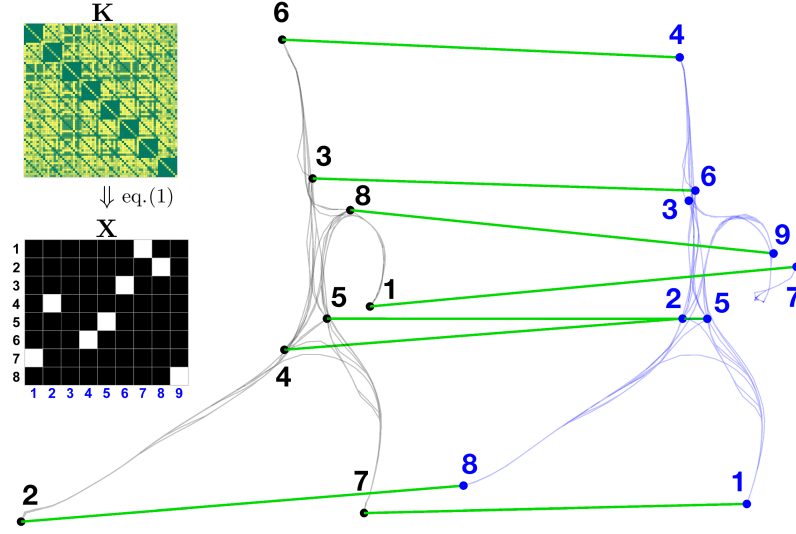


Figure 5.2: Graph Matching Optimisation Problem: Resulting elastic graph alignment and nodes matching for the generalised GM problem. Instances \mathcal{G}^A and \mathcal{G}^B in this case, the over-connected geodesic vascular graphs Π as in Fig. 5.1

4.3.1. Each geodesic edge is defined as the 3D shortest path joining a generic pair of nodes, by solving the Eikonal equation [98] over a vascular smoothly connected manifold. Note that both the over-connected geodesic vascular graph Π and the associated minimum spanning tree ζ are subsets of \mathcal{G} , and they can therefore be coherently represented with the same generic notation. Together with the definition of the undirected geodesic vascular graph \mathcal{G} , a set of edge- and node-attributes is introduced. The edge-attributes $\mathbf{e}_v = \{\mathbf{p}_v, l_v, u_v\}$ comprise the dense sampling \mathbf{p}_v of each shortest path in 3D (i.e. the point coordinates of the sequence as in Fig. 5.5 and Fig. 5.6), its associated euclidean length l_v and the geodesic integral energy u_v integrated along the path, as introduced in 4.3.1. The node-attributes $\mathbf{n}_i = \{\mathbf{c}_i, d_i\}$ include the spatial location \mathbf{c}_i as coordinates in 3D, and the node geodesic degree d_i defined as mean scalar value of the integral geodesic energy associated to the set of node-incident edges.

5.2 Graph Matching Optimisation Problem

As presented by Zhou and De la Torre [215], the problem of matching a pair of graphs \mathcal{G}^A and \mathcal{G}^B requires the definition of an affinity matrix \mathbf{K} to measure the similarity between each pair of nodes and edges. Given the graph \mathcal{G}^A comprising a

total of i_A nodes and given the graph \mathcal{G}^B comprising a total of i_B nodes, the square and symmetric affinity matrix $\mathbf{K} \in \mathbb{R}^{i_A \times i_B}$ encodes the similarity between nodes along its diagonal elements, whereas the edges similarity is encoded in the off-diagonal ones. After determining the similarity matrix \mathbf{K} , the problem of graph matching consists in finding the optimal correspondence \mathbf{X} among all the nodes (Fig. 5.2), so that a compatibility functional $J(\mathbf{X})$ is maximised with a quadratic assignment problem (QAP) [120],

$$\max J(\mathbf{X}) = \text{vec}(\mathbf{X})^T \mathbf{K} \text{vec}(\mathbf{X}). \quad (5.1)$$

The optimal correspondence matrix \mathbf{X} is constrained to be a unique mapping between a sub-set of nodes of graph \mathcal{G}^A and a sub-set of nodes of graph \mathcal{G}^B . In particular, each matched node in \mathcal{G}^A corresponds to one unique node in \mathcal{G}^B . In general, some nodes may not have a correspondence in the resulting graph matching. The term $\text{vec}(\mathbf{X})$ denotes the vectorisation of the correspondence matrix. The considered quadratic assignment problem for a graph matching has a NP-hard complexity. In literature, several approximating solutions formulated different relaxations strategies for a GM. As reported in [215], some of these relaxations were introduced with auxiliary objective functions and with matricial decomposition constraints, allowing the optimisation of a vast range of models based on node- and edge-attributes similarity metrics.

5.2.1 Vascular Graphs Similarity Metrics

Both node- and edge-similarity metrics are computed and embedded in an affinity matrix \mathbf{K} , by adopting the same matrix factorisation as described in [215]. The square symmetric similarity matrix \mathbf{K} is demonstrated to be factorised as a Kronecker product of two sets of structural connectivity matrices (here omitted for simplicity) and two affinity matrices. Among those, two structural connectivity matrices per graph encode the directed node-edge incidence, whereas the two other affinity matrices account for the nodes pairwise attributes similarities in $\mathbf{K}_{\mathbf{n}^{AB}}$ and for the edges pairwise attributes similarities in $\mathbf{K}_{\mathbf{e}^{AB}}$, as detailed in [215]. Being the

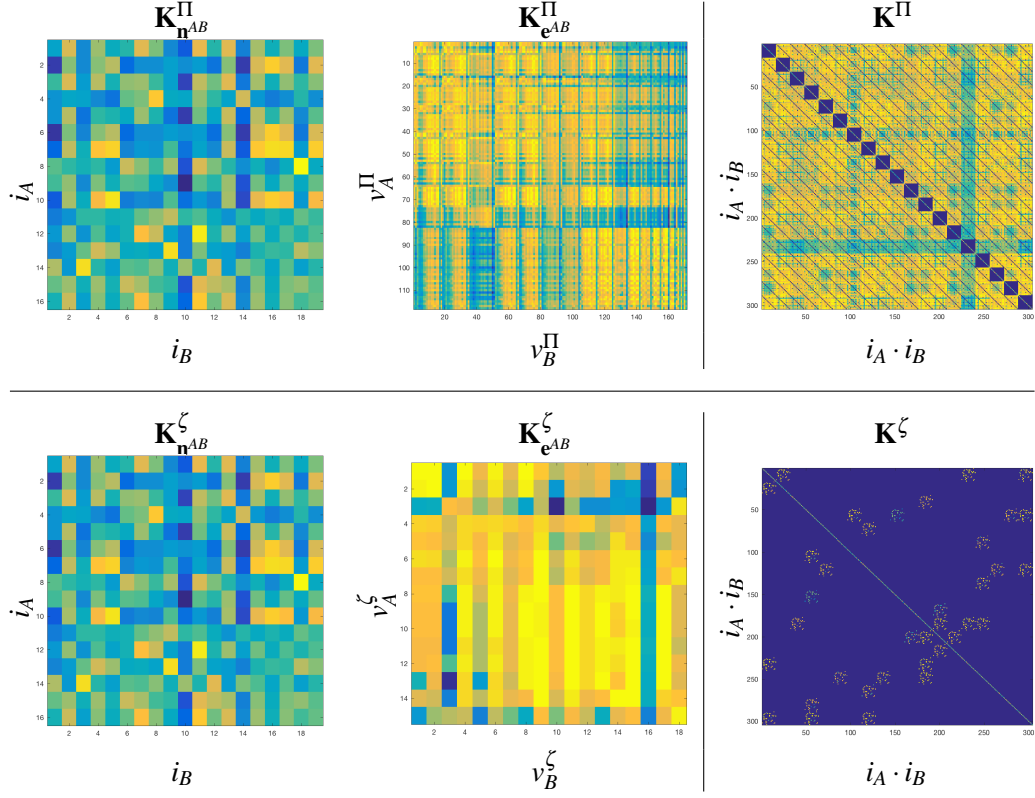


Figure 5.3: Vascular graphs' similarity metrics – Representative nodes and edges factorisation matrices, $\mathbf{K}_{\mathbf{n}}^{AB}$ and $\mathbf{K}_{\mathbf{e}}^{AB}$, together with the resulting affinity matrix \mathbf{K} for: a pair of Geodesic Vascular Graphs Π (top); the associated pair of minimum spanning trees ζ (bottom). Note the deprived information in the affinity matrix \mathbf{K}^ζ compared to \mathbf{K}^Π , due to the deterministic connectivity of the minimum spanning trees.

topology of the considered graphs fixed as a pre-defined adjacency list, the resulting affinity matrix \mathbf{K} is only modulated by the node- and edge-attributes. In particular, the node affinity matrix $\mathbf{K}_{\mathbf{n}}^{AB}$ measures the similarity between the i_A -th node in \mathcal{G}^A and the i_B -th node in \mathcal{G}^B , for a given set of node-attributes. Analogously, the edge affinity matrix $\mathbf{K}_{\mathbf{e}}^{AB}$ measures the similarity between each v_A -th edge in \mathcal{G}^A and each v_B -th edge in \mathcal{G}^B , for a given set of edge-attributes. If the similarities are measured as pairwise distance matrices between two sets of attributes, the associated node- and edge-affinity matrices can be defined as

$$\mathbf{K}_{\mathbf{n}}^{AB} = e^{-\left(\alpha_1 \frac{\mathbf{C}^{AB}}{\sigma_{\mathbf{C}}} + \alpha_2 \frac{\mathbf{D}^{AB}}{\sigma_{\mathbf{D}}}\right)} \quad \text{with } \alpha_1 + \alpha_2 = 1, \quad \text{and} \quad (5.2)$$

$$\mathbf{K}_{\mathbf{e}}^{AB} = e^{-\left(\beta_1 \frac{\mathbf{P}^{AB}}{\sigma_{\mathbf{P}}} + \beta_2 \frac{\mathbf{L}^{AB}}{\sigma_{\mathbf{L}}} + \beta_3 \frac{\mathbf{U}^{AB}}{\sigma_{\mathbf{U}}}\right)} \quad \text{with } \beta_1 + \beta_2 + \beta_3 = 1, \quad (5.3)$$

where \mathbf{C}^{AB} and \mathbf{D}^{AB} are the pairwise ℓ^2 -norm matrices between the two sets of node coordinates $\{\mathbf{c}_{i_A}, \mathbf{c}_{i_B}\}$, and geodesic degrees $\{d_{i_A}, d_{i_B}\}$. The matrices \mathbf{P}^{AB} , \mathbf{L}^{AB} and \mathbf{U}^{AB} are the pairwise average symmetric distance matrices of the connecting minimal paths $\{\mathbf{p}_{v_A}, \mathbf{p}_{v_B}\}$, and the pairwise ℓ^2 -norm matrices between the sets of the euclidean lengths $\{l_{v_A}, l_{v_B}\}$ and geodesic integral energies $\{u_{v_A}, u_{v_B}\}$, respectively. The normalisation factors $\sigma_{\mathbf{C}, \mathbf{D}, \mathbf{P}, \mathbf{L}, \mathbf{U}}$ are the standard deviations estimated from the off-diagonal elements of the associated distance matrices over the considered population of graphs. Lastly, the coefficients α and β modulate the combined contribution of non-homogeneous attributes similarities, i.e. geometrical, geodesic and topological, into the resulting affinity matrices $\mathbf{K}_{\mathbf{n}^{AB}}$ and $\mathbf{K}_{\mathbf{e}^{AB}}$. In particular, α_1 , β_1 and β_2 weigh the geometrical similarities among nodes and edges, whereas α_2 and β_3 represent the respective geodesic and topological trade-off. Note that in case of altered graphs, e.g. by introducing non-linear geometrical or topological deformations, both the affinity matrices $\mathbf{K}_{\mathbf{n}^{AB}}$ and $\mathbf{K}_{\mathbf{e}^{AB}}$ are determined *after* warping the graphs embedding with the considered non-linear deformations. This allows different relaxations of the graph matching problem to map all similarities, dissimilarities and deformations, in the specific model that is being optimised.

The Kronecker product between the structural connectivity matrices and both factorised affinity components $\mathbf{K}_{\mathbf{n}^{AB}}$ and $\mathbf{K}_{\mathbf{e}^{AB}}$ produced the complete affinity matrix \mathbf{K} . The implementation of the QAP solver is the same as the one presented in [215]. Both node- and edge-similarity metrics are shown in Fig. 5.3, together with the resulting affinity matrix \mathbf{K} for a representative pair of unaltered graphs with two realisations each, i.e. a pair of complete geodesic vascular graphs (Π) and the associated pair of minimum spanning trees (ζ). Both unaltered graphs have the same number of nodes, which resulted in identical node affinity matrices $\mathbf{K}_{\mathbf{n}^{AB}}^{\zeta}$, $\mathbf{K}_{\mathbf{n}^{AB}}^{\Pi}$. However, the reduced and deterministic connectivity pattern of the acyclic topologies is reflected in the smaller edge affinity matrix $\mathbf{K}_{\mathbf{e}^{AB}}^{\zeta}$ for the vascular trees, therefore a more sparse affinity matrix \mathbf{K}^{ζ} . Conversely, the complete edge affinity matrix $\mathbf{K}_{\mathbf{e}^{AB}}^{\Pi}$, for the over-connected topologies, shows an enhanced similarity overhead for the redundant set of edges. Were the graphs altered only with a geometrical deforma-

tion, this would have been reflected on the values of the respective node- and edge-affinity matrices. Conversely, by altering only the topology, e.g. by pruning connecting edges and deleting nodes, the associated node- and edge- affinity matrices would have shown both a reduced size (i.e. lower node- and edge-cardinality) and dissimilar values, due to the altered geodesic and topological attributes.

5.3 Elastic Registration Pipeline

Although some GM algorithms do not require any initialisation of the graphs within a normalised 3D reference space, a two-steps approach (Fig. 5.5 and Fig. 5.6) is proposed, by combining an early coarse alignment strategy to facilitate the further registration by reducing biases due to pure rigid mis-alignment.

5.3.1 Rigid Pre-alignment

The globally-optimal iterative closest point (Go-ICP) [208] is run on \mathcal{G}^A and \mathcal{G}^B as coarse geometrical initialisation. Here, the dense cloud of samples, i.e. the nodes coordinates $\{\mathbf{c}_{i_A}, \mathbf{c}_{i_B}\}$ and the sequences of edge points $\{\mathbf{p}_{v_A}, \mathbf{p}_{v_B}\}$, is retrieved for the spatial rigid pre-alignment. Go-ICP searches the entire 3D motion space, and, under the minimisation of an L_2 error metric based on a branch-and-bound scheme, guarantees the global optimality of the rigid mapping, even in the presence of noisy data, outliers, and partial samples overlap.

5.3.2 Fine Node Association with Graph Matching Algorithms

Classic GM algorithms employed in computer vision are considered for fine registration by adopting different relaxations of the QAP. Among those, the Graduated Assignment (GA) [76], the Spectral Matching (SM) [110], the Spectral Matching with Affine Constraints (SMAC) [51], the Probabilistic Matching (PM) [212], the Integer Projected Fixed Point (IPFP-U/SM) [111], the Re-weighted Random Walk Matching (RRWM) [47], and the current state-of-the-art, the non-rigid Factorized Graph Matching (FGM) [215] are all considered here. Briefly, the deformable graph matching problem, detailed in [215], formulates the unknown graph correspondence being constrained with an internal representation of a geometric transformation. Such internal representation model a composition of similar, affine, and

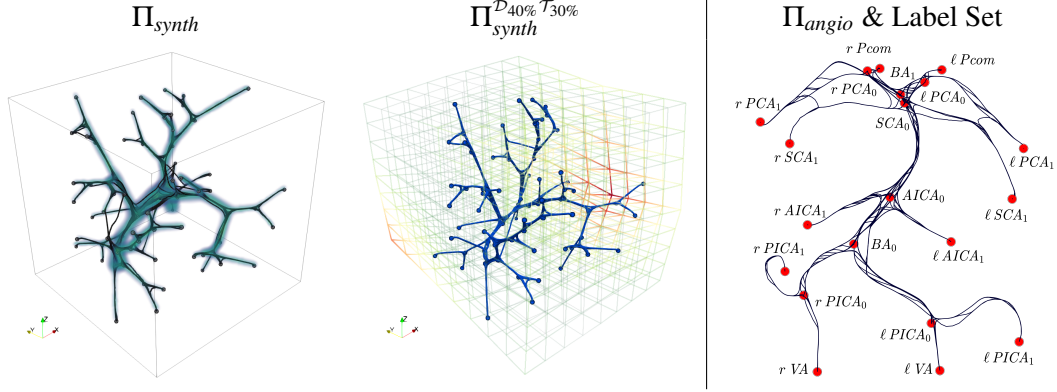


Figure 5.4: Topological vascular alignment: Experimental datasets. Left: Synthetic geodesic vascular graph Π_{synth} – Original instance and representative composition of simulated deformations. Right: Basilar Artery geodesic vascular graph (Π_{angio}) and label set [91].

non-rigid transformations, which are internally mapped to the compatibility function (Eq. 5.1), and subsequently estimated by optimising jointly the correspondence matrix \mathbf{X} and the composite transformation itself. The aforementioned algorithms configured for undirected graph realisations were considered in the following experimental set-up. All the algorithmic implementations are available from the online repository¹.

5.4 Experiments on Synthetic and Clinical Data

A set of 10 synthetic over-connected geodesic vascular graphs (Π_{synth}) and associated minimum spanning trees (ζ_{synth}) are obtained from 3D vascular tree images [82] (isotropic $100 \times 100 \times 100$ voxels), as in Sections 4.3 and 4.3.1. Each graph comprises 80 nodes, i.e. the vascular junction and end-points, over-connected within a neighbourhood of radius $v = 35$ (Fig. 5.4). A total of 10 fully over-connected geodesic vascular graphs (Π_{angio}) as well as the respective minimum spanning trees (ζ_{angio}) of the basilar artery are similarly derived from Time-of-Flight MRI angiographies ($0.35 \times 0.35 \times 0.5$ mm), where anatomical vascular junctions and endpoints were manually labelled (Fig. 5.4) following [91].

The geometrical attributes of synthetic graph datasets Π_{synth} and ζ_{synth} were randomly deformed with a non-linear geometrical displacement field (i.e. max mag-

¹<https://github.com/zhfe99/fgm>

nitude $\mathcal{D}_{30\%}$, $\mathcal{D}_{40\%}$, $\mathcal{D}_{50\%}$ of the graph spatial embedding). A series of topological pruning, i.e. $\mathcal{T}_{30\%}$, $\mathcal{T}_{40\%}$, and $\mathcal{T}_{50\%}$ reduced the original connectivity of the synthetic graph datasets. The latter was reflected on a reduced edge-affinity matrix and on the geodesic and topological attributes of the considered graphs. Also, a combination of both geometrical and topological alterations was introduced (Fig. 5.4) to model more complex, yet realistic, cases. The deformed graphs were rigidly aligned first as in section 5.3.1. Then both node- and edge-affinity matrices were determined as in section 5.2.1, considering the respective unaltered topologies as matching counterpart. Lastly, the fine graph matching problem was solved for each algorithm as in section 5.3.2. The accuracy of the GM is given by the percentage of correct correspondences as $\frac{\text{tr}(\mathbf{X}\mathbf{X}^{(\text{GT})T})}{\mathbf{1}_{i_A}^T \mathbf{X}^{(\text{GT})} \mathbf{1}_{i_B}} \cdot 100\%$, where $\text{tr}(\bullet)$ is the trace of the argument square matrix. \mathbf{X} is the correspondence matrix from the optimised graph matching problem between the pair of considered graphs, and $\mathbf{X}^{(\text{GT})}$ is the associated correspondence ground truth, accounting for the introduced deformations. The column vectors $\mathbf{1}_{i_A}$ and $\mathbf{1}_{i_B}$ encode unitary values for the same node cardinalities i_A and i_B , as in the respective pair of considered graphs. Differences between the registration performances of Π_{synth} and ζ_{synth} are evaluated with a paired Wilcoxon signed rank test.

Regarding the clinical dataset, both Π_{angio} and ζ_{angio} are pairwise aligned, covering all possible inter-subject combinations within the same dataset. The matching accuracy is given also here by the percentage of correct correspondence among the labelled nodes, as reported for the synthetic experiments. Differences in matching performances between Π_{angio} and ζ_{angio} for the considered GM techniques are evaluated with a paired Wilcoxon signed rank test.

5.4.1 Results of Matching Accuracy

5.4.1.1 Synthetic Instances

In Fig. 5.7, the GM accuracy is reported for the synthetic datasets, for each algorithm and for the simulated levels of deformation. As an initial configuration, the weights of the affinity metrics are arbitrarily defined as $\alpha = [0.5, 0.5]$, and $\beta = [0.25, 0.25, 0.5]$ in all cases. This is initially introduced to equally balance the

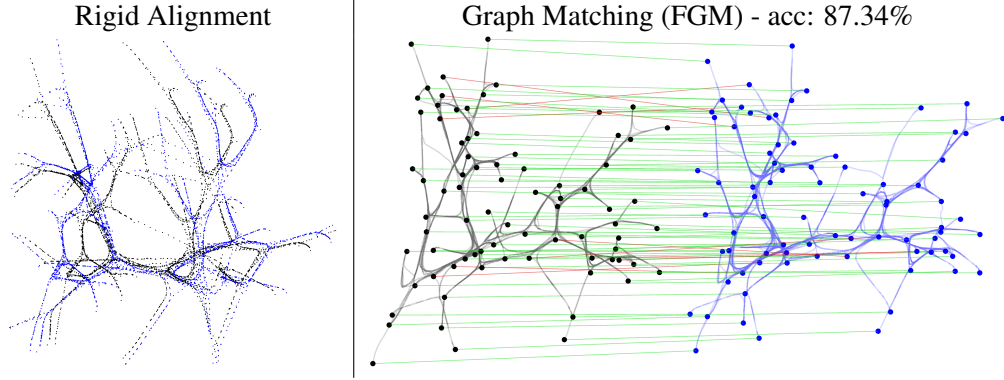


Figure 5.5: Alignment of synthetic geodesic vascular graphs Π_{synth} : Left. Rigid alignment of the geometrical embedding with Go-ICP [208]. Right: Fine Node association mapping with Graph Matching techniques (FGM). Correct matching is highlighted in green, whereas mismatched correspondences are shown in red.

similarity features, i.e. the contributions from the geometrical and geodesic components of the graphs' attributes. Similar trends of performances are observed for the considered GM algorithms across different levels of increasing deformation. Overall, FGM reported the best matching accuracy together with RRWM in both Π_{synth} and ζ_{synth} , whereas the other algorithms showed globally varying performances. Purely geometrical displacements did not affect the registration, whereas more severe topological pruning showed a visible drop of accuracy in both Π_{synth} and ζ_{synth} , as well as the combination of joint deformations at different degrees. Overall, better matching is found for Π_{synth} compared to ζ_{synth} at the same level of alteration. A significant accuracy drop ($p < 0.05$) is found for the registration of tree-like structures, proportional to the combined deformation. This suggests that the proposed registration pipeline would benefit from both geometrical and geodesic information arising from a more dense and redundant over-connected pattern, rather than an explicit vascular tree hierarchy, in the presence of non-linear deformations.

5.4.1.2 Clinical Cerebrovascular Topologies

The accuracy of the pairwise registration for both Π_{angio} and ζ_{angio} datasets is reported in Table 5.1. The affinity metrics trade-offs adopted here are the same as those for the synthetic experiments. Overall, a fairly good matching is obtained for the state-of-the-art FGM ($61.26 \pm 21.91\%$), as well as for GA ($65.16 \pm 20.39\%$)

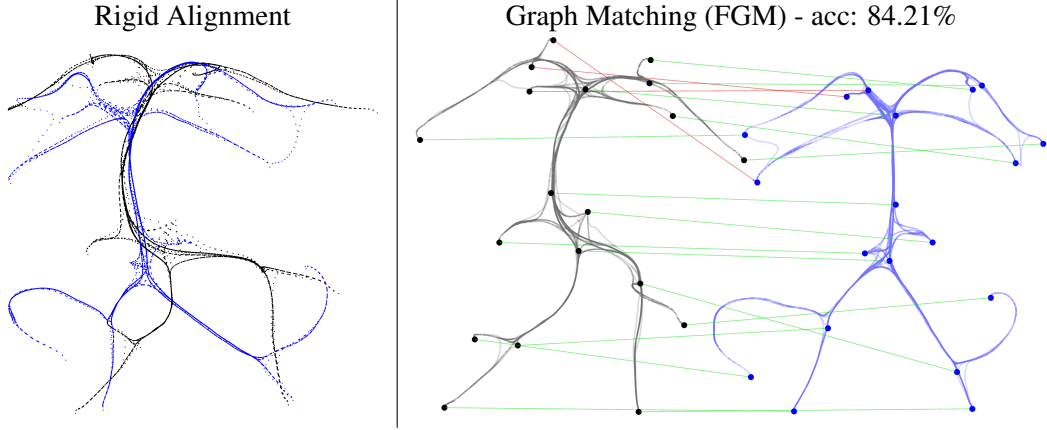


Figure 5.6: Alignment of Basilar Artery geodesic vascular graphs Π_{angio} : Left. Rigid alignment of the geometrical embedding with Go-ICP [208]. Right: Fine Node association mapping with Graph Matching techniques (FGM). Accuracy is evaluated on the correct correspondences, given the labelled association ground-truth. Correct matching is shown in green, whereas mismatched associations are shown in red.

and SM ($62.83 \pm 22.96\%$). The considered angiographic dataset presented large deformations and anatomically different variants (Fig. 5.4 and Fig. 5.6). In line with the synthetic experimental results, the registration of over-connected topologies (Π_{angio}) showed significantly higher accuracy ($p < 0.05$), compared to the respective hierarchical minimum spanning trees (ζ_{angio}). Globally, nodes mismatch occurred in correspondence of nodes with lower degree, where higher confusion is found for spatially close vascular end-points and neighbouring branches. Conversely, the correspondence of superior/inferior and left/right branches was correctly preserved in the majority of cases.

5.4.2 Cyclic and Non-isomorphic Anastomoses: Circle of Willis

In order to further evaluate the accuracy of the proposed elastic topological registration framework, an extra set of cerebrovascular topologies were considered as proof of concept. In this case, both cyclic anastomoses found in the complete Circle of Willis (CoW) and those presenting an incomplete cycle were evaluated with a similar approach. However, only the over-connected redundant geodesic vascular graph Π^{CoW} was considered here for the alignment of such topologies, since the acyclic minimum spanning tree cannot intrinsically model the complete anastomosis. Sim-

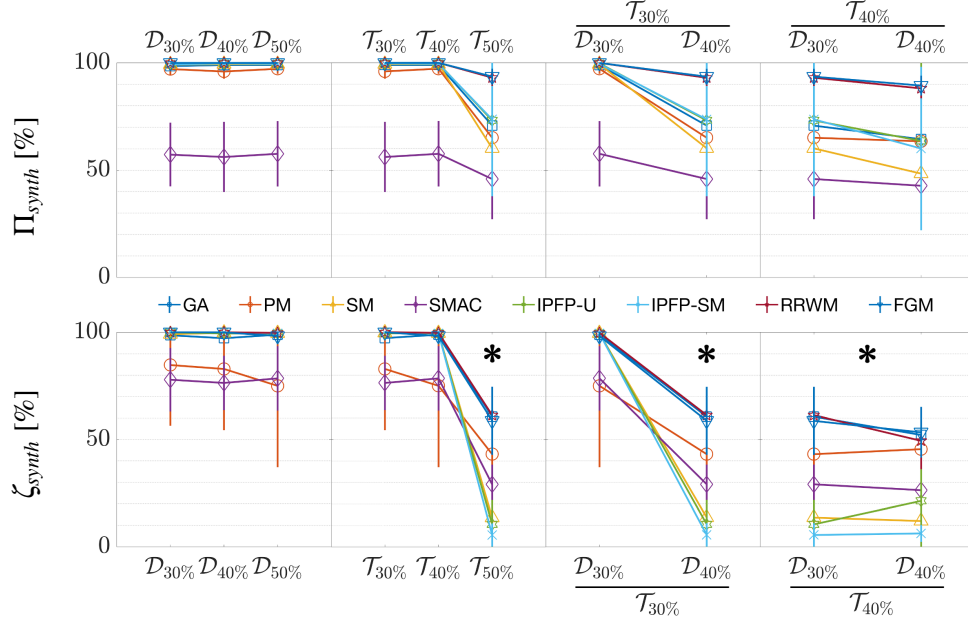


Figure 5.7: Synthetic Graph Matching Accuracy of different GM algorithms: Π_{synth} vs. ζ_{synth} for different levels of non-linear deformation.

ilarly to the clinical dataset, the annotation of connecting branch-points as well as terminal nodes was performed manually following [91] (Fig. 5.8). For qualitative evaluation purposes, in Fig. 5.9 (top) both a complete-to-complete anastomosis registration is presented, and a representative complete-to-incomplete one (Fig. 5.9 - bottom). In the first case, good correspondence is found for geometrically and

Table 5.1: Clinical Graph Matching Accuracy: Inter-subject registration of Π_{angio} vs. ζ_{angio} . Values are mean \pm SD, (median), * = $p < 0.05$.

Accuracy [%]	GA [76]	PM [212]	SM [110]	SMAC [51]
Π_{angio}	65.16 \pm 20.39 (66.67)	61.72 \pm 23.43 (60.86)	62.83 \pm 22.96 (62.07)	41.61 \pm 15.77 (40.05)
ζ_{angio}	44.76 \pm 23.37 (44.44*)	25.72 \pm 23.91 (20.71*)	43.03 \pm 20.38 (42.42*)	28.63 \pm 18.78 (24.12*)
Accuracy [%]	IPFP-U [111]	IPFP-SM [111]	RRWM [47]	FGM [215]
Π_{angio}	41.59 \pm 16.58 (40.59)	38.97 \pm 18.02 (37.52)	49.05 \pm 18.31 (49.14)	61.26 \pm 21.91 (66.67)
ζ_{angio}	20.77 \pm 16.19 (16.91*)	20.96 \pm 13.14 (18.75*)	44.53 \pm 20.86 (44.12)	48.64 \pm 22.39 (48.28*)

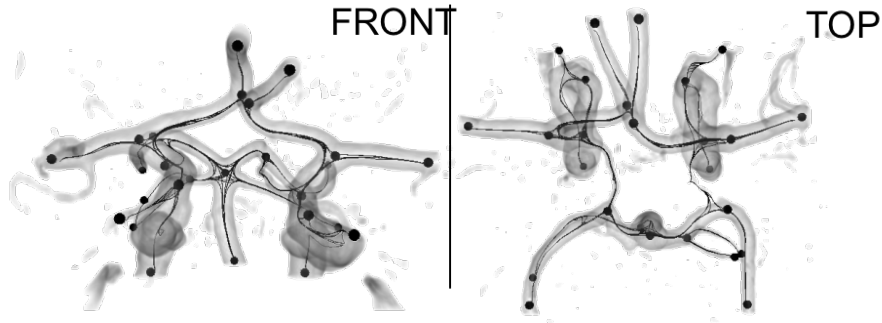


Figure 5.8: Cerebrovascular Cyclic Anastomosis: Circle of Willis (CoW) – Geodesic vascular graph (Π^{CoW}) and manually annotated landmarks [91], Front and Top view.

topologically different embedding of the complete anastomoses. Local minor mismatches are observed in the correspondence of a few terminal branches of the cyclic vascular topology. Regarding the elastic registration of strongly non-isomorphic topologies (complete-to-incomplete CoW alignment) the accuracy of the initial automatic registration overall shows an acceptable correspondence for the majority of landmarks, whereas major mismatches are found in the correspondence of the missing contra-lateral connecting branches of the incomplete anastomosis. Note that, at this stage, the accuracy is evaluated only on the perfectly matching nodes; the geometrical distance among mis-matching correspondences, as well as the topological mismatch relevance of terminal nodes vs. central hub nodes is currently not considered. This qualitative assessment shows encouraging results for the alignment of cyclic vascular structures. However the considered registration strategy may further require a more complete set of vascular features, as well as an iterative and more localised registration refinement together with a group-wise (rather than pair-wise) alignment approach for more complex, convoluted and strongly non-isomorphic topologies.

5.5 Observations and Remarks

A vascular topological alignment strategy was presented for the proposed VTrails framework, by making use of an undirected formulation of geodesic vascular graphs together with popular graph matching techniques employed in computer vision. The pairwise alignment was able to register similar topologies, in the presence of non-

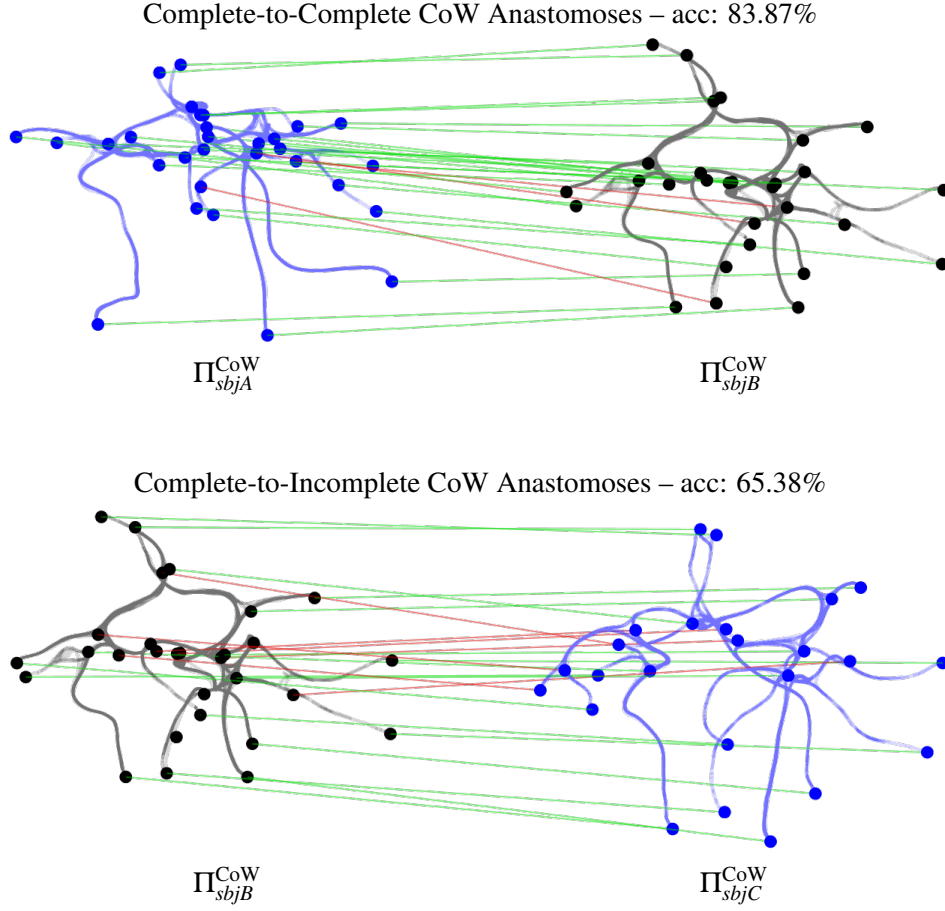


Figure 5.9: Vascular Topological Alignment: Elastic registration of cyclic anastomoses - Circle of Willis (CoW) using the over-connected geodesic vascular graphs Π for a representative set of subjects ($sbjA$, $sbjB$ and $sbjC$). Top: Complete-to-Complete anastomoses registration. Bottom: Complete-to-Incomplete anastomoses registration.

linear deformations of different degrees. The non-rigid node correspondence assignment is solved with a two-steps alignment comprising an optimal rigid registration of the network geometrical embedding, and a set of graph matching algorithms to solve the quadratic assignment problem.

For the first time, a general registration of vascular graphs could be performed by relaxing the explicit hierarchical vessel-tree structure or connectivity patterns specific of a vascular compartment as proposed in Section 4.3. This allowed to align noisy and uncertain over-connected topologies with possible cycles. Here, the use of multiple GM strategies, on the one hand, is motivated by the unconstrained formulation of the undirected geodesic vascular graphs (either the over-connected

graphs Π or the hierarchical and acyclic trees ζ). On the other hand, it is justified by the different connectivity patterns i.e. the different *graph lattice* of the introduced topologies. The latter can indeed dramatically differ from the connectivity patterns found in computer vision applications (i.e. 3D polygonal subdivision and/or triangulations in 2D). Therefore, established GM algorithms may show rather different performances.

Early results show fairly good matching for synthetic vascular graphs even in the presence of mild-to-moderate non-linear deformations. With the same registration pipeline, over-connected and redundant topologies are aligned, as well as hierarchical undirected tree-structures. Despite the tree-structures sharing the same similarity features, the graph matching reported significantly different accuracies (Fig. 5.7, and Table 5.1), where better node correspondences are found for the over-connected topologies. This suggests that the redundant connectivity pattern found in the complete graphs may enrich the registration search-space with distinctive cues. This is supported by observing the associated similarity metrics and the sparsity of the affinity matrices \mathbf{K}^Π and \mathbf{K}^ζ for a representative pair of over-connected geodesic vascular graphs and for the associated pair of acyclic minimum spanning trees (Fig. 5.3). Similarly, the registration of geodesic vascular graphs from angiographic datasets reported overall good matching, even in cases of large spatial deformations and anatomically different topologies. Conversely, the registration of the associated tree structures showed significantly lower accuracies, in line with the synthetic experimental results.

On the basis of this early evidence, the problem of vascular tree- and graph-registration could be generalised with a ‘multi-source’ network alignment. Further developments towards a more robust design for vascular applications may better incorporate features of a different nature, from geometrical, to geodesic, to topological. This would potentially include also other functional and bio-mechanical features, towards a more specific and vascular-oriented graph alignment framework with VTrails.

Although most of the GM algorithms considered in this work are used for 2D

applications in computer vision, their general formulation allows the alignment of any generic network, regardless of the dimensional embedding, and offer a rich ground for ad-hoc methodological developments. Among the considered GM algorithms, some are optimising the quadratic assignment problem by reducing the intrinsic NP-hard complexity with local matching approximations, others are based on the eigen-decomposition of the graph-Laplacian matrix (e.g. spectral matching), while some others incorporate an internal representation mapping a non-rigid transformation in the compatibility functional (i.e. the Factorised Graph Matching).

Given the over-connected topologies, the reason for the different observed performances among the considered GM techniques is still unclear. From an initial qualitative evaluation in Fig. 5.10 and Fig. 5.11, the density and depth of the graph affect the accuracy of the graph matching algorithm. Also, it can be observed that the redundant connecting edges, as well as the different patterns of the graph lattice and the spatial embedding of the topology itself may dramatically impair the graph-matching accuracy and performance.

For example, the graduated assignment, the probabilistic matching and the spectral matching algorithms perform fairly well with the inter-subject registration in the clinical dataset (Π_{angio}). However, the same algorithms produce rather poor alignments with the synthetic graphs (Π_{synth}). It can be observed that the clinical dataset shows pronounced topological (different branching) and geometrical non-linear deformations of the embedding; however the considered vascular anatomy has an intrinsic level of symmetry (i.e. left/right). Also, the clinical graphs show a rather limited extent, which can be easily partitioned into smaller sub-nets (e.g. superior/inferior and anterior/posterior). Such virtual sub-net partition resembles a lower-rank condensation and contraction of the network. A low-rank network representation seems to meet well the local matching approximations and the lower-rank spectral decomposition employed in the graduated assignment, probabilistic matching and spectral matching algorithms.

On the contrary, the synthetic dataset does not show a regular symmetry or any simplified features of the network. In this case, the graduated assignment, the prob-

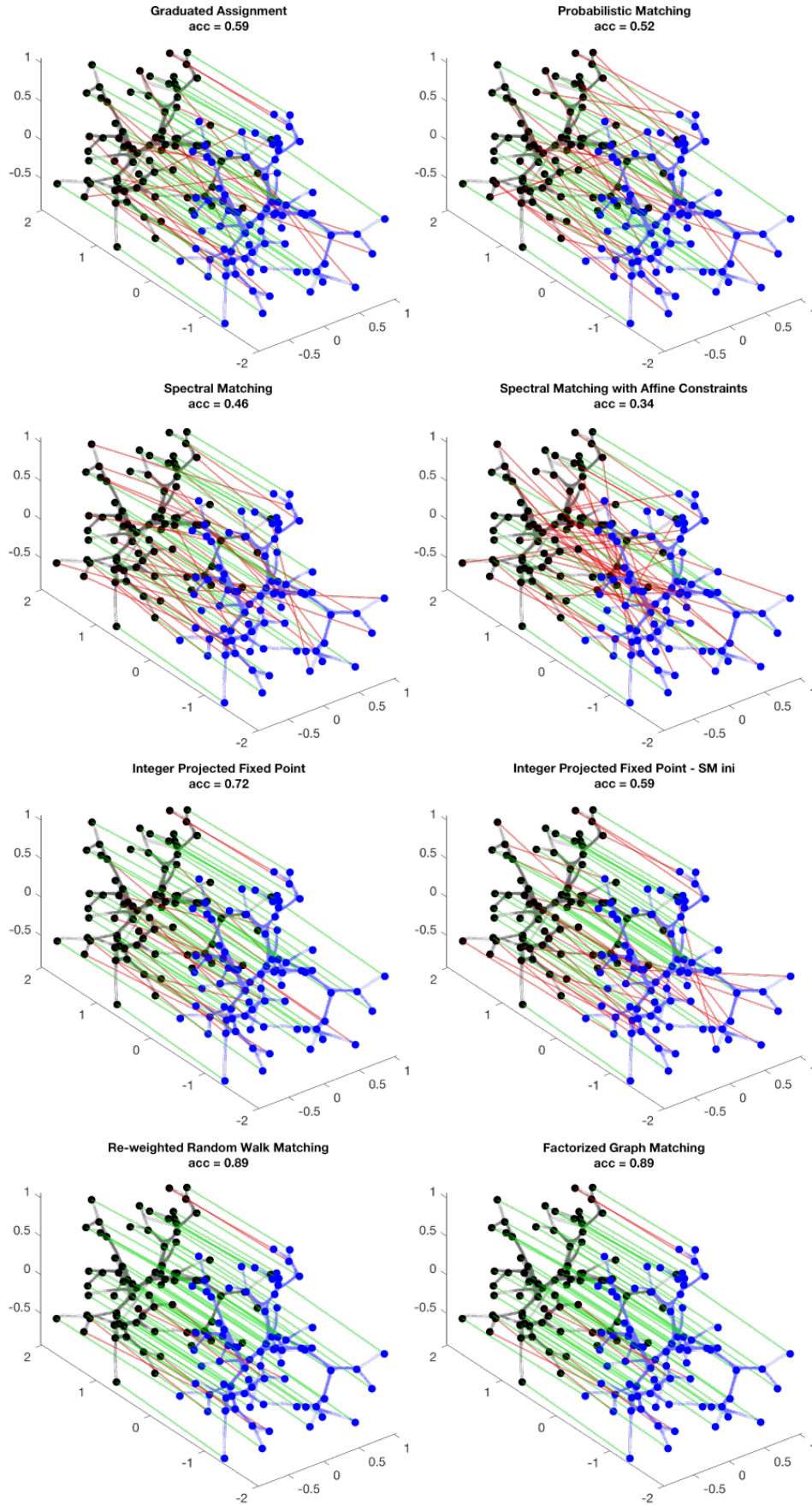


Figure 5.10: Representative Performance of Graph Matching Algorithms: Accuracy for Synthetic Geodesic Vascular Graphs Π_{synth}

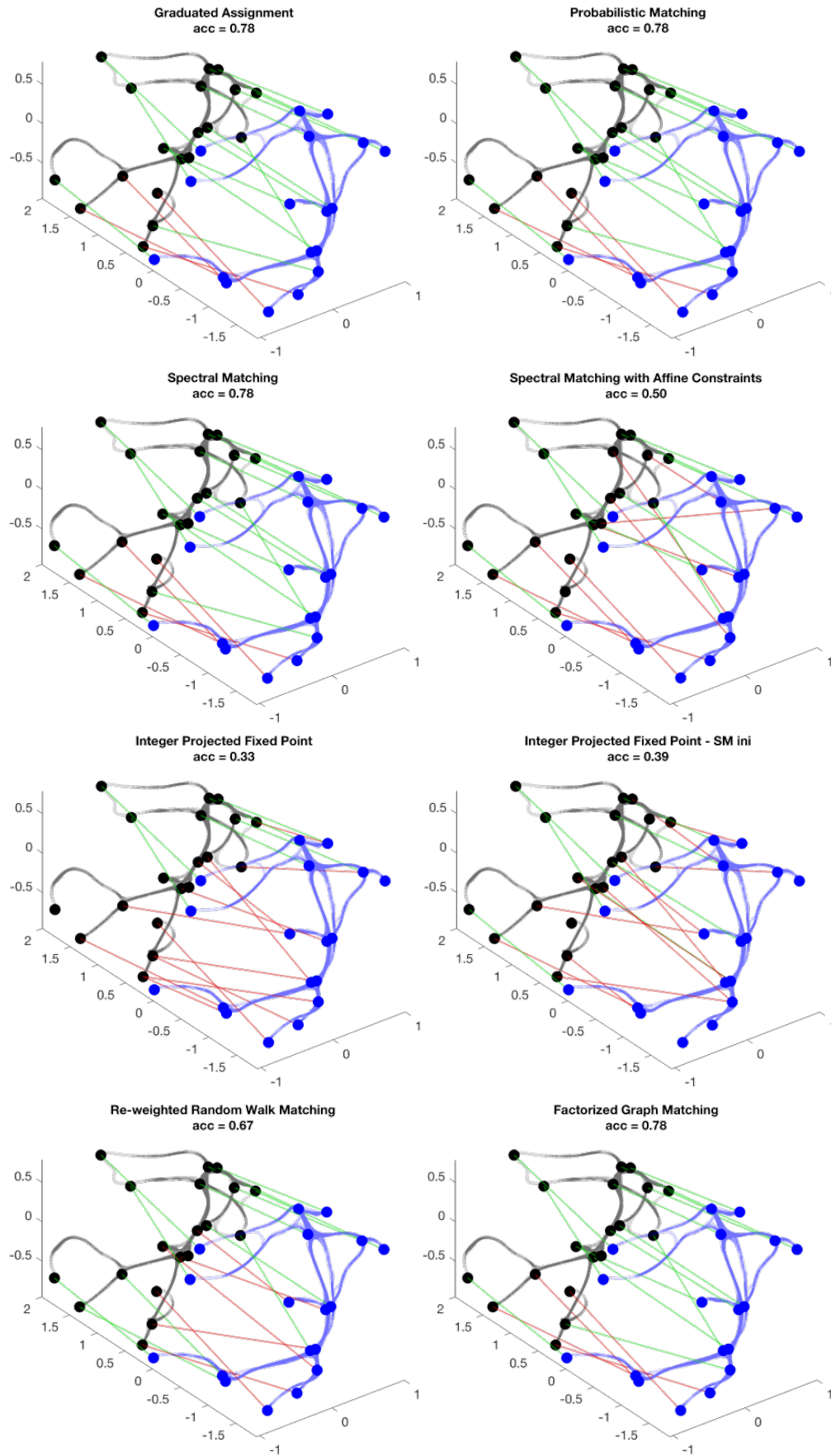


Figure 5.11: Representative Performance of Graph Matching Algorithms: Accuracy for Basilar Artery Geodesic Vascular Graphs Π_{angio}

abilistic matching and the spectral matching algorithms tend to fail the alignment, whereas GM algorithms such as the re-weighted random walk matching and the factorised graph matching seem to be rather robust to the complexity of the network, and have produced consistent alignment among both datasets.

Future designs and developments towards a more specific and vascular-oriented Graph Matching formulation would investigate the effect of different graph lattices and of the connectivity complexity, where the pair-wise registration strategy could be ultimately relaxed towards group-wise Graph Matching frameworks.

5.6 Perspectives on Group-wise Vascular Alignment

Extending quantitative vascular analyses to a population of subjects or a cohort of patients necessarily requires the consistent alignment of the underlying vascular topologies within a group-wise registration framework.

Currently, no formulation is available for the group-wise alignment of cerebrovascular structures, and in this section a collection of possible registration strategies are revised and analysed for the topological alignment of the proposed geodesic vascular graphs. As presented in the previous sections, a first *pair-wise* registration approach was introduced for similar and non-isomorphic vascular structures in the form of undirected connected graphs. Differently from group-wise registration frameworks developed for image-based datasets, the multiple and joint registration of cerebrovascular structures on an image-grid domain stands as an almost completely unexplored research field, and the definition of possible vectorial formulations are still an open technological challenge. Image-based group-wise registration strategies have been largely explored by [13, 62, 66], where all considered raster images are simultaneously warped onto a common space towards a tentatively-estimated group-mean instance, without necessarily selecting a particular one as template [211]. In more recent formulations [121, 211], the group-wise image registration is basically obtained either by an iterative graph shrinking approach, embedding individual images as nodes and the respective mapping transformations as geodesic pathways connecting the image-manifold graph. Alternatively,

the group-wise registration of largely deformed datasets is retrieved by iteratively and simultaneously warping images, following their spectral similarities with local diffeomorphisms [121].

In segmentation propagation and fusion applications, the estimation of a group-based voxel-wise prior follows an exhaustive pairwise alignment and propagation scheme, where multiple image sources are simultaneously mapped and eventually fused to new unseen data [33, 34]. Although sharper atlases can be recovered in such way, an exhaustive pairwise registration and propagation can sometimes be problematic in case of a limited and strongly clustered image-manifold, i.e. highly similar images within the same clusters, however strongly dissimilar ones among different sub-groups (healthy vs. diseased; age- or gender-related clusters). With this view, Cardoso et al. [33, 34] developed a more localised group-wise image registration framework based on geodesic information flows for segmentation and label fusion purposes. The group-wise information propagates between images within a more restricted neighbourhood (a sub-net) of the target, following geodesic paths in a spatially-variant graph, which embeds local patches of an implicit image-manifold.

All the aforementioned group-wise registration methods for image-based data rely, however, on the smoothness, continuity, differentiability and spatial consistency of the image-grid and data-support even when instances are projected to a low-dimensionality space, for more efficient information propagation. In these cases, concepts such as element-wise finite neighbourhood, and operators such as finite difference and integration, and processing paradigms such as (up- or down-)sampling are well-defined within a homogeneous and raster image-domain. Networks, and more generally native graph-embedding instances, on the contrary, do not benefit from the same linearities, and their group-wise alignment stands as an irreducibly challenging task. Despite their particular capability to well represent discontinuous, non-linear, and sparse data embedding, the individual network topology shows a more complex nature than raster 3D regular grids. As observed by Wu et al. [203], Laplacian or diffeomorphic constraints do not straightforwardly apply

to the deformation of the connectivity patterns for group-wise network alignment. Similarly, an algebraic edge-wise average of networks across individual instances may disregard the multivariate, multi-source attributes of non-isomorphic topologies, with unclear outcomes in terms of both noise- and scale-related biases. However, inspired by similar image-based group-wise registration approaches, recent works by Rekik et al. [161], Dhifallah and Rekik [57], and Wu et al. [203], proposed a constrained group-wise graph-shrinkage and network diffusion framework towards the estimation of brain connectivity atlases. A set of functional brain networks, in the form of connectomes, were iteratively shrunk and (locally-to-globally) diffused to obtain an average mean-group representation of the considered population. Although the main focus of the presented approaches was to determine a clustered connectome atlas, the underlying iterative graph-shrinking and diffusive strategy among clusters of similar brain networks could be projected to an early group-wise topological registration approach. The translation of such group-wise network alignment techniques to vascular topologies is currently under investigation. It is unclear, however, whether the straightforward application of a graph shrinkage and diffusion process may deteriorate (or well preserve) the structural connectivity of the inferred cerebral vasculature towards a virtual population-based centroid. Ideally, such a converging target should *sharply* embed the topological inter-subject variability of vascular structures in the form of an over-complete vascular network. Multi-source and geometrical features, as well as topological vascular branching, should be exhaustively kept and anatomically preserved after multiple diffusive iterations, reducing therefore unrecoverable information loss from anatomical landmarks decimation, and from vascular connection suppression and averaging. Also, it is unclear whether the generalisation of the matrix diffusion process in the form of a (*hyper-* or *super-*)graph of networks, as proposed in [203], would apply to vascular over-connected topologies of different connectivity patterns, size and dimensionality for the considered instances.

Recalling concepts in the previous Section 5.1 for the proposed pair-wise topological alignment, alternative group-wise network registration designs have been

proposed in computer vision applications showing a more unconstrained and generalised formulation. These involve extending the graph-matching optimisation problem to enable multiple instances to be jointly and simultaneously aligned together. Substantial work was recently presented by Yan et al. [205–207], Chen et al. [42], Solé-Ribalta and Serratosa [178] and Pachauri et al. [147] towards multi-graph matching strategies. In general, multi-graph matching methods build on pairwise graph matching solvers as a black-box [205]. As described in Chapter 5, graph matching methods incorporate both node-to-node and edge-to-edge structural similarities in a pairwise fashion. Under the assumption that similar topological instances do not mainly appear in isolation or in a pair, rather as a collection, and with the aim of finding the optimal joint matching across all topologies at once, state-of-the-art multi-graph matching techniques simultaneously leverage the *exhaustive* local pairwise matching affinity across pairs of networks, and enforce a global matching consistency by accounting for different mapping composition orders. As summarised in [205], several multi-graph matching formulations were proposed that focus on the *matching affinity*, i.e. maximising an objective affinity score; and on the *matching consistency*, i.e. the global correspondence over all (or a portion of) graph pairs, so that sequential pairwise matching in different composition orders shall lead to identical solutions. Solé-Ribalta and Serratosa [178] extended the aforementioned pairwise Graduated Assignment graph matching (Section 5.3.2) to multiple graphs, where each topology is first associated with an assignment matrix mapping the nodes to a virtual set, then the latter is updated following a deterministic annealing strategy to maximise the overall pairwise affinity score. Also, in this case, consistency is enforced with a tensorial representation of nodes matching and association likelihood, which is lastly binarised satisfying the one-to-one bijective constraint. Pachauri et al. [147] (*MatchSynch*) enforces matching consistency leveraging spectral analysis via eigendecomposition among the set of pairwise matching solutions. Chen et al. [42] (*MatchLift*) accounts for partial similarity, when only a subset of nodes can find a consistent correspondence in other graphs. Yan et al. [207] (*MatchOpt*) proposed an iterative consistency regularisation

strategy by updating in a rotation order the nodes assignment mapping for a set of graphs, with a permutation matrix in an alternate fashion, i.e. defining iteratively a different reference graph and updating the joint correspondence matrix with respect to the pairwise affinity matrices.

In a more recent formulation, Yan et al. [205] proposed to solve the multi-graph matching optimisation problem by adopting a composition-based affinity optimisation (CAO) scheme, which is gradually regularised with a scalar parameter, weighting the matching consistency (CAO-C) among multiple instances. This follows the assumption where, in the iterative optimisation, the matching affinity has a predominant role to delineate the initial joint correspondence, whereas it becomes less informative at later iterations, as the optimised affinity saturates. On the contrary, consistency becomes a relevant regulariser in later optimisation steps, coping with uncertainty and different noise-levels in the graphs, leading to overall improvement of the final matching accuracy.

Adopting the same notation as proposed in [205], the generalised multi-graph matching problem can be formulated also for the proposed geodesic vascular graphs:

$$\mathbf{X}_{ij}^* = \arg \max_{\mathbf{X}_{ij}} \sum_{i=1}^{N-1} \sum_{j=i+1}^N \text{vec}(\mathbf{X}_{ij})^T \mathbf{K}_{ij} \text{vec}(\mathbf{X}_{ij}), \quad \text{so that} \quad (5.4)$$

$$\mathbf{1}_{n_i}^T \mathbf{X}_{ij} = \mathbf{1}_{n_j}^T, \quad \text{and} \quad \mathbf{X}_{ij} \mathbf{1}_{n_j} = \mathbf{1}_{n_i}, \quad \text{and} \quad \mathbf{X}_{ij} = \mathbf{X}_{ik} \mathbf{X}_{kj} \Big|_{k=1, k \neq \{i,j\}}^N, \quad (5.5)$$

where, \mathbf{X}_{ij}^* is the jointly optimised correspondence matrix for any pair of graphs $\{\mathcal{G}_i, \mathcal{G}_j\}$ in the set $\mathbb{G} = \{\mathcal{G}_k\}_{k=1}^N$ of cardinality N . The pairwise affinity matrix \mathbf{K}_{ij} is a square matrix embedding the similarity between the considered pair of graphs and has the same form of those defined in Section 5.2.1. The vector $\mathbf{1}_n$ is a unitary column vector of size $n \times 1$. Note that with this notation, the nodes cardinality is expressed by $n_k|_{k=1, \dots, N}$ for each graph in \mathbb{G} . Also in eq. 5.5, the general formulation accounts for matchable common inlier nodes and the joint alignment consistency can be expressed with the composition $\mathbf{X}_{ij} = \mathbf{X}_{ik} \mathbf{X}_{kj} \Big|_{k=1, k \neq \{i,j\}}^N$ for the $N - 2$ intermediate permutations matchings (or *anchor graphs*) within the set \mathbb{G} .

Although the performance of different multi-graph matching strategies has

Table 5.2: Comparison of the Computational Complexity for the Current State-of-the-Art Multi-Graph Matching Algorithms. Table taken from Yan et al. [205].

<i>algorithm</i>	<i>time complexity</i>
CAO [205]	$O(N^3n^3 + N^2\tau_{\text{pair}})$
CAO-C [205]	$O(N^4n + N^3n^3 + N^2\tau_{\text{pair}})$
MatchLift [42]	$O(N^3n^3 + N^2\tau_{\text{pair}})$
MatchOpt [207]	$O(N^2n^4 + N^3n + N^2\tau_{\text{pair}})$
MatchSync [147]	$O(N^2n^3 + N^2\tau_{\text{pair}})$

only been evaluated on baselines for computer vision applications, the overall general formulation can be extended to multiple graphs of different natures, with increased flexibility for the alignment of non-isomorphic topologies, as observed in Section 5.5. Current state-of-the-art of multi-graph matching algorithms computational complexity is summarised in Table 5.2, as first reported in [205], where τ_{pair} represents the required computational time for each arbitrary pair-wise matching solver. Considering the computational complexity of the mentioned multi-graph matching techniques, the tentative translation to group-wise alignment of large sets of highly-dense geodesic vascular graphs would likely account for a prior individual topological optimisation step. The current computational bottleneck might be minimised by increasing the sparsity of the geodesic vascular graphs and, at the same time, by reducing the graph-embedding dimensionality. With this view, in future work a topological optimisation step should be first devised, which would conservatively retrieve a more compact vectorial representation, in order to accommodate a number of group-wise experimental set-ups.

Whilst the aforementioned multi-graph matching algorithms would jointly optimise a global correspondence solution over the topological instances as a whole, other group-wise topological alignment techniques employ a more localised approach by considering a number of graph partitions, sub-nets, cliques and breadth-first spanning tree projections to solve the problem of (sub-)graph isomorphism [63]. Although only a proof of concept has been proposed for the formulation in [63], the decomposition of a planar graph into a collection of non-disjoint sub-graphs of relatively small tree-width, covering the neighbourhood of each vertex, is shown to solve the problem of sub-graph matching for a number of configurations

in linear time, i.e. $O(n)$.

Theoretically, the combination of multi-graph matching formulations with a more localised graph-embedding could solve the group-wise topological alignment not only on a global scale, rather also on a finer level. Similarly to [33], the topologies could be jointly aligned by leveraging partitions, sub-nets, cliques and non-disjoint small trees from generic cerebrovascular graphs, therefore exploiting multiple local sub-nets of matching patterns within a neighbourhood of the target (Fig. 5.12). With this view, future developments would propose a multi-scale, hierarchical and topologically-preserving sub-graph decomposition, partition and re-combination strategy. Lastly, few other works [30, 46] addressed different multi-graph matching questions: 1) how to estimate a compatibility function such that the solution of the resulting graph matching best resembles the expected solution a human would provide; 2) how to infer a class of graphs which provides an optimal matching to all the instances in the given collection. In these cases, learning approaches are presented over graphs in order to determine an adequate matching criterion, and to estimate graph models from observed data, respectively. Although no application has been proposed for networks based on medical-imaging data, the mentioned learning strategies could implicitly improve group-wise topological alignment accuracies, given a substantial number of correctly labelled instances, for ad-hoc cerebrovascular applications.

In conclusion, a successful group-wise topological alignment strategy for geodesic vascular graphs would allow a tentative explicit definition of a vectorial cerebrovascular atlas at different levels of detail. In the following section, a virtual prior and a topological vectorial atlas for the neurovascular structures is postulated by fusing and merging multiple aligned topologies in a probabilistic, over-complete graph embedding.

5.6.1 Fusing Topologies towards Cerebrovascular Atlases

As previously mentioned, a consistent group-wise topological alignment of the brain vasculature among a cohort of subjects would determine a valid anatomical prior allowing: 1) the extraction of more accurate and refined subject-specific vas-

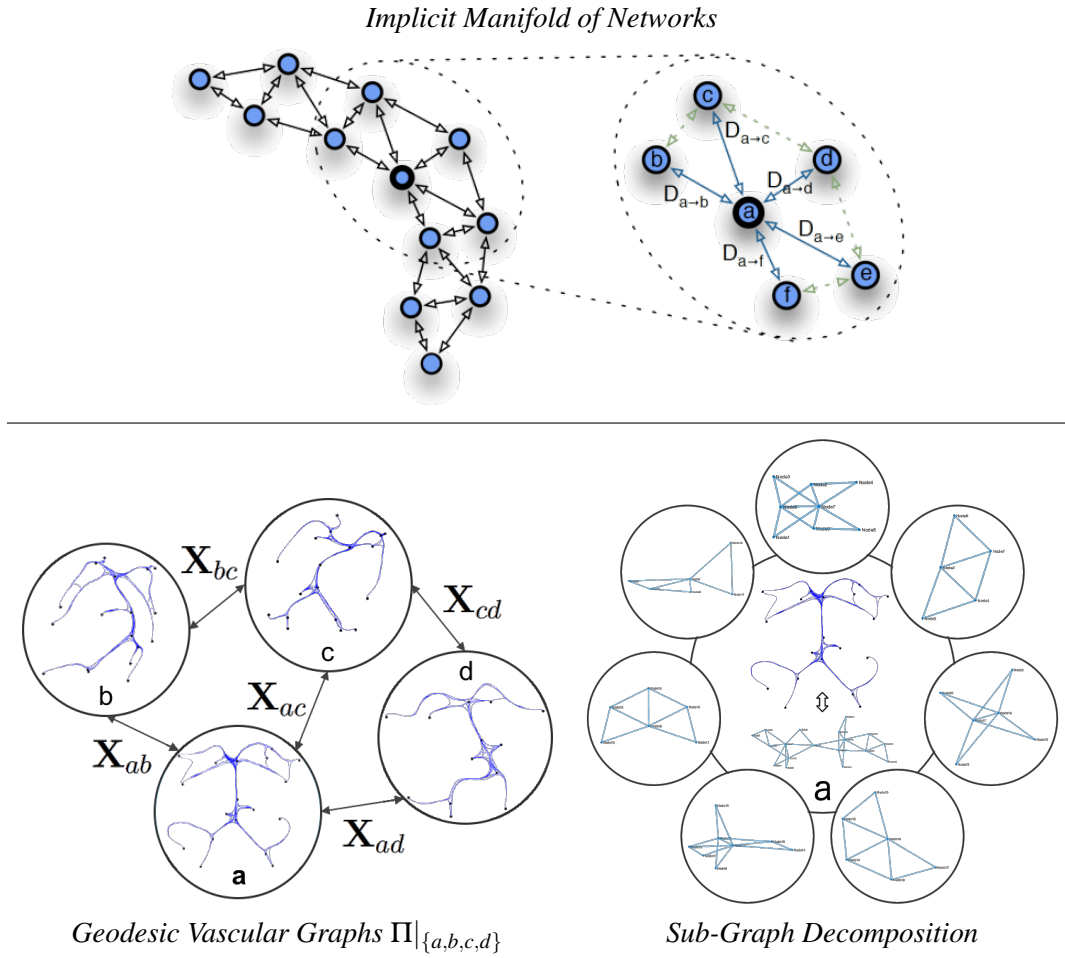


Figure 5.12: Group-wise Global-to-Local Topological Alignment and Matching Propagation: Top: possible adaptation of the implicit manifold to native networks, as first proposed in the Geodesic Information Flows by Cardoso et al. [33]. Bottom-Left: Geodesic Vascular Graphs $\Pi_{\{a,b,c,d\}}$ embedded on each node, given the pair-wise and jointly optimised correspondence matrices \mathbf{X} . Bottom-right: Partition and decomposition for a representative topology into sub-graphs, sub-nets and cliques.

cular graphs; 2) the automatic propagation of labels and anatomical landmarks, and, at the same time, 3) consistent statistical analyses over a *vectorial* population-based atlas of vascular features. However, the fusion of co-registered topologies and the integration of their associated vascular features and embedded biomarkers are not trivial. The resulting atlas, as well as its probabilistic connectivity-pattern prior, should *sharply* encode the topological variability of vascular structures in the form of an over-complete vascular network, i.e. a virtual class of *super-graph* consistently embedding all observed anatomical variants and realisations. In the previous

Section 5.6, early atlas-oriented formulations have only been proposed through diffusion approaches via averaging graphs' adjacency matrices of similar size. However, it is unclear whether embedded features as well as the topological branching of the considered geodesic vascular graphs would be anatomically preserved after multiple diffusive iterations. Averaging vascular graph embeddings by locally (or globally) disregarding anatomical and structural connecting patterns may indeed result in an unrecoverable information loss.

In the following, the definition of a cerebrovascular atlas is initially introduced by adopting a formulation similar to a multi-atlas framework. This allows the atlas estimation problem to be framed with a relatively reduced complexity, under the assumption of multiple atlases for similar cerebrovascular phenotypes. Then, the definition of a comprehensive atlas governed by informative matching flows is postulated by further relaxing the multi-atlas assumption.

A set of undirected geodesic vascular graphs $\mathbb{G} = \{\mathcal{G}_k\}_{k=1}^N$ of total cardinality N is assumed to be locally clustered under some similarity distance measure into M clusters $\{\mathbb{G}_{m=1,\dots,M}\} \in \mathbb{G}$, with each subset having a cardinality of $N_{m=1,\dots,M}$ so that $\sum_{m=1}^M N_m = N$. Each graph \mathcal{G}_k has the form of an over-connected redundant topology as introduced in Section 4.3. It is also assumed that the undirected geodesic vascular graphs are already jointly and optimally co-registered for each cluster, under a group-wise multi-graph matching formulation as in Section 5.6. Then, for each m cluster the associated mean fused atlas, \mathfrak{A}_m is defined as

$$\mathfrak{A}_m = \frac{2}{N_m(N_m - 1)} \cdot \frac{1}{W_m} \sum_{i=1}^{N_m-1} \sum_{j=i+1}^{N_m} w_{ij} \cdot (\mathbf{X}_{ij}^T \mathcal{G}_i \mathbf{X}_{ij}) \Big|_{n_i \leq n_j}, \quad (5.6)$$

$$\text{with } W_m = \sum_{i=1}^{N_m-1} \sum_{j=i+1}^{N_m} w_{ij} \quad (5.7)$$

the integral and normalising fusion weight. Here, for simplicity, each geodesic vascular graph \mathcal{G}_i has the form of a planar symmetric weighted adjacency matrix of size $n_i \times n_i (\times 1)$, where e.g. only a scalar ($\times 1$) vascular feature, e.g. the integral geodesic energy, is associated for the connecting minimal paths. \mathbf{X}_{ij} is the pair-wise

correspondence matrix which is jointly optimised within \mathbb{G}_m , expressing the node-to-node mapping correspondence among the considered geodesic vascular graph \mathcal{G}_i and any other $\mathcal{G}_j \in \mathbb{G}_m$. Note that in this formulation, and according to the aforementioned multi-graph matching framework, it is assumed a matching consistency accounting for an invertible mapping, i.e. $\mathbf{X}_{ij} = \mathbf{X}_{ji}^T$. The fusion weights w_{ij} are defined as

$$w_{ij} = \begin{cases} \frac{\text{tr}(\mathbf{X}_{ij} \mathbf{X}_{ij}^{(\text{GT})T})}{\mathbf{1}_{n_i}^T \mathbf{X}_{ij}^{(\text{GT})} \mathbf{1}_{n_j}} & \text{if } \mathbf{X}_{ij}^{(\text{GT})} \text{ known} \\ < 1 & \text{otherwise,} \end{cases} \quad (5.8)$$

where $\text{tr}(\bullet)$ is the trace of the resulting square matrix.

In this way, the fusion weights w_{ij} encode the resulting pair-wise alignment accuracy $\in [0, 1]$, 1 being the perfect match, in a controlled topological registration set-up, i.e. when the nodes-to-nodes mapping ground-truth $\mathbf{X}_{ij}^{(\text{GT})}$ is known beforehand for each pair $\{\mathcal{G}_i, \mathcal{G}_j\}$, by means of manual annotations of anatomical landmarks and labels. In a more general and uncontrolled set-up, i.e. $\mathbf{X}_{ij}^{(\text{GT})}$ is unknown and labels are automatically propagated, the fusion weights w_{ij} are, for simplicity, associated with a unitary value, under the ideal assumption that no mis-match occurs at the group-wise multi-graph matching level. The permutation matrix product $\mathbf{X}_{ij}^T \mathcal{G}_i \mathbf{X}_{ij}$ encodes the transformation mapping between \mathcal{G}_i and any other $\mathcal{G}_j \in \mathbb{G}_m$. In eq. 5.6, this is, however, only evaluated for topologies mapped from a lower dimensionality to a higher one, i.e. for graphs having nodes cardinality satisfying the relation $n_i \leq n_j$. Similarly to linear programming implementations, such permutation mapping enforces consistency with adjacency matrices of different dimensionality, and, in case of a perfect matching, avoids unrecoverable information loss. In other words, with a sequence of nested and dimensionally consistent sums, the smaller graph is always mapped onto the larger one, and its features are integrated over a set of common matchable inlier nodes (and edges), without discarding those from pair-wise *unmatchable* outlier nodes (and edges). This is consistent under the assumption that all topologies in \mathbb{G}_m share at least one matching correspondence throughout the whole set, i.e. *group-wise unmatchable* outlier nodes (and edges) do

not exist. In case the latter condition is not met, the subset of *group-wise unmatched* outliers will be conservatively kept by concatenating the associated residual nodes (and edges) to the resulting cluster atlas \mathfrak{A}_m . This formulation is omitted here for simplicity. It is worth noting that the cluster atlas \mathfrak{A}_m can be eventually decomposed with an element-wise matrix product

$$\mathfrak{A}_m = \mathfrak{P} \cdot \mathfrak{F}, \quad (5.9)$$

$$\text{with } \mathfrak{P} = \frac{2}{N_m(N_m - 1)} \cdot \frac{1}{W_m} \sum_{i=1}^{N_m-1} \sum_{j=i+1}^{N_m} w_{ij} \cdot \mathbf{X}_{ij}^T \mathcal{G}_i \mathbf{X}_{ij} \Big|_{n_i \leq n_j}, \quad (5.10)$$

where the group-wise merged prior \mathfrak{P} represents the data-driven, probabilistic and structural connectivity pattern(s) found for the average cluster atlas. In other words, given the common space of the average atlas graph \mathfrak{A}_m , \mathfrak{P} embeds the statistical occurrence of certain vascular branching and connections observed in the considered subset of the population. In particular, \mathfrak{P} is a sparse planar symmetric adjacency matrix with real values ranging $[0, 1]$. Intuitively, the scalar attribute component \mathfrak{F} embeds the mean vascular features, e.g. the aforementioned integral geodesic energy (or any other vascular feature and biomarker), as an average weighted adjacency matrix over the considered population \mathbb{G}_m . The purpose of such decomposition is twofold: 1) the group-wise probabilistic prior \mathfrak{P} can be fed with a feedback loop to the multi-graph matching level as a purely topological pre-conditioning matrix, with respect to new unseen vascular graphs. This would minimise possible mis-matching errors and increase the accuracy of the automatically propagated labels. 2) Simple statistical analyses of different vascular-related metrics can be locally performed on \mathfrak{F} for each connecting (sub-)branch, based on the embedded feature or biomarker, e.g. vascular tortuosity analysis in the posterior cerebrovascular structures for a set of subjects, considering the Basilar Artery as whole vs. local partitions of the Basilar Artery with respect to observed and occurring intermediate branch-points.

Lastly, assuming also multiple atlases share a joint and optimal mutual mapping among clusters, a tentative comprehensive atlas \mathfrak{A} from the initial set of multi-

atlases $\{\mathfrak{A}_{m=1,\dots,M}\}$ can be determined as

$$\mathfrak{A} = \frac{2}{M(M-1)} \sum_{i=1}^{M-1} \sum_{j=i+1}^M \left(\mathbf{X}_{ij}^{(\mathfrak{A})T} \mathfrak{A}_i \mathbf{X}_{ij}^{(\mathfrak{A})} \right) \Big|_{n_i \leq n_j} \quad (5.11)$$

where a similar integration and averaging is performed with respect to Eq. 5.6. In this case $\mathbf{X}_{ij}^{(\mathfrak{A})}$ is the pair-wise correspondence matrix for pairs of cluster atlases $\{\mathfrak{A}_i, \mathfrak{A}_j\}$, which is jointly optimised within \mathbb{G} . Also here, the same consistency-enforcing integration strategy is employed for atlases of different dimensionality, where common inlier matchable portions of each atlas are mapped and averaged starting from those with lower node cardinality. Similarly to Eq. 5.6, unrecoverable information loss is avoided for *unmatchable* outlier parts, as well as for the *matchable* inlier ones, under the assumption of a perfect matching.

Although this early formulation for a possible cerebrovascular atlas has not been validated, the theoretical fusion of co-registered non isomorphic topologies can consistently preserve the embedded information at different levels of detail. As shown in both Eq. 5.6 and Eq. 5.11, the correctness of the permutation mapping transform and of the subsequent fusion would mainly rely on the optimality of the group-wise topological alignment step, which has a critical relevance for the overall accuracy and anatomical meaning of the resulting atlases. The assumption of an ideal multi-graph matching, showing no joint mis-match among the considered set of graphs, is however unrealistic, given the *single-shot* pair-wise graph matching formulations, upon which the group-wise framework builds up. Also, early results in Section 5.4 currently show that a more vascular-oriented and contextualised parametrisation is needed specifically for over-connected geodesic vascular graphs. With this regard, a number of improvements and optimisations can be further introduced: 1) the fusion weights w_{ij} in Eq. 5.6 and Eq. 5.7 could model the effect of matching errors in case of a more general and uncontrolled set-up, i.e. when $\mathbf{X}_{ij}^{(\text{GT})}$ is unknown. As opposed to unitary values, w_{ij} could integrate a probability distribution, where the incorrect correspondences for multiple graph matching are captured with a softened Bayesian manner, as proposed by Williams

et al. [200]. 2) Since the uninformative and redundant connecting complexity of the uncertain vascular topologies may produce undesired confounding artifacts in the resulting (multi-)graph matching, a conservative optimisation of the proposed vascular networks could prune trivial connecting overhead, towards a more compact representation, i.e. overall reduction of nodes' and edges' cardinality. The resulting prior \mathfrak{P} would therefore embed a *sharper* vascular connectivity pattern representative of the observed population, and, at the same time, the computation of multiple topological alignments would boil down to a more efficient and high-throughput process for large vascular datasets.

Lastly, by relaxing the multi-cluster assumption, multiple and possibly heterogeneous undirected vascular graphs would populate the same manifold, where the alignment of each instance, as well as the propagation of labels, could be performed on a local neighbourhood of the target, following informative matching pattern flows. Although in the present formulation scalar vascular features are considered for the atlas' attribute component \mathfrak{F} , the embedding of multi-source vascular features of higher order would be consistently extended with *hyper-graphs*. With a more adequate and complete representation of data, these topologies would enrich the vascular atlas characterisation, where the analysis of population-based distributions could be performed without projecting values onto a scalar average domain.

In conclusion, with the advance of novel and efficient techniques for group-wise graph matching, along the lines of [148, 205], a complete set of experiments could be formulated in future works to validate the above theoretical formulation, specifically for cerebrovascular topologies and for a variety of multi-source attributes, i.e. geometrical, geodesic, topological, functional and bio-mechanical features.

In the following chapter, advances towards the extraction of functional and bio-mechanical vascular biomarkers are presented for the proposed VTrails framework. These first leverage the vectorial connectivity of the cerebrovascular structures, then a NURBS-based parametrisation of the bifurcating geometries is devised for hemodynamic simulations within an isogeometric analysis framework.

Chapter 6

Vascular Biomarkers

As mentioned in the previous chapters, the formulation of a vectorial cerebrovascular representation automatically encodes the possibility to locally characterise and analyse vascular features among a cross-sectionally or longitudinally co-registered cohort of subjects. This would ultimately allow to quantitatively monitor patients in the follow-up or to assess the evolution of neurovascular pathologies over a life-long horizon. More specifically, the analysis of clinically relevant biomarkers, such as vascular morphometric parameters (e.g. cross-sectional lumen boundaries, level of stenosis, aneurysm location, size and shape), functional markers (e.g. territorial supply, ischaemic events, local (de-)oxygenation, tracers wash-in/out), hemodynamic descriptors (e.g. blood flow, pressure drop, wall tension and sheer-stress) and surrogate vascular indices (e.g. familial and environmental risk factors), could be projected and performed on a discrete, non-uniform and highly non-linear graph domain, which might be representative of a heterogeneous population. However, population-based and group-wise analyses are currently limited to global, sometimes qualitative, cerebrovascular differences with incidental vascular findings in clinical trials in radiology.

The quantitative evaluation over a cohort of subjects is still a relatively unexplored research area. Early and preliminary work presented by Kwitt et al. [104], proposed to extend the concept of encoding cerebral blood vessel networks as spatial graphs. These would allow the quantification of graph similarities with a kernel-based discriminant classifier from full-brain angiographies to indicate

gender-related architectural differences in cerebral vasculature. However, the lack of a topologically-aware alignment framework for complex cerebrovascular networks limited the analysis, inference and prediction to a global level. As observed in Chapter 5, many of the processing steps require a complete embedding of features of different nature in the same homogeneous domain: from the inference of the most anatomically plausible realisation, to the delineation of uncertain and redundant graph underlying the vascular structure, to the automatic labelling, and ultimately to the propagation of information over vascular topologies. With this view, and by leveraging the connected topology of the inferred cerebrovascular graphs recovered so far, advances on biomarkers extraction and embedding from hemodynamic simulations are introduced into the VTrails framework and are presented in the following sections as further contribution of this thesis.

6.1 Biomarkers from Hemodynamic Simulations

A considerable research effort has been put in vascular biomechanical models to study and classify blood flow patterns and hemodynamic quantities of interest in cardiovascular and cerebrovascular applications [88,180,183,184,186]. Such hemodynamic quantities are typically obtained from computational fluid dynamics simulations, where the Navier-Stokes equations govern the three-dimensional theory of blood flow, under the assumptions of an incompressible, homogeneous, Newtonian fluid flow in a pre-defined domain. Despite the intrinsic non-Newtonian rheological behaviour of blood [130], its overall laminar (or weakly turbulent) flow can be simulated with numeric and finite elements methods, given a set of suitable initial boundary conditions [183]. These methods have been employed to estimate, for example, the vessel wall shear stress, wall tension, and the relative wall displacements following peaks and lows of the pulsating flow [88], as biomarkers for the formation of aneurysms and their associated risk of rupture. Other studies employed finite element simulations to investigate the pathogenesis of occlusive diseases in the cerebrovascular circulation [36,92,177]. In other cases, these methods offer an opportunity to predict potential benefits of surgical repair, where simulations are

used on patient-specific models to design optimal treatments based on prediction outcomes [127].

Computational fluid dynamic (CFD) simulations require the accurate reconstruction of a patient-specific geometric model of the underlying vasculature. Traditionally, patient-specific vascular modelling adopted finite element method (FEM) tessellation approaches to reconstruct the geometry and to perform computational fluid dynamic simulations in different applications [36, 74, 88, 182]. Since FEM-based hemodynamic simulations and fluid-solid interactions rely on the accurate geometrical modelling of the anatomy, the latter is usually determined with vascular lumen segmentation techniques. These, however, may suffer from long computational time, intensive user interaction and limited anatomical accuracy with poorly resolved angiographies [183]. Generally, the approximation of the FEM solution depends on the detail of the reconstructed finite element mesh, where often fine details and accurate simulations are usually coupled with increasing computational time. Overall, these simulations are computationally expensive and the complexity becomes intractable when a more regional or global assessment of blood flow is sought [45, 166], as for the whole arterial cerebrovascular system. Similar prohibitive simulations may occur when a series of localised geometrical perturbations are modelled to assess the effects of pathology and to evaluate several hemodynamic scenarios at different scales. For this reason, feasible applications are often limited to localised vascular portions, where all the hemodynamic quantities of interest can be fully resolved in space and time.

An alternative to costly-intensive computational fluid dynamics simulations for a more global assessment is given by vascular hemodynamic lumped-parameter and distributed network models [166]. These represent the behaviour of a collection of connected vessels by electrical analogs [199]. In other words, the simplified electrical analog models vessels' tubular mechanical features with three basic elements: resistance, compliance and inertance for a fully-dynamic equivalent. Given the closed-loop circuit formulation, modelling a Windkessel setup, pressure and flow-rate waveforms are simulated and measured at the vascular junctions and

along the branches, respectively. A number of cerebrovascular applications have been proposed in the past years, adopting lumped-parameter models: the physiological dynamics of cerebral blood flow regulation and control are investigated in [145, 179] combined with neurovascular coupling. The validation of reduced-order models for studying global flow features in cerebrovascular networks is given in [45], where the observed discrepancies between computational fluid dynamics simulations and lumped-parameter models are reduced with extra impedances at the bifurcation level, compensating for flow-rate inaccuracies from bifurcation angles. Onaizah et al. [146] studied the impact of obstructive and sclerotic changes within the carotid arteries, and the overall impedance and resulting blood supply to the brain. Ryu et al. [166] adopted a non-linear lumped-parametric model of the Circle of Willis to evaluate the compensatory role of collateral blood flow in occurrence of multiple occlusions at different levels of the arterial vasculature. Despite the reduced-order of the models which cannot fully model vascular fluid-structure interactions (i.e. wall-tissue stress information), the inexpensive computational cost allows an early evaluation of the mechanisms underlying the cerebral blood autoregulation. Also, the arbitrary scalability of the analog equivalents and the flexibility to account for vascular network perturbation, i.e. occlusions and different levels of stenoses, allow to compactly extend the analysis to larger networks, modelling at the same time different physio-pathological configurations.

On a more localised scale, however, computational fluid mechanic modelling is becoming increasingly important in personalised healthcare, where computational tools are combined with the individual anatomy and physio-pathological data to support diagnosis, therapeutic inference and planning medical intervention [190].

Despite reconstruction of a patient-specific vascular geometry suffering from technological challenges, patient-specific geometrical models provides surgical guidance. Also, particular cardio-/neuro-vascular applications, such as the custom-designed creation of medical devices (i.e. stents, bypass and recanalisation prostheses) require a patient-specific geometrical model to capture the underlying anatomy. The ability to locally extract a 3D geometrical parameterisation of human vas-

culature would empower and ease the translation to clinical care for two main reasons. On one hand, the development of vascular medical devices can be performed with computed aided design (CAD) software. In this case, the parametrisation of the structures using Non-Uniform Rational B-Splines (NURBS) is *de facto* the industrial bio-mechanical standard, as well a scale-free and inexpensive data-representation tool for virtual visualisation environments. On the other hand, isogeometric analysis (IGA) [90], a relatively recent framework governed by partial differential equations, enables the rapid simulation of bio-mechanic properties. Among those, blood-flow and hemodynamic quantities, as well as fluid-solid interactions at the interface, can be determined on the same parametric NURBS domain without further levels approximations.

With the introduction of IGA, an alternative and unified formulation of vascular geometries was proposed in [190, 214], where the subject-specific model was determined using parametric curves. With respect to traditional FEM-based models, few studies [77, 185] proposed a tentative integration of the vascular geometry in a CAD-compatible design framework, by employed NURBS-based libraries prior to rasterising the volumes into a tetrahedral mesh. A geometrical construction scheme was first introduced by Zhang et al. [214], which included an image segmentation step, followed by a geometrical parametrisation and simulation analyses. Parametric NURBS primitives [156] were employed to recover the anatomical vasculature relying on a dictionary of geometrical templates for topological junctions. Aiming at recovering also the typical smoothness of the anatomical structures, a fitting procedure adapted the junction templates on a pre-determined finite element mesh, enforcing circumferentially G^1 -continuity on the surface. Also, a fully-coupled monolithic formulation of the fluid-structure interaction for an incompressible diffusion on a hyper-elastic solid interface was detailed in [18], where a NURBS-based IGA framework numerically embeded the simulations solutions' domain. In contrast to traditional finite element tessellations, the NURBS-based parametrisation for the IGA simulations exactly represented the solution profile at the fluid-solid interface, which can predict biomarkers for the onset and development of vascular diseases.

Although [18, 214] provided a CAD-compatible integration and a monolithic formulation with an IGA framework, the geometrical construction process suffers from being a semi-automatic paradigm, and from a long computational time for large and complex vascular networks [190].

Following the aforementioned concepts and inspired by these recent frameworks, the extraction of biomarkers is addressed in the following sections for a global-network as well as for localised branching geometries. A set of hemodynamic quantities are derived to functionally characterise the cerebrovascular inferred topologies with VTrails. Leveraging both topological and geometrical representations of the vascular structure, further contributions to this thesis comprise:

1) the estimation of geometrical parameters and the local morphology of connected vessels with a series of geodesic snakes (i.e. active contours) segmenting a linearly reformatted angiographic volume along the connecting centerline or geodesic path.

2) A simplified hemodynamic model based on geometrical and bio-mechanical lumped-parameters and an analog-equivalent configuration that approximates the asymptotic values of blood flow and pressure drop for a global cerebrovascular network. In this case, autoregulation and compensation mechanisms are observed in simulated pathology, by perturbing the bio-mechanical lumped parameters of the analog-equivalents in healthy realisations. Also, the *resilience* of the cerebrovascular network, i.e. the capability to recover from pathological conditions and events, is evaluated for a set of clinically relevant cerebrovascular variants.

3) An automatic NURBS-based parametrisation of the underlying vascular structure is presented on a more localised scale towards the extraction of biomarkers from fluid-solid interactions at the interface. Focusing on the geometrical reconstruction of bifurcating vessels at the junction, fully-resolved (space and time) hemodynamic simulations are ultimately run to recover pressure values and blood flow velocities in a representative set of examples, as a proof of concept, by solving a canonical Stokes problem on the reconstructed vascular geometries with an isogeometric analysis framework [55].

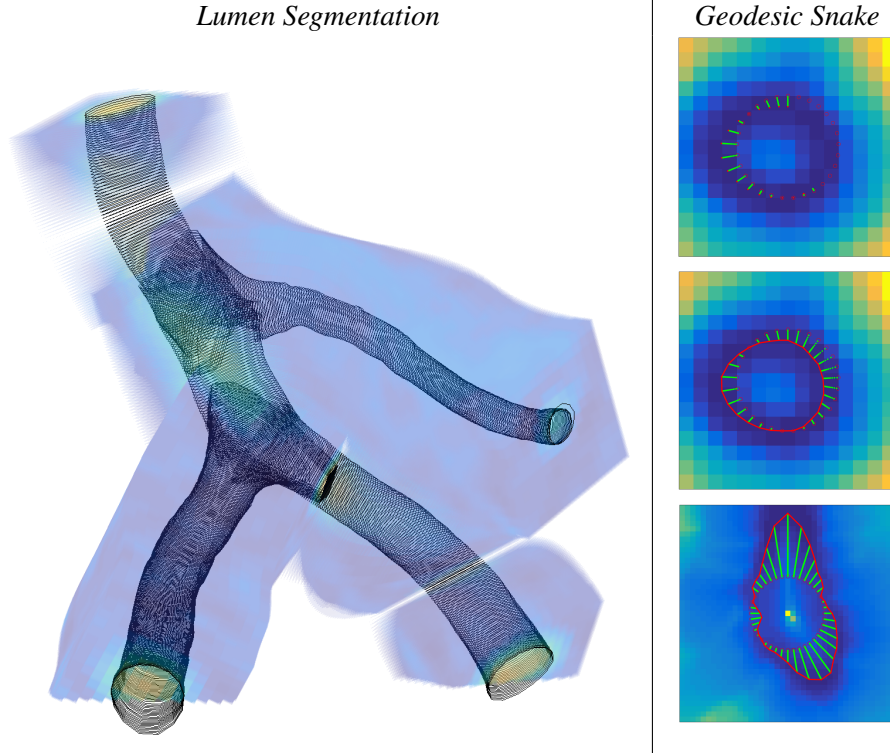


Figure 6.1: Lumen Segmentation with Cross-Sectional Geodesic Snakes. Representative phantom combined with the previously inferred vascular tree. Vessel lumen delineation are consistent along the tubular-like elongated structures, with local overlap at the respective junctions. Closed-contours are enforced using the geodesic snakes (active contour) formulation.

6.2 Lumen Segmentation with Geodesic Snakes

Following the concepts introduced by Cheng et al. [43], the delineation of vascular contours is obtained with closed geodesic snakes (*active contours*). From an angiographic image volume V , and a set of connected centerlines, the volumetric image is linearised per branch using a planar rigid transformation along the vessel centerline. Geodesic snakes are then derived from two antagonist level-sets that evolve on the reformatted image volume.

In detail, similarly to [94], considering an angiographic image V and a centerline, or a minimal path π , a reformatted image volume V_{rf} is obtained by re-sampling V along a series of orthogonal planes to π . This result in a set of 2D slices that are orderly stacked with a rigid transformation. Such a rigid transformation $\phi : \mathbb{R}^3 \rightarrow \mathbb{R}^3$ maps the canonical Cartesian coordinates of each slicing plane from

the angiographic image reference system onto a new reformatted reference system, i.e. $\{\mathbf{i}, \mathbf{j}, \mathbf{k}\} \xrightarrow{\phi} \{\mathbf{i}', \mathbf{j}', \mathbf{k}'\}$. In the new reformatted reference system the centerline (or minimal path π) is linearly mapped along the \mathbf{k}' axis for its entire length, whereas \mathbf{i}' and \mathbf{j}' are associated to a pair of orthogonal directions laying on the slicing plane. The size of the slices is determined with a pre-defined distal range with respect to the centreline, in order to capture both the vessel and the surrounding parenchyma. The resulting reformatted V_{rf} shows therefore a linearised tubular region of bright-contrast in the middle of the volume with dark-contrast background delimiting the respective boundaries of the tube.

Two antagonist level-sets propagate over V_{rf} to determine an implicit boundary functional as an energy potential for the delineation of geodesic snakes. Similarly to section 4.1, the antagonist energy potentials are numerically determined with a Fast Marching algorithm [175] assuming here an isotropic propagation medium. The two antagonist energy potentials \mathcal{U}_{int} and \mathcal{U}_{ext} are integrated as implemented in [102] for both V_{rf} and \bar{V}_{rf} respectively. As in section 3.3, \bar{V}_{rf} is the negative image of the reformatted volume V_{rf} , showing an opposite contrast of the structures. In this case, the speed magnitude of the propagating front is expressed by the voxel-wise values of the reformatted volumes. For the internal energy potential \mathcal{U}_{int} , the initialisation seeds consist in all points of the linearised centerline, these being *inside* the reformatted tubular structure. Conversely, the points corresponding to the corners of each slice in \bar{V}_{rf} , these being *outside* the reformatted tubular structure, are defined as the initial set of seeds for the external energy potential \mathcal{U}_{ext} .

It can be observed that the internal energy potential \mathcal{U}_{int} models the time of arrival for a diffusive process within the blood vessel, which propagates first along the lumen towards the vessel wall. The external energy potential \mathcal{U}_{ext} models instead the antagonist time of arrival, which represents the containing effect of parenchymal structures surrounding the vascular structure. By definition of the front propagation, both level-sets eventually leak into the mutual structures. A vascular boundary potential \mathcal{P} is determined as $\mathcal{P} = (\mathcal{U}_{int} + \mathcal{U}_{ext}) + |\mathcal{U}_{int} - \mathcal{U}_{ext}|$. This is motivated by combining their antagonist diffusion and their individual monotonically increasing

profiles as previously shown in Fig. 4.6, for a generic 1D case. The resulting form of the boundary potential \mathcal{P} implicitly encodes the geometrical locus of the competing frontier between the considered level-sets with local minima (valleys) in the neighbourhood of the tube's wall (Fig. 6.1).

Note that in this case, the back-tracing of the boundary potential \mathcal{P} reaches a unique global minimum along every radial direction joining the innermost part of the vessel (ideally a central point \mathbf{p}_A as in Fig. 4.6) with the surrounding parenchymal structures (i.e. any other point \mathbf{p}_B as in Fig. 4.6, surrounding the tubular structure).

A constrained geodesic active contour (G-snake) σ is therefore extracted leveraging the configuration of the reformatted volumes. In detail, the snake σ is adjusted on the local minima of the boundary energy potential \mathcal{P} following a radial motion direction. The geodesic snake σ is first initialised as a circular closed contour centred in the middle of the slice, then it evolves with a gradient descent towards the valleys so that an integral energy is jointly minimised along the snake at convergence (Fig. 6.1).

6.2.1 Accuracy of Geodesic Snakes

Full sets of angiographies available from [6, 28] are considered for quantitatively validating the geodesic snakes segmentation. Also, a MR time-of-flight angiography of the Circle of Willis is considered for a qualitative assessment. Each branch of 3D connected centerlines from [6, 28] is considered with the respective angiography to automatically recover the cross-sectional lumen segmentation with geodesic snakes. The accuracy of the proposed delineation is qualitatively evaluated in Fig. 6.2 for both local and full-brain examples. Quantitatively, the accuracy error is computed as the Euclidean distance between the delineated snakes and the closest points of the segmentation given as gold-standard (GS). Accuracy errors are reported in the following sections as average symmetric values $\bar{\epsilon}$, median ϵ_{Q_2} and Hausdorff-95 $\epsilon_{H_{95}}$ [mm] averaged per angiography (mean \pm SD), with respect to the collection of data in both repositories. In Fig. 6.2, both localised and whole-brain vessels are well delineated with geodesic snakes. Closed contours converge to the

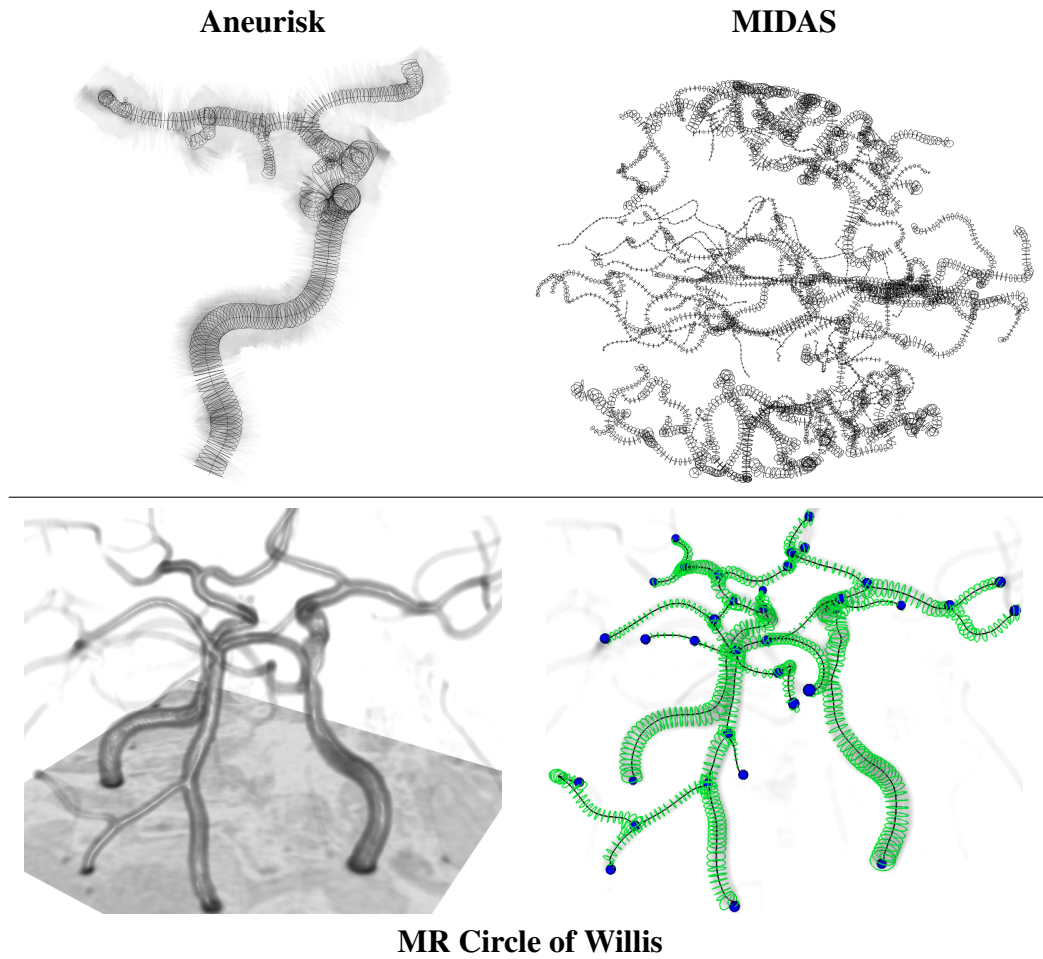


Figure 6.2: Vessel Segmentation with Geodesic Snakes: representative angiographies in [6] and [28] repositories (top); a MR time-of-flight angiography of the Circle of Willis (bottom).

neighbourhood of the vessel wall even in cases of tortuous and convoluted vascular structures. Note that, while this segmentation technique is not the principal contribution, it is primarily presented as a technical bridge between the acquired medical image volume and the need for an initial contour approximation. From the analysis, deviations are comparable to the voxel-size (table 6.1), with maximal errors limited to approximately 1 mm. Fluctuations are observed for smaller vessels and capillaries, where the formulation of geodesic snakes requires further regularisation due to local partial volume effects.

	$\bar{\epsilon}$	ϵ_{Q_2}	$\epsilon_{H_{95}}$
Aneurisk	0.21 ± 0.24	0.14 ± 0.04	0.65 ± 0.33
MIDAS	0.5 ± 0.35	0.45 ± 0.03	1.09 ± 0.07

Table 6.1: Accuracy of geodesic snakes vs. GS: average symmetric error $\bar{\epsilon}$, median ϵ_{Q_2} and Hausdorff-95 $\epsilon_{H_{95}}$ [mm] (mean \pm SD), averaging on the complete datasets in [6, 28].

6.3 Vascular Graph-based Analog-Equivalents

A scalable and fast simulation framework that statistically estimates functional biomarkers from asymptotic hemodynamic simulations is introduced here, leveraging lumped-parameters models and analog-equivalent physio-pathological configurations as proposed in [45, 146, 166]. To efficiently approximate the computational fluid dynamics, subject-specific vascular graphs from clinical angiographies are integrated in a closed-loop configuration, where bio-mechanical parameters are first estimated using the geodesic snakes and a simplification of the Euler fluid equation. Lastly, a perturbation strategy is devised to model the effects of stenosis, tortuosity, and occlusions on the analog-equivalents of phenotypical vascular topologies. Assuming that a latent autoregulation mechanism underlies major brain arteries, the simulated pressure/flow values suggest how the whole neurovascular network reacts to local alterations. As this may result in possible downstream changes in vessel wall tension, a new metric of neurovascular resilience is also provided to different pathological scenarios. Lastly, beyond estimating biomarkers, a putative

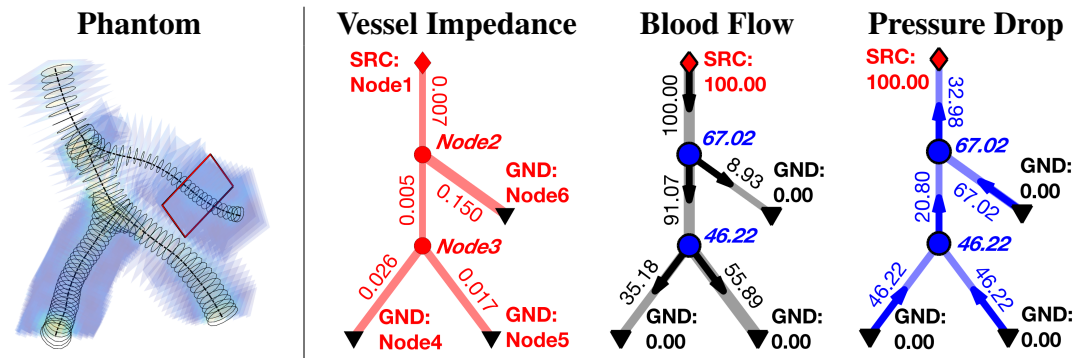


Figure 6.3: Hybrid Vascular Lumped-Parameters Model of a Phantom: lumen segmentation with geodesic snakes as in Section 6.2 (left); Impedance (red), Flow (gray) and Pressure drop (blue) asymptotic values (right).

graph sampling strategy is ultimately devised based on the same analog-equivalent formulation, which supports the topological inference of uncertain redundant vascular network by increasing the sparsity of a fully-connected neurovascular graph, while preserving its most biologically-plausible set of realisations.

6.3.1 Hybrid Vascular Lumped-Parameters Model

Hemodynamic quantities are obtained from simplifying the Euler fluid equation, governing the fluid dynamics in the continuum. Here, non-linearities and the shock of an incompressible flow transient are approximated by assuming a cylindrical model of the underlying branch geometry, where a rigid pipe runs with fixed radius along the vascular elongated direction (i.e. \mathbf{k}'), adopting the same notation of the reformatted reference system as in section 6.2. As demonstrated in [193], the axial motion of a fluid is derived from the Cauchy momentum of mass conservation to the differential Hagen-Poiseuille equation

$$q_{\mathbf{k}'}^{\max} = -\frac{1}{4\mu} \frac{\partial p}{\partial \mathbf{k}'} \cdot r^2, \quad (6.1)$$

under the assumption of a steady, i.e. $\frac{\partial \mathbf{q}}{\partial t} = 0$, fully-developed, i.e. $\frac{\partial q_{\mathbf{k}'}}{\partial \mathbf{k}'} = 0$, and axisymmetric flow \mathbf{q} , showing non-turbulent motion, i.e. with null flow velocity for both radial and swirl components. The maximum flow occurs at the centre of the pipe of radius r , and the constant average axial flow $\bar{q}_{\mathbf{k}'} = \frac{1}{2} q_{\mathbf{k}'}^{\max}$ integrates its parabolic profile over the pipe's cross-section. Integrating also a linearly decreasing pressure drop ∂p along the entire length l of the pipe, a constant, average, axial flow $Q = \bar{q}_{\mathbf{k}'}$ can be rewritten as

$$Q = \frac{\Delta P}{R}, \quad \text{with} \quad R = \frac{8\mu l}{\pi r^4} \quad \text{and} \quad r = \frac{1}{l} \int_l \sqrt{\frac{a(\sigma(\mathbf{k}'))}{\pi}} d\mathbf{k}', \quad (6.2)$$

with ΔP the integral pressure gradient, R the total integral resistance of the rigid pipe of radius r , and μ the constant blood viscosity. Here, the constant radius r is averaged along the pipe using the area of cross-sectional snakes $a(\sigma(\mathbf{k}'))$. Note that 'π' in Eq. 6.2 is the Archimedes' constant.

6.3.2 Graph-based Analog-Equivalent

Along with the hydraulic analogy of electric systems, analog-equivalent circuits are modelled as a set of connected lumped-parameters for the vascular network. A generic vascular graph $\mathcal{G} = (N, E)$ is defined as a set of nodes $j = 1, \dots, |N|$ (i.e. the branch-points), and the associated connecting edges (i.e. the vascular branches), encode in $E(j_1, j_2)$ the binary adjacency matrix. For each edge, the tubular features are converted into electrical impedance for an analog equivalent, where purely dynamic components vanish for a steady-state flow. The impedances of the connected pipes simplifies to real-valued resistances $R = f(l, r)$ as in eq. (6.2). These are embedded in the associated resistance-weighted adjacency matrix $R(j_1, j_2)$. In a similar form, the flow $Q(j_1, j_2)$ and the pressure drop $\Delta P(j_1, j_2)$ are translated into current and potential difference for each vascular branch, respectively. Simulating a closed-loop analog circuit, voltage generators as source of potentials (SRC_j) and potential grounds (GND_j) are introduced in the system in the correspondence of the j -th node. These model the pressure at the inlets or outlets of the network as node-wise potential boundary conditions (P_{BC}). By coupling linear lumped-parameters and the set of boundary conditions, the analog-equivalent circuit is solved using Kirchhoff's laws as a linear system of equations. As described in algorithm 1, C_{R-1} denotes the circuit admittance matrix. C_{R-1} initially maps the equivalent topological system where D_{R-1} and A_{R-1} represent the associated diagonal degree and the adjacency matrix respectively, as in a canonical graph Laplacian. The notation $C_{P_{BC}}$ represents the node-wise potential vector of boundary conditions, whereas P is the node-wise potential solution of the linear system of equations. The canonical passive sign convention is enforced as shown in Fig. 6.17.

6.3.3 Modelling Perturbations on Vascular Topologies

Perturbations and alterations of the vascular graphs can be introduced prior to recovering and solving the graph-based analog-equivalent, as in the previous section. In particular, two types of perturbations are introduced to account for changes in structural connectivity and flow resistance modulation. The structural connectivity perturbation is achieved by altering the topology of the neurovascular graph $\tilde{\mathcal{G}}(N, \tilde{E})$

```

1 Input:  $R, P_{BC}$ ; Output:  $P, \Delta P, Q$ 
2  $C_{P_{BC}} = \mathbf{0}_{|N| \times 1}$ ; ▷ Initialisation
3  $C_{R^{-1}} = D_{R^{-1}} - A_{R^{-1}}$ ; ▷ Circuit Admittance System
4 for all  $P_{BC_j} \in \{SRC, GND\}$  do
5    $C_{R^{-1}}(j, \forall j_2) = 0$ ;  $C_{R^{-1}}(j, j) = 1$ ;
6    $C_{P_{BC}}(j) = P_{BC_j}$ ; ▷ Include Boundary Conditions
7 end
8  $P = C_{R^{-1}}^{-1} C_{P_{BC}}$ ; ▷ Solve the Linear System
9 for all edges do
10    $\Delta P(j_1, j_2) = P(j_1) - P(j_2)$ ; ▷ Assign Potential Difference
11    $Q(j_1, j_2) = \Delta P(j_1, j_2) \cdot R(j_1, j_2)^{-1}$ ; ▷ Assign Current (Ohm's law)
12 end

```

Algorithm 1: Graph-based analog-equivalent system: definition and solver.

with a mask \mathcal{E} as $\tilde{E} = \mathcal{E} \cdot (E \cdot \mathcal{A})$. Here, the structural perturbation matrix \mathcal{E} follows a Bernoulli distribution of probability λ . These model random occlusions, which disrupt the connectivity by a factor $\varepsilon = (1 - \lambda)$, on average. A sparse adjacency matrix \mathcal{A} , of the same size of E , represents an anatomical prior where non-zero edges $\mathcal{A}(j_1, j_2)$ weight the likelihood of certain cerebrovascular connections. In general the anatomical prior \mathcal{A} is *unknown* for non-annotated graphs. This means that the sparse matrix is identically equivalent to $\mathcal{A} = \mathbf{1}_{|N| \times |N|}$, therefore vanishing in the structurally perturbed adjacency matrix \tilde{E} . Prior knowledge can be embedded in \mathcal{A} , if available, from manual annotations or known connectivity patterns.

The second type of perturbation modulates the resulting integral resistance. Effects such as vascular stenosis and vessel tortuosity are modelled for both reduced radii r and longer pipes' lengths l , respectively. These are element-wise embedded in the perturbed resistance matrix as $\tilde{R}_{\tilde{E}} = \mathcal{R} \cdot R_{\tilde{E}}$. Here, the resistance modulation $\mathcal{R}(j_1, j_2)$ for each edge follows a uniform distribution within the parameters range $[0, m < 1]$. Note that these perturbations are computationally very efficient, as they are defined as simple matrix-to-matrix element-wise transformations.

6.3.4 Preliminary Experiments: Vascular Trees

As initial sanity test of the implemented formulation, and in order to evaluate the scalability of the proposed approach to full-brain angiographies, a set of cerebrovascular trees of different details and depth are considered. In this case, the hemody-

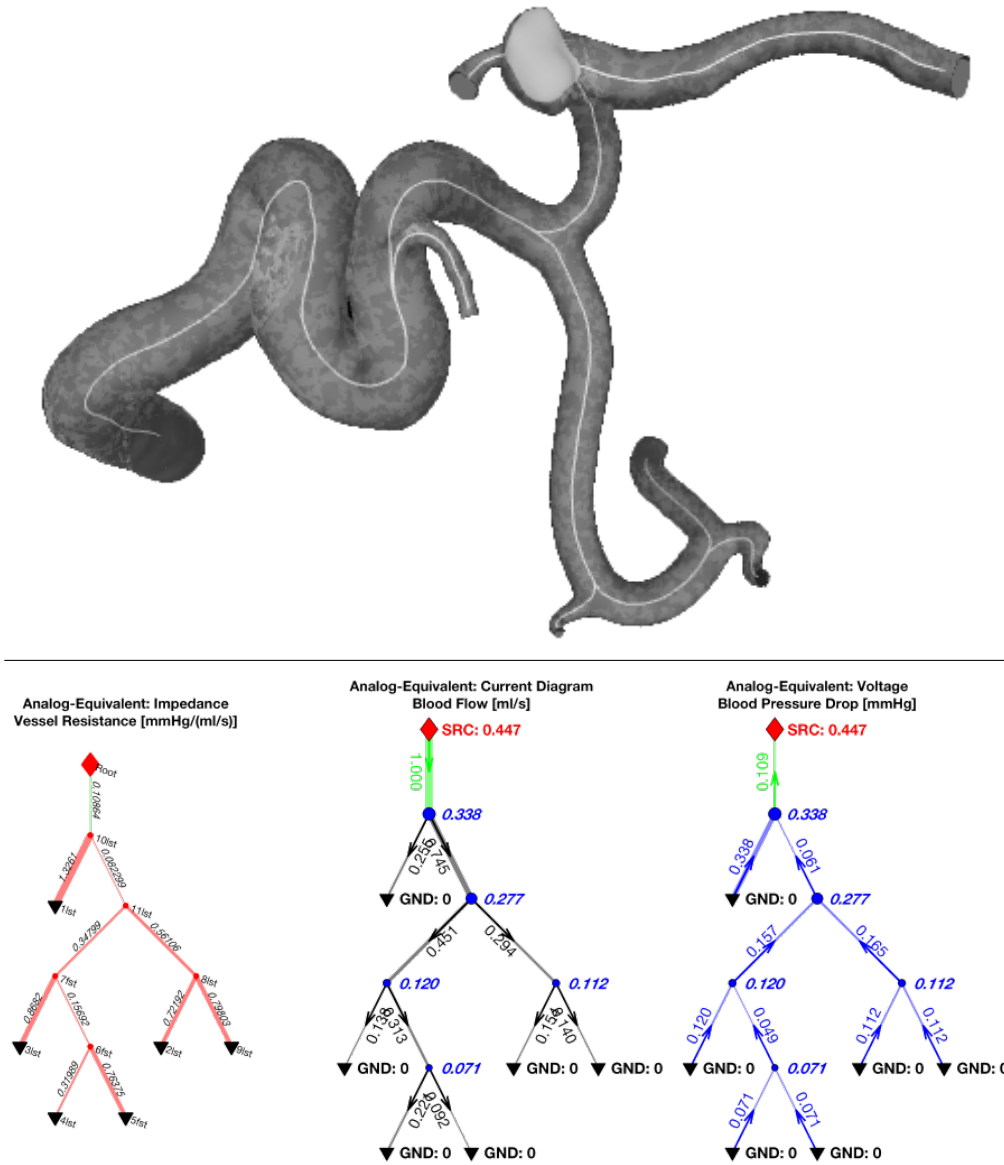


Figure 6.4: Hemodynamic analog equivalent and steady-state blood flow simulation with the described lumped-parameters model for a cerebral vascular tree from [6].

dynamic biomarkers are obtained with the lumped-parameter analog-equivalent model without any further perturbation. Note that, however, all the considered topologies are in the form of hierarchical (rooted) trees. In Fig. 6.4, the analog equivalent model for a cerebrovascular tree from [6] is shown together with the image-based spatial segmentation of the vascular structure. The impedance graph is automatically configured with a pressure-driven source at the root of the vascular tree, and analog equivalent grounds are placed in correspondence of terminal branches fol-

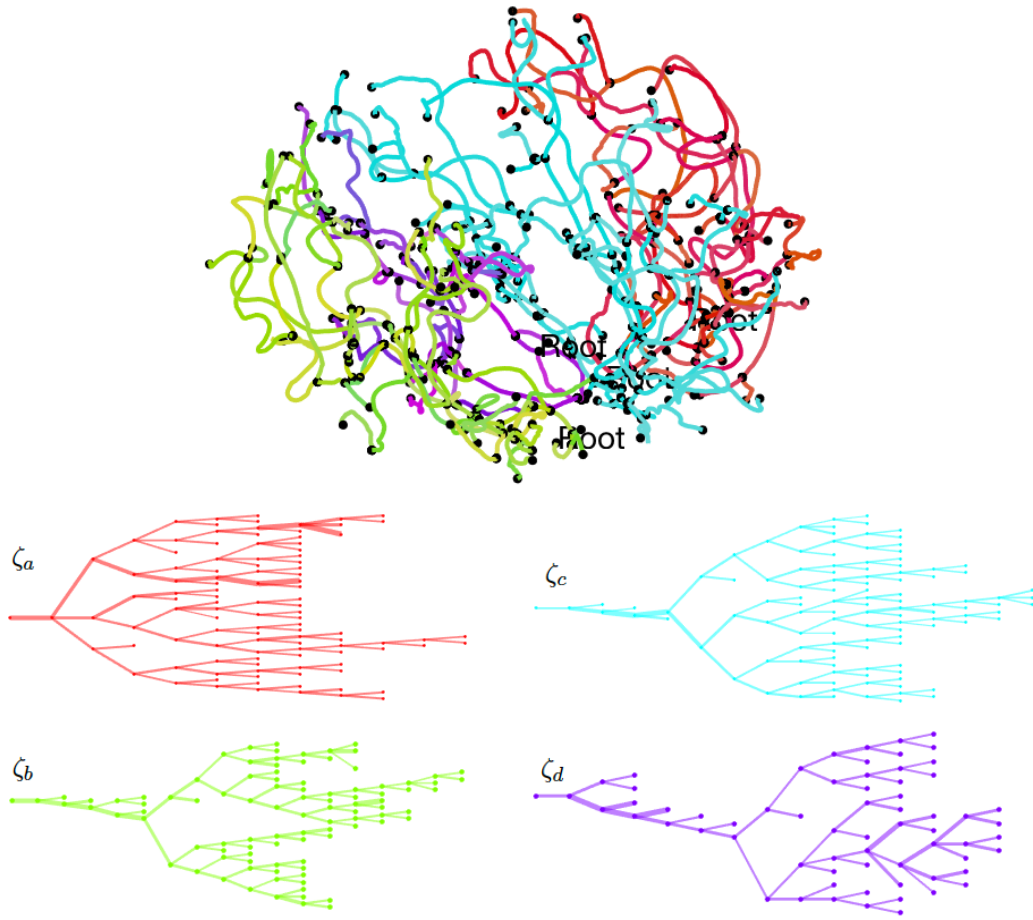


Figure 6.5: Full-brain set of deep-cerebral vascular trees from [28].

lowing the algorithm 1. Note that the first vascular branch in cascade to the voltage (pressure) source is referred as *sensing* resistance. This allows to normalise simulated blood flow values with respect to the *unknown* blood flow source (note that the analog circuit is modulated in voltage, at the source, not in current). After solving the linear system of equations, the respective blood flow is determined for each vascular branch, and the pressure is computed for each node, i.e. at the vascular junctions, and along each branch in the form of a pressure drop. By adopting the canonical notations, blood flow directions, as well as pressure drop ones, are visually highlighted with the passive sign convention. Similarly, blood flow and pressure drops in the main deep-brain arterial vessels are simulated for a whole cerebrovascular dataset. Fig. 6.5 shows a schematic representation of the geometrical and spatial embedding of the vascular trees and their associated vectorial connec-

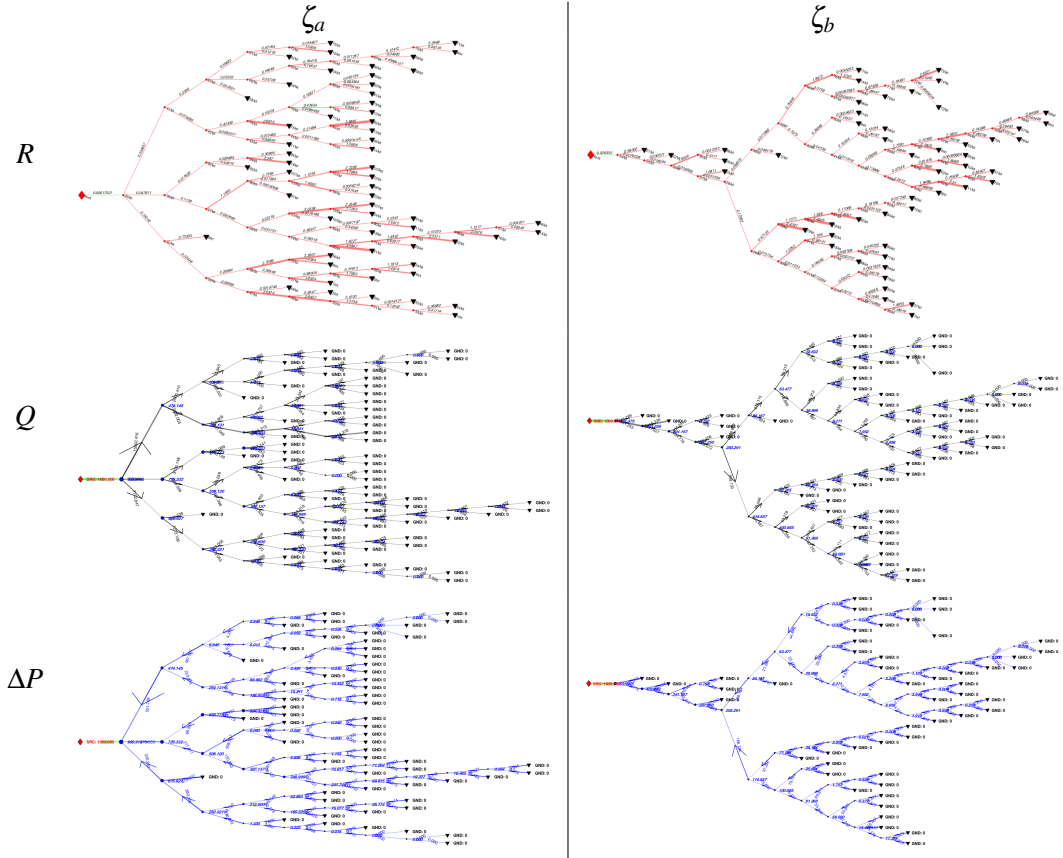


Figure 6.6: Hemodynamic analog equivalent and steady-state blood flow simulation for the deep-brain arterial trees ζ_a and ζ_b as in Fig. 6.5. Analog resistance equivalent R , simulated blood flow rate Q and blood pressure drops ΔP .

tivity. By adopting the same configuration for rooted trees, the analog impedance equivalents are automatically recovered and configured for all the vascular branches of the deep-brain arterial trees. Analogously, the associated blood flow partition, and pressure drop distributions are solved for the considered instances (Fig. 6.6 and 6.7). Whilst a full-brain simulation of the arterial vasculature would have been impractical with computational fluid dynamics simulations, in this case the solution for the considered lumped parameters was nearly instantaneous ($< 1 \times 10^{-3}$ s). Despite the different levels of approximation, an initial figure of territorial blood flow and pressure drop profiles is quantified for the vascular branches above the Circle of Willis. Results show partitions and distributions being in line with biologically compatible and physiological hemodynamic ratios, whereas, for some other topologies (e.g. ζ_d), functionally implausible hemodynamic values are reported. This is

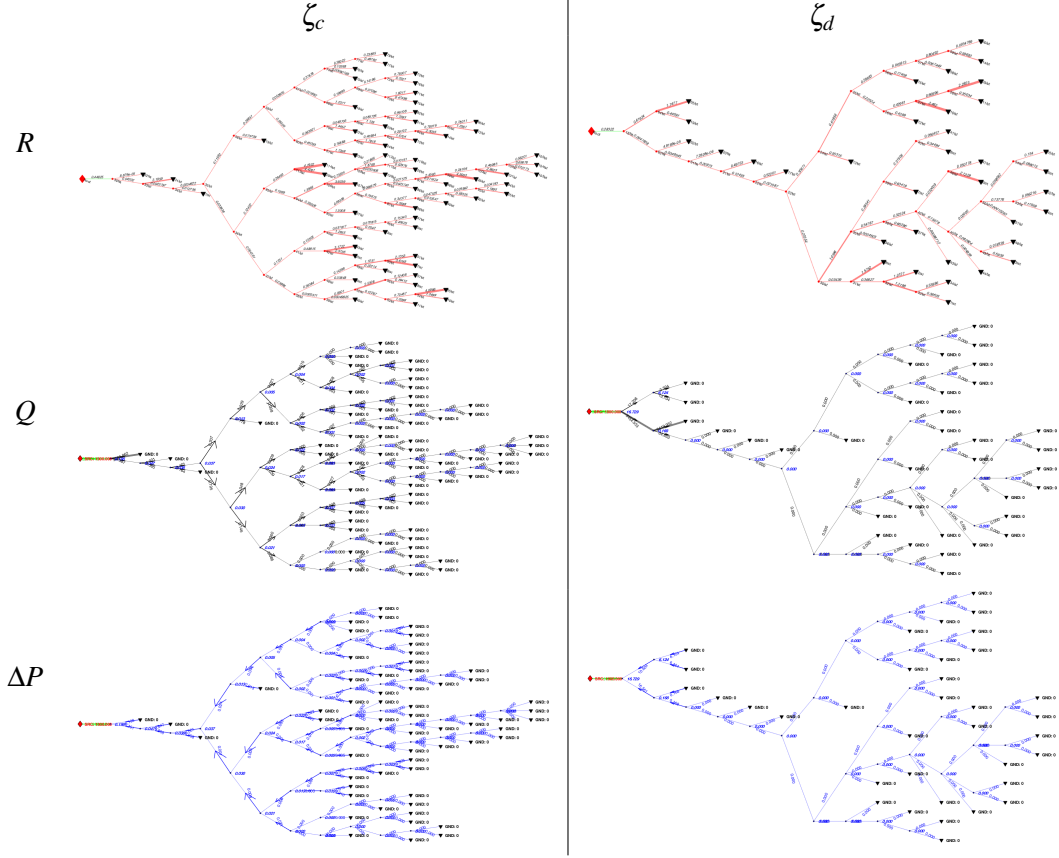


Figure 6.7: Hemodynamic analog equivalent and steady-state blood flow simulation for the deep-brain arterial trees ζ_c and ζ_d as in Fig. 6.5. Analog resistance equivalent R , simulated blood flow rate Q and blood pressure drops ΔP . Note the functionally implausible hemodynamic values for the entire sub-tree of ζ_d .

clear in Fig. 6.7 for both blood flow and pressure drops, where an entire sub-tree of the considered vasculature is not diffused. The interpretation of such realisation suggests either the occurrence of an ischaemic event, or an erroneous topological inference of the underlying hierarchical structure.

6.3.5 Neurovascular Resilience

A resilience index of the cerebrovascular network, i.e. the capability to recover and cope with pathological conditions and events, is introduced here for more general neurovascular topologies and configurations. By considering the aforementioned graph embedding comprising also possible perturbations within the same phenotypical realisation, flow (Q) and pressure (ΔP) are evaluated on an arbitrary number n of similar equivalents for comparison. The n simulated quantities are then aver-

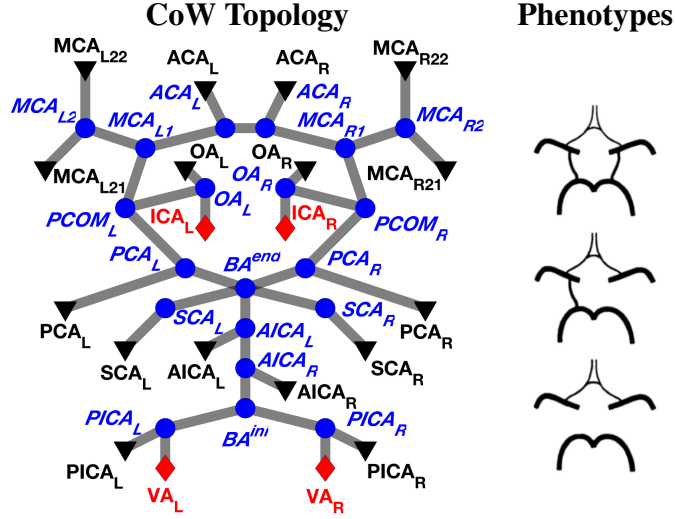


Figure 6.8: Circle of Willis: manually annotated landmarks and graph equivalent for an exact network, i.e. given the anatomical prior \mathcal{A} . Sources SRC (\diamond) and potential grounds GND (\blacktriangledown) are shown for the anatomical blood inlets and outlets.

aged for the same phenotype, for which a global network resilience metric is defined as

$$\rho_{\mathcal{G}} = \frac{1}{|\tilde{E}|} \sum_{|\tilde{E}_d|} \rho \quad \text{with} \quad \rho = \frac{(\Delta P \cdot Q)}{\pi r^2 l}, \quad (6.3)$$

where $|\tilde{E}|$ is the total number of vascular branches *after* the topological perturbation, being $|\tilde{E}_d|$ the diffused ones, i.e. those having non-zero Q and ΔP . The scalar resilience $\rho_{\mathcal{G}}$ is an integral surrogate for the branch functionality given the network perturbation. In other words, it is a scalar describing how resilient, or how affected, a branch is by a random perturbation anywhere in the neurovascular graph. Assuming healthy networks being well diffused, $\rho_{\mathcal{G}}$ is maximal for unperturbed equivalents, whereas it decreases for impairing modulations.

Datasets: Six MR time-of-flight angiographies of the Circle of Willis (CoW) are considered as experimental dataset. Each subject is classified into 3 different CoW phenotypes and manually labelled as in Fig. 6.8, and vascular graphs are extracted as in Chapter 4.

6.3.5.1 Controlled Simulations on *Exact* Topologies (CoW)

Pressure potentials are initialised at the anatomical inlets, whereas potential grounds are set at the terminal branches of the CoW (Fig. 6.8). Here, an anatomical prior

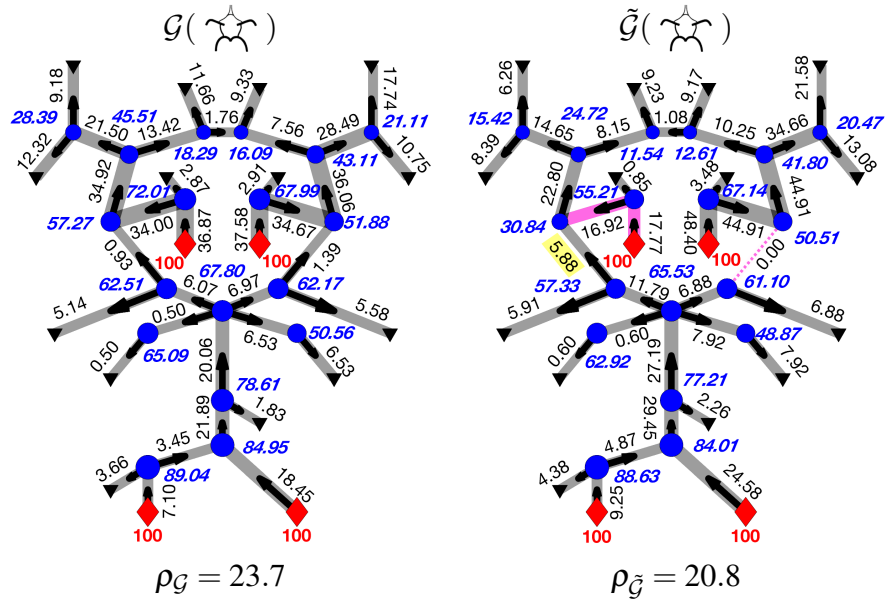


Figure 6.9: Autoregulation mechanisms: blood flow, pressure and network resilience ρ for unperturbed graphs, and for the simulated stenotic ICA and occluded PCOM - Full Cycle - Both PCOMs - Phenotype .

\mathcal{A} is given for the annotated graph. The autoregulation mechanisms are evaluated first by simulating a stenotic Internal Carotid Artery (ICA) and an occlusion of the Posterior Communicating Artery (PCOM), as a sanity test in a simple, yet realistic, scenario. In Fig. 6.9, Fig. 6.10 and Fig. 6.11, three different CoW phenotypes are shown after simulating asymptotic hemodynamic quantities in the controlled scenario. Biologically compatible autoregulation mechanisms are observed. On average, reduced flow and pressure values are found in the perturbed ipsi-lateral branch of the network, whereas minimally affected quantities are observed for the contra-lateral part. While flow is marginal in the PCOMs for the unperturbed network in Fig. 6.9, it increases (highlight) after the simulated stenosis and occlusion (purple edges), where the flow overdraft is compensated by the posterior circulation.

Similar autoregulation mechanisms are observed for the other phenotypes in Fig. 6.10 and Fig. 6.11, where major compensations are given by the anterior left-right circulatory contribution at the Anterior Communicating Artery (ACA) level. Flow readjustment were intrinsically different for different CoW phenotypes. Despite the relatively small ACA size, increased flow is observed (highlighted) contra-lateral to the simulated perturbation. As postulated, resilience indices ρ show a

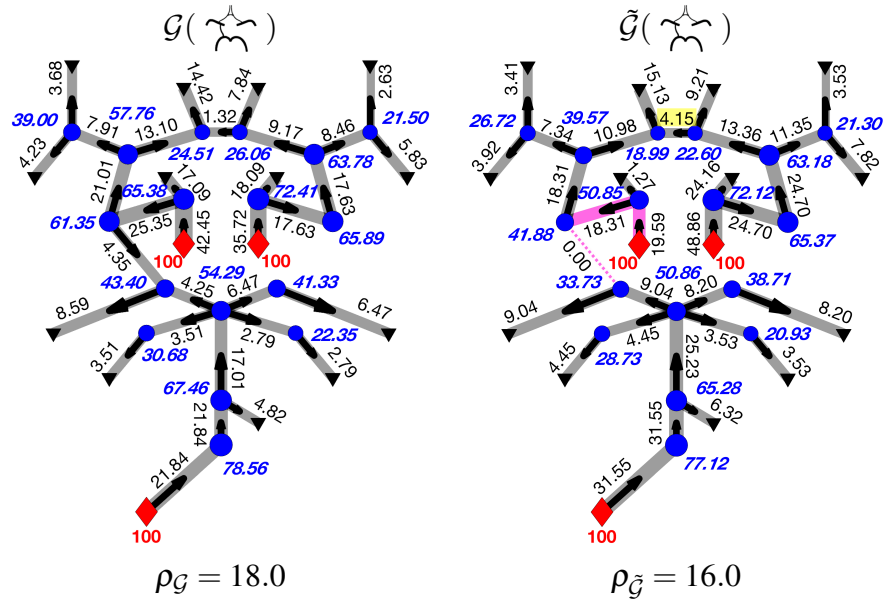


Figure 6.10: Autoregulation mechanisms: blood flow, pressure and network resilience ρ for unperturbed graphs, and for the simulated stenotic ICA and occluded PCOM - One Posterior Communicating Artery Phenotype .

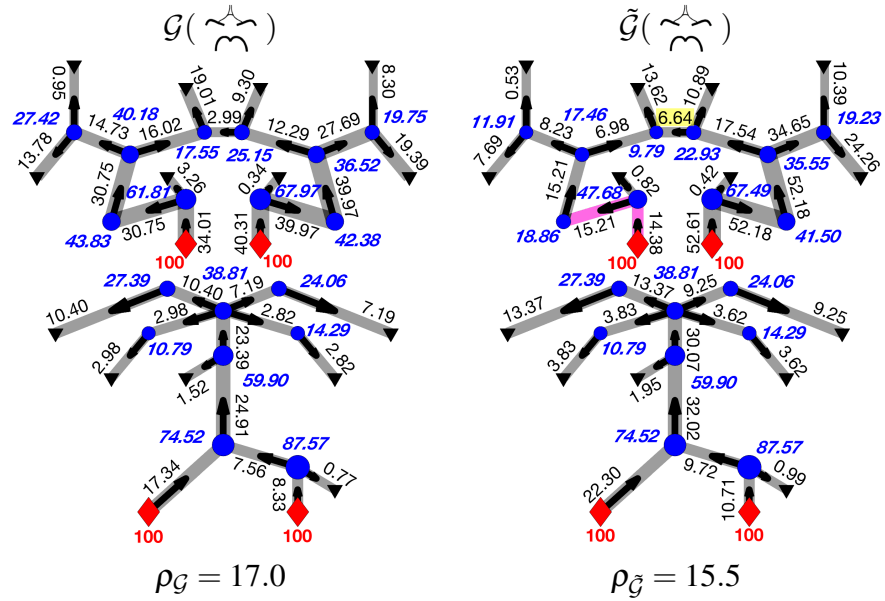


Figure 6.11: Autoregulation mechanisms: blood flow, pressure and network resilience ρ for unperturbed graphs, and for the simulated stenotic ICA and occluded PCOM - Absent Posterior Communicating Arteries Phenotype.

decreasing trend for the *same* perturbation on the different networks.

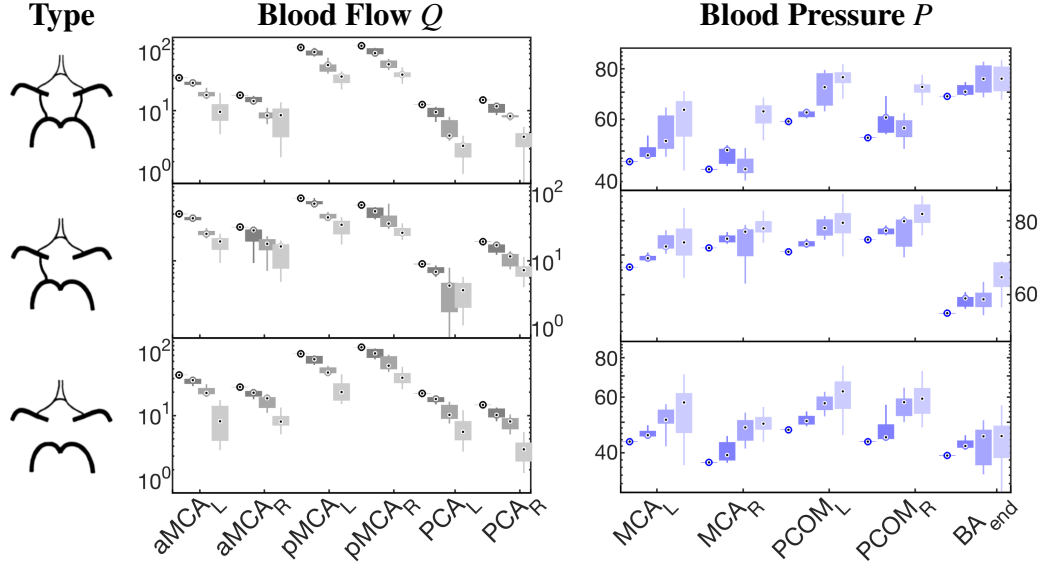


Figure 6.12: Flow and pressure distributions (boxplots) for unperturbed anatomically exact topologies and for 3 perturbation classes of increasing stenoses and tortuosity. Increasing perturbations from dark (unperturbed) to light colours.

6.3.5.2 Random Perturbations on *Exact* Topologies (CoW)

More simulations are computed by perturbing *only* the resistance-equivalents, where fluctuations in \mathcal{R} modulate both radius and length of the pipes. Perturbations account for 3 classes with maximal resistance increment $m^{\max} = 50\%$, and a total $n = 1000$ instances per class. In Fig. 6.12, flow and pressure distributions are depicted for a representative set of CoW edges and nodes. For each perturbation class (i.e $0 < m_1 < 0.2$, $0.2 < m_2 < 0.3$, and $0.3 < m_3 < 0.5$), the hemodynamic quantities are compared against the unperturbed values. On average, flow is decreased, in line with the overall increased impedance of the vascular network. Conversely, the distributed pressure increases progressively as the degree of perturbation, with relatively smaller ratio of increase at the basilar artery (BA) terminal point (BA^{end}).

As a second tier analysis, a hypertension histogram is fitted in Fig. 6.13 with a gamma distribution. Here, hypertension is defined as the pressure normalised by the mean cross-sectional area of the vessel. An unperturbed CoW shows a hypertension profile skewed towards low values; histograms shows a broader profile for increasing perturbations, with more small vessels reporting relatively high pressure. This suggests that increased hypertension tends to affect the whole CoW even for

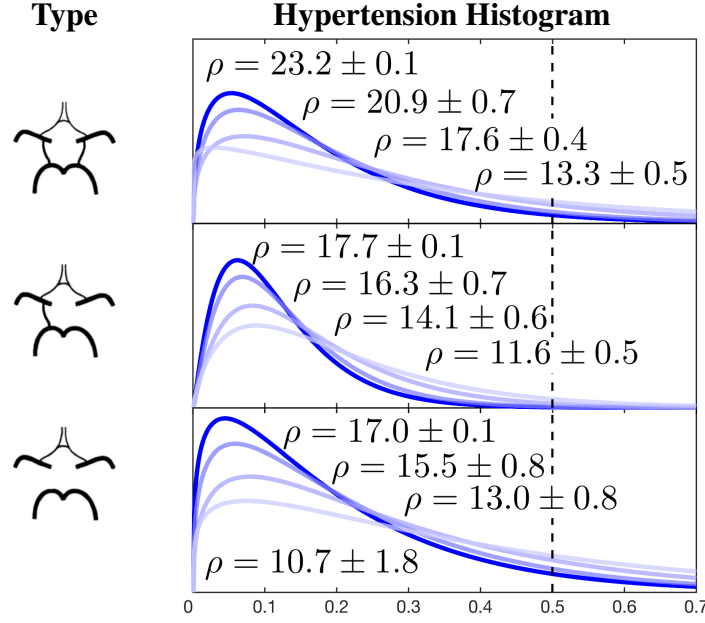


Figure 6.13: Hypertension histogram interpolated with a gamma function for unperturbed anatomically exact topologies and for 3 perturbation classes of increasing stenoses and tortuosity. Decreasing resilience indices ρ for increasing perturbations, from dark (unperturbed) to light blue (m_3).

localised stenoses (leftwards shift of the histogram), and increased risk of vascular rupture (larger area above a certain threshold, e.g. the dashed line in Fig. 6.13). A higher prevalence of zero-force is also observed in the simulated stenotic regions, suggesting higher risk of ischaemia. Resilience ρ was also found to decrease for all topologies at increasing levels of perturbation.

6.3.5.3 Perturbations on Redundant Uncertain Topologies (CoW)

So far, analyses assumed a specific realisation of a vascular graph. However, robustly extracting the vascular topology is a challenging task due to poor image resolution. As previously observed for some vascular trees, also for some erroneously extracted vascular graphs, i.e. those with the wrong connections, bio-mechanical properties exhibited abnormal values. Therefore, a viable solution to assess the plausibility of putative vascular graphs is here proposed using the *perturbed* simulation framework. Relaxing now the assumption of a known anatomical prior (i.e. vanishing \mathcal{A}), occlusive perturbations \mathcal{E} are introduced for a graph \mathcal{G} , which embeds

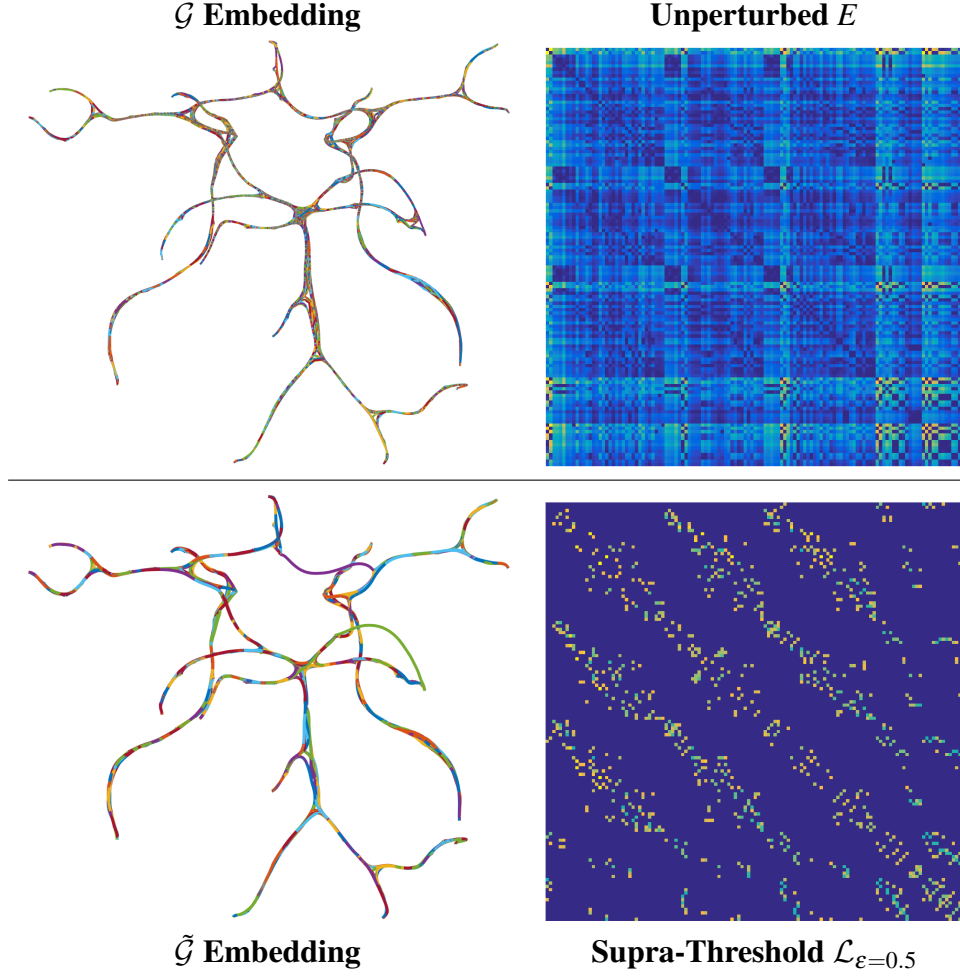


Figure 6.14: Vascular graph sampling with hemodynamically-compatible simulations: spatial and matricial embeddings of \mathcal{G} and $\tilde{\mathcal{G}}$, before and after pruning, respectively.

uncertainty among vascular junctions. Similar boundary conditions are initialised for those nodes closest to the annotated in/outlets; however, no resistance modulation is performed. Note that simulating complete occlusions on a redundant vascular network is equivalent to re-sampling the graph \mathcal{G} with subnets and evaluating their biological compatibility. Here, three classes of randomly occluded topologies $\tilde{\mathcal{G}}$ are generated for $\varepsilon = 0.2, 0.3, 0.5$, each with a total of $n = 1000$ instances. For each class, an inverse resilience adjacency matrix ρ^{inv} , of the same size as \tilde{E} , is determined as $\rho^{\text{inv}}(j_1, j_2) = \rho(j_1, j_2)^{-1}$, and an associated likelihood matrix \mathcal{L} is integrated for all simulations in each class. Specifically, $\mathcal{L} = \sum_n \rho_n \cdot \text{MST}(\rho_n^{\text{inv}})$, where MST is the minimum spanning tree maximising the resilience of each per-

turbed instance.

From these experiments putative re-sampled graphs $\tilde{\mathcal{G}}$ are obtained. These resulted in subsets of most hemodynamically-compatible branches from an initial fully-connected topology (Fig. 6.14). Major sparsity in the associated adjacency matrix is found for $\varepsilon = 0.5$ and by thresholding the likelihood \mathcal{L} above the median. Although the supra-threshold $\tilde{\mathcal{G}}$ shows a reduced redundancy in the connectivity pattern, the correct CoW phenotype is kept *intact*. Also, similar patterns are found for $\varepsilon = 0.2, 0.3$. This suggests that for a number of simulated instances that tend to infinity, and for different degrees of perturbations, a family of hemodynamically-compatible graphs statistically emerges from an uncertain and redundant graph, by jointly maximising the subnet resilience and by integrating overlapping minimal acyclic realisations.

6.3.5.4 Observations

Experimental results show the efficacy of lumped-parameters and analog equivalent models for the extraction of descriptive hemodynamic biomarkers. Blood flow and pressure drops along the vascular branches can be compactly retrieved and embedded in the vectorial vascular representations, constituting an early extension of a multi-source feature set for the vascular graphs. As shown for representative examples, the computed hemodynamic quantities provide an initial partition and distribution of functional parameters which can be scaled up to the whole cerebrovascular system. The adopted approximation cannot model vascular fluid-structure interactions, nor the effect of a pulsating flow and pressure as in fully-resolved computational fluid dynamic (CFD) simulations. However, the high-throughput (0.4 ± 0.2 ms per simulation), the arbitrary graph scalability, and the flexibility for network perturbation allow an early evaluation of the steady-state mechanisms underlying the cerebral autoregulation in a compact and reproducible way. The simulated measures of a subject-specific model, can subsequently be normalised, allowing therefore a more homogeneous group-wise analysis among a co-registered set of similar topologies. For three healthy CoW phenotypes autoregulation mechanisms and functional distributions are first evaluated with a controlled perturbation, then with

a series of random morphological modulations spanning over all the vascular network. Data-driven results on exact topologies are in line with the literature, where similar compensation strategies and distributions were observed in case-studies and on artificial physio-pathological models [45, 146, 166].

Whilst the proposed simulations can efficiently detect the occurrence of critical ischaemic events, when the topology is accurately recovered and modulations are simulated, also possible mis-connections in uncertain topologies can be detected at the same time. Specifically, a putative graph sampling is formulated for uncertain redundant topologies, where preliminary results suggest a family of compatible graphs statistically emerge from jointly maximising the subnet resilience and integrating overlapping minimal spanning trees. Notwithstanding the novelty of these preliminary results, which are the first for image-based simulations of clinically relevant neurovascular networks with perturbations, a more extensive validation is still required. Further developments will address more complete phenotypical dataset, together with a cohort of patients to longitudinally evaluate the resilience predictors associated to the clinical outcomes. Also, by relaxing the steady-state assumption, time-resolved analyses will account for coupling dynamic imaging modalities (e.g. arterial spin labelling) and pulsating hemodynamic simulations.

6.4 NURBS Parametrisation for Hemodynamics with Isogeometric Analysis

As previously observed, compact analog equivalents are not able to accurately model either the underlying vascular geometry, or fluid-solid interactions in fully-resolved hemodynamic simulations. However the increasing need for localised vascular analyses and for integrating simulations with personalised device design motivated the following contribution of this thesis. Leveraging both the connected structure of the vascular network and the segmented geometry using the formulated geodesic snakes, an automatic NURBS-based reconstruction (i.e. a parametrisation) is devised. Ideally, such a parametrisation should bridge the gap between the efficient and compact extraction of functional biomarkers and the *vectorisation*

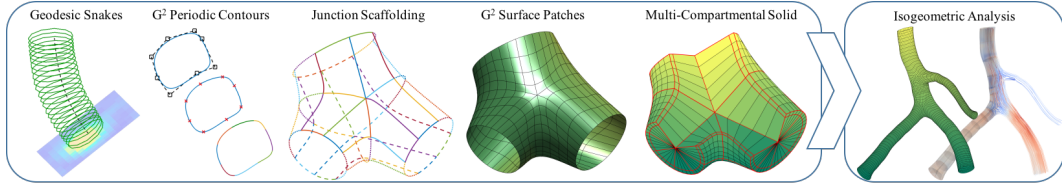


Figure 6.15: End-to-end parametrisation on vascular junctions: from geodesic snakes on clinical angiographies to hemodynamic simulations using IGA.

(along the lines of an image-tracing approach [173]) of the vascular structure from angiography, for personalised surgical repair integrating subject-specific CAD designs. Despite the advantages of NURBS to compactly model vascular geometry, and the seamless integration between NURBS geometry and IGA simulation solutions, as observed in section 6.1, currently available tools do not allow one to perform end-to-end subject-specific IGA flow simulations of vasculature.

Here, as a further contribution, a template-free parametrisation of vascular contours is introduced with a compact and regularised support using NURBS. Then a smooth geometry construction scheme optimises for a surface G^2 -continuity condition, with a focus on junctions. Lastly, an implicit partition of multi-compartmental vascular models for hemodynamic simulations is determined, being fully compatible with an IGA framework. In the diagram (Fig. 6.15) the processing workflow is shown for the proposed parametrisation.

6.4.1 Parametrisation Pipeline.

The parametrisation of the segmented vascular structure leverages first the graph-based subdivision into elongated tubular branches and topological junctions, and allows then a multi-compartmental partitioning of the vascular components. Given a wall thickness θ , both fluid-volume and vessel wall compartments are determined to further model fluid-solid interactions at the respective interface. Similarly to [214], purely tubular NURBS surfaces are determined by *lofting* ordered series of different closed NURBS contours as a whole. Such a surface reconstruction strategy accounts for shape and size variations along the tubular branches. Further insights on NURBS and the lofting operator can be found in [156] for reference and for a more detailed description. Conversely from tubular portions, surfaces at the junc-

tions cannot be directly modelled as tensor product between curvilinear NURBS primitives, and, because of the intrinsic non-linearity of the junction topology, a localised patch-based construction is required. With *patches*, a set of geometrical entities is identified, where one or more connected interfaces are mutually shared with the neighbouring ones. For simplicity, the complete parametrisation of bifurcations (i.e. junctions merging three main branches) is addressed in the following sections. These result in a piece-wise G^2 curvilinear junction scaffolding. The parametrisation of generic n-junctions can be extended by combining the following approach to multiple, partial and contiguous subdivisions of the n-junction in topological triplets. All junction (and tubular) surfaces are reconstructed (and regularised) with homogeneous adjacent Coons patches, where a surface G^2 -continuity optimisation strategy is devised at the boundaries. Lastly, the solid NURBS parametrisation is directly determined as tensor product coupling and interpolating regular pairs of multi-compartmental patch surfaces.

B-Splines and NURBS Parametric Primitives. The following parametrisation makes use of Non-Uniform Rational B-Splines (NURBS) instances, such as curvilinear segments, surface patches and solid hexahedral geometries defined on a homogeneous coordinate space. Both B-Spline and NURBS formulations are first introduced for curvilinear instances, then a generalisation is given for surface and

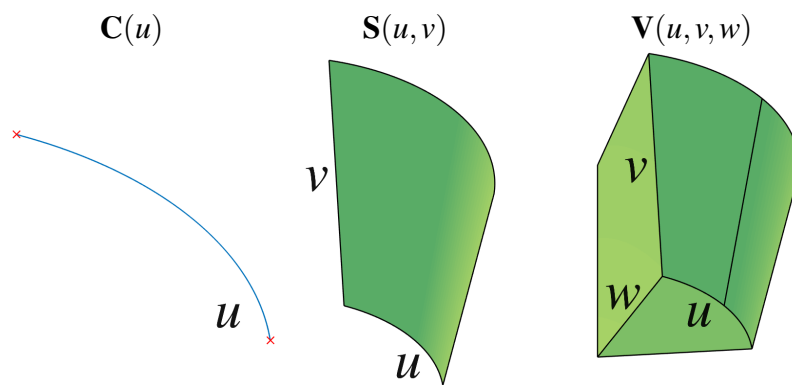


Figure 6.16: NURBS primitives adopted in the parametrisation. (Left) A curvilinear segment with form $C(u)$. (Centre) A non-planar quadrilateral surface patch of the form $S(u, v)$. (Right) A Hexahedral solid patch of the form $V(u, v, w)$. In the NURBS homogeneous space, u -, v -, and w -directions map the circumferential, the longitudinal and the radial tube directions, respectively.

solid patches. Lastly the adopted numeric parametrisation is detailed for the tubular and junction geometries.

Following concepts introduced by Piegl and Tiller in [156], an open p -th degree B-Spline curve is a piece-wise polynomial defined recursively by means of a knot-vector. A generic formulation for a curvilinear B-Spline segment $\mathbf{C}_{\text{BS}}(u)$ is given as

$$\mathbf{C}_{\text{BS}}(u) = \sum_{i=0}^m N_{i,p}(u) \mathbf{p}_i \quad 0 \leq u \leq 1, \quad (6.4)$$

where \mathbf{p}_i are the control points with 3D coordinates $[x_i, y_i, z_i]$, and $N_{i,p}(u)$ are the p -th degree B-Spline basis functions, defined on a non-periodic knot vector $\mathbf{U}^{(u)}$ of values u .

NURBS primitives are an extension of B-Splines, where each polynomial component is differently weighted with a specific weight ω_i . The main advantage of NURBS over B-Splines is that they can exactly represent conic sections such as circles and ellipses. For the same curvilinear segment in eq. 6.4, the NURBS-based formulation $\mathbf{C}(u)$ is given as

$$\mathbf{C}(u) = \frac{\sum_{i=0}^m N_{i,p}(u) \omega_i \mathbf{p}_i}{\sum_{i=0}^m N_{i,p}(u) \omega_i} \quad 0 \leq u \leq 1. \quad (6.5)$$

Alongside curvilinear NURBS primitives, also NURBS surfaces and volumes can be defined for higher dimensions. In case of a NURBS surface patch, two knot vectors $\mathbf{U}^{(u)}$ and $\mathbf{U}^{(v)}$ are considered, each of $p^{(u)}$ and $p^{(v)}$ degrees, respectively. Also a set of control points $\mathbf{p}_{i,j}$ and a set of weights $\omega_{i,j}$ determine the NURBS surface patch $\mathbf{S}(u, v)$ as

$$\mathbf{S}(u, v) = \frac{\sum_{i=0}^m \sum_{j=0}^n N_{i,j;p^{(u)},p^{(v)}}(u, v) \omega_{i,j} \mathbf{p}_{i,j}}{\sum_{i=0}^m \sum_{j=0}^n N_{i,j;p^{(u)},p^{(v)}}(u, v) \omega_{i,j}} \quad 0 \leq u \leq 1, \quad 0 \leq v \leq 1, \quad (6.6)$$

where $N_{i,j;p^{(u)},p^{(v)}}(u, v)$ is the tensor product of the 2 one-dimensional B-Spline basis functions $N_{i,p^{(u)}}(u)$ and $N_{j,p^{(v)}}(v)$. Such a formulation is similarly extended to solid NURBS patches $\mathbf{V}(u, v, w)$, considering a third knot-vector $\mathbf{U}^{(w)}$ of values w .

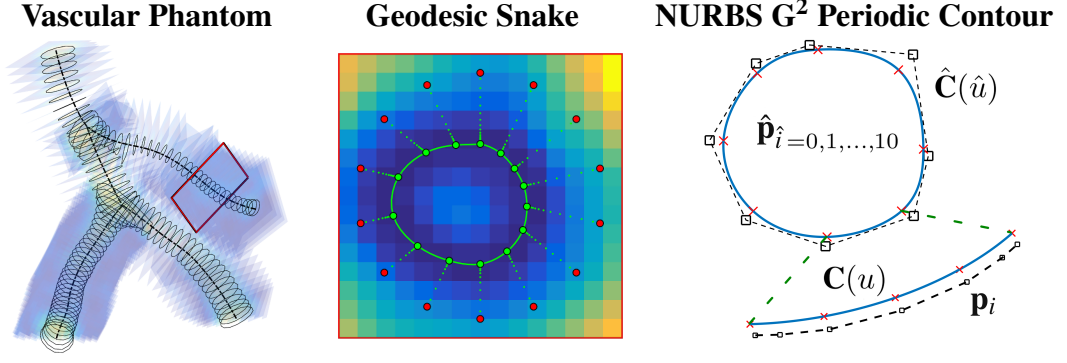


Figure 6.17: Cross-sectional segmentation of a vascular phantom. (Left-centre) Planar geodesic snake extraction as in section 6.2. (Right) Conversion of the snake into a closed parametric curve with a shape preserving fit. Eight unique control points $\hat{\mathbf{p}}_{\hat{i}=0,1,\dots,7}$ define the closed parametric contour $\hat{\mathbf{C}}(\hat{u})$. A geometrical G^2 condition enforces $\hat{\mathbf{p}}_0 = \hat{\mathbf{p}}_8$, $\hat{\mathbf{p}}_1 = \hat{\mathbf{p}}_9$, and $\hat{\mathbf{p}}_2 = \hat{\mathbf{p}}_{10}$. Eight open curvilinear segments $\mathbf{C}(u)$ are re-parametrised as separate patches, each preserving the geometrical G^2 condition. The boundary control points \mathbf{p}_0 and \mathbf{p}_7 of $\mathbf{C}(u)$ coincide in pairs with the internal $\hat{\mathbf{p}}_{\hat{i}}$ of $\hat{\mathbf{C}}(\hat{u})$ (green dashed lines).

The parametrisation of vascular structures presented in the following sections accounts for cubic B-Splines spanning the $\langle u, v, w \rangle$ domain for the respective NURBS curves $\mathbf{C}(u)$, quadrilateral surfaces $\mathbf{S}(u, v)$ and hexahedral solid volumes $\mathbf{V}(u, v, w)$, as shown in Fig. 6.16. In all these primitives, the homogeneous-coordinate space u maps the circumferential vessel direction; v maps the longitudinal vessel direction, and w maps the radial vessel direction. Otherwise stated, all patch-based entities are homogenised with a compact numeric parametrisation reported in table 6.2 in all u -, v - and w -directions.

Spline Degree	Control Points	Weights
$p = 3$	$i = 0, 1, \dots, 7$	$\omega_i = 1$
Euclidean Control Point	Knot Vector	
$\mathbf{p}_i = [x_i, y_i, z_i]$	$\mathbf{U}^{(u)} = \{0 \ 0 \ 0 \ 0 \ \frac{1}{4} \ \frac{1}{2} \ \frac{3}{4} \ 1 \ 1 \ 1 \ 1\}$	

Table 6.2: NURBS parametrisation for a curvilinear primitive $\mathbf{C}(u)$ along the circumferential direction u . Note that for curvilinear primitives along different directions, the longitudinal v or the radial w are considered, instead of u .

6.4.2 G^2 Periodic Closed Contours

Each cross-sectional geodesic snake is converted into a periodic closed curve $\hat{\mathbf{C}}(\hat{u})$ with a least-squares fitting procedure similar to [108]. By construction choice, eight unique control points are enforced for the parametrisation of each closed contour. Since a geometrical G^{p-1} curvilinear continuity paradigm enforces p control points to wrap around at the end of the polygonal set, a wrapping set of control points $\hat{\mathbf{p}}_{\hat{i}=0,1,\dots,10}$ are determined so that $\hat{\mathbf{p}}_0 = \hat{\mathbf{p}}_8$, $\hat{\mathbf{p}}_1 = \hat{\mathbf{p}}_9$, and $\hat{\mathbf{p}}_2 = \hat{\mathbf{p}}_{10}$. The control points $\hat{\mathbf{p}}_{\hat{i}}$ span an unclamped uniform knot vector $\hat{\mathbf{U}}^{(\hat{u})}$ defined by uniformly sampling the domain $\hat{u} = [0 - \frac{p}{8}, 1 + \frac{p}{8}]$ with $\hat{i} + p + 2$ knots. The determined G^2 -continuous closed curve $\hat{\mathbf{C}}(\hat{u})$ is shown in Fig. 6.17.

Since the parametrisation of bifurcating connecting junctions requires a set of adjacent patches, the periodic closed curve $\hat{\mathbf{C}}(\hat{u})$ is subdivided into eight regular curvilinear segments. This is obtained by first *clamping* the periodic closed curve and subsequently splitting it following a knot-insertion procedure [156], until reaching the maximum multiplicity per inserted knot. The resulting curvilinear segment has the form of $\mathbf{C}(u)$ as in table 6.2. The knot vector of each curvilinear segment is re-parametrised on the homogeneous domain $u = [0, 1]$. Note that each resulting curvilinear segment preserves the G^2 -continuity with the adjacent neighbouring ones. Although the parametrisation of the curvilinear segment $\mathbf{C}(u)$ shows a different set and number of *internal* control points \mathbf{p}_i , its first control point \mathbf{p}_0 and its last control point \mathbf{p}_6 correspond in contiguous pairs to the internal control points of the closed curve $\hat{\mathbf{C}}(\hat{u})$.

6.4.3 Junction Control Octagons and Scaffolding

In the following section, a geometrical parametrisation of a generic bifurcating junction is determined by means of spatial projections of control points coordinates. In each bifurcation, three proximal junction contours $(\Sigma^{(b)})_{b=1,2,3}$ having the form of $\hat{\mathbf{C}}$ are considered for the construction of the patch-based control octagons. These are depicted at the spatial extremity of the topological junction in Fig. 6.18 with dashed blue lines, and their vertices are represented by small squares. A projective approach similar to [213, 214] defines a set of directional vectors from the *non-*

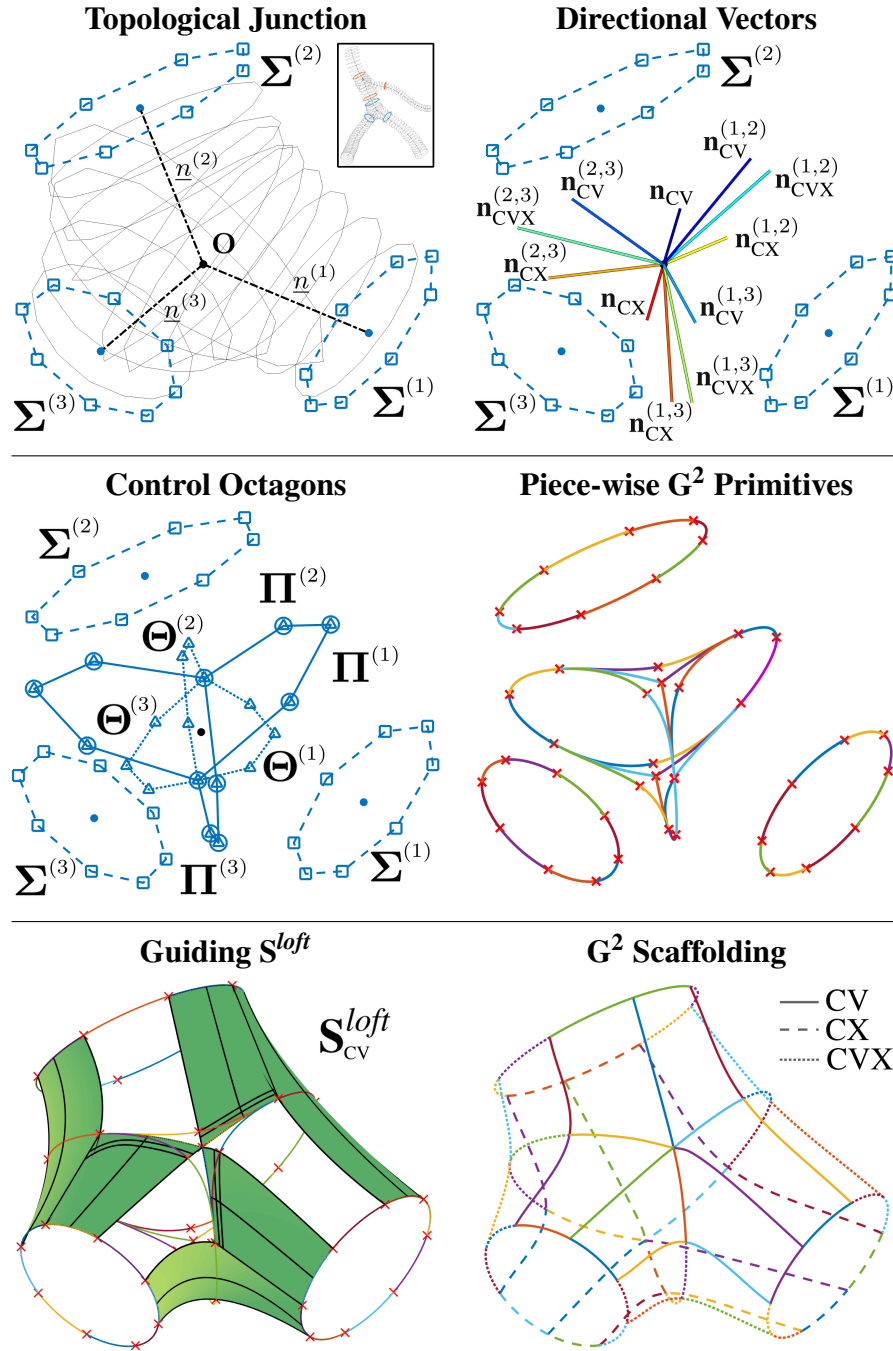


Figure 6.18: Junction parametrisation: (top) proximal octagons $\Sigma^{(b)}$ (dashed blue lines, square vertices) and mutually-intersecting contours; set of directional vectors (6.7) for CV, CX and CVX quadrants; (middle) construction of control octagons: non-planar projective $\Pi^{(b)}$ (solid blue lines, circle vertices), and planar capping $\Theta^{(b)}$ (dotted blue lines, triangular vertices); piece-wise G^2 NURBS curves of the control octagons along u ; (bottom) orderly lofting the curvilinear pieces along v on the CV quadrant for the guiding surfaces \mathbf{S}_{cv}^{loft} ; G^2 construction scaffolding, resulting in closed sets of quadrilateral acrs.

intersecting triplet proximal junction contours as

$$\begin{aligned}
 \mathbf{n}_{CV} &= \frac{1}{3} \sum_{b=1}^3 \mathbf{n}_{\perp}^{(b)}, & \mathbf{n}_{CVX}^{(1,2)} &= \frac{1}{2}(\mathbf{n}^{(1)} + \mathbf{n}^{(2)}), \\
 \mathbf{n}_{CX} &= -\mathbf{n}_{CV}, & \mathbf{n}_{CVX}^{(2,3)} &= \frac{1}{2}(\mathbf{n}^{(2)} + \mathbf{n}^{(3)}), \\
 & & \mathbf{n}_{CVX}^{(1,3)} &= \frac{1}{2}(\mathbf{n}^{(1)} + \mathbf{n}^{(3)}), \\
 \mathbf{n}_{CV}^{(1,2)} &= \frac{1}{2}(\mathbf{n}_{CVX}^{(1,2)} + \mathbf{n}_{CV}), & \mathbf{n}_{CX}^{(1,2)} &= \frac{1}{2}(\mathbf{n}_{CVX}^{(1,2)} + \mathbf{n}_{CX}), \\
 \mathbf{n}_{CV}^{(2,3)} &= \frac{1}{2}(\mathbf{n}_{CVX}^{(2,3)} + \mathbf{n}_{CV}), & \mathbf{n}_{CX}^{(2,3)} &= \frac{1}{2}(\mathbf{n}_{CVX}^{(2,3)} + \mathbf{n}_{CX}), \\
 \mathbf{n}_{CV}^{(1,3)} &= \frac{1}{2}(\mathbf{n}_{CVX}^{(1,3)} + \mathbf{n}_{CV}), & \mathbf{n}_{CX}^{(1,3)} &= \frac{1}{2}(\mathbf{n}_{CVX}^{(1,3)} + \mathbf{n}_{CX}),
 \end{aligned} \tag{6.7}$$

with $\mathbf{n}^{(b)}$ being the vector joining the junction centre of mass \mathbf{O} and the geometrical centroid of $\Sigma^{(b)}$ for each branch b . The perpendicular vector $\mathbf{n}_{\perp}^{(b)}$ is obtained as a pairwise cross-product, i.e. $\mathbf{n}_{\perp}^{(1)} = (\mathbf{n}^{(1)} \times \mathbf{n}^{(2)})$, $\mathbf{n}_{\perp}^{(2)} = (\mathbf{n}^{(2)} \times \mathbf{n}^{(3)})$, and $\mathbf{n}_{\perp}^{(3)} = (\mathbf{n}^{(3)} \times \mathbf{n}^{(1)})$. The above vectors, as depicted in Fig. 6.18, determine the directions of three projective non-planar construction octagons $\Pi^{(b)}$ at the junction origin \mathbf{O} . The same directional vectors spatially subdivide the bifurcation geometry in quadrants, i.e. concave (CV), convex (CX) and the respective interleaving sides (CVX).

For each branch b , the control points directions of the non-planar octagonal projections $\Pi^{(b)}$ are derived as pair-wise combination of the directional vectors

$$\begin{aligned}
 \Pi^{(1)} &= [\mathbf{n}_{CV}; \mathbf{n}_{CV}^{(1,2)}; \mathbf{n}_{CVX}^{(1,2)}; \mathbf{n}_{CX}^{(1,2)}; \mathbf{n}_{CX}; \mathbf{n}_{CX}^{(1,3)}; \mathbf{n}_{CVX}^{(1,3)}; \mathbf{n}_{CV}^{(1,3)}], \\
 \Pi^{(2)} &= [\mathbf{n}_{CV}; \mathbf{n}_{CV}^{(2,3)}; \mathbf{n}_{CVX}^{(2,3)}; \mathbf{n}_{CX}^{(2,3)}; \mathbf{n}_{CX}; \mathbf{n}_{CX}^{(1,2)}; \mathbf{n}_{CVX}^{(1,2)}; \mathbf{n}_{CV}^{(1,2)}], \\
 \Pi^{(3)} &= [\mathbf{n}_{CV}; \mathbf{n}_{CV}^{(1,3)}; \mathbf{n}_{CVX}^{(1,3)}; \mathbf{n}_{CX}^{(1,3)}; \mathbf{n}_{CX}; \mathbf{n}_{CX}^{(2,3)}; \mathbf{n}_{CVX}^{(2,3)}; \mathbf{n}_{CV}^{(2,3)}].
 \end{aligned} \tag{6.8}$$

The final control points coordinates of the non-planar projective octagons $\Pi^{(b)}$ are determined with a least-square fit. In particular, the coordinates of $\Pi^{(b)}$ are adjusted along the respective directions, by considering the spatial points cloud of the mutually-*intersecting* proximal contours at the junction (i.e. the grey intersecting rings in Fig. 6.18 enclosing the topological junction). In Fig. 6.18 the non-planar projective octagons $\Pi^{(b)}$ are depicted with solid blue lines and with small circles in

the correspondence of the vertices.

Together with the non-planar projective octagons $\Pi^{(b)}$, an extra set of three *planar* capping control octagons $\Theta^{(b)}$ are specifically defined for closing the concave and convex quadrants. The extra capping control octagons $\Theta^{(b)}$ are almost completely overlapped with the non-planar projective control octagons $\Pi^{(b)}$, since their control points are defined as pairwise geometrical average of neighbouring projective octagons $\Pi^{(b)}$. In Fig. 6.18, the planar capping octagons $\Theta^{(b)}$ are depicted with blue dotted lines and with small triangles in the correspondence of the vertices.

Each control octagon determines a piece-wise G^2 set of curvilinear segments as one-dimensional NURBS primitives. These primitives have the form of $\mathbf{C}(u)$ as in section 6.4.2, and are depicted with coloured lines in Fig. 6.18, delimited by red crosses. It can be observed that the planar and proximal control octagons $\Sigma^{(b)}$ produced planar G^2 closed contours. Similarly, non-planar projective octagons $\Pi^{(b)}$ produced non-planar G^2 closed contours. Conversely, portions of the planar closed contours for the capping control octagons $\Theta^{(b)}$ are depicted in Fig. 6.18. In particular, only three incident curvilinear primitives are shown for both the convex and the concave quadrants. These are the only unique curvilinear segments necessary to close the scaffolding of the bifurcating junction, since the remaining curvilinear portions of $\Theta^{(b)}$ coincide with those of the non-planar projective octagons $\Pi^{(b)}$. Note that all the piece-wise G^2 set of curvilinear segments are defined on the circumferential direction u of the tubular structures.

In order to determine a geometrical scaffolding enclosing the bifurcation with a set of quadrilateral non-planar and curvilinear polygons spanning both u and v , further connecting primitives must be defined along the longitudinal direction of the tubular structures. This is obtained with a series of guiding surface patches \mathbf{S}^{loft} . The guiding surface patches are determined by piece-wise lofting ordered sequence of curvilinear circumferential segments belonging to the set of the control octagons $\{\Sigma^{(b)}, \Pi^{(b)}, \Theta^{(b)}\}$ along the longitudinal direction v . The guiding surface patches \mathbf{S}^{loft} are first computed for all quadrants, then the boundary of the guiding surface

patches are extracted. These determine an initial set of contiguous curvilinear primitives on v , which mutually show G^0 -continuity at the terminal endpoints.

The obtained set of curvilinear primitives along u - and v -directions encloses the junction in a construction scaffolding, where a further curvilinear G^2 -continuous condition is enforced at the contiguous primitive boundaries along v . In particular, the respective tangential direction, as well as the one associated to the second derivative of the contiguous curvilinear primitives are imposed to be mutually equal. This is obtained with an iterative adjustment of the boundary control points coordinates until convergence. Note that along u , the curvilinear primitives of the construction scaffolding already satisfy the geometrical G^2 -continuity condition.

The resulting piece-wise G^2 -continuous construction scaffolding is then processed in adjacent quadrilateral non-planar curvilinear polygons (i.e. patches), these composed of four arcs of curves. Coons patches are determined for each quadrilateral polygon of the scaffolding at the junction, by bi-linearly blending the ruled surfaces [156] obtained from pairs of arcs.

As a side note, the same G^2 -continuous construction scaffolding is determined for the tubular portions. In a similar fashion, the complete tubular surface is first recovered with a lofting operation on an ordered sequence of circumferential octagonal snakes. Then, the complete tubular lofted surface is subdivided into eight piece-wise stripes running along the longitudinal direction of the tube, reproducing the octagonal subdivision patterns of the junctions. All resulting tubular surface patches (i.e. stripes) are regularised into adjacent homogeneous Coons patches.

6.4.4 Surface Coons Patches and G^2 Control Net

On a single-element scale, bi-linearly blended surface Coons patches exactly meet the four boundary arcs. However, multiple adjacent Coons patches sharing subsets of boundary curves do not necessarily show the same surface tangent planes at the interfaces. This may produce creases and curvature discontinuities in the joined surface along those boundary curves, resulting thus in an overall G^0 set of neighbouring surfaces. Given the proposed spatial subdivision, creases at the surface patch boundaries are particularly likely at junctions. This may be reflected on

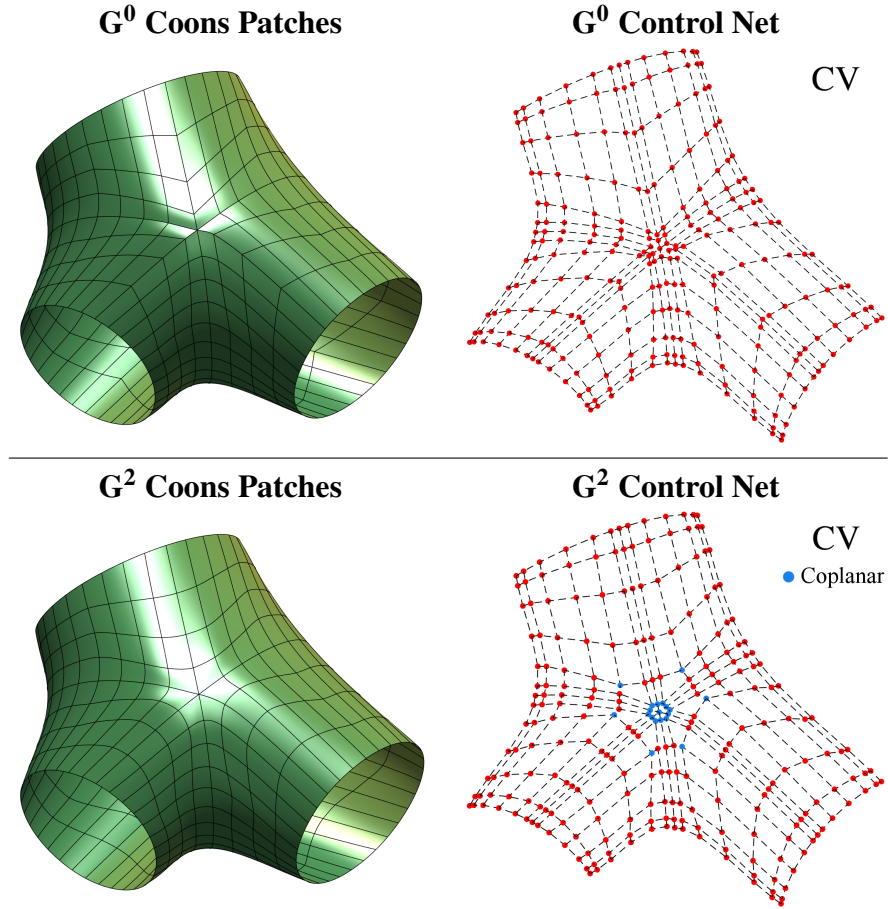


Figure 6.19: Patch-based junction surface: (top) G^0 -continuous set of Coons patches from the scaffolding; Hexagonal pattern of the CV quadrant and associated control net. Creases are observed at the boundaries/interfaces among the neighbouring patches; (bottom) optimised G^2 -continuous set of Coons patches with algorithm 2; resulting control net in the CV quadrant and coplanar neighbourhood of the control point corner in blue.

hexagonal patterns of adjacent patches, which are determined in correspondence of the CV or CX quadrants (Fig. 6.19). In particular, each patch pair-wise shares two boundary arcs on both u - and v -direction with two other adjacent patches towards the innermost part of the quadrant. Conversely, quadrilateral patterns of adjacent patches are obtained in correspondence of the CVX side quadrants, where, also in this case, pair-wise adjacency schemes are found in both u - and v -directions for all the considered patches.

To mitigate the effect of geometrical creases and discontinuities at the junctions, a pair-wise surface patch regularisation scheme is devised to enforce surface

smoothness. In particular, following [89], the geometrical G^2 -continuous condition for a single pair $(\mathbf{S}_1, \mathbf{S}_2)$ of adjacent Coons patches sharing a common arc along either u - or v -direction can be here formulated as

$$u\text{-direction} \left\{ \begin{array}{l} m_1 = m_2, \\ \mathbf{p}_{i,n_1}^{(1)} = \mathbf{p}_{i,0}^{(2)}, \\ \frac{\mathbf{p}_{i,n_1}^{(1)} - \mathbf{p}_{i,n_1-1}^{(1)}}{n_2} = f \frac{\mathbf{p}_{i,1}^{(2)} - \mathbf{p}_{i,0}^{(2)}}{n_1}, \\ (n_1^2 - n_1)(\mathbf{p}_{i,n_1}^{(1)} - \mathbf{p}_{i,n_1-1}^{(1)}) + (n_1 - n_1^2)(\mathbf{p}_{i,n_1-1}^{(1)} - \mathbf{p}_{i,n_1-2}^{(1)}) = \\ = f^2[(n_2^2 - n_2)(\mathbf{p}_{i,0}^{(2)} - \mathbf{p}_{i,1}^{(2)}) + (n_2 - n_2^2)(\mathbf{p}_{i,1}^{(2)} - \mathbf{p}_{i,2}^{(2)})], \\ \forall i = 0, 1, \dots, m_1; \end{array} \right. \quad (6.9)$$

$$v\text{-direction} \left\{ \begin{array}{l} n_1 = n_2, \\ \mathbf{p}_{m_1,j}^{(1)} = \mathbf{p}_{0,j}^{(2)}, \\ \frac{\mathbf{p}_{m_1,j}^{(1)} - \mathbf{p}_{m_1-1,j}^{(1)}}{m_2} = f \frac{\mathbf{p}_{1,j}^{(2)} - \mathbf{p}_{0,j}^{(2)}}{m_1}, \\ (m_1^2 - m_1)(\mathbf{p}_{m_1,j}^{(1)} - \mathbf{p}_{m_1-1,j}^{(1)}) + (m_1 - m_1^2)(\mathbf{p}_{m_1-1,j}^{(1)} - \mathbf{p}_{m_1-2,j}^{(1)}) = \\ = f^2[(m_2^2 - m_2)(\mathbf{p}_{0,j}^{(2)} - \mathbf{p}_{1,j}^{(2)}) + (m_2 - m_2^2)(\mathbf{p}_{1,j}^{(2)} - \mathbf{p}_{2,j}^{(2)})], \\ \forall j = 0, 1, \dots, n_1 \end{array} \right. \quad (6.10)$$

where, $\{m_1, n_1\}$ and $\{m_2, n_2\}$ are the control points cardinalities along u - and v -directions, respectively for $\mathbf{S}_1(u, v)$ and $\mathbf{S}_2(u, v)$, and f is an arbitrary real positive scalar. Applying the G^2 -continuous conditions on the single pair of surface patches consists in adjusting the coordinates of neighbouring control points in the correspondence of the interface of the pair $(\mathbf{S}_1, \mathbf{S}_2)$ along either the circumferential direction (with eq. 6.9) or along the longitudinal direction (with eq. 6.10). Note that, given the homogeneous parametrisation of the patch-based curvilinear primitives in table 6.2, all control points cardinalities already coincide. The conditions require the pair of patches $(\mathbf{S}_1, \mathbf{S}_2)$ are adjacent (i.e. G^0), have the same tangent (i.e. G^1) and all second derivative directions are equal (i.e. G^2).

As defined, such geometrical G^2 -continuous conditions applies solely to adjacent surface patches considered in pairs. Also, the control points either on the u -direction or on the v -direction can be adjusted one at the time. In the particular case of hexagonal sets of adjacent patches, as found in the correspondence of both the

concave and convex quadrants of a junction, the geometrical G^2 -continuous conditions have to be jointly applied for all neighbouring pairs of surface patches along both u - and v -directions. This is obtained with an ad-hoc symmetric regularisation paradigm reported in algorithm 2, where each surface patch is iteratively regularised by adjusting the boundary control points coordinates by considering all combinations of neighbouring pairs.

For a total set of k surface patches $\{\mathbf{S}_k\}$, the comprehensive set all possible surface pairs are determined as $\{(\mathbf{S}_1, \mathbf{S}_2), (\mathbf{S}_1, \mathbf{S}_3), \dots, (\mathbf{S}_{k-1}, \mathbf{S}_k)\}$. Note that the order of the surface pairs is not relevant, therefore $(\mathbf{S}_1, \mathbf{S}_2) = (\mathbf{S}_2, \mathbf{S}_1)$. This results in a total set of $\frac{k \cdot (k-1)}{2}$ different surface patches pairs. After determining all the neighbouring pairs, a symmetric regularisation paradigm is iteratively optimised onto the whole set of surface patches until convergence (Fig. 6.19), as described in algorithm 2. Temporary sets of unilaterally adjusted instances $\{\mathbf{S}_k^{(u)}\}$ and $\{\mathbf{S}_k^{(v)}\}$ along the u - and v -directions are initialised as void. Then, for each existing adjacent pair, new instances of *aligned* surface patches, i.e. $\mathbf{S}_{k-1}^{(\bullet)*}$ and $\mathbf{S}_k^{(\bullet)*}$ for the generic pair $(\mathbf{S}_{k-1}, \mathbf{S}_k)$, are determined by adjusting the boundary control points of the considered pair, along either the circumferential or longitudinal directions using eq. 6.9 or eq. 6.10, respectively. Each determined instance is then concatenated in the temporary set associated to the specific k -th patch. As all adjacent pairs have been separately adjusted in multiple independent instances, a regularised surface patch $\bar{\mathbf{S}}_k$ is obtained by geometrically averaging corresponding control points coordinates within the joint set of unilaterally adjusted instances $\left\{ \{\mathbf{S}_k^{(u)}\}, \{\mathbf{S}_k^{(v)}\} \right\}$. Lastly, the k -th surface patch is updated by replacing it with the regularised one. This is iterated until convergence, i.e. up to a small tolerance factor evaluated on the finite difference between surface normals of the regularised pairs of adjacent patches at the interface.

The iterative regularisation paradigm as in algorithm 2 implements in practice a geometrical relaxation of control points coordinates as a trade-off between *competing* geometrical G^2 -continuous conditions over the considered surface patch \mathbf{S}_k and the neighbouring ones. In this case, symmetrical consistency is obtained for

the k -th patch by equally and geometrically averaging the associated control points, i.e. the patch control net in Fig. 6.19, in all the respective unilaterally adjusted instances.

Lastly, a planar condition is enforced in the neighbourhood of the shared corner for both the concave and convex quadrants, where a subset of boundary control points (blue points in Fig. 6.19) of the junction hexagonal patterns are projected onto the locally regressed interpolating plane.

```

1 Input: set of pairs  $\{(\mathbf{S}_1, \mathbf{S}_2), (\mathbf{S}_1, \mathbf{S}_3), \dots, (\mathbf{S}_{k-1}, \mathbf{S}_k)\}$ , from  $k$  patches  $\{\mathbf{S}_k\}$ 
2 Output: set of patches  $\{\mathbf{S}_k\}$ 
3 Initialisation:  $\{\mathbf{S}_k^{(v)}\} = \{\}$ ,  $\{\mathbf{S}_k^{(u)}\} = \{\}$ ,  $\forall k$ .
4 while not converged do
5   for all pairs do
6     if  $(\mathbf{S}_{k-1}, \mathbf{S}_k)$  adjacent on  $u$  then
7        $[\mathbf{S}_{k-1}^{(v)*}, \mathbf{S}_k^{(v)*}] = \text{adjust } \mathbf{p}(\mathbf{S}_{k-1}, \mathbf{S}_k);$  ▷  $v$ -dir (eq. 6.10)
8        $\{\mathbf{S}_{k-1}^{(v)}\} \leftarrow \mathbf{S}_{k-1}^{(v)*};$ 
9        $\{\mathbf{S}_k^{(v)}\} \leftarrow \mathbf{S}_k^{(v)*};$  ▷ concatenate
10    end
11    if  $(\mathbf{S}_{k-1}, \mathbf{S}_k)$  adjacent on  $v$  then
12       $[\mathbf{S}_{k-1}^{(u)*}, \mathbf{S}_k^{(u)*}] = \text{adjust } \mathbf{p}(\mathbf{S}_{k-1}, \mathbf{S}_k);$  ▷  $u$ -dir (eq. 6.9)
13       $\{\mathbf{S}_{k-1}^{(u)}\} \leftarrow \mathbf{S}_{k-1}^{(u)*};$ 
14       $\{\mathbf{S}_k^{(u)}\} \leftarrow \mathbf{S}_k^{(u)*}$  ▷ concatenate
15    end
16  end
17  for all  $k$  adjusted patches do
18     $\bar{\mathbf{S}}_k = \text{average } \mathbf{p}(\{\{\mathbf{S}_k^{(u)}\}, \{\mathbf{S}_k^{(v)}\}\});$  ▷ mean  $\mathbf{p}^{(k)}$ 
19     $\mathbf{S}_k = \bar{\mathbf{S}}_k;$  ▷ update patch
20  end
21 end

```

Algorithm 2: Symmetric regularisation paradigm jointly optimising a G^2 -continuity condition along both u - and v -directions for a set of neighbouring surface patches $\{\mathbf{S}_k\}$.

6.4.5 Multi-compartmental Solid Patches

Patch-based solids are determined as volume tensor product between curvilinear primitives delimiting pairs of surface patches along a radial direction w . In detail, the blood-fluid volume $\mathbf{V}_{\text{bf}}(u, v, w)$, representing the innermost region of the vessel,

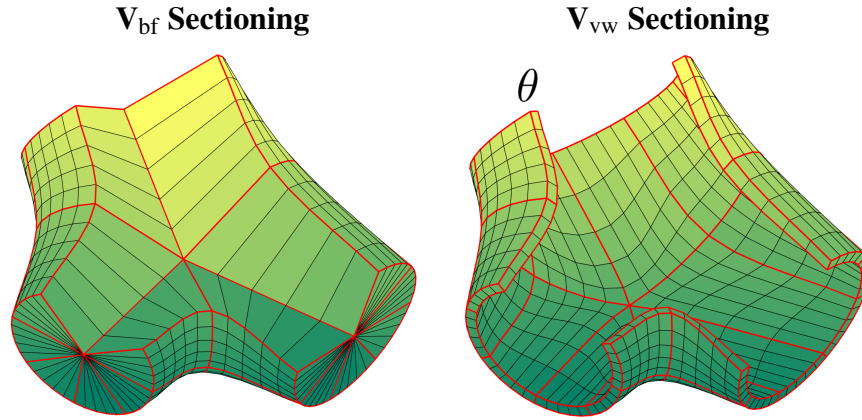


Figure 6.20: Multi-compartmental partition of the junction: patch-based inner blood-fluid (V_{bf}) and outer vessel wall (V_{vw}), given a constant wall thickness θ . Individual patches are delineated in red; sectioning view by resecting the CV quadrant.

is determined with a collapsed solid annulus, where the innermost set of degenerate surface patches coincide with the topological centerline of the junction (or tubular) portion. Similarly, the outer vessel wall volume $V_{vw}(u, v, w)$ is determined with the same annulus parametrisation, where a wall thickness θ separates the coupling between the inner- and outer-most surface patches along the radial direction w . For simplicity, a constant vessel wall thickness θ is considered to model subject-specific physiological cases. Note that a data-driven estimation can be performed following [10], or arbitrarily defined to account for parametric geometrical perturbations of the vessel wall induced by pathology, simulating thus the effects of stenoses and saccular or fusiform aneurysms. The obtained patch-based solids are by construction regularised with the parametrisation in table 6.2 and both V_{bf} and V_{vw} are fully complementary, as they share the innermost surface as mutual boundary interface.

6.4.6 Parametrisation Validation

Datasets Synthetic junctions with different geometries are randomly generated for evaluating the parametrisation in the presence of local perturbations on the construction octagons, validating the G^2 continuity of the proposed model. Also, representative cases from [6], together with a cerebral vascular phantom, are considered to evaluate the geometrical bifurcation parametrisation on real angiographic data.

Lastly, cerebrovascular structures are fully parametrised for representative fluid dynamic simulations using an IGA framework.

6.4.6.1 Synthetic Bifurcations

A balanced set of 450 synthetic junctions are generated accounting for different levels of perturbations (Fig. 6.21), resembling the physio-pathological variability. Isometric, yet asymmetric, bifurcations (\mathbf{J}_{\angle}) are determined with unitary and regular control octagons and different incidental branch-directions. Junctions with different branch directions, elongation and cross-sectional size (\mathbf{J}_{Σ}) are obtained by randomly perturbing the proximal junction contours. Similarly, junctions with perturbations also at the respective projective construction octagons (\mathbf{J}_{Π}) are considered for the parametrisation evaluation. In table 6.3 the geometrical consistency of the reconstructed surface patches is evaluated as the root mean square error (ϵ) of the numeric Jacobian and Hessian values, computed at the patch interfaces. Average Jacobian ϵ values are limited to a maximal numeric value of approximately 1×10^{-2} in both u – and v –directions, for all the considered perturbations. Deviations of the Hessian ϵ values are observed for increasing perturbation on the geometries, where maximal errors are found for the symmetric uv – and vu –components. Both Jacobian and Hessian directional components vanish at the junction boundaries of a CV/CX quadrant, as the geometry approaches the planar region in the neighbourhood of the shared corner.

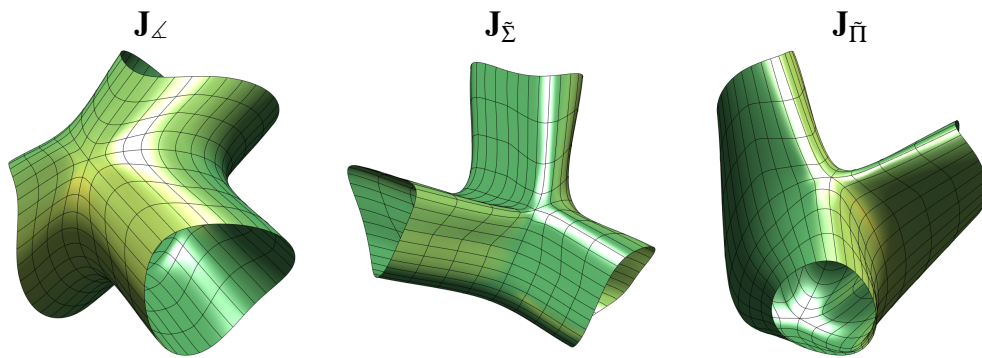


Figure 6.21: Representative set of synthetic junctions for the evaluation of the patch-based parametrisation and surface continuity. \mathbf{J}_{Σ} and \mathbf{J}_{Π} model strong variations induced by pathology with irregular cross-sections and swollen junctions for stenoses and aneurysms, respectively.

6.4.6.2 Clinical Angiographic Modelling and Simulations

The parametrisation paradigm is applied to real angiographic data, where all vascular bifurcations, as well as all tubular portions, are automatically determined from the geodesic snakes segmentation. Fig. 6.22 and Fig. 6.23 shows representative examples of a phantom and a cerebrovascular structure from [6]. The proposed parametrisation accurately captures the underlying anatomy, concurrently optimising the surface G^2 -continuity condition in all patches. A multi-compartmental partition of the structures is implicitly determined, imposing an arbitrary vessel wall thickness θ , accounting for the complementary inner blood-fluid volume and the outer vessel wall one.

The reconstructed subject-specific models are then considered for a representative hemodynamic simulation within an IGA framework, where a multi-patch Stokes' problem is configured on blood-fluid volume domain. In detail, the parametrisation of the phantom resulted in a total of 216 solid patches for the inner blood-fluid volume, with a construction computational time of approximately 20 s. Similarly, the parametrisation of a more extensive cerebrovascular artery from [6] determined a total set of 376 contiguous patches in approximately 60 s. Simulations were performed using *geoPDEs* IGA framework [55], where the surface geometry was initialised as Dirichlet boundary condition for the solution of the canonical Stokes' problem. Both geometry parametrisation and fluid dynamic simulations were performed on a single 3.1 GHz Intel Core i7 machine. A qualitative assess-

ε	$\frac{\partial}{\partial u}$	$\frac{\partial}{\partial v}$	$\frac{\partial^2}{\partial u^2}$	$\frac{\partial^2}{\partial u \partial v}$	$\frac{\partial^2}{\partial v^2}$
\mathbf{J}_{\angle}	6.8×10^{-4} ($4.8 \times 10^{-6}, 5.7 \times 10^{-3}$)	7.8×10^{-4} ($4.8 \times 10^{-6}, 5.7 \times 10^{-3}$)	0.18 (0.13, 0.22)	0.34 (0.18, 0.56)	0.11 (0.04, 0.15)
$\mathbf{J}_{\tilde{\Sigma}}$	7.7×10^{-3} ($6.9 \times 10^{-6}, 0.03$)	2.5×10^{-3} ($1 \times 10^{-3}, 0.01$)	0.21 (0.14, 0.28)	0.67 (0.39, 0.92)	0.1 (0.03, 0.16)
$\mathbf{J}_{\tilde{\Pi}}$	8.8×10^{-3} ($7.6 \times 10^{-5}, 0.03$)	3.1×10^{-3} ($1.3 \times 10^{-3}, 0.01$)	0.26 (0.19, 0.35)	0.4 (0.1, 0.78)	0.11 (0.03, 0.18)

Table 6.3: Root mean square errors ε of both Jacobian and Hessian components evaluated at the boundaries of the surface patches for the synthetic junctions \mathbf{J}_{iso} , $\mathbf{J}_{\tilde{\Sigma}}$ and $\mathbf{J}_{\tilde{\Pi}}$. Median values are reported together with the first- and third-quartile respectively.

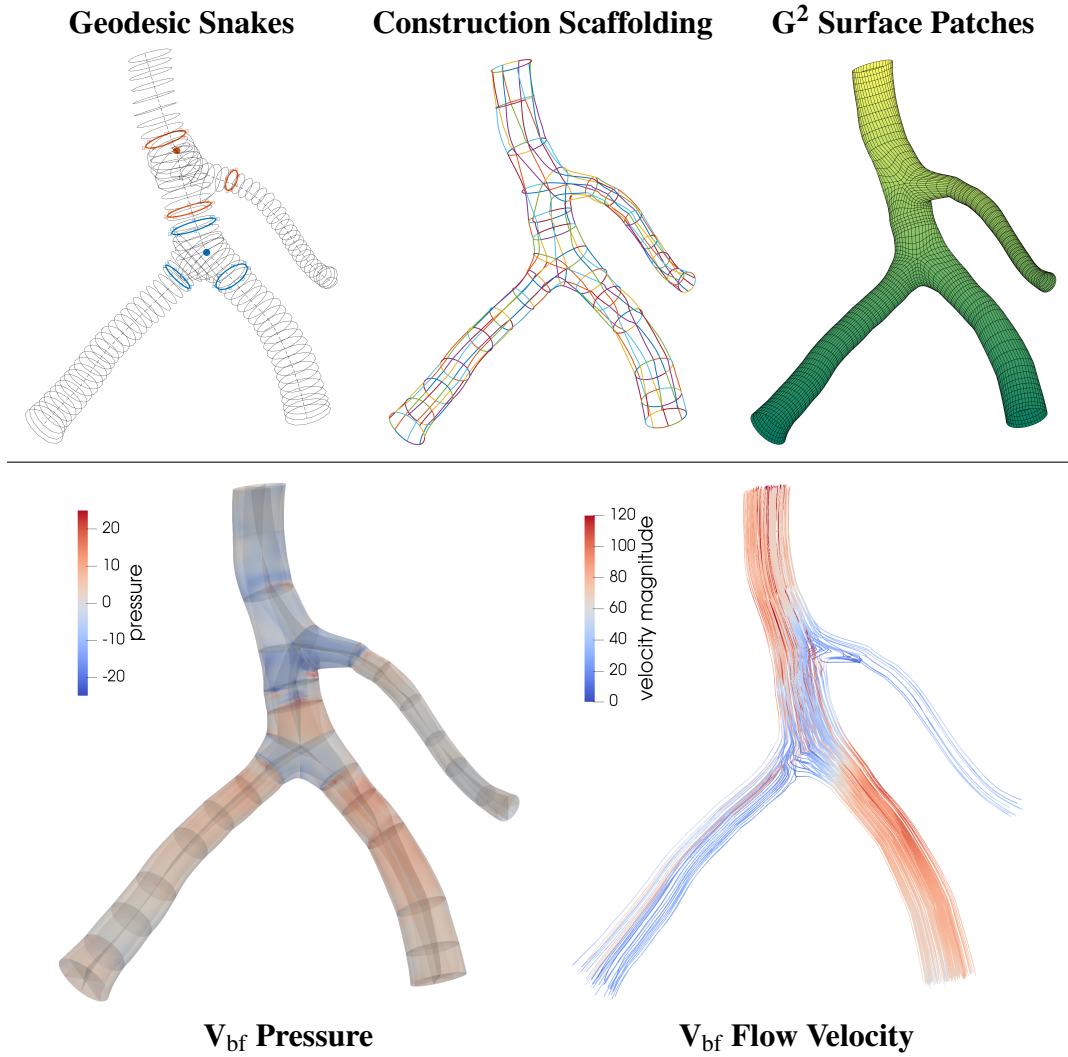


Figure 6.22: Clinical angiographic modelling & fluid dynamic simulations using an IGA framework: (top) tubular phantom construction outline and associated fluid pressure and velocity streamlines computed within the V_{bf} domain.

ment of the resulting blood-flow velocity streamlines and the associated pressure values is shown in Fig. 6.22 and Fig. 6.23, for the considered representative cases.

6.4.6.3 Observations

The introduced NURBS-based parametrisation of bifurcating tubular structures smoothly and compactly models vascular geometries for hemodynamic simulations using an isogeometric analysis framework. The proposed end-to-end paradigm recovers an implicit fluid-solid partitioning of the structures, concurrently optimising a surface G^2 -continuity condition at the interfaces. In particular, junctions are

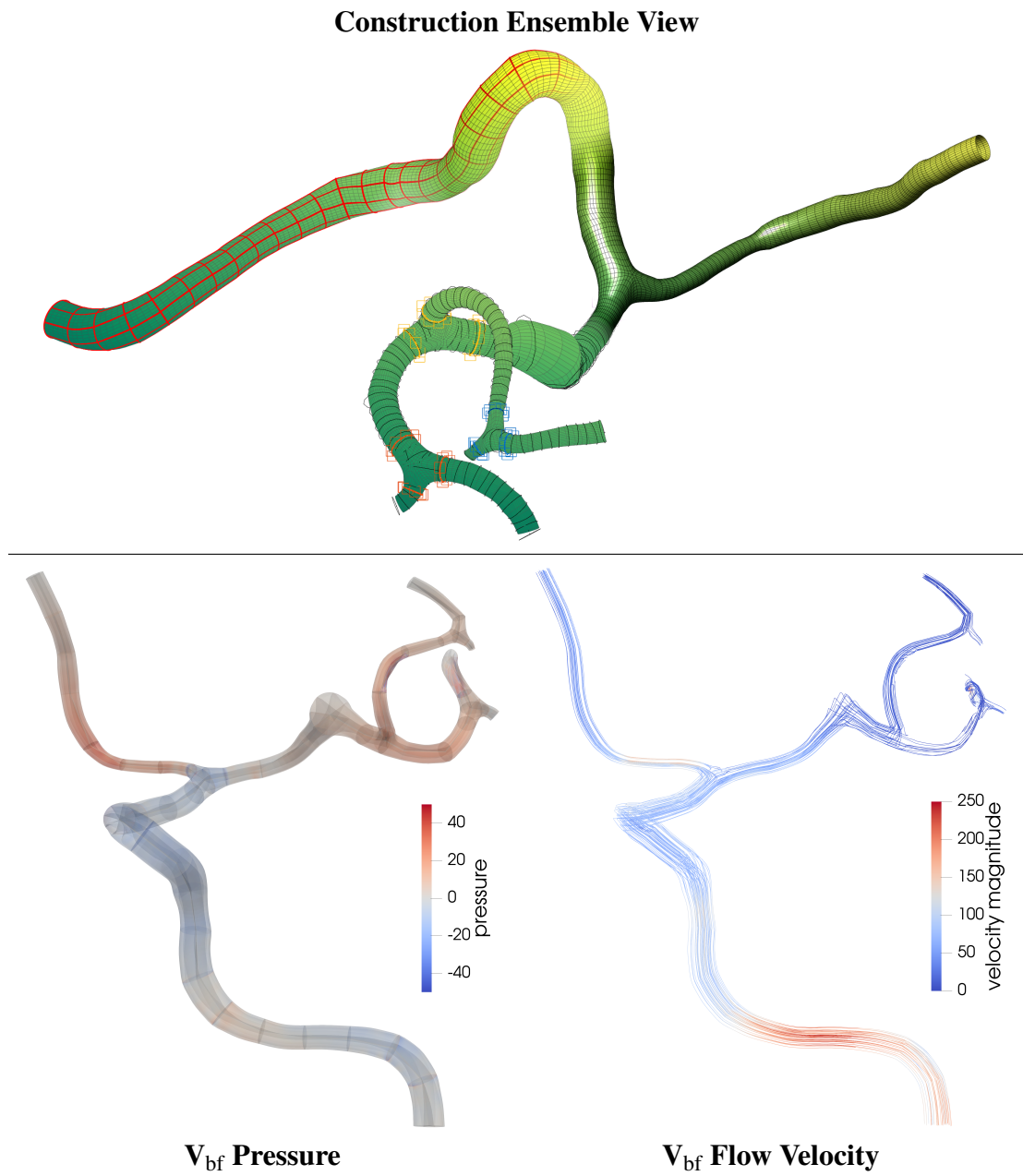


Figure 6.23: Clinical angiographic modelling & fluid dynamic simulations using an IGA framework: cerebral artery with aneurysm – fusion of multi-step construction paradigm and fluid dynamic simulations using *geoPDEs* [55], solving a canonical Stokes’ problem.

smoothly recovered with an efficient template-free design, which reported consistent differential continuity at the interfaces, even for strongly irregular geometries. Similarly to [214], the octagonal parametrisation represents a compact trade-off between anatomical detail and construction complexity. Qualitative results on clinical angiographic data support the translation of the proposed methodologies towards automated hemodynamic and biomechanical hyper-elastic simulations within an IGA framework. The simulations performed with the *geoPDEs* tool-kit [55] reported a comprehensive computational time of approximately 450 s (7.5 minutes) and approximately 3000 s (50 minutes) for the phantom and for the clinical cerebral artery, respectively. Yet far from real-time, more advanced formulations may allow future simulations in cardio- and neurovascular scenarios, where the vascular graft geometry is optimally modified for the purpose of improving hemodynamic outcomes [127], and where manufacturers can predict the patient-specific device performance prior to deployment [183].

6.5 Observations and Remarks

In this chapter, the extraction of biomarkers is addressed for a global-network as well as for localised branching geometries, by deriving a set of hemodynamic quantities to functionally characterise the cerebrovascular topologies inferred with VTrails.

Leveraging both topological and geometrical representations of the vascular structure, the geometrical parameters and the local vessel morphology is estimated first with a series of geodesic snakes. These segmented a linearly reformatted image volume along the connected centerlines with an antagonist level-set formulation. Snakes' deviations from the ground-truth are comparable to the voxel size in the considered angiographic set. Errors fluctuated for smaller vessels and capillaries, where the formulation of geodesic snakes may require further regularisation due to localised partial volume effects. Although the vascular lumen segmentation strategy employed geodesic snakes in an independent and separated processing pipeline with respect to the initial connectivity extraction, as in section 4.1, it can be observed that

both approaches derive from a similar level-set formulation. With a more optimised and unified processing pipeline, both minimal connecting paths and vascular luminal contours could be jointly and simultaneously determined. This would allow in future work a more spatially regularised vectorial segmentation with increased geometrical accuracy. In particular, the spatial coordinates of the extracted minimal paths could be spatially constrained to lie in the vicinity of the actual tubular centreline, and, at the same time, a more centred geodesic path would compensate for initialisation biases of the cross-sectional active contours delineation.

From such a geometrical characterisation, a simplified hemodynamic model condensed bio-mechanical lumped-parameters into an analog-equivalent configuration, based on the connected topology of the vasculature. This compact representation approximates asymptotic values of blood flow and pressure drop for a global network, where autoregulation mechanisms are observed in simulated pathology. Perturbations of the bio-mechanical lumped parameters are introduced in the analog-equivalents to model the effect of stenosis, tortuosity and complete occlusions in critical ischaemic events. A resilience index is introduced to represent the capability of the neurovascular network to recover from simulated perturbations and to compensate for possible pathological scenarios. The proposed formulation is evaluated for a set of clinically relevant cerebrovascular structures, where the observed asymptotic distributions of blood flow and pressure drops along the vascular branches are in line with the literature. Similar compensation strategies and distributions were observed in case-studies and on artificial physio-pathological models [45, 146, 166]. From a computational perspective, lumped-parameters resulted in an efficient and compact modelling strategy for the extraction of descriptive hemodynamic biomarkers, which can be scaled up to the whole cerebrovascular system. Also, their flexibility towards network perturbations allowed an early evaluation of the mechanisms underlying the cerebral compensation, as well as a putative graph sampling strategy for unknown over-connected topologies. However, the current approximation is not able to model vascular fluid-structure interactions, nor the effect of a pulsating flow and pressure as in fully-resolved CFD simulations. Therefore a

dynamic extension of the model, together with a more extensive validation, is required in future work with respect to state-of-the-art computational fluid dynamic simulations.

Lastly, an automatic NURBS-based parametrisation is presented for bifurcating vascular structures, where the extraction of biomarkers from fluid-solid interactions at the interface can be ultimately allowed on a more localised scale, as a proof of concept. The geometrical parametrisation of bifurcations is detailed using NURBS curves. The proposed automatic parametrisation can, on the one hand, bridge the gap between the challenging extraction of functional biomarkers in a compact, smooth and homogeneous solution domain with IGA, and, on the other hand, pave the way towards the *vectorisation* of the vascular structure from angiography, for personalised surgical repair integrating subject-specific CAD designs. Comparisons among simulations with different graph-based and NURBS geometrical parametrisations cannot be straightforwardly performed at the current stage. The presented NURBS parametrisation is currently limited to bifurcating tubular structures, in the presented proof of concept. Conversely, the vascular structures modelled with analog-equivalent graphs include junctions with more than three incident tubes. In future work, a complete parametrisation scheme can be devised on the basis of the advances introduced in this chapter, allowing therefore for vectorial representations and simulations on an arbitrarily complex neurovascular structure.

With this view, and inspired by statistical shape theory in computational anatomy [152], the translation of segmented vessels from angiographies to vascular networks could be cast, in future developments, in a fully-vectorial environment transcending a finite and quantised raster spatial grid. Specifically, the vectorial parametrisation of connectivity models for the inferred topologies could be extended to $2D$, $3D$ and higher-dimensional manifolds of parametric curves with NURBS. Since NURBS can model pre-defined shapes as well as free-form shapes, where the numeric evaluation is computationally stable with a relatively coarse set of parameters, by means of a further stretch, the free-form parametric manifold of multiple vascular structures could ultimately populate a group-wise stratifica-

tion of cerebrovascular instances, both longitudinally and cross-sectionally. At the same time, by projecting back the parametric model onto a subject-specific level, co-registered geometries with intra-operative imaging modalities would provide augmented guidance for neurovascular interventions, accounting for currently unavailable cerebral intra-vascular *3D* catheter routing for stenting, recanalisation and aneurysm coiling, as well as extra-vascular virtual visualisations for motion planning and (un)safe insertion-points in stereotactic brain surgery.

Chapter 7

Discussion

This thesis presents an end-to-end set of modular methodologies towards a novel vectorial framework, VTrails, for image-based vascular segmentation. The introduced advances produced a completely new class of geometrical and topological vessel representations, showing accurate and reproducible performances in neurovascular applications, with respect to the currently available state-of-the-art. This demonstrated the versatility and usefulness of the proposed VTrails framework, in a clinical research set-up, from extracting patient-specific models supporting interventional neuroradiology and vascular surgery, to further population-wise studies of comparative neurology, neurovascular phylogenetics, and cerebrovascular disease progression on a larger scale.

In Chapter 3, a vessel enhancement filtering approach is presented by first introducing a compact filter-bank of Steerable Laplacian of Gaussian Swirls (SLoGS). The enhancement of tortuous tubular structures is formulated under a unified multi-resolution, curvilinear- and rotation-invariant digital filtering framework. The proposed method is mathematically consistent and simultaneously synthesises both scalar and high-order vascular saliency maps from multi-modal 3D angiographies. The scalar connected vesselness map smoothly recovers fragmented and convoluted structures, with local maxima at the tubular mid-line, showing a continuous Gaussian profile. Also, for the first time, the voxel-wise tensor field consistently incorporates vascular anisotropy and directionality, as a unified method, without either separately fitting the image-data or regularising the tensor's positive-definiteness a

posteriori. Although fitting a tensor on vascular data is a viable alternative, a fitting procedure on noisy data might produce noisy directional features, as well as poor or missing anisotropic features for disconnected and fragmented vascular structures, in absence of contrast or signal. The comparison with established and widely used tubular ridge detectors and vascular enhancement techniques, such as the Frangi filter and the Optimally Oriented Flux, demonstrated the robustness of the proposed filtering approach with respect to noisy, degraded and poorly resolved angiographies in a number of synthetic and real clinical cases. Leveraging the intrinsic blood vessels' connectedness, the composition of the synthesised maps ultimately determines a smoothly connected Riemannian vesselness potential.

In Chapter 4, a connectivity-oriented anisotropic level-set over the synthesised Riemannian vesselness potential is formulated under the assumption that vessels join by minimal paths. More specifically, two approaches are devised: from a greedy connectivity paradigm with a concurrent and competitive minimal-path extraction scheme, to an exhaustive geodesic search within the smoothly connected Riemannian vesselness potential. Despite the optimal formulation of the anisotropic level-set, the proposed greedy connecting solution is intrinsically acyclic and therefore limited towards modelling full-brain vascular structures. At the same time, its results is more prone to mis-connections and short-cuts. The exhaustive connectivity paradigm, conversely, accounts for an independent connecting redundancy of the underlying vascular network, where possible resulting anatomical inconsistencies are not hierarchically encoded. Also, the exhaustive topological inference is able to model at the same time cyclic topologies from anatomical anastomoses at different scales, e.g. the complete Circle of Willis and finer cortical capillaries. The inference of anatomical deep-brain vascular trees is performed by extracting minimum spanning trees over the inferred over-connected network. Quantitative geometrical and topological comparisons with the associated gold-standard manual annotations and with connected centerline ground-truth from popular vascular segmentation toolkits, i.e. the Vascular Modelling ToolKit (*VMTK*) and *TubeTK*, reported overall comparable accuracies at different levels of the vascular network,

in a number of simulated configurations.

In Chapter 5, a pair-wise topological registration strategy is presented for redundant over-connected geodesic vascular graphs. By means of a coarse-to-fine registration approach, the topological alignment is solved with popular graph matching techniques employed in computer vision applications. The nodes' correspondence mapping between pairs of undirected geodesic vascular graphs builds on an affinity metric, which leverages geometrical, geodesic and connectivity-based features of the topologies, and lastly optimises a quadratic assignment problem. For the first time, a non-rigid topological alignment is introduced for connected vessels, by relaxing the hierarchical and acyclic constraint of vascular trees, and by disregarding any topological prior from specific anatomical compartments. The redundant connectivity patterns of the considered topologies favour the correspondence of landmarks in a set of experiments on synthetic and clinical data, accounting for non-linearly deformed topologies and similar, yet strictly non-isomorphic, anatomical instances. This is observed by comparing the accuracy and overall performance of graph matching techniques with respect to the associated acyclic instances. Also, in this case, fully cyclic topologies, e.g. those underlying anatomical anastomoses such as the complete Circle of Willis, could be consistently aligned within the same pair-wise graph matching framework. These promising lines of evidence pave the way towards more refined and vascular-oriented formulations and towards group-wise topological alignment strategies, where the trade-off between affinity metrics from multi-source features and the redundant connecting overhead of the graph lattice may affect the resulting alignment performance for the definition of a data-driven cerebrovascular atlas.

Lastly, in Chapter 6, the vectorial embeddings of geodesic vascular graphs are enriched with a representative set of biomarkers from hemodynamic simulations. First, spatial delineations of the vascular lumen are obtained with geodesic snakes (active contours) over a reformatted angiographic image from the underlying connected graph of centerlines and minimal paths. The recovered geometry is then condensed in bio-mechanical lumped-parameters for asymptotic hemody-

namic simulations. These employ the topology of the vasculature to determine a closed-loop analog equivalent circuit, simulating steady-state blood flow rate and pressure drop values for a number of configurations and anatomical variants. Perturbations, modelling tortuosity, ischaemic events, occlusions and different levels of stenoses, simulate the resilient mechanisms underlying the cerebral blood autoregulation for whole-brain vascular networks, approximating and bypassing highly intensive and prohibitive finite-element fluid dynamic simulations. Also, a more localised parametrisation of vascular geometries is introduced for fully-resolved fluid dynamic simulations using an isogeometric analysis framework. Parametric NURBS curves, surfaces and volumes automatically reconstruct the underlying vascular junctions and branches, allowing for the estimation of localised hemodynamic quantities and, in the ultimate instance, of functional biomarkers from fluid-solid interactions at the interface, without introducing further approximations to the solution profile. The same geometrical parametrisation integrates applications of personalised healthcare and surgical repair with subject-specific CAD designs.

Current Limitations Throughout the body of this thesis, different contributions have been presented under the same unified framework VTrails, covering an umbrella of multi-disciplinary tasks. Despite the harmonisation effort to provide a set of automatic tools and methodologies for cerebrovascular image analysis, a number of technical and technological limitations are still present and deserve further investigation in future work. Among the technical shortcomings, several parameters, early initialisation and configurations, which have been proposed for the considered datasets, may sensibly differ, for example, on a different collection of multi-modal angiographies and on a different set of selected features for the topological alignment. With this view, a finer tuning step for parameters and a more extensive sensitivity analysis for the initialisation and configuration of different optimisation problems should be performed, towards a more efficient processing (currently strictly off-line) and robust analysis with respect of multi-source vascular features with the introduction of further anatomical prior knowledge. Prior to translating the intro-

duced methodologies to clinical practice, a more extensive validation must also address current limitations with the interpretation of early results, and an experimental proof for neurovascular applications of the postulated multi-graph matching techniques, as well as of the theoretical formulation of a cerebrovascular (multi-)atlas should be provided. Among those, some of the current limitations are rather determined by the lack of an available framework, or of any viable and computationally feasible solution, due to the intrinsic intractable complexity of the task. A further complexity reduction is indeed required for the proposed VTrails framework; the over-connected geodesic graph conservatively embeds a high degree of redundancy. Such informative overhead is counter-intuitive to the visual assessment of vascular structures and can dramatically impact the computational complexity of downstream processing. Also, the lack of a predictive model for therapeutic inference on the long term, currently restricts the analysis and evaluation of the cerebrovascular physio-pathology to a single time-point. Regarding these latter technological limitations, future research directions are addressed in the following section, towards a topological optimisation of vascular networks and patient-specific models for life-long risk prediction.

7.1 Future Research Directions

As previously observed, there are still many derived problems, open challenges and associated conceptual ideas that are worth pursuing. In the following, two main concepts and research directions are presented. Along with the vectorial connectivity of brain vessels, as formulated in Chapter 4, technological advances involving the topological simplification, optimisation and decomposition of a geodesic vascular graph are mentioned in the following section, towards a more intuitive, compact yet non-hierarchical representation of the analysed vasculature. Then, a long-term vision for individual risk prediction models from a population-based prior is briefly introduced. This leverages emerging machine intelligence frameworks towards the customisation of cardio- and neurovascular healthcare, from prevention, event-prediction, up to optimal therapeutic intervention.

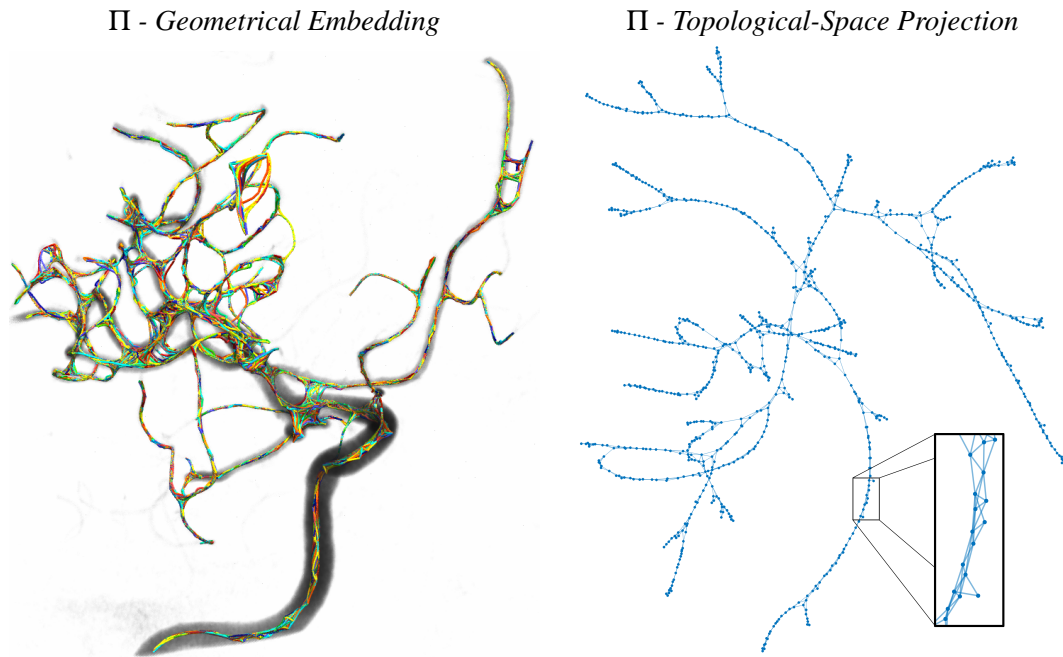


Figure 7.1: Redundant and Over-Connected Geodesic Vascular Graph Π . Comparison of the geometrical and purely topological embedding of the network. Local uninformative connecting overhead, here in the elongated linear segments (graph's *flares*) can be conservatively simplified, streamlining the topology towards a more compact and sparse representation.

7.1.1 Topological Optimisation of Vascular Networks

The introduced formulation of an over-connected, redundant and uncertain vascular graph has the advantage of providing a number of topological cues for the pair-wise alignment, as observed in Section 5.5. Also, the uncertain and non-hierarchical nature of the undirected vascular topologies allows more flexibility towards the inference of the most meaningful anatomical realisation of the underlying vascular structure, potentially reducing short-cuts and mis-connections from kissing-vessel artifacts which cannot be avoided, per se, with a hierarchical and straightforward minimum spanning tree extraction. In this way, the resulting redundant and over-connected topology shows a consistently increased level of complexity, which however impairs the intuitive interpretation of the underlying vascular network, and can dramatically exacerbate, or even impede, further group-wise computational processing (see Section 5.6). With this view, conservative topological simplifications and optimisation strategies can be devised to slim down the overhead of connecting

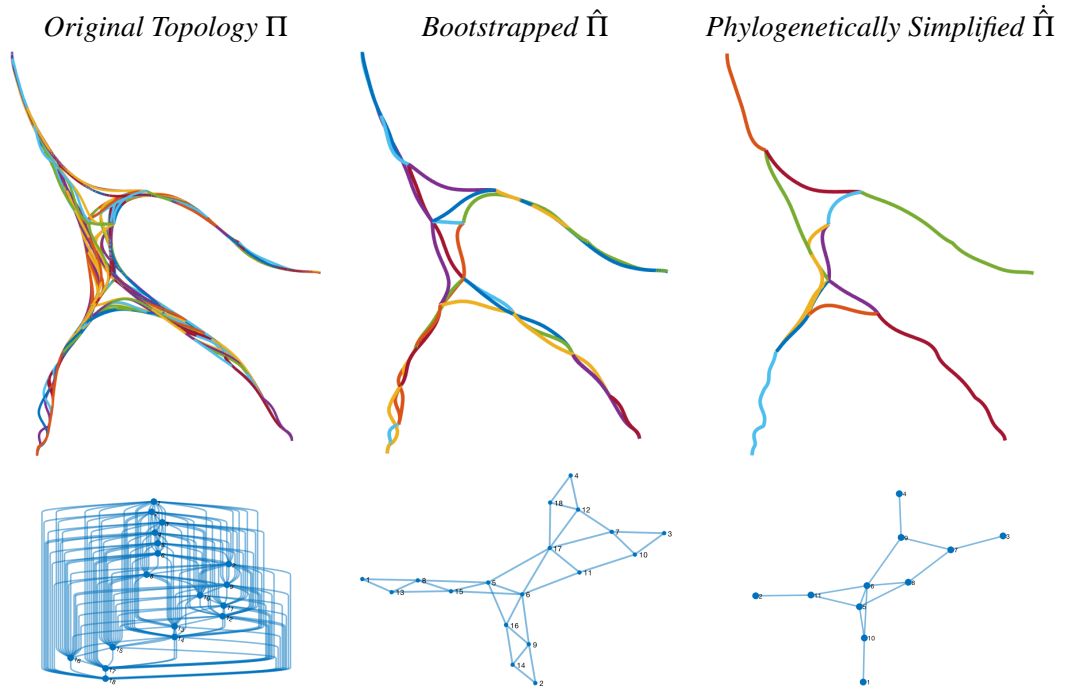


Figure 7.2: Topological Optimisation Strategies. From the original over-connected geodesic vascular graph Π of the Basilar Artery phantom, a bootstrapped version ($\hat{\Pi}$) and a further phylogenetically simplified one ($\hat{\hat{\Pi}}$) are retrieved, conservatively reducing both nodes' and edges' cardinalities and increasing the overall graph compactness. Note that graph's flares are eventually simplified, whereas the connecting uncertainty at the vascular junction is preserved, as well as possible topological cycles.

redundancy.

Graph bootstrapping, phylogenetic simplification, and network decomposition stand as viable strategies to reduce the intrinsic complexity of the over-connected geodesic vascular graphs. With a graph bootstrapping, a more compact topology is obtained by increasing the overall sparsity of the embedding and of the associated adjacency matrix. Similar to the putative graph sampling approach in Section 6.3.5.3, individual nodes, edges, and local sets of cliques (Fig. 7.2) can be selectively pruned based on a sequence of statistical tests relying on topologically perturbing the graph, i.e. by performing a random sampling of the topology on multiple levels. The topological pruning scheme for individual nodes, edges, and local sets of cliques would therefore follow a resilience-maximising paradigm with respect to the simulated topological perturbations of the network. Topological per-

turbations accounting for simulated alterations of the hemodynamic network, i.e. occlusions and different levels of stenoses, may elicit resilient mechanisms underlying the neurovascular network, for which the most anatomically meaningful realisation or a family of sub-graphs statistically emerge from the over-connected pool of geodesics.

A phylogenetic network simplification can be subsequently applied, given the prior information of the generative inference of the vascular network (see Section 4.3.0.3 – for *ancestor* and *offspring* nodes), to further reduce both node and edge cardinalities in correspondence of graph's *flares*, i.e. the over-connected elongated linear segments (Fig. 7.1). Conversely to the redundant connectivity pattern at the vascular junctions (Fig. 7.2), which should be preserved for pair-wise and group-wise topological alignment purposes, the dense, yet uninformative, connecting overhead of certain vascular branches can be opportunely reduced with a consistent split-merge phylogenetic paradigm. It is worth noting that the inference of the over-connected network, as introduced in Section 4.3, can be described with an evolutionary topological development and diversification which iteratively follows generations of new seeds (or nodes) and connecting edges, similar to a biological process. Therefore, a phylogenetic network simplification would backtrack those most meaningful *ancestor* nodes and edges, and would conservatively preserve the relevant originators of the inferred topology by possibly pruning the overhead of uninformative *offspring*, as in the case of elongated flares. As shown in Fig. 7.2, the combined approaches lead to a redundant geodesic vascular graph with minimal complexity along the elongated branches, which preserves at the same time both the redundant connectivity at the branch-points and possible unknown cyclic structures underlying the vascular network.

Lastly, a hierarchical network decomposition strategy can be devised towards the extraction of local sub-net matching patterns. These not only would determine a localised matching pattern paradigm for group-wise topological registrations and label propagation on re-combined graph partitions, sub-nets, and overlapping cliques, as postulated in Section 5.6, but they can also allow a number of further sub-net

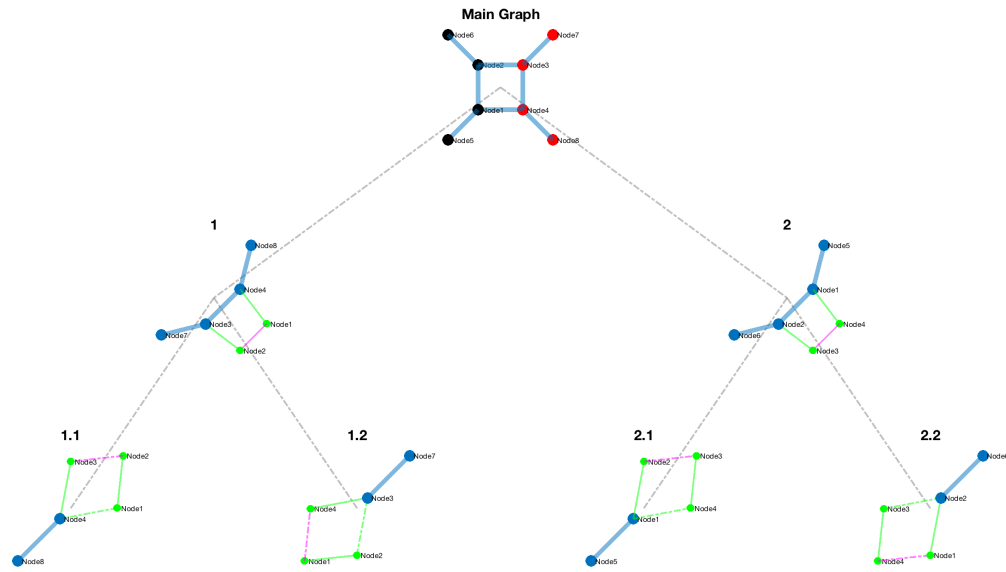


Figure 7.3: Graph Hierarchical Partition and Decomposition. Representative toy example of a condensed network, where non-disjoint sub-nets and topological partitions can be derived and further re-combined, allowing flexibility for multi-scale graph-cuts. Green and pink edges are non-disjoint shared sub-graph cliques and inherited ones, respectively, throughout the topological decomposition.

analyses on multiple non-disjoint samples of the vascular network (Fig. 7.3). Under the assumption of a condensed network embedding the union of several connecting portions at different network-scale levels, the topological inference of the cerebrovascular network could be guided towards the global and comprehensive arterial and venous structure as a whole, where vascular anastomoses of different size, from the complete Circle of Willis, up to the smaller cycles in the capillary bed, are consistently modelled and preserved.

7.1.2 Patient-Specific Models for Life-Long Risk Prediction

A prospective complete ensemble of cerebrovascular features, these all embedded in a consistent population-based vectorial atlas, would automatically propagate the collected information to new unseen data allowing for clinical inference with statistical power. A number of neurovascular critical applications for serious life-threatening conditions could benefit from such informative prior propagation, these ranging from prevention, event prediction, early diagnosis and, ultimately, optimal treatment. Among these, stroke-related life-long risk modelling and prediction strategies play a major role for the next-generation of fully-customised cardio-

and neurovascular care. Given the relevant incidence of stroke world-wide (the second most frequent cause of death after coronary artery disease), considering also the widespread and long-lasting collateral complications (psychological and behavioural impacts, cognitive impairment, induced weakness or paralysis), and accounting for the (un)sustainable and economical impact on the life-long rehabilitation costs, therapeutic care, and associated comorbidities and disorders, future large-scale clinical trials would include a comprehensive collection of multi-source clinical indices and multi-modal angiographies at different time-points among subjects at risk. Quantitative and subject-specific vascular models, comprising morphometric features, structural and hemodynamic topological resilience, could be automatically integrated (and so forth updated) with other vascular functional indices, clinical history, familial heredity and predisposition, and further characterised by ethnic phenotypes, environmental and behavioural agents. This would constitute a vectorial instance in the healthcare system database, where, after coherently propagating a population-based informative prior, the risk of stroke, as well as the prediction of concurrent complications would be determined by means of emerging machine-intelligence algorithms. With this view, a population-based prior could be tentatively retrieved with an extra harmonisation effort for heterogeneous datasets from ongoing studies. Among these, Biobank UK and SABRE (Southall And Brent REvisited) are currently collecting and analysing a complete spectrum of comprehensive longitudinal and cross-sectional data, together with angiographies, associated biomarkers, clinical reports and possible pathological outcomes. Quantifying the individual risk of stroke would be a clinical application stemming from a population-based analysis over vectorial neurovascular representations. Yet still far from translating such an application into the clinical practice, a similar concept could however leverage multi-source and image-based analyses to eventually predict the likelihood of an ischaemic event within a certain time-frame. Data from patients who would undergo regular medical scans, e.g. in the head-neck anatomical compartment, could converge in a collective anonymised dataset where ad-hoc analyses would automatically run in background by means of machine-

intelligence algorithms. This would ultimately provide a supplementary report, or a low-dimensional neurovascular representation notifying of potential anomalies. These would suggest early risks of neurovascular complications or provide an estimated likelihood of pathological development within a certain confidence as support to early clinical decision-making. This envisioned clinical application would, on the one hand, impact the personalised healthcare with minimal disruption, without therefore performing large-scale and costly-intensive population screening. Also, for those subjects identified at low neurovascular risk, specific indications could be given, e.g. dietary prescriptions, lifestyle adjustments and preventive medications. On the other hand, for those subjects identified as potentially at high-risk, a more adequate monitoring and a more prompt intervention and therapeutic planning could be provided, improving dramatically the quality of life.

7.2 Closing Remarks

This thesis introduces a novel vascular vectorial framework, VTrails, which transversally covers an umbrella of multi-disciplinary tasks. From image-based processing and vessel enhancement, to topological inference and graph-based connectivity paradigms, VTrails explores also non-linear and non-isomorphic vascular alignment strategies, and the simultaneous integration of multi-source features in the same graph embedding, from geometrical, to geodesic, to functional and hemodynamic biomarkers with a global-to-local vectorial approach. All these methodological contributions are contextualised and cohesively linked together by the common thread of vascular connectedness. The whole framework and each technical advance is designed to integrate well within a translational and clinical research set-up, with applications in neuroradiology. The contributions presented throughout the body of this thesis represent essential building-blocks and the modular processing foundation for prospective impactful analyses on a larger scale; from group-wise population studies, to patient-specific vascular models in personalised healthcare.

Appendix A

Open Source Effort

Along with the methodological formulation presented in this thesis, an open-source implementation was made during the PhD, towards the early release of a public vascular tool-kit under the Berkeley Software Distribution (BSD) license.

A.1 VTrails

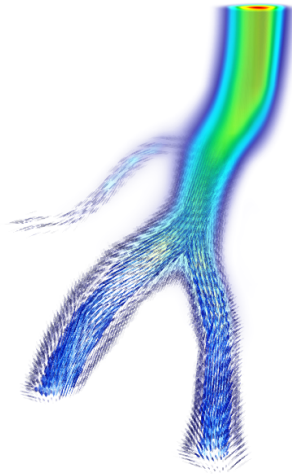


Figure A.1: The logo of the VTrails toolkit, available at <https://vtrails.github.io/VTrailsToolkit/>

The released project software, VTrails (Vascular/Vectorial Trails), is publicly available on GitHub <https://vtrails.github.io/VTrailsToolkit/> as an open-source, Matlab-based set of modular functions. The project aims at extracting geodesic vascular minimum spanning trees from angiographic data by solving a connectivity-optimised anisotropic level-set over a voxel-wise tensor field

representing the orientation of the underlying vasculature.

The first release features 4 main functionalities:

- SLoGS filterbank generation;
- Filtering an angiography with SLoGS and synthesise the Riemannian vesselness map;
- Infer the geodesic vascular graph with the connectivity-optimised anisotropic level-set;
- Extract and refine the vascular minimum spanning trees.

Following here a brief overview of the processing pipeline:

```

1  %%% VTrails Pipeline %%%
2
3  % 0) [NECESSARY] INSTALL VTrails Toolkit
4  >> INSTALL_VTrails
5
6  % NB. If you are experiencing compiling issues or installation problems,
7  % please configure the matlab coder, using the most recent gcc or clang compiler.
8
9  % 0a) [On Request] Create your own Dictionary of Filtering SLoGS Kernels
10 >> VTrailsSLoGS3D_MAIN;
11
12 % NB. this step requires to further specify the desired
13 % Dictionary of Filtering Kernels to 'VTrailsFilter3D_MAIN'.
14 % NB. this function is available *on request* (not included package).
15 % Tutorial -- https://youtu.be/f3LahhqzHFc
16
17 % 1) Filter the Image with the SLoGS Filterbank
18 >> scales_range = [0.1:0.1:1.0];
19 >> JobDumpDirPath = VTrailsFilter3D_MAIN( 'path/ImgFileName.nii' , 'path/
    MaskFileName.nii' , scales_range );
20
21 % NB. Define the scale_range along with the vascular information content and the
    desired level of detail.
22 % As rule of thumb: avoid big gaps from subsequent scales.
23 % NB. VTrailsFilter3D_MAIN imports automatically nifti files (.nii,.nii.gz)
24
25 % 1a) Integrate the Multi-Resolution Filter Responses over Scales
26 >> min_scale = min(scales_range);
27 >> max_scale = max(scales_range);

```

```

28 >> MaxMAP = VTF3D_integrateMaxMultiScaleResponses('PathFolder', JobDumpDirPath
    , ...
29                                     'ScalesRange', [min_scale ,
                                                    max_scale] );
30
31 % 1b) Determine the Organised Seeds for the Geodesic Connectivity Paradigm
32 >> arbitraryQuantileThreshold = 0.75;
33 >> verboseFLAG = true;
34 >> MaxMAP.OS = VTF3D_AlignVesselSeeds3D( double(MaxMAP.CVMsmth) , MaxMAP.US ,...
35                                     arbitraryQuantileThreshold , verboseFLAG
                                     );
36
37 % NB. the arbitraryQuantileThreshold is a scalar in [0,1], being 0 = all the
    points,
38 % and 1 = only the max value, respectively.
39
40 % 1c) Sort the Organised Seeds as initial Connected Components
41 >> [ MaxMAP.SortedOS ,...
42     MaxMAP.ConnectedSegmentsOS ,...
43     MaxMAP.BrachPointsOS ] = VTF3D_SortConnectedComponents( MaxMAP.OS ,
    verboseFLAG );
44
45 % NB. Sort and organise the Seeds and Connected Components prior to the exhaustive
    Connectivity Paradigm.
46
47 % 2) Determine the Over-Connected Geodesic Vascular Graph
48 >> DATA = VTrailsConnectingGeodesicGraph3D_MAIN( MaxMAP , 'PathFolder' ,
    JobDumpDirPath );
49
50 % NB. Connect the initial Seeds with the exhaustive Connectivity Paradigm, by
    following
51 % an Anisotropic Level-Set over the Riemannian Vesselness potential (CVM, TF).
52
53 % 3) Extract the Vascular Tree(s) as Geodesic Minimum Spanning Tree(s) - optional
    Pruning and Refinement
54 >> GeodesicMSTs = VTrailsRefine3D_ConnectedGraph2VTrailsTree_MAIN( DATA , '
    PruningLengthThresholdMM' , 10 );
55
56 % NB. Determine the Acyclic topology as the geodesic Minimum Spanning Tree (MST)
    or a forest of geodesic MSTs,
57 % accordingly with the connected components in the vascular graph.
58
59 % 4) Visualise Results
60 >> VTA3D_visualiseRiemannianVesselness( MaxMAP.CVM , MaxMAP.TF , MaxMAP.
    TFValidityMSK );
61 >> VTA3D_visualiseConnectingGeodesicGraph( DATA.exploredminPath , DATA.GGM );

```

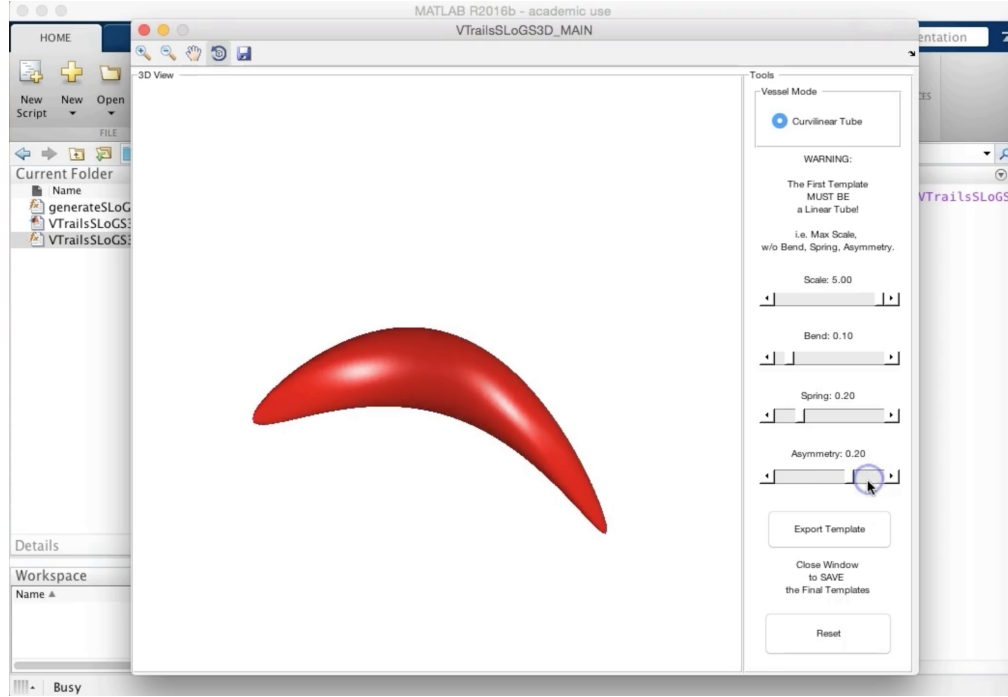


Figure A.2: Graphic User Interface for the Definition of an Arbitrary Dictionary of Filtering SLoGS Kernels. Tutorial: <https://youtu.be/f3LahhgzHFc>

```
62 >> VTA3D_visualiseGeodesicMinimumSpanningTree( GeodesicMSTs , MaxMAP.CVM );
```

SLoGS Filterbank Generation An arbitrary dictionary of filtering SLoGS kernels can be defined with a user-interface as shown in Fig. A.2. By modulating a scale factor, two curvilinear parameters accounting for in-plane bending and off-plane tilting, and an asymmetric index, multiple curvilinear templates can be obtained. Note this preliminary step is optional, since the same dictionary of filtering kernels employed throughout the body of this thesis is already included in the release for reproducibility purposes.

Filtering the Angiography with SLoGS and Synthesise the Riemannian Vesselness Map The function `VTrailsFilter3D_MAIN.m` is used to automatically synthesise the 3D Connected Vesselness Map (CVM) and the associated Tensor Field (TF) via filtering the angiographic image with the SLoGS Filterbank.

```
1  %%% VTrails: Synthesis of 3D Connected Vesselness Map & Tensor Field via SLoGS %%%
2
3  %% Function Call:
4
```

```

5 >> JobDumpDirPath = VTrailsFilter3D_MAIN( imgFileName , mskFileName , Scales ,
      varargin );
6
7 %% Inputs:
8 %
9 % - imgFileName: NIFTY filename of the 3D Angiographic Image Volume
10 %   NB: It is assumed BRIGHT Vessels on DARK Background!
11 % - mskFileName: NIFTY filename of the 3D bw mask for the Angiographic
12 %               Image Volume. It can be empty [] if none.
13 % - Scales: Scales range interval ]0,1]. E.g. [0.1 : 0.1 : 1.0]
14 %
15 %               [OPTIONAL]
16 %
17 % - ['AutoDenoise']: Bool Option for Automatic Denoise
18 %               (Mean Filter) - Default: False.
19 % - ['AutoDenoiseMedian']: Bool Option for Automatic Denoise
20 %               (Median Filter) - Default: False.
21 % - ['BoneStrip']: Approximated Maximal Intensity Value for Blood Vessels,
22 %               when Bones are present in the image (e.g. CT Angio.)
23 %               This allows an initial Bone-masking or Skull-Stripping.
24 %               Estimate [max] relative to the orig image scale range.
25 %               Default: [];
26 % - [UpdateDFKsMO]: Boolean flag to Enable/Disable Update of the Dictionary
27 %               of Filtering Kernels already aligned to previous Main
28 %               Orientations (DFKsMO). Default: False.
29 % - [SIQthr]: Seeds Intensity Quantile threshold -- Default: 0.9
30 % - [SIQthrFIX]: Scalar boolean flag to disable progressive increase of
31 %               SIQthr at higher resolutions. Default: False.
32 % - [PowerFactor]: Scalar real value to enhance the original image
33 %               dynamic contrast following the law:
34 %               Img_enhanced = Img.^PowerFactor;
35 %               Default: 1.0
36 % - ['SkipTFflag']: Bool Option for Skipping the Tensor Field Synthesis -
37 %               Default: False.
38 % - ['Dictionary']: Complete filename of the User-Defined Disctionary of
39 %               SLoGS to be used. -
40 %               Default: '<VTrailsROOTDir>/libs/DFKs_MAIN.mat'
41 % - [FullDump]: Scalar boolean flag to export the complete set of outputs.
42 %               Default: False.
43
44
45 %% Outputs:
46 %   For each selected Scale, the method will export a .mat file in a
47 %   dedicated folder located in the function directory, which contains the
48 %   'MAP' structure listing the following fields:
49 %

```

```

50 % - GRID: Structure with Image Grid and Scales' infos for Resampling.
51 % - IMG: Header of the input nifty Images.
52 % - CVM: Scalar Connected Vesselness Map obtained with SLoGS
53 % - BDM: Scalar Vessel Boundaries Map obtained with \deltaSLoGS
54 % - BGM: Scalar Vessel Background Map obtained with \nuSLoGS
55 % - TFLE: Vascular Tensors Field synthesized with SLoGS in the
56 %         Log-Euclidean Domain
57 % - [TF]: Vascular Tensors Field synthesized with SLoGS in the
58 %         Euclidean Domain -- optional with 'FullDump'
59 % - SSsIDX: list of Un-Organised Seeds TO BE Aligned to the vessels with
60 %         'VTF3D_AlignVesselSeeds3D.m' (after Multi-Scale Integration.)
61 % - US: Logical Volume of Un-organised Seeds

```

Infer the Geodesic Vascular Graph with the Connectivity-optimised Anisotropic

Level-Set The function `VTrailsConnectingGeodesicGraph3D_MAIN.m` is used to automatically infer the over-connected vascular topology (graph) by running an anisotropic level-set (Fast Marching) over the Riemannian vesselness potential (CVM and TF) and by enforcing a self-organising exhaustive connectivity paradigm.

```

1  %% VTrails: Geodesic Connectivity Paradigm for Over-Connected Vascular Graphs %%
2
3  %% Function Call:
4  >> DATA = VTrailsConnectingGeodesicGraph3D_MAIN(MAP,varargin)
5
6  %% Inputs:
7  %
8  % - MAP: structure containing Image-related features, the Riemannian
9  %         Vesselness potential and the initial Seeds for the Level-Set.
10 %         NB: MAP can be either a single-scale output from the function:
11 %            'VTrailsFilter3D_MAIN.m' or it can be a multi-scale integrated
12 %            filter-response (MaxMAP) as from the function:
13 %            'VTF3D_IntegrateMaxMultiScaleResponses.m'.
14 %
15 %         MAP *MUST* contain the following Fields:
16 %
17 % * IMG: Header of the input nifty Images.
18 % * GRID: Structure with Image Grid and Scales' infos for Resampling.
19 % * CVM: Integral Scalar Connected Vesselness Map obtained with SLoGS
20 % * TF: Integral Vascular Tensors Field synthesized with SLoGS in the
21 %         Euclidean Domain -- can be [empty] for automatically FITTING
22 %         the Tensor Field over the CVM, or it can be a scalar equal to 1,
23 %         for the ISOTROPIC Front Propagation.
24 % * ConnectedSegmentsOS: struct containing the list of SORTED Connected

```

```

25 %                               Components from the Organised Seeds.
26 %
27 %                               Other [optional] Fields:
28 %
29 % - [CVMsmth]: As CVM, but slightly smoothed for local maxima.
30 % - [BDM]: Integral Scalar Vessel Boundaries Map obtained with \deltaSLoGS
31 % - [BGM]: Integral Scalar Vessel Background Map obtained with \nuSLoGS
32 % - [TFLE]: Integral Vascular Tensors Field synthesized with SLoGS in
33 %           the Log-Euclidean Domain
34 % - [TFValidityMSK]: Binary Mask for non-isotropic Tensors.
35 % - [ACC]: Internal Variable for Across-Scales Integration Regularisation
36 % - [US]: Scalar Volume of Un-Organised Seeds TO BE Aligned to the
37 %         vessels with 'VTF3D_AlignVesselSeeds3D.m'
38 % - [OS]: Scalar Volume of Organised Seeds, aligned to the
39 %         vessels with 'VTF3D_AlignVesselSeeds3D.m'
40 % - [SortedOS]: Scalar Volume of Organised and SORTED Seeds, each
41 %               consisting in a labelled (numeric) path, obtained with
42 %               'VTF3D_SortConnectedComponents'.
43 % - [BranchPoints]: list of early junctions detected with
44 %                   'VTF3D_SortConnectedComponents'.
45 %
46 % CONFIGURATION INPUTS:
47 %
48 % - ['Mask']: Validity Mask for Domain exploration (i.e. ~Barriers). -
49 %             Default: true(size(MAP.CVM))
50 % - ['SPDPowerFactor']: Power of the Vesselness Speed Potential (SPD). -
51 %             Default: 1
52 % - ['VNRradiusMM']: Radius of Visible Seeds Neighborhood - limit the
53 %                   exploration of the domain to a restricted spherical
54 %                   neighborhood of the given Seed. - Default: 20 [mm]
55 % - ['NodeDistTHR']: Node Distance Threshold for Adaptive Graph Refinement.
56 %                   - Default: 3 [mm]
57 % - ['PathFolder']: Path Folder for Data Exporting - Default: [pwd,'/']
58 % - ['QExplore']: Quantile of Geodesic Exploration - to restrict the
59 %                 exploration of the domain accordingly with a geodesic
60 %                 metric. - Default: 0.5
61 % - ['FullDump']: Binary Scalar Flag for enabling FULL DUMP of all
62 %                 variables. - Default: false
63 %
64 %% Outputs:
65 %
66 % - DATA: structure containing the Over-connected Vascular Graph.
67 %
68 %           DATA will contain the following Fields:
69 %
70 % * GGM: Geodesically Weighted Connectivity Matrix of the Over-Connected

```

```

71 %           Vascular Graph.
72 % * exploredminPath: struct containing the list of all the extracted and
73 %           explored connecting geodesics (minimal paths).
74 % * MST: Minimum Spanning Tree(s) Matrix obtained from GGM with
75 %           'Kruskal' method.
76 % * OrigSeedsIDX: list of Original Seeds;
77 % * ExtraSeedsIDX: list of automatically generated Seeds, during the
78 %           self-arranging refinement;
79 % * IMG: as in MAP (input)
80 % * GRID: as in MAP (input)
81 %
82 %           Other functional fields (for traceability):
83 %
84 % * SPDPowerFactor: value of 'SPDPOWERFACTOR'.
85 % * VisibleNeighborhoodRadius_mm: value of 'VNRADIUSMM'.
86 % * NodeDistanceTHR_mm: value of 'NODEDISTTHR'.
87 % * GradientDescentStopTHR: automatically determined value.
88 % * PathFolder: string with the Path Folder for Data Exporting.
89 % * QExplore: value of 'QEXPLORE'.
90 % * VisibleNeighborhoodRadius_vx: as in 'VNRADIUSMM', but VOXELs.
91 % * VisibilityBall: Logical Volume created by 'VNRADIUSMM'.
92 %
93 %           [Other Fields are present when 'FULLDUMP' is enabled]

```

Extract and Refine the Vascular Minimum Spanning Trees The function `VTrailsRefine3D_ConnectedGraph2VTrailsTree_MAIN.m` is used to automatically extract and refine the geodesic minimum spanning tree - or a forest of minimal trees, from the initial over-connected vascular graph.

```

1  %% VTrails: Extract and Refine Geodesic Minimum Spanning Tree from Over-Connected
   Vascular Graphs %%
2
3  %% Function Call:
4
5  >> [GeodesicMSTs, GeodesicMSTsMatrix] =
      VTrailsRefine3D_ConnectedGraph2VTrailsTree_MAIN( DATA , varargin );
6
7  %% Inputs:
8  %
9  % - DATA: structure containing Image-related features, and the
10 %           Over-connected Vascular Graph.
11 %           NB: DATA is the output of the function:
12 %           'VTrailsConnectingGeodesicGraph3D_MAIN.m'
13 %
14 %           DATA *MUST* contain the following Fields:

```

```

15 %
16 % * IMG: Header of the input nifty Images.
17 % * GRID: Structure with Image Grid and Scales' infos for Resampling.
18 % * GGM: Geodesically Weighted Connectivity Matrix of the Over-Connected
19 %       Vascular Graph.
20 % * exploredminPath: struct containing the list of all the extracted and
21 %       explored connecting geodesics (minimal paths).
22 % * MST: Minimum Spanning Tree(s) Matrix obtained from GGM with
23 %       'Kruskal' method.
24 % * OrigSeedsIDX: list of Original Seeds;
25 % * ExtraSeedsIDX: list of automatically generated Seeds, during the
26 %       self-arranging refinement;
27 %
28 % CONFIGURATION INPUTS:
29 %
30 % - ['PruningLengthThresholdMM']: Length of leaves that should be pruned. -
31 %       Default: 5 [millimeters]
32 % - ['PruningIterativeSteps']: Number of steps for the iterative pruning. -
33 %       Default: 1
34 % - ['VicinityTHR_Leaves']: Threshold for spatially close leaves, that
35 %       should be merged together. -
36 %       Default: 1.5 [normalised units]
37 % - ['VicinityTHR_Nodes']: Threshold for spatially close nodes, that
38 %       should be welded together. -
39 %       Default: 3 [normalised units]
40 % - ['LeavesPruningROI']: ROI-based Mask for removing sputious leaves after
41 %       masking the Over-Connected Geodesic Graph
42 %       accodring to anatomical vascular territories. -
43 %       Default: [] (empty) -- This will be removed in
44 %       future releases!
45 % - ['TreeRootSeed']: Coordinate of the user-defined Root of the Tree(s).
46 %       [Root_X Root_Y Root_Z] array. - Default: [0 0 0]
47 % - ['SupervisedSeeds']: Bool flag for user-defined vs. automatic seeds. -
48 %       Default: true
49 % - ['GroupIDs2ConsiderRange']: max value of output trees (in case of a
50 %       Forest of MSTs) - Default: 1 -- Set to
51 %       'inf' for all MSTs.
52 % - ['GroupIDs2Consider']: when the identifier(s) of the MSTs is known
53 %       beforehand, use this parameter to select the
54 %       MSTs. - Default: [] (empty).
55 % - ['PadSize']: number of padding samples for smoothing the 3D coordinates
56 %       of the extracted MSTs edges. - Default: 5
57 % - ['ResampleRatio']: resampling ratio for smoothing/resampling the 3D
58 %       coordinates of the extracted MSTs edges. -
59 %       Default: 0.1
60 % - ['PathFolder']: exporting path folder. - Default: as in DATA.PathFolder

```



```

61
62
63 %% Outputs:
64 %
65 % - GeodesicMSTs: structure containing the 3D embedding, geodesic
66 %             information, and edge-connectivity of the extracted
67 %             Minimum Spanning Tree(s).
68 %             NB. in case multiple MSTs are obtained (Forest of MSTs),
69 %             the same structure lists all the elements with respective
70 %             group-identifiers.
71 %
72 %     GeodesicMSTs will contain the following Edges-related Fields:
73 %
74 % * CGPathContinuous: 3D sequence of coordinates for the conneted path.
75 % * CGPathID: Identifying label of the path (for the considered MST).
76 % * GeodesicEnergy: Integral value of the Geodesic Energy along the
77 %             3D connecting path.
78 % * GroupID: Identifier of the MST (in case of a forest of MSTs)
79 % * CGPathAdjacencyList: List of connecting edges (or paths) with respect
80 %             to the considered one.
81 % * EuclideanLength: Integral Euclidean length of the 3D connecting path.
82 % * isLeaf: Bool flag (true if the connecting edge is a leaf).
83 % * isRoot: Bool flag (true if the tree ROOT belongs to that edge).
84 %
85 % - GeodesicMSTsMatrix: structure containing the connectivity matrix
86 %             (adjacencies) for vectorial visualisation and
87 %             representation.
88 %
89 %     GeodesicMSTsMatrix will contain the following Fields:
90 %
91 % * M: Sparse matrix encoding the adjacency of the connected edges.

```

Demos In the current release two demos are included: `VTrailsDEMO_01.m` and `VTrailsDEMO_02.m`. These comprise a fully-automatic configuration of VTrails for the extraction of vascular trees from regional cerebral angiographies. In Fig. A.3, the visualisation of intermediate steps and of the resulting vectorial segmentation is given for `VTrailsDEMO_01.m`.

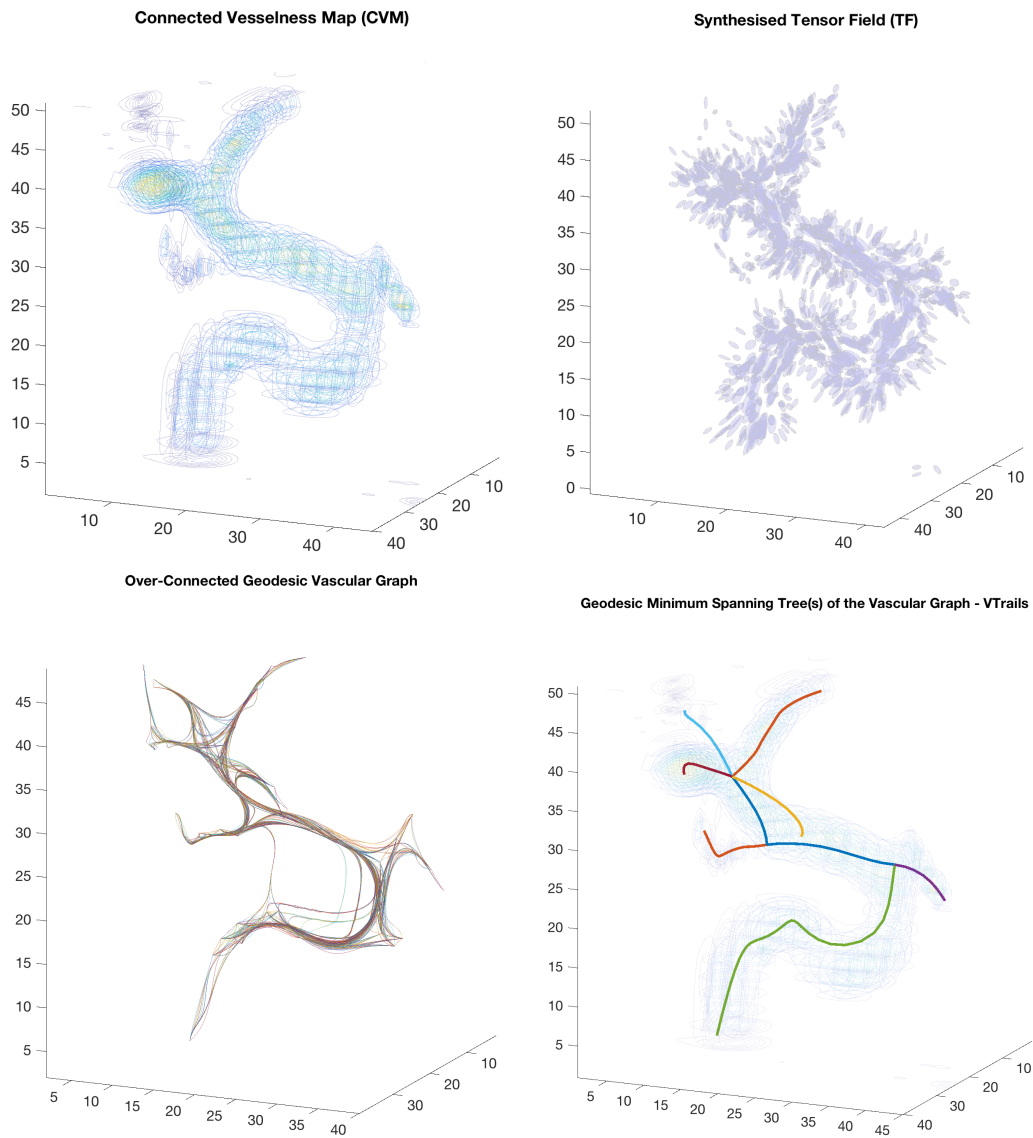


Figure A.3: VTrails Demo: Fully-automatic processing pipeline for the extraction of vascular trees from angiographic images. `VTrailsDEMO_01.m` – Connected Vesselness Map, Tensor Field, Over-Connected Geodesic Vascular Graph and resulting Minimum Spanning Tree.

Bibliography

- [1] D. Adalsteinsson and J. A. Sethian. A fast level set method for propagating interfaces. *Journal of Computational Physics*, 118(2):269 – 277, 1995.
- [2] C. Adams, Y. Abdulla, E. Torres, and R. Poston. Periventricular lesions in multiple sclerosis: their perivenous origin and relationship to granular ependymitis. *Neuropathology and Applied Neurobiology*, 13(2):141–152, 1987.
- [3] G. Agam, S. G. Armato, and C. Wu. Vessel tree reconstruction in thoracic CT scans with application to nodule detection. *IEEE Transactions on Medical Imaging*, 24(4):486–499, April 2005.
- [4] G. Agam and C. Wu. Probabilistic modeling based vessel enhancement in thoracic CT scans. In *2005 IEEE Computer Society Conference on Computer Vision and Pattern Recognition (CVPR'05)*, volume 2, pages 649–654 vol. 2, June 2005.
- [5] R. Annunziata, A. Kheirkhah, P. Hamrah, and E. Trucco. Scale and curvature invariant ridge detector for tortuous and fragmented structures. In *International Conference on Medical Image Computing and Computer-Assisted Intervention – MICCAI*, pages 588–595. Springer, 2015.
- [6] L. Antiga, T. Passerini, M. Piccinelli, and A. Veneziani. AneuriskWeb, the Aneurisk dataset repository. *URL: <http://ecm2.mathcs.emory.edu/aneuriskweb/>*, 2011.

- [7] L. Antiga, M. Piccinelli, L. Botti, B. Ene-Iordache, A. Remuzzi, and D. A. Steinman. An image-based modeling framework for patient-specific computational hemodynamics. *Medical and Biological Engineering and Computing*, 2008.
- [8] L. Antiga and D. Steinman. The Vascular Modeling Toolkit. URL: <http://www.vmtk.org>, 2008.
- [9] L. Antiga and D. A. Steinman. VMTK: vascular modeling toolkit, 2012.
- [10] A. M. Arias-Lorza, J. Petersen, A. van Engelen, M. Selwaness, A. van der Lugt, W. J. Niessen, and M. de Bruijne. Carotid artery wall segmentation in multispectral MRI by coupled optimal surface graph cuts. *IEEE Transactions on Medical Imaging*, 35(3):901–911, 2016.
- [11] V. Arsigny, P. Fillard, X. Pennec, and N. Ayache. Log-Euclidean metrics for fast and simple calculus on diffusion tensors. *Magnetic Resonance in Medicine*, 2006.
- [12] M. S. Arulampalam, S. Maskell, N. Gordon, and T. Clapp. A tutorial on particle filters for online nonlinear/non-Gaussian Bayesian tracking. *IEEE Transactions on Signal Processing*, 50(2):174–188, 2002.
- [13] J. Ashburner and K. J. Friston. Computing average shaped tissue probability templates. *Neuroimage*, 45(2):333–341, 2009.
- [14] S. Aylward, E. Bullitt, S. Pizer, and D. Eberly. Intensity ridge and widths for tubular object segmentation and description. In *Mathematical Methods in Biomedical Image Analysis, Proceedings of the Workshop on*, pages 131–138. IEEE, 1996.
- [15] S. Aylward, D. Pace, A. Enquobahrie, M. McCormick, C. Mullins, C. Goodlett, and P. Reynolds. TubeTK, segmentation, registration, and analysis of tubular structures in images. URL: <http://www.tubetk.org/> – Kitware Inc., 2012.

- [16] S. R. Aylward and E. Bullitt. Initialization, noise, singularities, and scale in height ridge traversal for tubular object centerline extraction. *IEEE Transactions on Medical Imaging*, 21(2):61–75, Feb 2002.
- [17] C. Bauer and H. Bischof. A novel approach for detection of tubular objects and its application to medical image analysis. In *Joint Pattern Recognition Symposium*, pages 163–172. Springer, 2008.
- [18] Y. Bazilevs, V. M. Calo, T. J. Hughes, and Y. Zhang. Isogeometric fluid-structure interaction: theory, algorithms, and computations. *Computational mechanics*, 43(1):3–37, 2008.
- [19] C. B. Beggs. Venous hemodynamics in neurological disorders: an analytical review with hydrodynamic analysis. *BMC Medicine*, 11(1):142, May 2013.
- [20] F. Benmansour and L. D. Cohen. Tubular structure segmentation based on minimal path method and anisotropic enhancement. *International Journal of Computer Vision*, 92(2):192–210, 2011.
- [21] F. Benmansour, L. D. Cohen, M. W. K. Law, and A. C. S. Chung. Tubular anisotropy for 2D vessel segmentation. In *2009 IEEE Conference on Computer Vision and Pattern Recognition*, pages 2286–2293, June 2009.
- [22] R. A. Bergman, A. K. Afifi, and R. Miyauchi. Illustrated encyclopedia of human anatomic variation: Circle of Willis. URL: <http://www.anatomyatlases.org/AnatomicVariants/>, 2007.
- [23] S. Bériault, Y. Xiao, D. L. Collins, and G. B. Pike. Automatic SWI venography segmentation using conditional random fields. *IEEE Transactions on Medical Imaging*, 34(12):2478–2491, 2015.
- [24] N. P. Bhatia and G. P. Szegő. *Stability Theory of Dynamical Systems*. Springer Science & Business Media, 2002.
- [25] H. Bogunovic, J. Pozo, R. Cardenes, L. San Roman, and A. Frangi. Anatomical labeling of the Circle of Willis using maximum a posteriori probability

- estimation. *IEEE Transactions on Medical Imaging*, 32(9):1587–1599, Sept 2013.
- [26] C. Boldak, Y. Rolland, C. Toumoulin, and J. Coatrieux. An improved model-based vessel tracking algorithm with application to computed tomography angiography. *Biocybernetics And Biomedical Engineering*, 23(1):41–64, 2003.
- [27] S. Bouix, K. Siddiqi, and A. Tannenbaum. Flux driven automatic centerline extraction. *Medical Image Analysis*, 9(3):209 – 221, 2005.
- [28] E. Bullitt. Healthy MR database: Designed database of MR brain images of healthy volunteers. *ITK-TubeTK*, 2007.
- [29] E. Bullitt, S. Aylward, A. Liu, J. Stone, S. K. Mukherji, C. Coffey, G. Gerig, and S. M. Pizer. 3D graph description of the intracerebral vasculature from segmented MRA and tests of accuracy by comparison with X-Ray angiograms. In *Biennial International Conference on Information Processing in Medical Imaging*, pages 308–321. Springer, 1999.
- [30] T. S. Caetano, J. J. McAuley, L. Cheng, Q. V. Le, and A. J. Smola. Learning graph matching. *IEEE Transactions on Pattern Analysis and Machine Intelligence*, 31(6):1048–1058, 2009.
- [31] M. J. Cardoso, M. J. Clarkson, M. Modat, and S. Ourselin. On the extraction of topologically correct thickness measurements using Khalimsky’s cubic complex. In *Biennial International Conference on Information Processing in Medical Imaging*, pages 159–170. Springer, 2011.
- [32] M. J. Cardoso, M. Modat, T. Vercauteren, and S. Ourselin. Scale factor point spread function matching: Beyond aliasing in image resampling. In *International Conference on Medical Image Computing and Computer-Assisted Intervention*, pages 675–683. Springer, 2015.

- [33] M. J. Cardoso, M. Modat, R. Wolz, A. Melbourne, D. Cash, D. Rueckert, and S. Ourselin. Geodesic information flows: spatially-variant graphs and their application to segmentation and fusion. *IEEE Transactions on Medical Imaging*, 34(9):1976–1988, 2015.
- [34] M. J. Cardoso, R. Wolz, M. Modat, N. C. Fox, D. Rueckert, and S. Ourselin. Geodesic information flows. In *International Conference on Medical Image Computing and Computer-Assisted Intervention – MICCAI*, pages 262–270. Springer, 2012.
- [35] G. Carlsson. Topology and data. *Bulletin of the American Mathematical Society*, 46(2):255–308, 2009.
- [36] J. R. Cebal, M. A. Castro, J. E. Burgess, R. S. Pergolizzi, M. J. Sheridan, and C. M. Putman. Characterization of cerebral aneurysms for assessing risk of rupture by using patient-specific computational hemodynamics models. *American Journal of Neuroradiology*, 26(10):2550–2559, 2005.
- [37] S. Cetin, A. Demir, A. Yezzi, M. Degertekin, and G. Unal. Vessel tractography using an intensity based tensor model with branch detection. *IEEE Transactions on Medical Imaging*, 32(2):348–363, 2013.
- [38] S. Cetin and G. Unal. A higher-order tensor vessel tractography for segmentation of vascular structures. *IEEE Transactions on Medical Imaging*, 34(10):2172–2185, 2015.
- [39] A. Charnoz, V. Agnus, G. Malandain, S. Nicolau, M. Tajine, and L. Soler. Design of robust vascular tree matching: Validation on liver. In *Biennial International Conference on Information Processing in Medical Imaging*, pages 443–455. Springer, 2005.
- [40] A. Charnoz, V. Agnus, G. Malandain, L. Soler, and M. Tajine. Tree matching applied to vascular system. In *International Workshop on Graph-Based Representations in Pattern Recognition*, pages 183–192. Springer, 2005.

- [41] H. Chen, L. Yu, Q. Dou, L. Shi, V. C. Mok, and P. A. Heng. Automatic detection of cerebral microbleeds via deep learning based 3D feature representation. In *Biomedical Imaging (ISBI), 2015 IEEE 12th International Symposium on*, pages 764–767. IEEE, 2015.
- [42] Y. Chen, L. Guibas, and Q. Huang. Near-optimal joint object matching via convex relaxation. In *International Conference on Machine Learning*, pages 100–108, 2014.
- [43] Y. Cheng, X. Hu, J. Wang, Y. Wang, and S. Tamura. Accurate vessel segmentation with constrained B-snake. *IEEE Transactions on Image Processing*, 24(8):2440–2455, 2015.
- [44] C.-L. Chin, B.-J. Lin, G.-R. Wu, T.-C. Weng, C.-S. Yang, R.-C. Su, and Y.-J. Pan. An automated early ischemic stroke detection system using CNN deep learning algorithm. In *Awareness Science and Technology (iCAST), 2017 IEEE 8th International Conference on*, pages 368–372. IEEE, 2017.
- [45] C. Chnafa, K. Valen-Sendstad, O. Brina, V. Pereira, and D. Steinman. Improved reduced-order modelling of cerebrovascular flow distribution by accounting for arterial bifurcation pressure drops. *Journal of Biomechanics*, 51:83 – 88, 2017.
- [46] M. Cho, K. Alahari, and J. Ponce. Learning graphs to match. In *Proceedings of the IEEE International Conference on Computer Vision*, pages 25–32, 2013.
- [47] M. Cho, J. Lee, and K. M. Lee. Reweighted random walks for graph matching. In *European Conference on Computer Vision*, pages 492–505. Springer, 2010.
- [48] A. C. S. Chung, J. A. Noble, and P. Summers. Vascular segmentation of phase contrast magnetic resonance angiograms based on statistical mixture modeling and local phase coherence. *IEEE Transactions on Medical Imaging*, 23(12):1490–1507, Dec 2004.

- [49] Y. Cointepas, I. Bloch, and L. Garnero. A cellular model for multi-objects multi-dimensional homotopic deformations. *Pattern Recognition*, 34(9):1785–1798, 2001.
- [50] M. Couprie. Topological maps and robust hierarchical Euclidean skeletons in cubical complexes. *Computer Vision and Image Understanding*, 117(4):355–369, 2013.
- [51] T. Cour, P. Srinivasan, and J. Shi. Balanced graph matching. In *Advances in Neural Information Processing Systems*, pages 313–320, 2007.
- [52] J. M. Coutinho, J. J. Gerritsma, S. M. Zuurbier, and J. Stam. Isolated cortical vein thrombosis: systematic review of case reports and case series. *Stroke*, 45(6):1836–1838, 2014.
- [53] A. Dasgupta and S. Singh. A fully convolutional neural network based structured prediction approach towards the retinal vessel segmentation. In *Biomedical Imaging (ISBI 2017), 2017 IEEE 14th International Symposium on*, pages 248–251. IEEE, 2017.
- [54] M. De Bruijne, B. Van Ginneken, W. J. Niessen, M. Loog, and M. A. Viergever. Model-based segmentation of abdominal aortic aneurysms in CTA images. In *Medical Imaging 2003*, pages 1560–1571. International Society for Optics and Photonics, 2003.
- [55] C. de Falco, A. Reali, and R. Vázquez. GeoPDEs: a research tool for isogeometric analysis of PDEs. *Advances in Engineering Software*, 42(12):1020–1034, 2011.
- [56] T. Deschamps and L. D. Cohen. Fast extraction of tubular and tree 3D surfaces with front propagation methods. In *Object Recognition Supported by User Interaction for Service Robots*, volume 1, pages 731–734 vol.1, 2002.

- [57] S. Dhifallah and I. Rekik. Clustering-based multi-view network fusion for estimating brain network atlases of healthy and disordered populations. *Journal of Neuroscience Methods*, 2018.
- [58] E. W. Dijkstra. A note on two problems in connexion with graphs. *Numerische Mathematik*, 1(1):269–271, 1959.
- [59] P. Dłotko and R. Specogna. Topology preserving thinning of cell complexes. *IEEE Transactions on Image Processing*, 23(10):4486–4495, 2014.
- [60] P. Dokládal, C. Lohou, L. Perroton, and G. Bertrand. Liver blood vessels extraction by a 3-D topological approach. In *International Conference on Medical Image Computing and Computer-Assisted Intervention – MICCAI*, pages 98–105. Springer, 1999.
- [61] J. Donahue, L. Anne Hendricks, S. Guadarrama, M. Rohrbach, S. Venugopalan, K. Saenko, and T. Darrell. Long-term recurrent convolutional networks for visual recognition and description. In *Proceedings of the IEEE Conference on Computer Vision and Pattern Recognition*, pages 2625–2634, 2015.
- [62] S. Durrleman, P. Fillard, X. Pennec, A. Trouvé, and N. Ayache. Registration, atlas estimation and variability analysis of white matter fiber bundles modeled as currents. *NeuroImage*, 55(3):1073–1090, 2011.
- [63] D. Eppstein. Subgraph isomorphism in planar graphs and related problems. In *Graph Algorithms And Applications I*, pages 283–309. World Scientific, 2002.
- [64] E. Farkas and P. G. Luiten. Cerebral microvascular pathology in aging and Alzheimer’s disease. *Progress in Neurobiology*, 64(6):575 – 611, 2001.
- [65] A. Feragen, J. Petersen, M. Owen, P. Lo, L. H. Thomsen, M. M. Wille, A. Dirksen, and M. de Bruijne. A hierarchical scheme for geodesic anatomical labeling of airway trees. In *International Conference on Medical Image*

- Computing and Computer-Assisted Intervention – MICCAI*, pages 147–155. Springer, 2012.
- [66] P. T. Fletcher, S. Venkatasubramanian, and S. Joshi. The geometric median on Riemannian manifolds with application to robust atlas estimation. *NeuroImage*, 45(1):S143–S152, 2009.
- [67] C. Florin, N. Paragios, and J. Williams. Particle filters, a quasi-monte carlo solution for segmentation of coronaries. In *International Conference on Medical Image Computing and Computer-Assisted Intervention – MICCAI*, pages 246–253. Springer, 2005.
- [68] C. Florin, N. Paragios, and J. Williams. Globally optimal active contours, sequential Monte Carlo and on-line learning for vessel segmentation. In *European Conference on Computer Vision*, pages 476–489. Springer, 2006.
- [69] A. F. Frangi, W. J. Niessen, R. M. Hoogeveen, T. van Walsum, and M. A. Viergever. Model-based quantitation of 3-D magnetic resonance angiographic images. *IEEE Transactions on Medical Imaging*, 18(10):946–956, Oct 1999.
- [70] A. F. Frangi, W. J. Niessen, K. L. Vincken, and M. A. Viergever. Multiscale vessel enhancement filtering. In *International Conference on Medical Image Computing and Computer-Assisted Intervention – MICCAI*, pages 130–137. Springer, 1998.
- [71] Y. Fridman. *Extracting Branching Object Geometry via Cores*. PhD thesis, University of North Carolina at Chapel Hill, 2004.
- [72] Y. Fridman, S. M. Pizer, S. Aylward, and E. Bullitt. Segmenting 3D branching tubular structures using cores. In *International Conference on Medical Image Computing and Computer-Assisted Intervention – MICCAI*, pages 570–577. Springer, 2003.

- [73] O. Friman, M. Hindennach, C. Kühnel, and H.-O. Peitgen. Multiple hypothesis template tracking of small 3D vessel structures. *Medical Image Analysis*, 14(2):160–171, 2010.
- [74] F. J. Gijsen, J. J. Wentzel, A. Thury, B. Lamers, J. C. Schuurbiers, P. W. Serruys, and A. F. Van der Steen. A new imaging technique to study 3-D plaque and shear stress distribution in human coronary artery bifurcations in vivo. *Journal of Biomechanics*, 40(11):2349–2357, 2007.
- [75] T. A. Gillette, K. M. Brown, and G. A. Ascoli. The DIADEM metric: Comparing multiple reconstructions of the same neuron. *Neuroinformatics*, 9(2):233, Apr 2011.
- [76] S. Gold and A. Rangarajan. A graduated assignment algorithm for graph matching. *IEEE Transactions on Pattern Analysis and Machine Intelligence*, 18(4):377–388, 1996.
- [77] F. Graziano, V. Russo, W. Wang, D. Khismatullin, and A. Ulm. 3D computational fluid dynamics of a treated vertebrobasilar giant aneurysm: a multistage analysis. *American Journal of Neuroradiology*, 34(7):1387–1394, 2013.
- [78] J. C. Grotta, D. Chiu, M. Lu, S. Patel, S. R. Levine, B. C. Tilley, T. G. Brott, E. C. Haley, et al. Agreement and variability in the interpretation of early CT changes in stroke patients qualifying for intravenous rtPA therapy. *Stroke*, 30(8):1528–1533, 1999.
- [79] M. A. Gülsün and H. Tek. Robust vessel tree modeling. In *International Conference on Medical Image Computing and Computer-Assisted Intervention – MICCAI*, pages 602–611. Springer, 2008.
- [80] E. M. Haacke and J. R. Reichenbach. *Susceptibility weighted imaging in MRI: basic concepts and clinical applications*. John Wiley & Sons, 2014.

- [81] E. M. Haacke, Y. Xu, Y.-C. N. Cheng, and J. R. Reichenbach. Susceptibility weighted imaging (SWI). *Magnetic Resonance in Medicine*, 52(3):612–618, 2004.
- [82] G. Hamarneh and P. Jassi. VascuSynth: Simulating vascular trees for generating volumetric image data with ground-truth segmentation and tree analysis. *Computerized Medical Imaging and Graphics*, 34(8):605–616, 2010.
- [83] K. Hameeteman, M. Zuluaga, M. Freiman, L. Joskowicz, O. Cuisenaire, L. F. Valencia, M. Gulsun, K. Krissian, J. Mille, W. Wong, M. Orkisz, H. Tek, M. H. Hoyos, F. Benmansour, A. Chung, S. Rozie, M. van Gils, L. van den Borne, J. Sosna, P. Berman, N. Cohen, P. Douek, I. Sanchez, M. Aissat, M. Schaap, C. Metz, G. Krestin, A. van der Lugt, W. Niessen, and T. van Walsum. Evaluation framework for carotid bifurcation lumen segmentation and stenosis grading. *Medical Image Analysis*, 2011.
- [84] M. Hernández-Hoyos, A. Anwander, M. Orkisz, J.-P. Roux, P. Douek, and I. E. Magnin. A deformable vessel model with single point initialization for segmentation, quantification, and visualization of blood vessels in 3D MRA. In *International Conference on Medical Image Computing and Computer-Assisted Intervention – MICCAI*, pages 735–745. Springer, 2000.
- [85] S. Hirsch, J. Reichold, M. Schneider, G. Székely, and B. Weber. Topology and hemodynamics of the cortical cerebrovascular system. *Journal of Cerebral Blood Flow & Metabolism*, 32(6):952–967, 2012.
- [86] H. Homann. Implementation of a 3D thinning algorithm. *Insight Journal*, 421, 2007.
- [87] M. H. Hoyos, P. Orłowski, E. Piktowska-Janko, P. Bogorodzki, and M. Orkisz. Vascular centerline extraction in 3D MR angiograms for phase contrast MRI blood flow measurement. *International Journal of Computer Assisted Radiology and Surgery*, 1(1):51–61, 2006.

- [88] M.-C. Hsu and Y. Bazilevs. Blood vessel tissue prestress modeling for vascular fluid–structure interaction simulation. *Finite Elements in Analysis and Design*, 47(6):593 – 599, 2011. The Twenty-Second Annual Robert J. Melosh Competition.
- [89] G. Hu, H. Cao, X. Wang, and X. Qin. G-2 continuity conditions for generalized Bézier-like surfaces with multiple shape parameters. *Journal of Inequalities and Applications*, 2017(1):248, 2017.
- [90] T. J. Hughes, J. A. Cottrell, and Y. Bazilevs. Isogeometric analysis: CAD, finite elements, NURBS, exact geometry and mesh refinement. *Computer Methods in Applied Mechanics and Engineering*, 194(39-41):4135–4195, 2005.
- [91] J. R. Jenkins. *Atlas of Neuroradiologic Embryology, Anatomy, and Variants*. Lippincott Williams & Wilkins, 2000.
- [92] L.-D. Jou, G. Wong, B. Dispensa, M. T. Lawton, R. T. Higashida, W. L. Young, and D. Saloner. Correlation between luminal geometry changes and hemodynamics in fusiform intracranial aneurysms. *American Journal of Neuroradiology*, 26(9):2357–2363, 2005.
- [93] R. E. Kalman. A new approach to linear filtering and prediction problems. *Journal of Basic Engineering*, 82(1):35–45, 1960.
- [94] A. Kanitsar, D. Fleischmann, R. Wegenkittl, P. Felkel, and M. E. Gröller. CPR: Curved planar reformation. In *Proceedings of the Conference on Visualization*, pages 37–44. IEEE Computer Society, 2002.
- [95] M. Kerschnitzki, P. Kollmannsberger, M. Burghammer, G. N. Duda, R. Weinkamer, W. Wagermaier, and P. Fratzl. Architecture of the osteocyte network correlates with bone material quality. *Journal of Bone and Mineral Research*, 28(8):1837–1845, 2013.

- [96] C. S. Kidwell, J. A. Chalela, J. L. Saver, S. Starkman, M. D. Hill, A. M. Demchuk, J. A. Butman, N. Patronas, J. R. Alger, L. L. Latour, M. L. Luby, A. E. Baird, M. C. Leary, M. Tremwel, B. Ovbiagele, A. Fredieu, S. Suzuki, J. P. Villablanca, S. Davis, B. Dunn, J. W. Todd, M. A. Ezzeddine, J. Haymore, J. K. Lynch, L. Davis, and S. Warach. Comparison of MRI and CT for detection of acute intracerebral hemorrhage. *Jama*, 292(15):1823–1830, 2004.
- [97] H. Y. Kim and S. A. De Araújo. Grayscale template-matching invariant to rotation, scale, translation, brightness and contrast. In *Pacific-Rim Symposium on Image and Video Technology*, pages 100–113. Springer, 2007.
- [98] R. Kimmel and J. A. Sethian. Computing geodesic paths on manifolds. *Proceedings of the National Academy of Sciences*, 95(15):8431–8435, 1998.
- [99] C. Kirbas and F. Quek. A review of vessel extraction techniques and algorithms. *ACM Computing Surveys (CSUR)*, 36(2):81–121, 2004.
- [100] T. M. Koller, G. Gerig, G. Szekely, and D. Dettwiler. Multiscale detection of curvilinear structures in 2-D and 3-D image data. In *Proceedings of IEEE International Conference on Computer Vision*, pages 864–869, Jun 1995.
- [101] H. Kong, H. C. Akakin, and S. E. Sarma. A generalized Laplacian of Gaussian filter for blob detection and its applications. *IEEE Transactions on Cybernetics*, 43(6):1719–1733, 2013.
- [102] E. Konukoglu, M. Sermesant, O. Clatz, J.-M. Peyrat, H. Delingette, and N. Ayache. A recursive anisotropic fast marching approach to reaction diffusion equation: Application to tumor growth modeling. In *Biennial International Conference on Information Processing in Medical Imaging*, pages 687–699. Springer, 2007.
- [103] K. Krissian, G. Malandain, N. Ayache, R. Vaillant, and Y. Troussset. Model-based detection of tubular structures in 3D images. *Computer Vision and Image Understanding*, 80(2):130 – 171, 2000.

- [104] R. Kwitt, D. Pace, M. Niethammer, and S. Aylward. Studying cerebral vasculature using structure proximity and graph kernels. In *International Conference on Medical Image Computing and Computer-Assisted Intervention – MICCAI*, pages 534–541. Springer, 2013.
- [105] C. Lacoste, G. Finet, and I. E. Magnin. Coronary tree extraction from X-ray angiograms using marked point processes. In *3rd IEEE International Symposium on Biomedical Imaging: Nano to Macro, 2006.*, pages 157–160, April 2006.
- [106] M. W. Law and A. C. Chung. Three dimensional curvilinear structure detection using optimally oriented flux. In *European Conference on Computer Vision*, pages 368–382. Springer, 2008.
- [107] M. W. K. Law and A. C. S. Chung. Efficient implementation for spherical flux computation and its application to vascular segmentation. *IEEE Transactions on Image Processing*, 18(3):596–612, March 2009.
- [108] E. T. Lee. Choosing nodes in parametric curve interpolation. *Computer-Aided Design*, 21(6):363–370, 1989.
- [109] J. Lee, P. Beighley, E. Ritman, and N. Smith. Automatic segmentation of 3D micro-CT coronary vascular images. *Medical Image Analysis*, 11(6):630 – 647, 2007.
- [110] M. Leordeanu and M. Hebert. A spectral technique for correspondence problems using pairwise constraints. In *IEEE International Conference on Computer Vision*, volume 2, pages 1482–1489. IEEE, 2005.
- [111] M. Leordeanu, M. Hebert, and R. Sukthankar. An integer projected fixed point method for graph matching and map inference. In *Advances in Neural Information Processing Systems*, pages 1114–1122, 2009.

- [112] D. Lesage, E. D. Angelini, I. Bloch, and G. Funka-Lea. A review of 3D vessel lumen segmentation techniques: Models, features and extraction schemes. *Medical Image Analysis*, 13(6):819–845, 2009.
- [113] D. Lesage, E. D. Angelini, G. Funka-Lea, and I. Bloch. Adaptive particle filtering for coronary artery segmentation from 3D CT angiograms. *Computer Vision and Image Understanding*, 151:29 – 46, 2016. Probabilistic Models for Biomedical Image Analysis.
- [114] E. Levy, R. Mehta, R. Gupta, R. Hanel, A. Chamczuk, D. Fiorella, H. Woo, F. Albuquerque, T. Jovin, M. Horowitz, and L. Hopkins. Self-expanding stents for recanalization of acute cerebrovascular occlusions. *American Journal of Neuroradiology*, 28(5):816–822, 2007.
- [115] R. Li and S. Ourselin. Accurate curvilinear modelling for precise measurements of tubular structures. In *Digital Image Computing: Techniques and Applications; Proceedings of the VII Biennial Australian Pattern Recognition Society Conference, DICTA 2003*, page 243, 2003.
- [116] R. Liao, D. Luc, Y. Sun, and K. Kirchberg. 3-D reconstruction of the coronary artery tree from multiple views of a rotational X-ray angiography. *International Journal of Cardiac Imaging*, 2009.
- [117] J. K. Lin and P. Dayan. Curved Gaussian models with application to the modeling of foreign exchange rates. In *Computational Finance*. MIT Press, 1999.
- [118] Q. Lin. *Enhancement, extraction, and visualization of 3D volume data*. PhD thesis, Linköping University Electronic Press, 2003.
- [119] P. Liskowski and K. Krawiec. Segmenting retinal blood vessels with deep neural networks. *IEEE Transactions on Medical Imaging*, 35(11):2369–2380, 2016.

- [120] E. M. Loiola, N. M. M. de Abreu, P. O. Boaventura-Netto, P. Hahn, and T. Querido. A survey for the quadratic assignment problem. *European Journal of Operational Research*, 176(2):657–690, 2007.
- [121] H. Lombaert, L. Grady, X. Pennec, N. Ayache, and F. Cheriet. Spectral log-demons: diffeomorphic image registration with very large deformations. *International Journal of Computer Vision*, 107(3):254–271, 2014.
- [122] L. Lorigo, O. Faugeras, W. Grimson, R. Keriven, R. Kikinis, A. Nabavi, and C.-F. Westin. CURVES: Curve evolution for vessel segmentation. *Medical Image Analysis*, 5(3):195 – 206, 2001.
- [123] P. Y. Lum, G. Singh, A. Lehman, T. Ishkanov, M. Vejdemo-Johansson, M. Alagappan, J. Carlsson, and G. Carlsson. Extracting insights from the shape of complex data using topology. *Scientific Reports*, 3, 2013.
- [124] M. E. MacDonald and R. Frayne. Cerebrovascular MRI: a review of state-of-the-art approaches, methods and techniques. *NMR in Biomedicine*, 2015.
- [125] R. Manniesing and W. Niessen. Local speed functions in level set based vessel segmentation. In *International Conference on Medical Image Computing and Computer-Assisted Intervention – MICCAI*, pages 475–482. Springer, 2004.
- [126] R. Manniesing, M. A. Viergever, and W. J. Niessen. Vessel enhancing diffusion: a scale space representation of vessel structures. *Medical Image Analysis*, 10(6):815 – 825, 2006.
- [127] A. L. Marsden, J. A. Feinstein, and C. A. Taylor. A computational framework for derivative-free optimization of cardiovascular geometries. *Computer Methods in Applied Mechanics and Engineering*, 197(21-24):1890–1905, 2008.
- [128] C. Mathers, D. M. Fat, and J. T. Boerma. *The Global Burden of Disease: 2004 Update*. World Health Organization, 2008.

- [129] A. M. Mendrik, E.-J. Vonken, A. Rutten, M. A. Viergeever, and B. van Ginneken. Noise reduction in computed tomography scans using 3-D anisotropic hybrid diffusion with continuous switch. *IEEE Transactions on Medical Imaging*, 28(10):1585–1594, 2009.
- [130] E. W. Merrill and G. A. Pelletier. Viscosity of human blood: transition from Newtonian to non-Newtonian. *Journal of Applied Physiology*, 23(2):178–182, 1967.
- [131] O. Merveille, H. Talbot, L. Najman, and N. Passat. Curvilinear structure analysis by ranking the orientation responses of path operators. *IEEE Transactions on Pattern Analysis and Machine Intelligence*, 40(2):304–317, 2018.
- [132] C. Metz, M. Schaap, A. V. D. Giessen, T. V. Walsum, and W. Niessen. Semi-automatic coronary artery centerline extraction in computed tomography angiography data. In *2007 4th IEEE International Symposium on Biomedical Imaging: From Nano to Macro*, pages 856–859, April 2007.
- [133] J. Mille, R. Boné, and L. D. Cohen. Region-based 2D deformable generalized cylinder for narrow structures segmentation. In *European Conference on Computer Vision*, pages 392–404. Springer, 2008.
- [134] J. Mille and L. D. Cohen. Deformable tree models for 2D and 3D branching structures extraction. In *2009 IEEE Computer Society Conference on Computer Vision and Pattern Recognition Workshops*, pages 149–156, June 2009.
- [135] J. Mo and L. Zhang. Multi-level deep supervised networks for retinal vessel segmentation. *International Journal of Computer Assisted Radiology and Surgery*, 12(12):2181–2193, 2017.
- [136] S. Moccia, E. D. Momi, S. E. Hadji, and L. S. Mattos. Blood vessel segmentation algorithms — review of methods, datasets and evaluation metrics. *Computer Methods and Programs in Biomedicine*, 158:71 – 91, 2018.

- [137] N. R. Mollet, F. Cademartiri, C. A. van Mieghem, G. Runza, E. P. McFadden, T. Baks, P. W. Serruys, G. P. Krestin, and P. J. de Feyter. High-resolution spiral computed tomography coronary angiography in patients referred for diagnostic conventional coronary angiography. *Circulation*, 112(15):2318–2323, 2005.
- [138] S. Monti, S. Coccozza, P. Borrelli, S. Straub, M. E. Ladd, M. Salvatore, E. Tedeschi, and G. Palma. MAVEN: an algorithm for multi-parametric automated segmentation of brain veins from gradient echo acquisitions. *IEEE Transactions on Medical Imaging*, 36(5):1054–1065, 2017.
- [139] S. Moriconi, M. A. Zuluaga, H. R. Jäger, P. Nachev, S. Ourselin, and M. J. Cardoso. VTrails: Inferring vessels with geodesic connectivity trees. In *International Conference on Information Processing in Medical Imaging*, pages 672–684. Springer, 2017.
- [140] A. Mosinska, J. Tarnawski, and P. Fua. Active learning and proofreading for delineation of curvilinear structures. In *International Conference on Medical Image Computing and Computer-Assisted Intervention – MICCAI*, pages 165–173. Springer, 2017.
- [141] T. Neumann-Haefelin, M. E. Moseley, and G. W. Albers. New magnetic resonance imaging methods for cerebrovascular disease: Emerging clinical applications. *Annals of Neurology*, 47(5):559–570, 2000.
- [142] W. L. Nowinski, I. Volkau, Y. Marchenko, A. Thirunavuukarasuu, T. T. Ng, and V. M. Runge. A 3D model of human cerebrovasculature derived from 3T magnetic resonance angiography. *Neuroinformatics*, 7(1):23–36, 2009.
- [143] S. D. Olabarriaga, J. M. Rouet, M. Fradkin, M. Breeuwer, and W. J. Niessen. Segmentation of thrombus in abdominal aortic aneurysms from CTA with nonparametric statistical grey level appearance modeling. *IEEE Transactions on Medical Imaging*, 24(4):477–485, April 2005.

- [144] D. H. O’Leary and M. L. Bots. Imaging of atherosclerosis: carotid intima–media thickness. *European Heart Journal*, 31(14):1682–1689, 2010.
- [145] M. S. Olufsen, A. Nadim, and L. A. Lipsitz. Dynamics of cerebral blood flow regulation explained using a lumped parameter model. *American Journal of Physiology-Regulatory, Integrative and Comparative Physiology*, 282(2):R611–R622, 2002. PMID: 11792673.
- [146] O. Onaizah, T. Poepping, and M. Zamir. A model of blood supply to the brain via the carotid arteries: Effects of obstructive vs. sclerotic changes. *Medical Engineering & Physics*, 49:121 – 130, 2017.
- [147] D. Pachauri, R. Kondor, and V. Singh. Solving the multi-way matching problem by permutation synchronization. In *Advances in Neural Information Processing Systems*, pages 1860–1868, 2013.
- [148] H.-M. Park and K.-J. Yoon. Consistent multiple graph matching with multi-layer random walks synchronization. *Pattern Recognition Letters*, 2018.
- [149] N. Passat, C. Ronse, J. Baruthio, J.-P. Armspach, and C. Maillot. Magnetic resonance angiography: From anatomical knowledge modeling to vessel segmentation. *Medical Image Analysis*, 10(2):259 – 274, 2006.
- [150] M. Pawlik and N. Augsten. Tree edit distance: Robust and memory-efficient. *Information Systems*, 56(Supplement C):157 – 173, 2016.
- [151] M. Pechaud, R. Keriven, and G. Peyre. Extraction of tubular structures over an orientation domain. In *2009 IEEE Conference on Computer Vision and Pattern Recognition*, pages 336–342, June 2009.
- [152] X. Pennec. *Statistical Computing on Manifolds: From Riemannian Geometry to Computational Anatomy*, pages 347–386. Springer Berlin Heidelberg, Berlin, Heidelberg, 2009.
- [153] J. Petersen, M. Modat, M. J. Cardoso, A. Dirksen, S. Ourselin, and M. de Bruijne. Quantitative airway analysis in longitudinal studies using

- groupwise registration and 4D optimal surfaces. In *International Conference on Medical Image Computing and Computer-Assisted Intervention – MICCAI*, pages 287–294. Springer, 2013.
- [154] R. Phellan, A. Peixinho, A. Falcão, and N. D. Forkert. Vascular segmentation in TOF MRA images of the brain using a deep convolutional neural network. In *MICCAI Workshop - Intravascular Imaging and Computer Assisted Stenting, and Large-Scale Annotation of Biomedical Data and Expert Label Synthesis*, pages 39–46, 2017.
- [155] M. Piccinelli, A. Veneziani, D. A. Steinman, A. Remuzzi, and L. Antiga. A framework for geometric analysis of vascular structures: Application to cerebral aneurysms. *IEEE Transactions on Medical Imaging*, 28(8):1141–1155, Aug 2009.
- [156] L. Piegl and W. Tiller. *The NURBS book*. Springer Science & Business Media, 2012.
- [157] J. Princen and A. Bradley. Analysis/synthesis filter bank design based on time domain aliasing cancellation. *IEEE Transactions on Acoustics, Speech, and Signal Processing*, 34(5):1153–1161, 1986.
- [158] F. K. H. Quek and C. Kirbas. Vessel extraction in medical images by wave-propagation and traceback. *IEEE Transactions on Medical Imaging*, 20(2):117–131, Feb 2001.
- [159] A. Raabe, J. Beck, S. Rohde, J. Berkefeld, and V. Seifert. Three-dimensional rotational angiography guidance for aneurysm surgery. *Journal of Neurosurgery*, 105(3):406–411, 2006.
- [160] A. Radford, L. Metz, and S. Chintala. Unsupervised representation learning with deep convolutional generative adversarial networks. *arXiv preprint arXiv:1511.06434*, 2015.

- [161] I. Rekik, G. Li, W. Lin, and D. Shen. Estimation of brain network atlases using diffusive-shrinking graphs: Application to developing brains. In *Information Processing in Medical Imaging*, pages 385–397, Cham, 2017. Springer International Publishing.
- [162] D. N. Reshef, Y. A. Reshef, H. K. Finucane, S. R. Grossman, G. McVean, P. J. Turnbaugh, E. S. Lander, M. Mitzenmacher, and P. C. Sabeti. Detecting novel associations in large data sets. *Science*, 334(6062):1518–1524, 2011.
- [163] M. Rochery, I. H. Jermyn, and J. Zerubia. New higher-order active contour energies for network extraction. In *IEEE International Conference on Image Processing 2005*, volume 2, pages II–822–5, Sept 2005.
- [164] M. Rochery, I. H. Jermyn, and J. Zerubia. Higher order active contours. *International Journal of Computer Vision*, 69(1):27–42, 2006.
- [165] Y. Rouchdy and L. D. Cohen. Geodesic voting for the automatic extraction of tree structures. Methods and applications. *Computer Vision and Image Understanding*, 117(10):1453–1467, 2013.
- [166] J. Ryu, X. Hu, and S. C. Shadden. A coupled lumped-parameter and distributed network model for cerebral pulse-wave hemodynamics. *Journal of Biomechanical Engineering*, 137(10):101009, 2015.
- [167] P. K. Saha, G. Borgefors, and G. S. di Baja. A survey on skeletonization algorithms and their applications. *Pattern Recognition Letters*, 76:3–12, 2016.
- [168] P. K. Saha, R. Strand, and G. Borgefors. Digital topology and geometry in medical imaging: a survey. *IEEE Transactions on Medical Imaging*, 34(9):1940–1964, 2015.
- [169] Y. Sato, S. Nakajima, N. Shiraga, H. Atsumi, S. Yoshida, T. Koller, G. Gerig, and R. Kikinis. Three-dimensional multi-scale line filter for segmentation and visualization of curvilinear structures in medical images. *Medical Image Analysis*, 2(2):143–168, 1998.

- [170] M. Schaap, R. Manniesing, I. Smal, T. Van Walsum, A. Van Der Lugt, and W. Niessen. Bayesian tracking of tubular structures and its application to carotid arteries in CTA. In *International Conference on Medical Image Computing and Computer-Assisted Intervention – MICCAI*, pages 562–570. Springer, 2007.
- [171] M. Schaap, I. Smal, C. Metz, T. van Walsum, and W. Niessen. Bayesian tracking of elongated structures in 3D images. In *Biennial International Conference on Information Processing in Medical Imaging*, pages 74–85. Springer, 2007.
- [172] J. Schmidhuber. Deep learning in neural networks: An overview. *Neural Networks*, 61:85–117, 2015.
- [173] P. J. Schneider. An algorithm for automatically fitting digitized curves. In *Graphics gems*, pages 612–626. Academic Press Professional, Inc., 1990.
- [174] E. Serradell, M. A. Pinheiro, R. Sznitman, J. Kybic, F. Moreno-Noguer, and P. Fua. Non-rigid graph registration using active testing search. *IEEE Transactions on Pattern Analysis and Machine Intelligence*, 37(3):625–638, March 2015.
- [175] J. A. Sethian. A Fast Marching level set method for monotonically advancing fronts. *Proceedings of the National Academy of Sciences*, 93(4):1591–1595, 1996.
- [176] R. Shahzad, O. Dzyubachyk, M. Staring, J. Kullberg, L. Johansson, H. Ahlström, B. P. Lelieveldt, and R. J. van der Geest. Automated extraction and labelling of the arterial tree from whole-body MRA Data. *Medical Image Analysis*, 2015.
- [177] M. Shojima, M. Oshima, K. Takagi, R. Torii, M. Hayakawa, K. Katada, A. Morita, and T. Kirino. Magnitude and role of wall shear stress on cerebral aneurysm: computational fluid dynamic study of 20 middle cerebral artery aneurysms. *Stroke*, 35(11):2500–2505, 2004.

- [178] A. Solé-Ribalta and F. Serratos. Graduated assignment algorithm for multiple graph matching based on a common labeling. *International Journal of Pattern Recognition and Artificial Intelligence*, 27(01):1350001, 2013.
- [179] B. Spronck, E. G. H. J. Martens, E. D. Gommer, and F. N. van de Vosse. A lumped parameter model of cerebral blood flow control combining cerebral autoregulation and neurovascular coupling. *American Journal of Physiology-Heart and Circulatory Physiology*, 303(9):H1143–H1153, 2012. PMID: 22777421.
- [180] D. Steinman, D. Vorp, and C. Ethier. Computational modeling of arterial biomechanics: Insights into pathogenesis and treatment of vascular disease. *Journal of Vascular Surgery*, 37(5):1118 – 1128, 2003.
- [181] A. Szymczak, A. Tannenbaum, and K. Mischaikow. Coronary vessel cores from 3D imagery: a topological approach. In *Medical Imaging*, pages 505–513. International Society for Optics and Photonics, 2005.
- [182] B. T. Tang, C. P. Cheng, M. T. Draney, N. M. Wilson, P. S. Tsao, R. J. Herfkens, and C. A. Taylor. Abdominal aortic hemodynamics in young healthy adults at rest and during lower limb exercise: quantification using image-based computer modeling. *American Journal of Physiology-Heart and Circulatory Physiology*, 2006.
- [183] C. Taylor and J. Humphrey. Open problems in computational vascular biomechanics: Hemodynamics and arterial wall mechanics. *Computer Methods in Applied Mechanics and Engineering*, 198(45):3514 – 3523, 2009. Models and Methods in Computational Vascular and Cardiovascular Mechanics.
- [184] C. A. Taylor and M. T. Draney. Experimental and computational methods in cardiovascular fluid mechanics. *Annual Review of Fluid Mechanics*, 36:197–231, 2004.
- [185] C. A. Taylor, T. J. Hughes, and C. K. Zarins. Computational investigations in vascular disease. *Computers in Physics*, 10(3):224–232, 1996.

- [186] C. A. Taylor, T. J. Hughes, and C. K. Zarins. Finite element modeling of blood flow in arteries. *Computer Methods in Applied Mechanics and Engineering*, 158(1):155 – 196, 1998.
- [187] R. Toledo, X. Orriols, X. Binefa, P. Radeva, J. Vitria, and J. J. Villanueva. Tracking elongated structures using statistical snakes. In *Proceedings IEEE Conference on Computer Vision and Pattern Recognition. CVPR 2000 (Cat. No.PR00662)*, volume 1, pages 157–162 vol.1, 2000.
- [188] R. Toledo, X. Orriols, P. Radeva, X. Binefa, J. Vitria, C. Canero, and J. J. Villanuev. Eigensnakes for vessel segmentation in angiography. In *Proceedings 15th International Conference on Pattern Recognition. ICPR-2000*, volume 4, pages 340–343 vol.4, 2000.
- [189] J. A. Tyrrell, E. di Tomaso, D. Fuja, R. Tong, K. Kozak, R. K. Jain, and B. Roysam. Robust 3-D modeling of vasculature imagery using superellipsoids. *IEEE Transactions on Medical Imaging*, 26(2):223–237, Feb 2007.
- [190] B. Urick, T. M. Sanders, S. S. Hossain, Y. J. Zhang, and T. J. Hughes. Review of patient-specific vascular modeling: Template-based isogeometric framework and the case for CAD. *Archives of Computational Methods in Engineering*, pages 1–24, 2017.
- [191] R. van ’t Klooster, P. J. de Koning, R. A. Dehnavi, J. T. Tamsma, A. de Roos, J. H. Reiber, and R. J. van der Geest. Automatic lumen and outer wall segmentation of the carotid artery using deformable three-dimensional models in MR angiography and vessel wall images. *Journal of Magnetic Resonance Imaging*, 35(1):156–165, 2012.
- [192] A. Vasilevskiy and K. Siddiqi. Flux maximizing geometric flows. *IEEE Transactions on Pattern Analysis and Machine Intelligence*, 24(12):1565–1578, Dec 2002.
- [193] M. d. Vitturi. Navier-Stokes equations in cylindrical coordinates. 2016.

- [194] X. Wang, Y. Liu, Z. Wu, X. Mou, M. Zhou, M. A. G. Ballester, and C. Zhang. Automatic labeling of vascular structures with topological constraints via HMM. In *International Conference on Medical Image Computing and Computer-Assisted Intervention – MICCAI*, pages 208–215. Springer, 2017.
- [195] P. G. Ward, N. J. Ferris, P. Raniga, D. L. Dowe, A. C. Ng, D. G. Barnes, and G. F. Egan. Combining images and anatomical knowledge to improve automated vein segmentation in MRI. *Neuroimage*, 165:294–305, 2018.
- [196] J. M. Wardlaw, E. E. Smith, G. J. Biessels, C. Cordonnier, F. Fazekas, R. Frayne, R. I. Lindley, et al. Neuroimaging standards for research into small vessel disease and its contribution to ageing and neurodegeneration. *The Lancet Neurology*, 12(8):822 – 838, 2013.
- [197] E. A. Warnert, J. C. Rodrigues, A. E. Burchell, S. Neumann, L. E. Ratcliffe, N. E. Manghat, A. D. Harris, Z. H. Adams, A. K. Nightingale, R. G. Wise, J. F. Paton, and E. C. Hart. Is high blood pressure self-protection for the brain? *Circulation Research*, 2016.
- [198] J. Weickert. Coherence-enhancing diffusion filtering. *International Journal of Computer Vision*, 31(2):111–127, 1999.
- [199] N. Westerhof, J.-W. Lankhaar, and B. E. Westerhof. The arterial Windkessel. *Medical & Biological Engineering & Computing*, 47(2):131–141, Feb 2009.
- [200] M. L. Williams, R. C. Wilson, and E. R. Hancock. Multiple graph matching with Bayesian inference. *Pattern Recognition Letters*, 18(11):1275 – 1281, 1997.
- [201] S. Wörz and K. Rohr. A new 3D parametric intensity model for accurate segmentation and quantification of human vessels. In *International Conference on Medical Image Computing and Computer-Assisted Intervention – MICCAI*, pages 491–499. Springer, 2004.

- [202] S. Wörz and K. Rohr. Cramér-Rao bounds for estimating the position and width of 3D tubular structures and analysis of thin structures with application to vascular images. *Journal of Mathematical Imaging and Vision*, 30(2):167–180, 2008.
- [203] G. Wu, B. Munsell, P. Laurienti, and M. K. Chung. GRAND: Unbiased connectome atlas of brain network by groupwise graph shrinkage and network diffusion. In G. Wu, I. Rekik, M. D. Schirmer, A. W. Chung, and B. Munsell, editors, *Connectomics in NeuroImaging*, pages 127–135, Cham, 2018. Springer International Publishing.
- [204] H. Xue, C. Malamateniou, J. Allsop, L. Srinivasan, J. V. Hajnal, and D. Rueckert. Automatic extraction and matching of neonatal cerebral vasculature. In *IEEE International Symposium on Biomedical Imaging: Nano to Macro*, pages 125–128. IEEE, 2006.
- [205] J. Yan, M. Cho, H. Zha, X. Yang, and S. M. Chu. Multi-graph matching via affinity optimization with graduated consistency regularization. *IEEE Transactions on Pattern Analysis and Machine Intelligence*, 38(6):1228–1242, 2016.
- [206] J. Yan, Y. Li, W. Liu, H. Zha, X. Yang, and S. M. Chu. Graduated consistency-regularized optimization for multi-graph matching. In *European Conference on Computer Vision*, pages 407–422. Springer, 2014.
- [207] J. Yan, J. Wang, H. Zha, X. Yang, and S. M. Chu. Consistency-driven alternating optimization for multigraph matching: a unified approach. *IEEE Trans. Image Processing*, 24(3):994–1009, 2015.
- [208] J. Yang, H. Li, D. Campbell, and Y. Jia. Go-ICP: a Globally Optimal Solution to 3D ICP Point-Set Registration. *IEEE Transactions on Pattern Analysis and Machine Intelligence*, 38(11):2241–2254, 2016.
- [209] D. R. Yavagal and K. Atchaneeyasakul. Cerebrovascular variants in posterior circulation. *Circulation Research*, 119(12):1267–1269, 2016.

- [210] P. J. Yim, J. J. Cebral, R. Mullick, H. B. Marcos, and P. L. Choyke. Vessel surface reconstruction with a tubular deformable model. *IEEE Transactions on Medical Imaging*, 20(12):1411–1421, Dec 2001.
- [211] S. Ying, G. Wu, Q. Wang, and D. Shen. Hierarchical unbiased graph shrinkage (HUGS): A novel groupwise registration for large data set. *NeuroImage*, 84:626 – 638, 2014.
- [212] R. Zass and A. Shashua. Probabilistic graph and hypergraph matching. In *IEEE Conference on Computer Vision and Pattern Recognition*, pages 1–8. IEEE, 2008.
- [213] X. Zhang, C. Jin, P. Hu, X. Zhu, W. Hou, J. Xu, C. Wang, Y. Zhang, Z.-D. Ma, and H. Smith. NURBS modeling and isogeometric shell analysis for complex tubular engineering structures. *Computational and Applied Mathematics*, 36(4):1659–1679, 2017.
- [214] Y. Zhang, Y. Bazilevs, S. Goswami, C. L. Bajaj, and T. J. Hughes. Patient-specific vascular NURBS modeling for isogeometric analysis of blood flow. *Computer Methods in Applied Mechanics and Engineering*, 196(29-30):2943–2959, 2007.
- [215] F. Zhou and F. De la Torre. Factorized graph matching. *IEEE Transactions on Pattern Analysis and Machine Intelligence*, 38(9):1774–1789, 2016.
- [216] M. A. Zuluaga, R. Rodionov, M. Nowell, S. Achhala, G. Zombori, M. J. Cardoso, A. Miserocchi, A. W. McEvoy, J. S. Duncan, and S. Ourselin. SEEG trajectory planning: combining stability, structure and scale in vessel extraction. In *International Conference on Medical Image Computing and Computer-Assisted Intervention – MICCAI*, pages 651–658. Springer, 2014.
- [217] M. A. Zuluaga, R. Rodionov, M. Nowell, S. Achhala, G. Zombori, A. F. Mendelson, M. J. Cardoso, A. Miserocchi, A. W. McEvoy, J. S. Duncan, and

S. Ourselin. Stability, structure and scale: improvements in multi-modal vessel extraction for SEEG trajectory planning. *International Journal of Computer Assisted Radiology and Surgery*, 10(8):1227–1237, 2015.